

**AGH**  
**University of Science and Technology**

---

FACULTY OF COMPUTER SCIENCE, ELECTRONICS AND TELECOMMUNICATIONS

DEPARTMENT OF ELECTRONICS



PH.D. THESIS

KAMIL STASZEK

**BROADBAND MEASUREMENTS OF SCATTERING  
PARAMETERS UTILIZING BUTLER MATRICES**

SUPERVISOR:

D.Sc. Sławomir Gruszczyński, prof. AGH

Kraków 2015



**BROADBAND MEASUREMENTS OF SCATTERING  
PARAMETERS UTILIZING BUTLER MATRICES**

KAMIL STASZEK

Copyright © 2015 Kamil Staszek

AGH UNIVERSITY OF SCIENCE AND TECHNOLOGY  
DEPARTMENT OF ELECTRONICS

Supervisor

D.Sc. Sławomir Gruszczynski, prof. AGH

Declaration

I hereby declare that the work in this Thesis is my own original work, except where indicated in the text.

The Thesis is based on the following publications:

K. Staszek, S. Gruszczynski and K. Wincza, "Broadband measurements of S-parameters utilizing 4 x 4 Butler matrices," *IEEE Transactions on Microwave Theory and Techniques*, vol. 61, no. 4, pp. 1692–1699, April 2013.

K. Staszek, S. Gruszczynski and K. Wincza, "Theoretical limits and accuracy improvement of reflection coefficient measurements in six-port reflectometers," *IEEE Transactions on Microwave Theory and Techniques*, vol. 61, no. 8, pp. 2966–2974, August 2013.

K. Staszek, S. Gruszczynski and K. Wincza, "Broadband measurements of S-parameters with the use of a single 8 x 8 Butler matrix," *IEEE Transactions on Microwave Theory and Techniques*, vol. 62, no. 2, pp. 352–360, February 2014.

K. Staszek, S. Gruszczynski and K. Wincza, "Design and accuracy analysis of a broadband six-port reflectometer utilizing coupled-line directional couplers," *Microwave and Optical Technology Letters*, vol. 55, no. 7, pp. 1485–1490, July 2013.

K. Staszek, S. Gruszczynski and K. Wincza, "Accurate broadband multiport reflectometer," *Microwave and Optical Technology Letters*, vol. 56, no. 12, pp. 2884–2887, December 2014.

K. Staszek, S. Gruszczynski and K. Wincza, "Broadband Butler matrices with the use of high-pass LC sections as left-handed transmission lines," *Radioengineering*, vol. 23, no. 1, pp. 236–243, April 2014.

K. Staszek, S. Gruszczynski K. Wincza and A. Rydosz, "Broadband measurements of reflection coefficient with the use of Butler matrix," in *Proc. of International Microwave and Optoelectronics Conference IMOC 2013*, Rio de Janeiro, Brazil, August 2013, pp. 1–4.

K. Staszek, P. Kaminski, A. Rydosz, S. Gruszczynski and K. Wincza, "A least-squares approach to the calibration of multiport reflectometers," in *Proc. of International Microwave & RF Conference IMArc 2013*, New Delhi, India, December 2013, pp. 1–4.

K. Staszek, S. Gruszczynski and K. Wincza, "Application of the 4 x 4 Butler matrix consisting of tapered-coupled-line directional couplers in an ultra-broadband multiport reflectometer," in *Proc. of The Second International Conference on Technological Advances in Electrical, Electronics and Computer Engineering TAAECE 2014*, Kuala Lumpur, Malaysia, March 2014, pp. 1–6.

K. Staszek, S. Gruszczynski and K. Wincza, "Ultra-broadband six-port reflectometer," in *Proc. of the 14th Mediterranean Microwave Symposium MMS 2014*, Marrakech, Morocco, December 2014, pp. 1–4.

K. Staszek, S. Gruszczynski and K. Wincza, "Compact multiport system for broadband measurement of S-parameters," in *Proc. of German Microwave Conference GeMiC 2015*, Nuernberg, Germany, March 2015, pp. 1–4.

Work presented in this Thesis was supported in part by the Polish Ministry of Science and Higher Education under grant no. 0163/IP2/2011/71, in part by the National Science Centre under grant no. DEC–2013/09/N/ST7/01219, in part by DOCTUS – Lesser Poland Scholarship Fund for PhD Students under contract no. ZS.4112-58/12 and in part by the statutory research of AGH University of Science and Technology under grants no. 15.11.230.076 and no. 15.11.230.146.

February 2015

# **BROADBAND MEASUREMENTS OF SCATTERING PARAMETERS UTILIZING BUTLER MATRICES**

KAMIL STASZEK

## **Abstract**

Scattering parameters are widely used form of description for linear microwave components. Their measurements are inseparable in microwave engineering. Usually for such measurements vector network analyzers in microwave laboratories are utilized. However, in many applications, especially those requiring compact and low-cost measuring equipment, the multiport measurement technique can be used. It is a method allowing for the determination of scattering parameters in terms of both magnitude and phase by simple scalar power measurements.

The key component of each multiport measuring system is a dedicated power distribution network, which provides appropriate signals' relations enabling correct measurement. In the Thesis it is shown, that in such systems classic Butler matrices can be applied instead of dedicated multiport networks. The presented analysis reveals that utilizing Butler matrices one can measure both reflection and transmission coefficients and the measuring set-up can be simplified with respect to the classic solutions. The Thesis presents theoretical analysis of several proposed measuring systems involving Butler matrices being capable of broadband operation. It is presented that the multiport systems, in which the role of power division networks is performed by Butler matrices, feature a number of possible configurations in contrast to the classic systems, in case of which only one system's arrangement can be applied. Furthermore, universal calibration techniques applicable for arbitrary measuring systems for the measurement of reflection and transmission coefficients in wide operational frequency range are proposed.

The application of Butler matrices instead of dedicated six-ports in multiport measurements forces to compare the measurement accuracy of the proposed systems with those, in which classic six-ports are utilized. A comprehensive studies of the measurement errors have shown that the systems incorporating Butler matrices provide higher measurement accuracy than the classic solutions. Further analysis of the measurement error sources has led to the development of novel multiport systems featuring a tunable power distribution, which provide an enhanced measurement accuracy for scattering parameters having small magnitudes. As it is shown such a property can be easily implemented in systems involving Butler matrices.

All the multiport systems theoretically investigated in the Thesis have been developed for an experimental verification in broad frequency range. The measurements of exemplary microwave components prove that the Butler matrices can serve in multiport measuring systems. Moreover, they provide higher measurement accuracy than the classic six-port reflectometers, which confirms the theoretical investigation. Finally, the concept of multiport systems featuring tunable power distribution has been verified for two proposed systems involving a classic Butler matrix. The obtained results clearly show the enhanced measurement accuracy, certifying the novel class of tunable multiport measuring systems.



# SZEROKOPASMOWE POMIARY PARAMETRÓW ROZPROSZENIA OBWODÓW MIKROFALOWYCH Z WYKORZYSTANIEM MACIERZY BUTLERA

KAMIL STASZEK

## Streszczenie

Parametry rozproszenia stanowią powszechną formę opisu liniowych obwodów mikrofalowych, a ich pomiar jest nieodłączną częścią techniki mikrofalowej. Zazwyczaj do tego rodzaju pomiarów w laboratoriach mikrofalowych stosuje się wektorowe analizatory sieci. Jednak w przypadku wielu zastosowań, w szczególności gdy wymagana jest miniaturyzacja oraz niskie koszty aparatury pomiarowej, atrakcyjną alternatywą staje się wielowrotowa technika pomiaru. Jest to metoda umożliwiająca wyznaczenie zespolonych parametrów rozproszenia poprzez skalarny pomiar mocy.

Kluczowym elementem każdego systemu wielowrotowego jest sieć podziału mocy, która zapewnia odpowiednie relacje sygnałów niezbędnych do wykonania pomiaru. W niniejszej rozprawie wykazano, że w systemach wielowrotowych w miejsce dedykowanych sześciowrotowych obwodów podziału mocy zastosować można klasyczne macierze Butlera. Z przedstawionej analizy wynika, iż przy użyciu macierzy Butlera możliwy jest pomiar zarówno współczynnika odbicia, jak i współczynnika transmisji przy jednoczesnym uproszczeniu układu pomiarowego w stosunku do klasycznych rozwiązań. W rozprawie przedstawiono analizę teoretyczną kilku zaproponowanych systemów pomiarowych, w których zastosowano szerokopasmowe macierze Butlera. Wykazano, że w opracowanych systemach wyróżnić można znaczną ilość możliwych konfiguracji układowych w przeciwieństwie do klasycznych systemów sześciowrotowych, w przypadku których istnieje tylko jedna poprawna konfiguracja. Ponadto zaproponowano uniwersalne techniki kalibracji dowolnych systemów wielowrotowych dla pomiaru współczynnika odbicia, jak i współczynnika transmisji, które stosować można w szerokim zakresie częstotliwości.

Zastosowanie macierzy Butlera w zastępstwie dedykowanych układów sześciowrotowych skłania do porównania zaproponowanych systemów z układami klasycznymi pod względem dokładności pomiaru. Poprzez wnikliwą analizę błędów pomiaru wykazano, że systemy pomiarowe wykorzystujące macierze Butlera zapewniają większą dokładność pomiaru niż rozwiązania klasyczne. Dalsze badania nad źródłem błędów pomiaru doprowadziły do opracowania nowej klasy systemów pomiarowych o strojonym podziale mocy, które zapewniają zwiększoną precyzję pomiaru parametrów rozproszenia o małym module. Jak pokazano, strojony podział mocy z łatwością zrealizować można w systemach wykorzystujących macierze Butlera.

Wielowrotowe systemy pomiarowe przedstawione w niniejszej rozprawie poddane zostały weryfikacji eksperymentalnej w szerokopasmowych pomiarach parametrów rozproszenia. Otrzymane wyniki potwierdziły, że macierze Butlera z powodzeniem stosować można w systemach wielowrotowych, a uzyskiwana w ten sposób dokładność pomiaru jest wyższa niż w przypadku rozwiązań klasycznych. Weryfikacji eksperymentalnej poddano również dwa opracowane szerokopasmowe systemy o strojonym podziale mocy. Przeprowadzone z ich użyciem pomiary parametrów rozproszenia wykazały znaczną poprawę precyzji pomiaru, uzasadniając użyteczność nowej klasy wielowrotowych systemów pomiarowych.



I would like to express my great gratitude to PROF. SŁAWOMIR GRUSZCZYŃSKI for motivation during my PhD studies and for supervising the research presented in the Thesis. I am very thankful to DR KRZYSZTOF WINCZA for his constant encouragement and enormous help in my research. Special thanks are also extended to my colleagues IZABELA SŁOMIAN, ILONA PIEKARZ, JAKUB SOROCKI and PIOTR KAMIŃSKI for excellent teamwork. Finally, I would like to thank and dedicate this Thesis to my lovely wife MONIKA, who inspired me and provided constant support during my research activity.

Author



# Contents

<b>1. Introduction</b> .....	27
1.1. Principles of Multiport Measurement Technique .....	27
1.2. Butler Matrices .....	31
1.3. Description and Aim of This Work .....	34
<b>2. Reflection Coefficient Measurements</b> .....	37
2.1. Classic Six-Port Reflectometers .....	37
2.1.1. Six-Port Design .....	37
2.1.2. Design of Ultra-Broadband Classic Six-Port Reflectometer.....	39
2.2. Application of Butler Matrices in Reflection Coefficient Measurements .....	41
2.2.1. Reflectometer Utilizing Classic $4 \times 4$ Butler Matrix.....	41
2.2.2. Reflectometer Based on $4 \times 4$ Butler Matrix Consisting of Tapered-Coupled-Line Directional Couplers .....	43
2.2.3. Reflectometer Utilizing Classic $8 \times 8$ Butler Matrix.....	45
2.3. Calibration for Reflection Coefficient Measurements .....	48
2.3.1. Comparison of Direct Analytical Approach and Numerical Procedure for Calibration of Multiport Reflectometers .....	48
2.3.2. Multiport Calibration .....	50
2.3.3. Error Box Calibration.....	52
2.3.4. Choice of Calibration Standards in Broadband Calibration.....	54
2.3.5. Description of Utilized Calibration Standards .....	55
2.4. Measurement Accuracy Analysis of Multiport Reflectometers .....	57
2.4.1. Theoretical Limitations on Multiport Measurements .....	58
2.4.2. Magnitude and Phase Measurement Error Distribution.....	62
2.5. Experimental Verification .....	67
2.5.1. Broadband Six-Port Reflectometer .....	68
2.5.2. Ultra-Broadband Six-Port Reflectometer.....	70
2.5.3. Broadband Reflectometer Utilizing Classic $4 \times 4$ Butler Matrix .....	73

2.5.4. Ultra-Broadband Reflectometer Based on $4 \times 4$ Butler Matrix Consisting of Tapered-Coupled-Line Directional Couplers .....	75
2.5.5. Broadband Reflectometer Incorporating Classic $8 \times 8$ Butler Matrix.....	76
2.5.6. Analysis of Measurement Results.....	78
2.6. Conclusions .....	79
<b>3. Transmission Coefficient Measurements .....</b>	<b>81</b>
3.1. Measurements With the Use of Two Classic $4 \times 4$ Butler Matrices .....	81
3.1.1. Theoretical Analysis .....	82
3.1.2. Calibration for Transmission Coefficient Measurements Using System Composed of Two Butler Matrices .....	83
3.1.3. Influence of Model Simplification on Transmission Coefficient Measurements .....	87
3.2. Measurements With the Use of Single $8 \times 8$ Butler Matrix.....	90
3.2.1. Theoretical Analysis .....	90
3.2.2. Model of Single-Multiport Reflectometer for $S$ -Parameter Measurements .....	91
3.2.3. Calibration of Single Reflectometer for $S$ -Parameter Measurements.....	94
3.3. Analysis of Calibration Standards for Broadband Calibration.....	96
3.4. Experimental Verification.....	98
3.4.1. Broadband Measurements of Transmission Coefficient With the Use of Two Classic $4 \times 4$ Butler Matrices .....	99
3.4.2. Broadband Measurements of Transmission Coefficient Utilizing Single $8 \times 8$ Butler Matrix.....	101
3.4.3. Analysis of Measurement Results.....	103
3.5. Conclusions .....	104
<b>4. <math>S</math>-parameter Measurements With the Use of Tunable Multiport Systems .....</b>	<b>107</b>
4.1. Tunable System With Isolator .....	107
4.1.1. Theoretical Analysis .....	108
4.1.2. Application of External Directional Coupler .....	109
4.1.3. Application of Adjustable Attenuator .....	111
4.2. Tunable System Without Isolator .....	112
4.2.1. Theoretical Analysis .....	112
4.3. Measurement Accuracy for Measuring Systems Featuring Scalable Circle Centers' Distribution.....	115
4.4. Calibration Accuracy for Measuring Systems Featuring Scalable Circle Centers' Distribution.....	115
4.5. Experimental Verification.....	117
4.5.1. Broadband Measuring System With Isolator .....	117

---

4.5.2. Broadband Measuring System Without Isolator .....	122
4.5.3. Analysis of Measurement Results .....	136
4.6. Conclusions .....	138
<b>5. Summary</b> .....	<b>139</b>
<b>Author's Achievements</b> .....	<b>143</b>
<b>Bibliography</b> .....	<b>157</b>



## List of Figures

1.1	Incident and reflected waves related to an arbitrary two-port network.....	27
1.2	Power distribution in an arbitrary multiport passive power division network with one-port DUT connected. ....	28
1.3	Geometric interpretation of reflection coefficient measurement. ....	29
1.4	Incorrect arrangement of circle centers leading to an ambiguous measurement results. ....	30
1.5	Several intersection points resulting from circles radii deteriorated by noise and measurement inaccuracy of the applied power meters. ....	30
1.6	Schematic diagram of an ideal $4 \times 4$ Butler matrix consisting of four 3dB/90° directional couplers and two 45° phase shifters [84]. (Copyright © 2014, Radioengineering).....	32
1.7	Schematic diagram of an ideal $8 \times 8$ Butler matrix consisting of twelve 3dB/90° directional couplers and eight phase shifters. ....	33
2.1	Schematic diagram of the investigated six-port [24], [80].....	38
2.2	Circle centers' distribution of the six-port presented in Fig. 2.1 [80]. (Copyright © 2013, Wiley Periodicals, Inc.) .....	38
2.3	Circle centers' distribution of the six-port with inserted additional section of transmission line having electrical length $\Theta_{TL} = 210^\circ$ [80]. (Copyright © 2013, Wiley Periodicals, Inc.) .....	39
2.4	Schematic diagram of the proposed ultra-broadband six-port reflectometer (a) and schematic diagram of the simplified Magic-T circuit (b) [86]. (Copyright © 2014, IEEE) .....	40
2.5	Schematic diagram of a multiport measuring system with a $4 \times 4$ Butler matrix allowing for reflection coefficient measurements [79]. (Copyright © 2013, IEEE) .....	41
2.6	Schematic diagram of the proposed multiport reflectometer with a single $4 \times 4$ Butler matrix utilizing tapered-coupled-line directional couplers [37], [83] (Copyright © 2014, SDIWC). ....	44
2.7	Schematic diagram of the proposed multiport measuring system with a single $8 \times 8$ Butler matrix allowing for reflection coefficient measurement [85]. (Copyright © 2014, IEEE) .....	46
2.8	All possible distributions of circle centers related to the $8 \times 8$ Butler matrix. The last distribution, containing only two circle centers cannot be utilized in measurements, due to ambiguous results [85]. (Copyright © 2014, IEEE) .....	47

2.9	The distance between the circle center $c_4$ and the origin of a complex plane as a comparison between the calibration procedures based on direct analytical approach and on numerical algorithm [79]. (Copyright © 2013, IEEE) .....	49
2.10	Actual reflectometer modeled as an ideal reflectometer connected to an error box network [31], [89]. (Copyright © 2013, IEEE) .....	52
2.11	The influence of operating frequency on calibration reflections' distribution. The optimal reflections' distribution for properly chosen offset value at a given frequency $f_1$ (a) and the corresponding distribution for frequency $f_2 \approx 2f_1$ (b) [88]. (Copyright © 2013, IEEE) .....	54
2.12	The angles of calibration standards obtained with the use of offset A. ....	56
2.13	Minimum angle differences for four offsets utilized in the calibration procedure. ....	56
2.14	Chosen offset number vs. measurement frequency.....	57
2.15	The minimum angle difference corresponding to the chosen offset vs. measurement frequency.....	57
2.16	Influence of power measurement uncertainty on the circles radii. Ideal case with a single intersection point (a). Real case with detectors uncertainty taken into account (b). Detailed view of the rings' intersection area – RIA, where dashed lines present circles from Fig. 2.16a and solid lines present the borders of rings for the case of $\Gamma = 0$ (c) [81]. (Copyright © 2013, IEEE) .....	59
2.17	The comparison of RIA for seven analyzed multiports with assumed power detector uncertainty equal to $\pm 0.1$ dB.....	61
2.18	Circle centers' distribution and the corresponding distribution of the maximum measurement error for seven analyzed multiport reflectometers: SPid2 (a) and (b), SPell (c) and (d), SPstd (e) and (f), BM4x4 <sub>3p</sub> (g) and (h), BM8x8 <sub>4p</sub> (i) and (j), SPid1 (k) and (l), BM8x8 <sub>7p</sub> (m) and (n). The assumed power detectors uncertainty $\Delta_{PD} = \pm 0.1$ dB.....	65
2.19	The analysis of rings intersection area in a close proximity of one of the circle centers. The distinct irregularity of intersection area is seen [81]. (Copyright © 2013, IEEE) .....	66
2.20	The maximum magnitude (a) and phase (b) measurement error vs. magnitude of reflection coefficient for seven different multiport reflectometers. The assumed power detectors uncertainty $\Delta_{PD} = \pm 0.1$ dB. ....	66
2.21	The maximum magnitude (a) and phase (b) measurement error vs. magnitude of reflection coefficient for seven different multiport reflectometers, for reflection coefficient magnitude range from -20 dB to 0 dB. The assumed power detectors uncertainty $\Delta_{PD} = \pm 0.1$ dB.....	66
2.22	Cross-sectional view of the stripline layers used for the design of the broadband six-port reflectometer [80]. (Copyright © 2013, Wiley Periodicals, Inc.) .....	68
2.23	Layout of the presented broadband six-port reflectometer [80]. Top metallization layer is marked black, whereas bottom metallization layer is marked gray. (Copyright © 2013, Wiley Periodicals, Inc.) .....	68

2.24	Circle centers' distribution of the six-port presented in Fig. 2.23. Results of electromagnetic calculations [80]. (Copyright © 2013, Wiley Periodicals, Inc.).....	69
2.25	Results of the calibration procedure for the broadband six-port reflectometer described in Subsection 2.1.1: magnitude (a) and phase (b) of circle centers, circle centers' distribution on a complex plane (c) and the magnitude of reflection coefficient seen at the measuring port (d).....	69
2.26	Reflection coefficients of a set of shorted attenuators measured using the broadband six-port reflectometer described in Subsection 2.1.1: magnitude (a) and phase (b). Solid lines represents the measurements obtained with the use of the proposed reflectometer, dashed lines correspond to the reference values. ....	70
2.27	Cross-sectional view of the dielectric structure used for the design of the ultra-broadband six-port reflectometer [86]. (Copyright © 2014, IEEE).....	70
2.28	Return loss and phase shift of the designed single-section Schiffman phase shifter. Results of electromagnetic calculations [86]. (Copyright © 2014, IEEE).....	71
2.29	Layout of the proposed ultra-broadband six-port reflectometer [86]. Top metallization layer is marked black, whereas bottom metallization layer is marked gray. (Copyright © 2014, IEEE). ....	71
2.30	Circle centers' distribution of the proposed ultra-broadband six-port reflectometer obtained with the use of electromagnetic calculations: magnitude (a) and phase (b) of circle centers [86]. (Copyright © 2014, IEEE).....	72
2.31	Results of the calibration procedure for the ultra-broadband six-port reflectometer described in Subsection 2.1.2: magnitude (a) and phase (b) of circle centers, circle centers' distribution on a complex plane (c) and the magnitude of reflection coefficient seen at the measuring port (d) [86]. (Copyright © 2014, IEEE).....	72
2.32	Reflection coefficients of a set of shorted attenuators measured using the ultra-broadband six-port reflectometer described in Subsection 2.1.2: magnitude (a) and phase (b). Solid lines represents the measurements obtained with the use of the proposed reflectometer, dashed lines correspond to the reference values. ....	73
2.33	Results of the calibration procedure for the reflectometer utilizing $4 \times 4$ Butler matrix described in Subsection 2.2.1: magnitude (a) and phase (b) of circle centers, circle centers' distribution on a complex plane (c) and the magnitude of reflection coefficient seen at the measuring port (d).....	74
2.34	Reflection coefficients of a set of shorted attenuators measured using the reflectometer utilizing $4 \times 4$ Butler matrix described in Subsection 2.2.1: magnitude (a) and phase (b). Solid lines represents the measurements obtained with the use of the proposed reflectometer, dashed lines correspond to the reference values. ....	74

2.35 Results of the calibration procedure for the reflectometer utilizing $4 \times 4$ Butler matrix consisting of tapered-coupled-line directional couplers described in Subsection 2.2.2: magnitude (a) and phase (b) of circle centers, circle centers' distribution on a complex plane (c) and the magnitude of reflection coefficient seen at the measuring port (d) [83]. (Copyright © 2014, SDIWC).....	75
2.36 Reflection coefficients of a set of shorted attenuators measured using the reflectometer utilizing $4 \times 4$ Butler matrix consisting of tapered-coupled-line directional couplers described in Subsection 2.2.2: magnitude (a) and phase (b). Solid lines represents the measurements obtained with the use of the proposed reflectometer, dashed lines correspond to the reference values.....	76
2.37 Results of the calibration procedure for the reflectometer utilizing $8 \times 8$ Butler matrix described in Subsection 2.2.3: magnitude (a) and phase (b) of circle centers, circle centers' distribution on a complex plane (c) and the magnitude of reflection coefficient seen at the measuring port (d).....	77
2.38 Reflection coefficients of a set of shorted attenuators measured using the reflectometer utilizing $8 \times 8$ Butler matrix described in Subsection 2.2.3: magnitude (a) and phase (b). Solid lines represents the measurements obtained with the use of the proposed reflectometer, dashed lines correspond to the reference values.....	77
2.39 Maximum magnitude (a) and phase (b) measurement error vs. the magnitude of the measured reflection coefficient for five broadband reflectometers described in Section 2.5. ....	78
3.1 Schematic diagram of a multiport measuring system with two $4 \times 4$ Butler matrices allowing for transmission coefficient measurements [79]. ....	82
3.2 All possible distributions of circle centers related to the multiport measuring system incorporating two $4 \times 4$ Butler matrices. ....	83
3.3 Signal flow in the multiport measuring system composed of two $4 \times 4$ Butler matrices for transmission coefficient measurements: graph of the entire measuring system with all imperfect parameters (a), graph of the measuring system with neglected imperfect isolations (b), graph of the measuring system with imperfect isolations and with assumed perfect impedance match of all components (c). ....	84
3.4 Estimated maximum relative power reading error vs. magnitude of the measured transmission coefficient (black lines) for four different values of isolations $I$ compared to the $\pm 0.1$ dB uncertainty of the power meters (gray line). ....	88
3.5 Estimated maximum error of transmission coefficient measurements introduced by the utilization of simplified formula (3.5) for an ideally matched two-port having zero-insertion loss ( $S_{21} = S_{12} = 1$ ). ....	90

3.6	Schematic diagram of the proposed multiport measuring system with a single $8 \times 8$ Butler matrix allowing for reflection and transmission coefficients measurements [85]. (Copyright © 2014, IEEE) .....	91
3.7	The flow graph of a single multiport reflectometer having imperfect isolation between its ports, allowing for the measurements of $S$ -parameters: graph of the entire measuring system (a), graph of the extracted multiport having imperfectly isolated ports with an isolator connected (b), graph of the measuring system with the multiport created from the actual multiport and isolator (c) [85]. (Copyright © 2014, IEEE) .....	93
3.8	Exemplary distribution of calibration standards for a given frequency. The maximum angle difference $\Delta$ is shown. ....	96
3.9	Phase of the analyzed calibration standards listed in Table 2.5 vs. frequency. ....	97
3.10	Maximum angle difference calculated for the analyzed calibration standards listed in Table 2.5 vs. frequency. ....	98
3.11	Results of the calibration procedure for the measuring system utilizing two $4 \times 4$ Butler matrices described in Subsection 3.1.1: magnitude (a) and phase (b) of circle centers, circle centers' distribution on a complex plane (c), impedance match of the measuring ports and isolation between measuring ports (d). ....	100
3.12	Transmission coefficients of a set of attenuators measured using the measuring system utilizing $4 \times 4$ Butler matrices described in Subsection 3.1.1: magnitude (a) and phase (b). Solid lines represents the measurements obtained with the use of the presented system, dashed lines correspond to the reference values. ....	100
3.13	$S$ -parameters of the bandpass filter measured using the measuring system utilizing $4 \times 4$ Butler matrices described in Subsection 3.1.1: magnitude (a) and phase (b). Solid lines represents the measurements obtained with the use of the presented system, dashed lines correspond to the reference values. Reflection coefficient is marked black, whereas transmission coefficient is marked gray. ....	101
3.14	Measured transmission coefficients of the utilized isolator $S_{IS21}$ and $S_{IS12}$ and isolation of the utilized $8 \times 8$ Butler matrix between the measuring port and the port to which the isolator is connected $S_{BM9,11}$ .....	102
3.15	Results of the calibration procedure for the measuring system involving the single $8 \times 8$ Butler matrix. Calibration constants $A$ (a), $B$ (b) and $C$ (c) vs. frequency. ....	102
3.16	Transmission coefficients of a set of attenuators measured using the measuring system utilizing the single $8 \times 8$ Butler matrix described in Subsection 3.2.1: magnitude (a) and phase (b). Solid lines represents the measurements obtained with the use of the presented system, dashed lines correspond to the reference values. ....	102

3.17	<i>S</i> -parameters of the bandpass filter measured using the measuring system utilizing the single $8 \times 8$ Butler matrix described in Subsection 3.2.1: magnitude (a) and phase (b). Solid lines represents the measurements obtained with the use of the presented system, dashed lines correspond to the reference values. Reflection coefficient is marked black, whereas transmission coefficient is marked gray.....	103
3.18	Maximum magnitude (a) and phase (b) measurement error vs. the magnitude of the measured transmission coefficient for two broadband measuring systems described in Section 3.4. ....	104
4.1	Schematic diagram of the proposed tunable measuring system with an isolator [87]. (Copyright © 2015, IEEE) .....	108
4.2	Signal flow for the transmission between port #1 and port #2 of the directional coupler connected to a $4 \times 4$ Butler matrix. Signal paths corresponding to imperfections of the Butler matrix are marked gray [82]. (Copyright © 2014, Wiley Periodicals, Inc.) .....	109
4.3	Schematic diagram of the proposed measuring system composed of a $4 \times 4$ Butler matrix and two directional couplers. ....	112
4.4	The maximum magnitude (a) and phase (b) measurement error for the measuring systems featuring scalable circle centers' distributions presented in Sections 4.1 and 4.2. The assumed power detectors uncertainty $\Delta_{PD} = \pm 0.1$ dB.....	115
4.5	The optimal distribution of four calibration standards for calibration accuracy analysis [81]. (Copyright © 2013, IEEE) .....	116
4.6	The maximum calibration error in a sense of distance between the genuine circle center and the one calculated in calibration vs. the magnitude of circle centers' distribution. The assumed power detectors uncertainty $\Delta_{PD} = \pm 0.1$ dB [81]. (Copyright © 2013, IEEE).....	116
4.7	Results of the calibration procedure for the tunable measuring system with isolator described in Subsection 4.1.1 for theoretical magnitude of circle centers' distribution equal to 1: magnitude (a) and phase (b) of circle centers, circle centers' distribution on a complex plane (c) and the magnitude of reflection coefficient seen at the measuring port (d). The additional circle center resulting from the use of the additional coupler is marked gray.....	118
4.8	Results of the calibration procedure for the tunable measuring system with isolator described in Subsection 4.1.1 for theoretical magnitude of circle centers' distribution equal to 0.79: magnitude (a) and phase (b) of circle centers, circle centers' distribution on a complex plane (c) and the magnitude of reflection coefficient seen at the measuring port (d). The additional circle center resulting from the use of the additional coupler is marked gray.....	119

- 4.9 Results of the calibration procedure for the tunable measuring system with isolator described in Subsection 4.1.1 for theoretical magnitude of circle centers' distribution equal to 0.63: magnitude (a) and phase (b) of circle centers, circle centers' distribution on a complex plane (c) and the magnitude of reflection coefficient seen at the measuring port (d). The additional circle center resulting from the use of the additional coupler is marked gray..... 120
- 4.10 Results of the calibration procedure of the tunable measuring system with isolator described in Subsection 4.1.1 for transmission coefficient measurements. Calibration constants  $A$  (a),  $B$  (b) and  $C$  (c) vs. frequency..... 120
- 4.11 Reflection coefficients of a set of attenuators terminated with a short-circuit measured using the tunable measuring system with isolator described in Subsection 4.1.1: magnitude (a) and phase (b). Solid lines represents the measurements obtained with the use of the presented system, dashed lines correspond to the reference values. .... 121
- 4.12 Transmission coefficients of a set of attenuators measured using the tunable measuring system with isolator described in Subsection 4.1.1: magnitude (a) and phase (b). Solid lines represents the measurements obtained with the use of the presented system, dashed lines correspond to the reference values. .... 121
- 4.13  $S$ -parameters of the bandpass filter measured using the tunable measuring system with isolator described in Subsection 4.1.1: magnitude (a) and phase (b) of reflection coefficient and magnitude (c) and phase (d) of transmission coefficient. The measurement results have been obtained for three different magnitudes of circle centers' distribution: 1.00, 0.79 and 0.63. Solid lines represents the measurements obtained with the use of the presented system, dashed lines correspond to the reference values [87]. (Copyright © 2015, IEEE)..... 122
- 4.14 Results of the calibration procedure for reflection coefficient measurements utilizing the tunable measuring system without isolator described in Subsection 4.2.1 for theoretical magnitude of circle centers' distribution equal to 1: magnitude (a) and phase (b) of circle centers, circle centers' distribution on a complex plane (c) and the magnitude of reflection coefficient seen at the measuring port (d). .... 124
- 4.15 Results of the calibration procedure for reflection coefficient measurements utilizing the tunable measuring system without isolator described in Subsection 4.2.1 for theoretical magnitude of circle centers' distribution equal to 0.89: magnitude (a) and phase (b) of circle centers, circle centers' distribution on a complex plane (c) and the magnitude of reflection coefficient seen at the measuring port (d)..... 125
- 4.16 Results of the calibration procedure for reflection coefficient measurements utilizing the tunable measuring system without isolator described in Subsection 4.2.1 for theoretical magnitude of circle centers' distribution equal to 0.79: magnitude (a) and phase (b) of circle centers, circle centers' distribution on a complex plane (c) and the magnitude of reflection coefficient seen at the measuring port (d). .... 126

4.17 Results of the calibration procedure for reflection coefficient measurements utilizing the tunable measuring system without isolator described in Subsection 4.2.1 for theoretical magnitude of circle centers' distribution equal to 0.71: magnitude (a) and phase (b) of circle centers, circle centers' distribution on a complex plane (c) and the magnitude of reflection coefficient seen at the measuring port (d). .....	127
4.18 Results of the calibration procedure for reflection coefficient measurements utilizing the tunable measuring system without isolator described in Subsection 4.2.1 for theoretical magnitude of circle centers' distribution equal to 0.50: magnitude (a) and phase (b) of circle centers, circle centers' distribution on a complex plane (c) and the magnitude of reflection coefficient seen at the measuring port (d). .....	128
4.19 Results of the calibration procedure for transmission coefficient measurements utilizing the tunable measuring system without isolator described in Subsection 4.2.1 for theoretical magnitude of circle centers' distribution equal to 1: magnitude (a) and phase (b) of circle centers, circle centers' distribution on a complex plane (c), impedance match of the measuring ports and isolation between measuring ports (d). .....	129
4.20 Results of the calibration procedure for transmission coefficient measurements utilizing the tunable measuring system without isolator described in Subsection 4.2.1 for theoretical magnitude of circle centers' distribution equal to 0.89: magnitude (a) and phase (b) of circle centers, circle centers' distribution on a complex plane (c), impedance match of the measuring ports and isolation between measuring ports (d).....	130
4.21 Results of the calibration procedure for transmission coefficient measurements utilizing the tunable measuring system without isolator described in Subsection 4.2.1 for theoretical magnitude of circle centers' distribution equal to 0.79: magnitude (a) and phase (b) of circle centers, circle centers' distribution on a complex plane (c), impedance match of the measuring ports and isolation between measuring ports (d).....	131
4.22 Results of the calibration procedure for transmission coefficient measurements utilizing the tunable measuring system without isolator described in Subsection 4.2.1 for theoretical magnitude of circle centers' distribution equal to 0.71: magnitude (a) and phase (b) of circle centers, circle centers' distribution on a complex plane (c), impedance match of the measuring ports and isolation between measuring ports (d). .....	132
4.23 Results of the calibration procedure for transmission coefficient measurements utilizing the tunable measuring system without isolator described in Subsection 4.2.1 for theoretical magnitude of circle centers' distribution equal to 0.50: magnitude (a) and phase (b) of circle centers, circle centers' distribution on a complex plane (c), impedance match of the measuring ports and isolation between measuring ports (d). .....	133
4.24 Reflection coefficients of a set of attenuators terminated with a short-circuit measured using the tunable measuring system without isolator described in Subsection 4.2.1: magnitude (a) and phase (b). Solid lines represents the measurements obtained with the use of the presented system, dashed lines correspond to the reference values. ....	134

- 
- 4.25 Transmission coefficients of a set of attenuators measured using the tunable measuring system without isolator described in Subsection 4.2.1: magnitude (a) and phase (b). Solid lines represents the measurements obtained with the use of the presented system, dashed lines correspond to the reference values. .... 134
- 4.26 Transmission coefficients of the attenuator having attenuation of 50 dB measured with different magnitudes of circle centers' distribution. Solid lines represents the measurements obtained with the use of the presented system, dashed line corresponds to the reference values. .... 135
- 4.27 *S*-parameters of the highpass filter measured using the tunable measuring system without isolator described in Subsection 4.2.1: magnitude (a) and phase (b) of reflection coefficient and magnitude (c) and phase (d) of transmission coefficient. Solid lines represents the measurements obtained with the use of the presented system, dashed lines correspond to the reference values. .... 135
- 4.28 Maximum magnitude (a) and phase (b) measurement error vs. the magnitude of the measured reflection coefficient for the broadband tunable measuring system without isolator described in Subsection 4.5.2. .... 137
- 4.29 Maximum magnitude (a) and phase (b) measurement error vs. the magnitude of the measured transmission coefficient for the broadband tunable measuring system without isolator described in Subsection 4.5.2. .... 137



## List of Tables

1.1	Phase difference between two adjacent output ports of an ideal $4 \times 4$ Butler matrix ( $j + 1$ and $j$ ) for different choice of the excited input port $i$ .....	32
1.2	Phase difference between two adjacent output ports of an ideal $8 \times 8$ Butler matrix ( $j + 1$ and $j$ ) for different choice of the excited input port $i$ .....	33
2.1	Distribution of circle centers for different choice of measuring port and port with short-circuit, when the $4 \times 4$ Butler matrix is fed either at port #1 or #2 and $\Gamma_C = -1$ . ....	42
2.2	Distribution of circle centers for different choice of measuring port and port with short-circuit, when the $4 \times 4$ Butler matrix is fed either at port #3 or #4 and $\Gamma_C = -1$ . ....	43
2.3	Distribution of circle centers for different choice of measuring port and port with short-circuit, when the $4 \times 4$ Butler matrix is fed either at port #1 or #2 and $\Gamma_C = -1$ [83]. (Copyright © 2014, SDIWC) .....	44
2.4	Distribution of circle centers for different choice of measuring port and port with short-circuit, when the $4 \times 4$ Butler matrix is fed either at port #3 or #4 and $\Gamma_C = -1$ [83]. (Copyright © 2014, SDIWC) .....	45
2.5	Characterization of the calibration standards allowing for calibration of the broadband reflectometers presented in this Chapter. ....	55
2.6	Frequency dependance of the calibration standards realized as open-circuit, short-circuit and cascade connections of open- or short-circuits with chosen offsets. ....	56
2.7	Circle center distributions and corresponding theoretical limits of measured reflection coefficient magnitude for seven different multiports, assuming $\Delta_{PD} = \pm 0.1$ dB .....	61
3.1	Parameters of two $4 \times 4$ Butler matrices utilized in the measuring system. ....	99
4.1	Distribution of circle centers for reflection coefficient measurements, assuming $A = 0$ dB, $C_2 = 3$ dB, $n$ – port of Butler matrix, to which switch SW is connected and $k$ – port of Butler matrix, to which adjustable attenuator is connected.....	114
4.2	Distribution of circle centers for transmission coefficient measurements, assuming $A = 0$ dB, $C_2 = 3$ dB, $n$ – port of Butler matrix, to which switch SW is connected and $k$ – port of Butler matrix, to which adjustable attenuator is connected.....	114

- 4.3 Applied attenuation of the adjustable attenuator and the corresponding theoretical magnitude of circle centers' distribution [87]..... 118
- 4.4 Attenuations of the adjustable attenuator and corresponding theoretical magnitude of circle centers' distributions for reflection and transmission coefficient measurements. .... 123

# 1. Introduction

## 1.1. Principles of Multiport Measurement Technique

The nature of microwave measurements differs significantly from the measurements in lower frequency ranges. The measurements of voltages and currents are questionable for high frequencies, where it is often very difficult to correctly define circuit's topology and terminals at which such quantities could be measured. For convenient measurements at microwave frequencies the scattering parameters ( $S$ -parameters) have been introduced, which relate the waves incident  $a_i$  to Device Under Test (DUT) and waves reflected from it  $b_i$  shown in Fig. 1.1. The  $S$ -parameters of a given  $N$ -port microwave network are usually represented in matrix form  $[S]^{N \times N}$ , which allows for complete characterization of any linear device:

$$\begin{bmatrix} b_1 \\ b_2 \\ \dots \\ b_N \end{bmatrix} = \begin{bmatrix} S_{11} & S_{12} & \dots & S_{1N} \\ S_{21} & S_{22} & \dots & S_{2N} \\ \dots & \dots & \dots & \dots \\ S_{N1} & S_{N2} & \dots & S_{NN} \end{bmatrix} \begin{bmatrix} a_1 \\ a_2 \\ \dots \\ a_N \end{bmatrix} \quad (1.1)$$

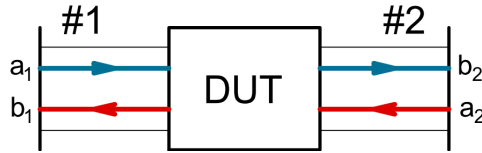


**Figure 1.1:** Incident and reflected waves related to an arbitrary two-port network.

Scattering parameters have become the most common form of microwave devices' description, therefore, their measurements are a paramount issue in microwave engineering and have been used for years. Usually, to obtain the particular  $S$ -parameters in terms of both magnitude and phase, vector network analyzers (VNAs) are utilized. However, such analyzers are relatively complicated systems, since they include frequency converters, local oscillators and phase detectors [9]. The high complexity of VNAs results in limited measurement accuracy, particularly at higher frequencies [70] and results in high costs. The above drawbacks related to  $S$ -parameter measurements have led at the beginning of 1970s to the development of the multiport measurement techniques first introduced by G. F. Engen and C. A. Hoer [28], [24]. These techniques constitute a new approach to complex scattering parameters' measurements, in which a measuring system consists of a linear passive multiport network ensuring a proper power division, microwave signal source, and several power meters [24], [27]. Simultaneously,

the elimination of frequency conversion and mixing significantly decreases the requirement for stability of the frequency source [25]. Moreover, all imperfections of the utilized elements can be taken into account by a suitable calibration procedure, therefore, their impact on the measurement accuracy can be significantly decreased or even eliminated [25], [60], which results in relaxed requirements related to the precision of utilized elements.

The main principle of the multiport measurement technique can be explained with the power distribution in an arbitrary linear passive multiport network with Device Under Test connected to one of its ports, as it is illustrated in Fig. 1.2. The signal  $a_1$  applied to the multiport network is distributed to the port with DUT connected, as well as to the other ports of a multiport, at which the power is measured (blue lines in Fig. 1.2). The power reflected from DUT is distributed by the multiport (red lines in Fig. 1.2) to all ports with power meters connected except the one, at which only the power delivered from source is measured (reference power measurement at  $N^{\text{th}}$  port). It has to be noted that in practical realizations the isolation between the port with DUT connected and the port, at which the reference power is measured is imperfect, which has been marked using dashed line. Moreover, imperfect impedance match of all the utilized components results in occurrence of signal loops similar to the one presented for  $k^{\text{th}}$  port, to which DUT is connected. However, all these imperfections do not influence the measurement conditions, since they can be taken into account by the appropriate calibration procedure [60] (to increase legibility in Fig. 1.2, not relevant signals have been neglected).

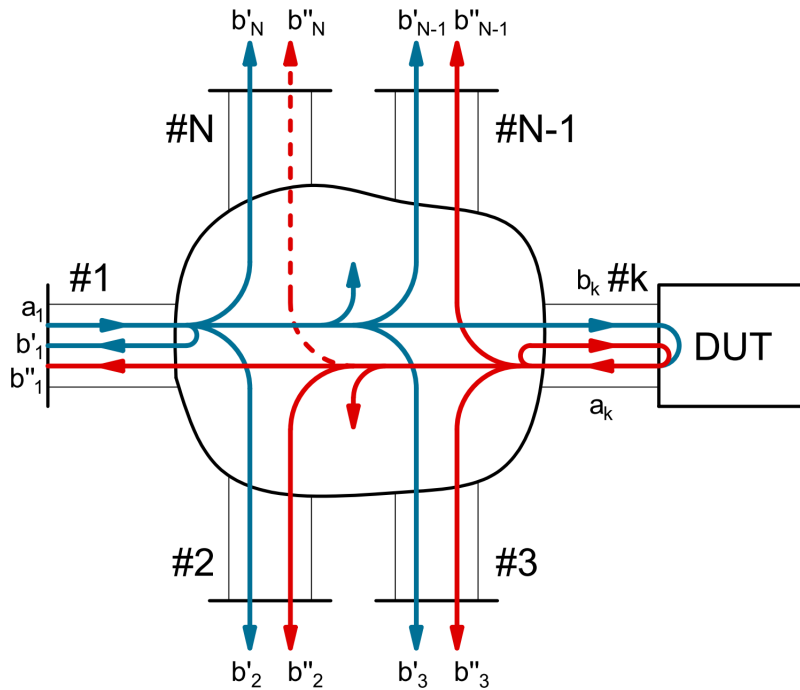


**Figure 1.2:** Power distribution in an arbitrary multiport passive power division network with one-port DUT connected.

Utilizing basic microwave theory one can obtain the relation between the power  $P_i$  measured at  $i^{\text{th}}$  port and the measured reflection coefficient of DUT  $\Gamma$  [27]:

$$p_i = \frac{P_i}{P_N} = q_i \left| \frac{1 + A_i \Gamma}{1 + A_0 \Gamma} \right|^2 \quad (1.2)$$

where  $p_i$  – normalized power,  $P_N$  – reference power measured at  $N^{\text{th}}$  port and  $q_i$ ,  $A_i$  and  $A_0$  ( $A_i$ ,  $A_0$  are complex values) are the calibration constants ( $i = 2, 3, \dots, N-1$  and  $i \neq k$ ). Analyzing (1.2) one can observe, that it represents a set of equations, which describe circles on a complex plane. The center of the  $i^{\text{th}}$  circle  $c_i$  and its radius  $R_i$  are as follows:

$$c_i = \frac{\Re[-A_i + r_i A_0]}{d_i} + j \frac{\Im[A_i - r_i A_0]}{d_i} \quad (1.3)$$

$$R_i = \frac{\sqrt{r_i} |A_i - A_0|}{d_i} \quad (1.4)$$

where

$$r_i = \frac{p_i}{q_i} \quad (1.5)$$

$$d_i = |A_i|^2 - r_i |A_0|^2 \quad (1.6)$$

Hence, the measured reflection coefficient  $\Gamma$ , being the solution of (1.2), can be interpreted geometrically as intersection point of circles, as illustrated in Fig. 1.3 [24], [10]. Equations (1.3) and (1.4) are in general the clue to the multiport measurement technique. If  $|A_i| \gg |A_0|$  (which is always true in practical realizations) it can be observed, that the location of the circle centers on a complex plane is the immanent feature of the measuring system, resulting from the structure of applied multiport network, whereas the circles radii are proportional to the measured power  $p_i$ . Therefore, having appropriately distributed circles on a complex plane, one can determine an arbitrary value of reflection coefficient  $\Gamma$ .

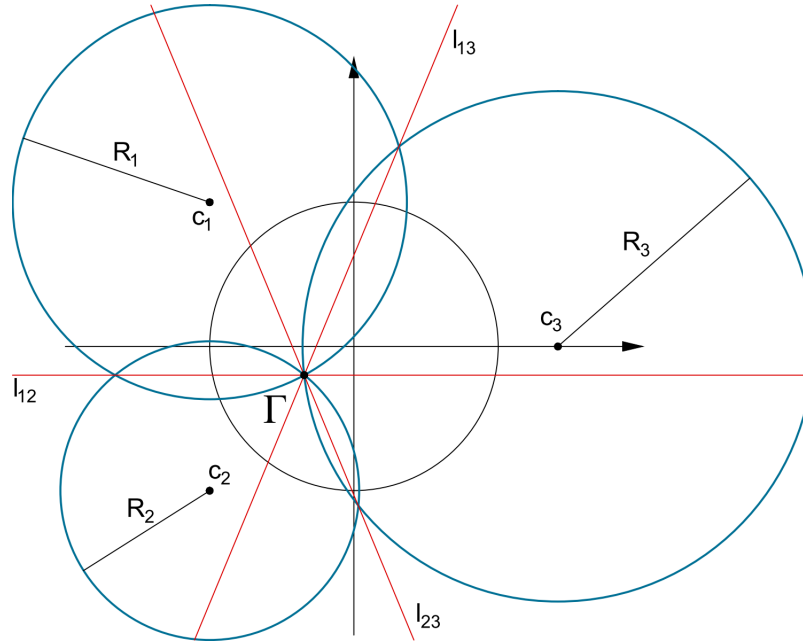


**Figure 1.3:** Geometric interpretation of reflection coefficient measurement.

From the above consideration one can see that to ensure a proper and unambiguous measurement three circles are necessary. Moreover, their mutual arrangement cannot be arbitrary. Fig. 1.4 shows three circles having centers located on a straight line. Such a circle centers' distribution leads to ambiguous measurement results, therefore, it cannot be utilized in practice.

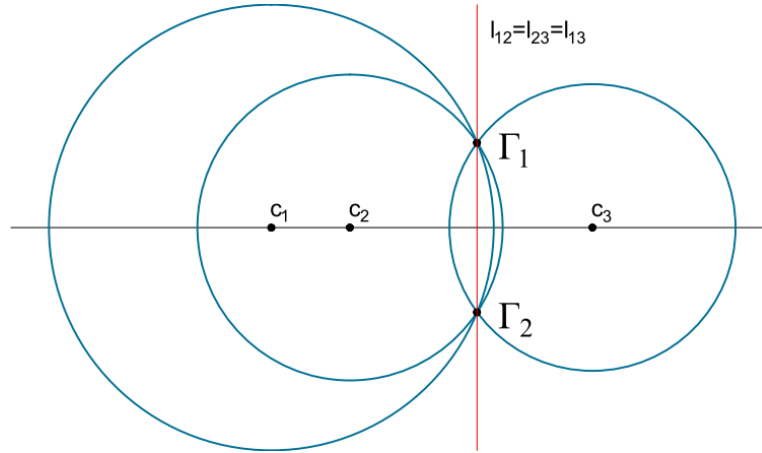


**Figure 1.4:** Incorrect arrangement of circle centers leading to an ambiguous measurement results.

As it is shown in Fig. 1.3, the measured value of reflection coefficient is a point of circles' intersection. However, noise and the measurement inaccuracy of the applied power meters affect the measured power values, deteriorating circles radii. As a result one can obtain several intersection points of pairs of circles, as shown in Fig. 1.5. In that case the resulting value  $\Gamma$  is determined as the intersection of red lines  $l_{ij}$  seen in Fig. 1.3 and in Fig. 1.5, given by:

$$2x\Re[c_i - c_j] + 2y\Im[c_i - c_j] - |c_i|^2 + |c_j|^2 + R_i^2 - R_j^2 = 0 \quad (1.7)$$

where  $i$  and  $j$  are the indices of circles, for which the line  $l_{ij}$  is calculated. It is worth mentioning that these lines have a single intersection point for an arbitrary set of three circles [7]. To enhance the measurement accuracy, a higher number of circles is required, which corresponds to multiport networks with higher number of ports, at which the power is measured. In literature, a large variety of multiports has been reported, including the simplest four-ports [9], ten-ports [68] or even more complicated networks according to the accuracy requirements. For higher number of circles the approximation of a genuine reflection coefficient  $\Gamma$  is calculated utilizing the least-squares approach [26], [89].

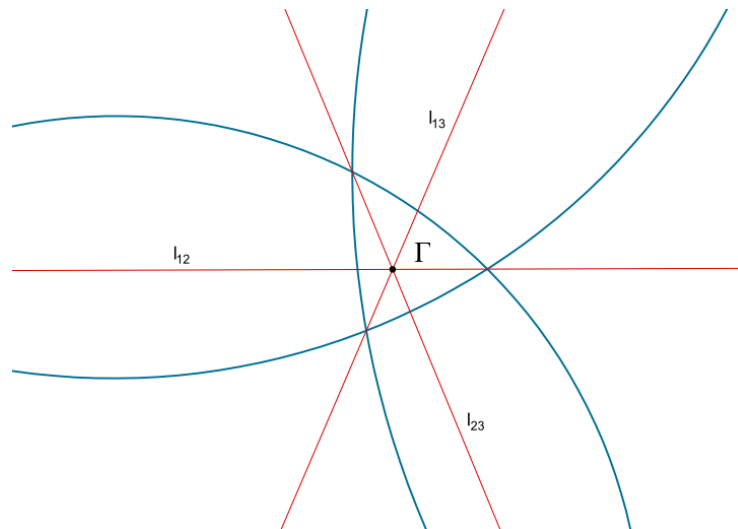


**Figure 1.5:** Several intersection points resulting from circles radii deteriorated by noise and measurement inaccuracy of the applied power meters.

As it has been stated above, the multiport measurement technique is considered as an attractive alternative for vector network analyzers, due to its simplicity and incomparably lower costs. Moreover, its generality allows for its application in both microstrip and waveguide techniques, also in millimeter-wave frequency range [71]. Furthermore, the appropriately constructed multiport measurement systems allow for determining not only reflection coefficient, but also transmission coefficient of measured devices [17], [47], [61], [15], [41], [40], [45], [18]. Due to all the mentioned advantages the utilization of multiport measurement technique in contemporary electronics is very wide. Apart from the measurements of complex  $S$ -parameters it is utilized also in:

- microwave receivers for decoding QPSK modulated signals [92], [76], [102], [69], [56], [99], [72],
- the measurements of high-power transistors, where the level of measured power does not allow for direct utilization of vector network analyzers [4], [5], [20], [21], [32], [3],
- absorption measurements of biological samples, where a wide frequency band and high-power performance are required [48], [42],
- microwave diversity imaging, where information about magnitude and phase of reflected signals allows for obtaining 3D image [63], [22], [38], [1], [6], [50],
- systems for the measurement of complex permittivity [51], [90], [46], [58], [33],
- direction-finding applications [12], [54], [91], [103], [44], [57],
- anti-collision systems for traffic safety [53], [52], [67].

## 1.2. Butler Matrices

Butler matrices are commonly known microwave networks widely described in literature [11], [78], [106], [62], [19], [30], [36] and can be good candidates for application in multiport measurement technique. They feature unique properties which make them suitable for wide range of applications in contemporary electronics, e.g. as beamforming networks of multibeam antennas [106] or in direction finding systems [62]. A conventional  $4 \times 4$  Butler matrix consists of four 3dB/90° directional couplers and two 45° phase shifters, as presented in Fig. 1.6. Assuming an ideal  $4 \times 4$  Butler matrix, in which four directional couplers ensure 90°-phase shift for signal transmitted to the direct port and 0°-phase shift for signal transmitted to the coupled port, the exemplary phase relations for the entire  $4 \times 4$  Butler matrix may be expressed as follows [84]:

$$\arg [S_{61}] - \arg [S_{51}] = -90^\circ - (-45^\circ) = -45^\circ \quad (1.8)$$

$$\arg [S_{71}] - \arg [S_{61}] = -45^\circ - 90^\circ - (-90^\circ) = -45^\circ \quad (1.9)$$

$$\arg [S_{81}] - \arg [S_{71}] = -90^\circ - 90^\circ - (-45^\circ - 90^\circ) = -45^\circ \quad (1.10)$$

$$\arg [S_{62}] - \arg [S_{52}] = 0^\circ - (-90^\circ - 45^\circ) = 135^\circ \quad (1.11)$$

$$\arg [S_{72}] - \arg [S_{62}] = -90^\circ - 45^\circ - 90^\circ - 0^\circ = -225^\circ \Leftrightarrow 135^\circ \quad (1.12)$$

$$\arg [S_{82}] - \arg [S_{72}] = -90^\circ - (-90^\circ - 45^\circ - 90^\circ) = 135^\circ \quad (1.13)$$

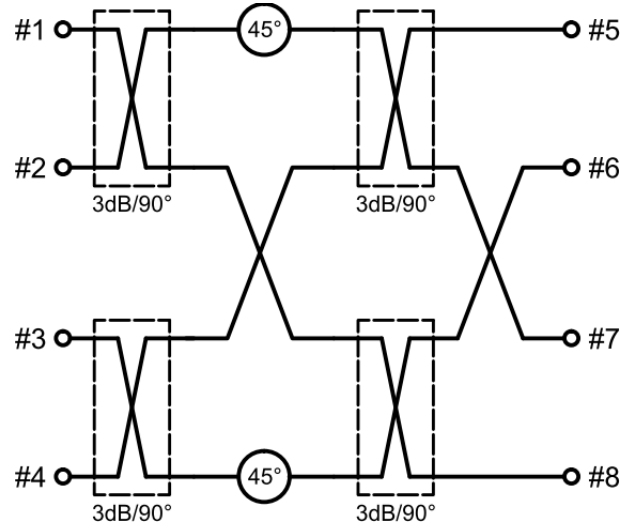


**Figure 1.6:** Schematic diagram of an ideal  $4 \times 4$  Butler matrix consisting of four  $3\text{dB}/90^\circ$  directional couplers and two  $45^\circ$  phase shifters [84]. (Copyright © 2014, Radioengineering)

As it can be observed the  $4 \times 4$  Butler matrix ensures equal division of power applied to one of four input ports to all four output ports, providing differential phases of the signals measured between adjacent output ports depending on the excited input port [78]. The differential phase value for an ideal  $4 \times 4$  Butler matrix for different choice of the input port, at which the Butler matrix is excited are listed in Table 1.1.

**Table 1.1:** Phase difference between two adjacent output ports of an ideal  $4 \times 4$  Butler matrix ( $j + 1$  and  $j$ ) for different choice of the excited input port  $i$

Excited input port	Phase difference
$i$	$\arg [S_{j+1,i}] - \arg [S_{j,i}]$
1	$-45^\circ$
2	$+135^\circ$
3	$-135^\circ$
4	$+45^\circ$

Due to their relatively low complexity,  $4 \times 4$  Butler matrices are most broadly utilized, however, higher order Butler matrices can be also realized. Fig. 1.7 shows the schematic diagram of an ideal  $8 \times 8$  Butler matrix. As it is seen comparing to the  $4 \times 4$  Butler matrix, the  $8 \times 8$  Butler matrix constitutes a considerably more complex circuit. It is composed of twelve  $3\text{dB}/90^\circ$  directional couplers and eight phase shifters ensuring  $22.5^\circ$ ,  $45^\circ$  and  $67.5^\circ$  phase shift. As it can be observed an ideal  $8 \times 8$  Butler matrix provides also equal power division from a chosen input port to all output ports. To determine the phase difference between adjacent output ports of an ideal  $8 \times 8$  Butler matrix a similar analysis to the one presented above can be performed. As a result one obtains eight different values of differential phase, which are listed in Table 1.2.

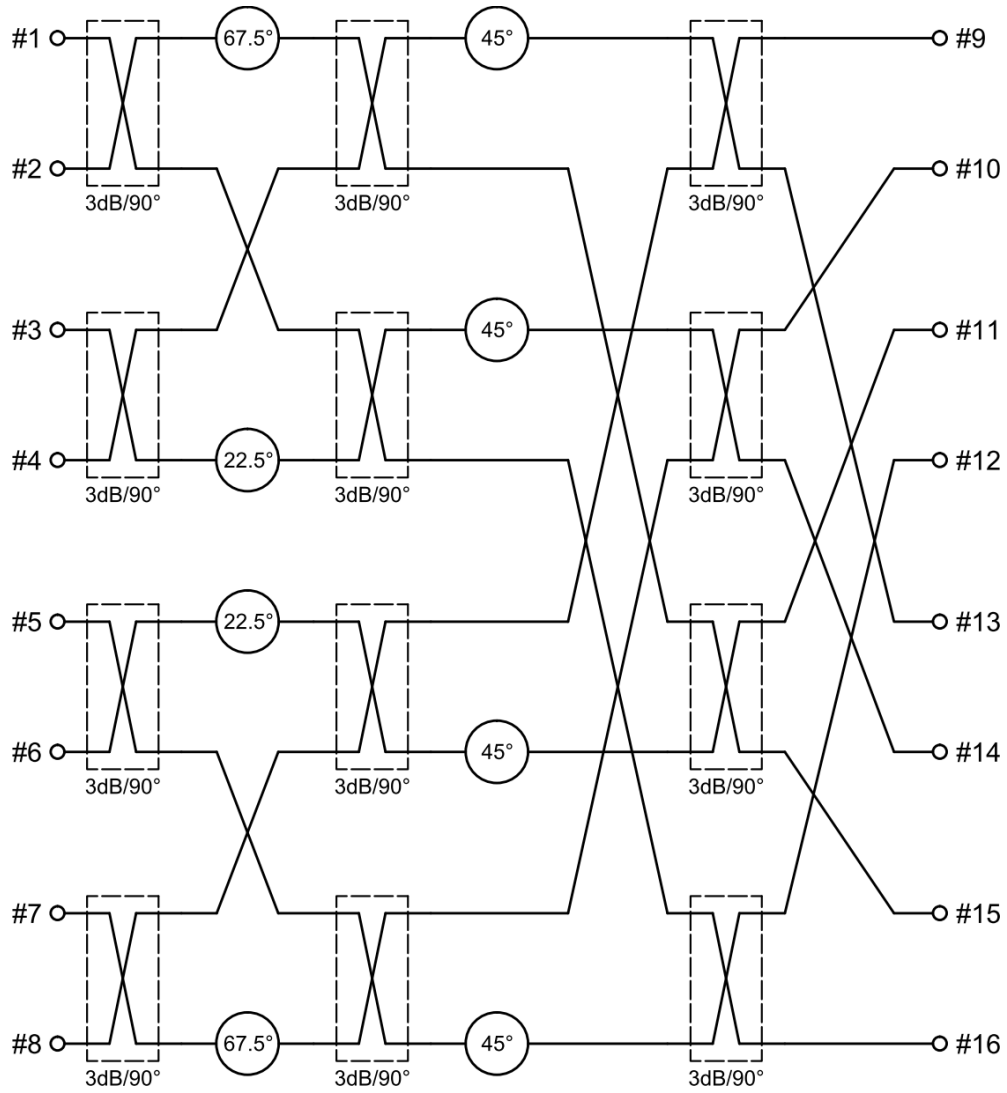


**Figure 1.7:** Schematic diagram of an ideal  $8 \times 8$  Butler matrix consisting of twelve  $3\text{dB}/90^\circ$  directional couplers and eight phase shifters.

**Table 1.2:** Phase difference between two adjacent output ports of an ideal  $8 \times 8$  Butler matrix ( $j + 1$  and  $j$ ) for different choice of the excited input port  $i$

Excited input port	Phase difference
$i$	$\arg [S_{j+1,i}] - \arg [S_{j,i}]$
1	$-22.5^\circ$
2	$+157.5^\circ$
3	$-112.5^\circ$
4	$+67.5^\circ$
5	$-67.5^\circ$
6	$+112.5^\circ$
7	$-157.5^\circ$
8	$+22.5^\circ$

Butler matrices, apart from their order, can be realized using different techniques, the choice of which determines the operational frequency range. Examples of  $4 \times 4$  Butler matrices realized utilizing branch-line directional couplers can be found in [19], [30]. The main drawback of such solutions is a narrow bandwidth, which can be, however, significantly increased by the application of coupled-line directional couplers [36], [13]. Furthermore, by the application of coupled-line directional couplers one can significantly reduce the size of Butler matrices.  $8 \times 8$  Butler matrices, due to their high complexity, are rarely presented in literature. For instance, in [93] an exemplary  $8 \times 8$  Butler matrix realized in LTCC technology has been shown, in which 40 layers appropriately stacked have been used.

Besides the broadband 3dB/90° coupled-line directional couplers, another crucial components of broadband Butler matrices are phase shifters providing a constant-value phase shift within a desired frequency range. For their realization several methods have been proposed. The commonly used technique is the application of a section of uncoupled transmission line having appropriate electrical length (45° - in case of  $4 \times 4$  Butler matrix) [8]. However, such an approach does not allow for a broadband operation of the resulting Butler matrices. To obtain a significantly wider bandwidth, within which constant phase shift is ensured, one can utilize a tandem connection of two 3dB/90° directional couplers and transmission-line sections in reference channels [94]. This technique provides the required 45° phase shift, and in addition realizes a transmission line crossover. Another well-known method of phase shift realization are Schiffman phase shifters, which provide a broadband differential phase shift [77], [74] and at the same time compact size. The design of broadband Butler matrices consisting of multisection directional couplers, in which Schiffman 'C' sections have been applied can be found in [36], [97] and [96]. Additionally, in [39] the design of a Butler matrix is presented, in which 45° phase shifters are realized as the half-wavelength open stubs in order to improve the differential phase response between the adjacent output ports.

### 1.3. Description and Aim of This Work

The Thesis presents a comprehensive analysis of the application of Butler matrices in multipoint measurements of scattering parameters. The purpose of this dissertation is to introduce multipoint measuring systems, in which the role of a dedicated power division network is performed by a classic Butler matrix, and to show that such systems can provide higher measurement accuracy in comparison to the classic six-port-based systems. This work has been divided into five chapters. The first Chapter introduces the fundamentals of the multipoint measurement technique and provides a general description of Butler matrices.

The second Chapter presents the measurements of reflection coefficients with the use of multipoint technique. The Chapter begins with description of two classic six-port reflectometers, in which the proposed modifications allow for broadband operation. Further, three novel measuring systems developed by the Author are presented, in which classic Butler matrices instead of classic six-ports are utilized. Moreover, a calibration procedure applicable for an arbitrary multipoint reflectometer is proposed and the measurement accuracy for several multipoint reflectometers is investigated. A deep insight into a general principle of the multipoint technique has allowed for an analysis of the measurement error distribution,

as well as for the estimation of the measurement accuracy. Finally, the measurement results obtained during the experimental verification of five developed systems are presented and discussed.

In the third Chapter the transmission coefficient measurements are investigated. The Author proposes two systems utilizing classic Butler matrices, which feature a significant simplification in comparison to the corresponding multiport systems reported in literature. Two calibration techniques have been proposed, which provide enhanced measurement accuracy and can be applied in systems having an arbitrary number of ports, at which the power is measured. The Chapter is concluded by the experimental verification of the developed systems.

The fourth Chapter presents the novel class of multiport measuring systems proposed by the Author, which feature a tunable power distribution. In particular, two broadband systems allowing for the measurements of reflection and transmission coefficients are shown. The concept of the tunable power distribution is discussed in terms of calibration and measurement accuracy. The Chapter ends with the analysis of the measurement results obtained by the experimental verification of two developed systems with the emphasis of the advantages resulting from the tunable power distribution.

The last Chapter concludes the major achievements presented in the Thesis and indicates further possible directions of development in the field of multiport measurement technique.

In this work the Author aims to prove the following theses:

- I. The application of Butler matrices as measuring multiports allows for the measurement of complex scattering parameters of microwave components.
- II. A modification of measurement system utilizing Butler matrix allows for decrease of the measurement uncertainty.
- III. The application of a set of phase shifters allows for the calibration of a multiport measurement system in a multi-octave frequency range.



## 2. Reflection Coefficient Measurements

In this Chapter the measurements of reflection coefficient with the use of multiport technique is investigated. Five multiport reflectometers are presented, among which two are the classic six-ports modified in order to ensure their broadband operation, and three reflectometers are the novel measuring systems proposed by the Author, in which Butler matrices are applied as power division networks. A complete theoretical investigation of each reflectometer is presented. Further, the Author proposes the calibration procedure, which provides enhanced measurement accuracy and can be applied for an arbitrary multiport reflectometer. Moreover, the comprehensive analysis of the measurement accuracy introduced by the Author is presented. Finally, the experimental verification of five investigated reflectometers operating in a broad frequency range is shown. The obtained measurement results confirm the theoretical investigation and the usability of the proposed reflectometers in the measurements of reflection coefficient.

In the following Chapter the Author cites his investigation on the reflection coefficient measurements recently published in [80], [86], [79], [81], [88], [85], [89] and in [83].

### 2.1. Classic Six-Port Reflectometers

In this Section, two broadband six-port reflectometers are presented, in which the utilization of 3dB/90° coupled-line directional couplers allows for broadband operation. The first six-port is based on single-section coupled-line directional couplers and, due to the equalization of electrical lengths of particular transmission lines, ensures high stability of the measuring system parameters over a wide frequency range. In the second design two additional modifications with respect to the classic solution have been utilized, which significantly improve its performance. The application of a simplified Magic-T circuit instead of a commonly used Wilkinson power divider, together with the utilization of multisection coupled-line directional couplers, have allowed for obtaining the operational bandwidth exceeding one decade. Moreover, the modification allowing to eliminate the seventh, unused port has been proposed.

#### 2.1.1. Six-Port Design

Fig. 2.1 presents a schematic diagram of a six-port originally designed by Engen [24]. It is composed of four quadrature directional couplers and a power divider. The reflectometer is excited at port #1, the measured device (DUT) is connected to port #2, the reflected power is measured at ports #3 – #5, the reference power is measured at port #6, and port #7 is unused (terminated with a matched load).

A key issue related to the reflectometer design is its circle centers' distribution, which allows to verify the usefulness of such a system in microwave measurements of reflection coefficient [27], [24]. If ideal components and lossless transmission lines are assumed, circle centers' distribution of the investigated six-port is as follows:  $c_3 = j$ ,  $c_4 = -1 - j$  and  $c_5 = 1 - j$  at the center frequency ( $c_i$  is the circle center corresponding to the port  $\#i$ , at which the power  $P_i$  is measured) [80].

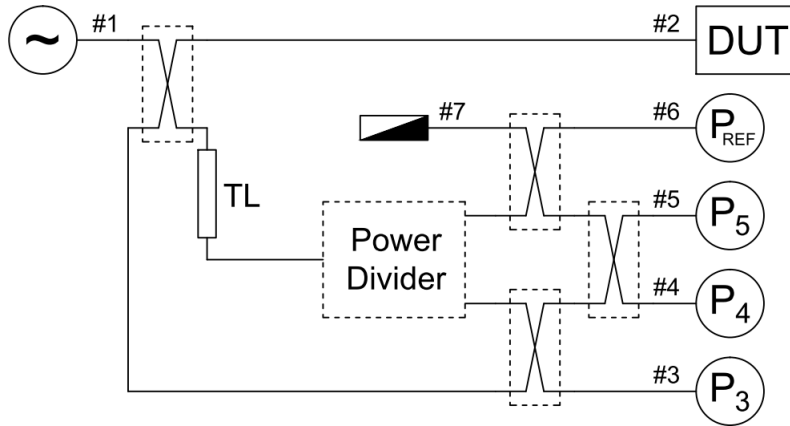


**Figure 2.1:** Schematic diagram of the investigated six-port [24], [80].

Assuming that the six-port presented in Fig 2.1 is composed of four ideal single-section 3dB/90° directional couplers and a Wilkinson power divider, the circle centers' distribution of the considered reflectometer is as presented in Fig. 2.2.

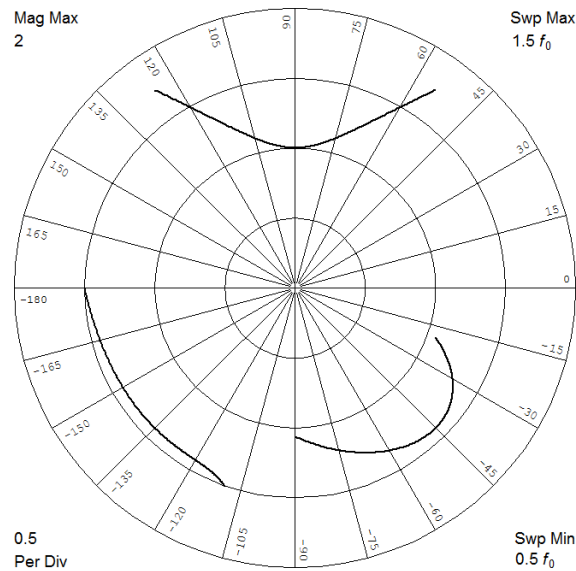


**Figure 2.2:** Circle centers' distribution of the six-port presented in Fig. 2.1 [80]. (Copyright © 2013, Wiley Periodicals, Inc.)

As it can be observed the circle centers' distribution depends on frequency, which can affect the measurement accuracy in a wide frequency range. To minimize the impact of the frequency on the spread of circle centers a modification may be proposed, in which a transmission line section TL is introduced. Fig. 2.3 presents the circle centers' distribution calculated assuming that the electrical length of the inserted transmission line section is equal to  $\Theta_{TL} = 210^\circ$  at the center frequency. As it is seen the

introduced modification significantly reduces the displacement of each circle center in frequency within the entire investigated frequency range [80].

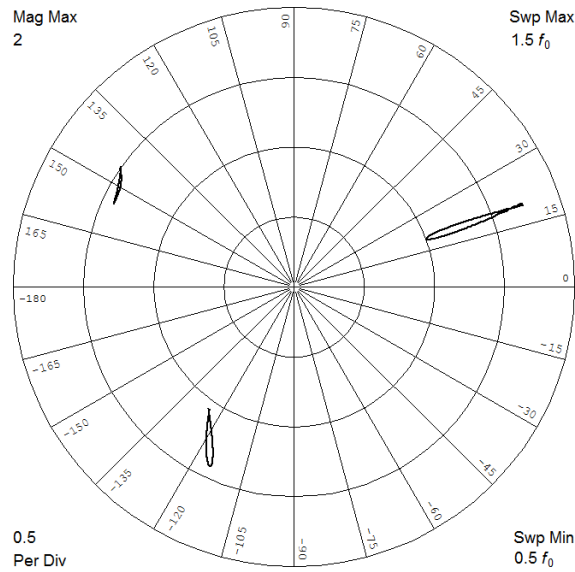


**Figure 2.3:** Circle centers' distribution of the six-port with inserted additional section of transmission line having electrical length  $\Theta_{TL} = 210^\circ$  [80]. (Copyright © 2013, Wiley Periodicals, Inc.)

### 2.1.2. Design of Ultra-Broadband Classic Six-Port Reflectometer

A wideband operation of the six-port can be ensured, as it has been shown in Subsection 2.1.1 by the realization of directional couplers in coupled-line technique. However, the resulting bandwidth in such reflectometers is limited by the utilized Wilkinson power divider. In contrary, in the proposed ultra-broadband six-port network, the in-phase power division has been provided by a simplified magic-T circuit. It ensures  $0^\circ$ -phase difference and perfect impedance match over a wide frequency range. The schematic diagram of the proposed reflectometer is shown in Fig. 2.4. The six-port reflectometer network is composed of four coupled-line directional couplers (A – D), Magic-T circuit and additional transmission line TL. The reflectometer is excited at port #1, the device under test (DUT) is connected to port #2, the reflected power is measured at ports #3 – #5, whereas the reference power is measured at port #6. It can be observed, that the entire circuit is similar to the classic six-port introduced by Engen [24], however, one can distinguish three major modifications [86]:

- *Application of the simplified Magic-T circuit*

As it can be observed in Fig. 2.4, the Magic-T network is applied to ensure an equal in-phase power division [55]. Hence, there is no need to apply the symmetric Magic-T network being composed of two  $270^\circ$ -long transmission lines and two Schiffman phase shifters. For the application in six-port reflectometer the simplified circuit presented in Fig. 2.4b is sufficient. The simplified Magic-T circuit can be designed with the use of the directional coupler utilized in the six-port structure, ensuring an appropriately wide operational bandwidth.

- *Connection of the unused, isolated couplers ports'*

The classic six-port reflectometer, as it can be observed in [24], [80], has an additional, unused

port, which is a consequence of the directional couplers' utilization. Therefore, its termination with a matched load is necessary. On the other hand, the applied Magic-T provides also one unused port (port #4 in Fig. 2.4b) and it would be required to terminate this port with matched load as well, which leads to the total number of eight ports of the proposed reflectometer. Taking into account that both mentioned ports are isolated with respect to the general signal flow in the proposed six-port reflectometer, they can be connected with a section of transmission line, which reduces the total number of reflectometer's ports to six. It must be emphasized that imperfect isolations of the utilized components result in the occurrence of an additional signal loop which can be, however, taken into account by the applied calibration procedure. Moreover, it can be said, that if the isolation of the utilized directional couplers is not worse than 20 dB, the modification of power distribution, is not noticeable.

- *Additional uncoupled transmission line for tuning the power distribution*

The transmission line inserted between coupler A and Magic-T circuit (TL in Fig. 2.4a) allows for equalizing electrical lengths of paths for reference signal and signal related to the measured reflection coefficient, exactly with the same manner as described in Subsection 2.1.1. Choosing a proper electrical length of the inserted transmission line TL one can stabilize the location of the circle centers over a wide frequency range, ensuring higher accuracy of calibration and subsequent measurements [80].

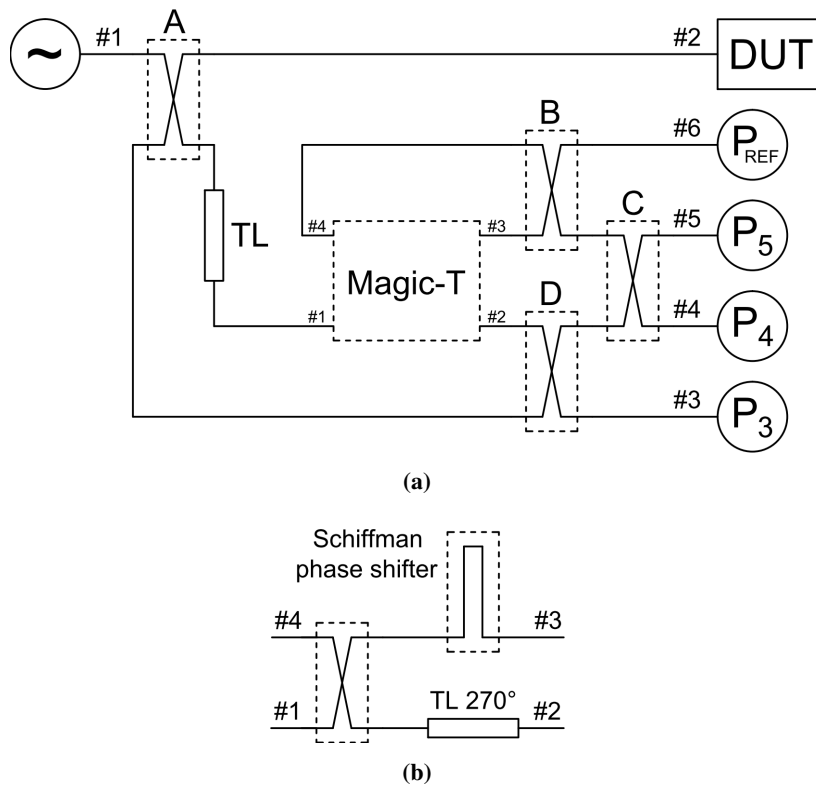


**Figure 2.4:** Schematic diagram of the proposed ultra-broadband six-port reflectometer (a) and schematic diagram of the simplified Magic-T circuit (b) [86]. (Copyright © 2014, IEEE)

## 2.2. Application of Butler Matrices in Reflection Coefficient Measurements

In this Section, three novel multiport reflectometers are presented, in which Butler matrices are used instead of dedicated multiports. The performed theoretical analysis shows, that such Butler matrices serving as multiport networks provide an advantageous power distribution allowing for precise measurement of complex reflection coefficient. Moreover, the proposed solutions feature a large number of possible system configurations, each having different power division. By taking advantage of different system configurations one can increase the measurement accuracy.

### 2.2.1. Reflectometer Utilizing Classic $4 \times 4$ Butler Matrix

As it has been pointed in Section 1.1, the main principle related to the reflection coefficient measurement with the use of multiports is to provide the sum of two signals to each of power detectors connected to a multiport power division network [24]. In case of a Butler matrix, it may be done by connecting a reflective element to ports isolated with respect to the chosen measuring port. The power delivered from signal source reflects from both the examined device and the applied reflective element, hence, the power meters have to be connected to the ports, that are isolated with respect to the excitation port of the Butler matrix. One of the possible configurations of a measuring system allowing for reflection coefficient measurements with the use of a  $4 \times 4$  Butler matrix is shown in Fig. 2.5. All the remaining possible connections are considered further in this Subsection. As it is seen, a measured device (DUT) is connected to port #5, a reflective element is connected to port #6, the signal is applied to port #1, the reflected power is measured at ports #2, #3 and #4, whereas, port #8 is used for measuring a reference power, and port #7 is not used [79].

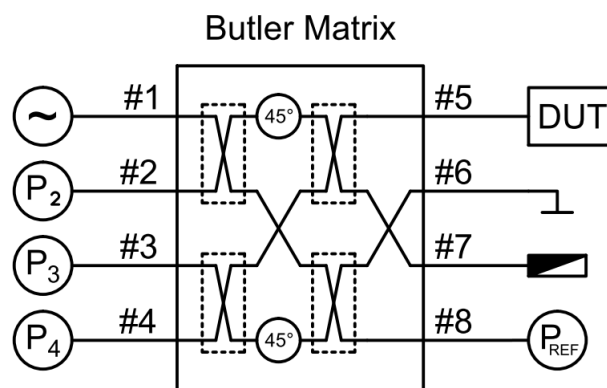


**Figure 2.5:** Schematic diagram of a multiport measuring system with a  $4 \times 4$  Butler matrix allowing for reflection coefficient measurements [79]. (Copyright © 2013, IEEE)

According to the description given in Section 1.1, results of measurements with the use of multiport technique may be interpreted geometrically as an intersection of three circles [24], [27] on a complex plane. Therefore, to ensure a proper measurement precision, the mutual distribution of these circle centers has to be considered. For an ideal  $4 \times 4$  Butler matrix, the relation between the power measured at the Butler matrix's input ports and unknown reflection coefficient  $\Gamma$  is as follows [79]:

$$p_{imgr} = \frac{P_{imgr}}{P_{REF}} = |S_{gm}\Gamma S_{ig} + S_{rm}\Gamma_C S_{ir}|^2 \quad (2.1)$$

where  $p$  – normalized power,  $P$  – measured power,  $P_{REF}$  – reference power measured at port #8,  $i$  – number of port at which power is measured (ports #1 – #4),  $m$  – number of port to which power is supplied (#1 – #4),  $g$  – number of measuring port (port #5 – #8) and  $r$  – number of port with connected reflective element having reflection coefficient  $\Gamma_C$  (port #5 – #8) and  $S_{XX}$  are the scattering parameters of the utilized  $4 \times 4$  Butler matrix. The circle centers  $c$  can be derived from (2.1) as follows:

$$c_{imgr} = -\frac{S_{gm}S_{ig}}{S_{rm}S_{ir}}\Gamma_C \quad (2.2)$$

From analysis of the system shown in Fig. 2.5 one can distinguish 48 possible ways for choosing excitation port, the port to which the measured device is connected, and the port to which reflective element is connected. For each system configuration the distribution of the circle centers can be found. All the obtainable circle centers' distributions with respect to the input port, at which a Butler matrix is excited and assuming that as a reflective element a short-circuit is used, are gathered in Table 2.1 and in Table 2.2.

**Table 2.1:** Distribution of circle centers for different choice of measuring port and port with short-circuit, when the  $4 \times 4$  Butler matrix is fed either at port #1 or #2 and  $\Gamma_C = -1$ .

		Number of short-circuited port $r$			
		5	6	7	8
Number of measuring port $g$	5				
	6				
	7				
	8				

It can be observed that not all combinations provide a circle centers' distribution ensuring three different points  $c$ , which are necessary for an unambiguous determination of measured reflection coefficient  $\Gamma$ , e.g. if the Butler matrix is excited at port #1, and the measured device and the reflective element are connected to ports #5 and #7, respectively, two of the three circles have identical center positions. As the further analysis reveals, for each choice of measuring port and exciting port there are two possibilities of reflective element connection. Moreover, for each chosen input port, at which the Butler matrix is excited, all combinations consisting of three different circle centers are equivalent and provide the same measurement accuracy, since in each case the mutual arrangement of circle centers is

the same. The presented results correspond to a short-circuit serving as the reflective element, however, the utilization of elements having  $\Gamma_C \neq -1$  is possible. It is worth mentioning that the reference power can be measured at any of the output ports i.e. #5 – #8, to which neither measured device nor reflective element is connected. In a practical realization, the reference power measurement should be done at the port having the best isolation with respect to the measuring port.

**Table 2.2:** Distribution of circle centers for different choice of measuring port and port with short-circuit, when the  $4 \times 4$  Butler matrix is fed either at port #3 or #4 and  $\Gamma_C = -1$ .

		Number of short-circuited port $r$			
		5	6	7	8
Number of measuring port $g$	5				
	6				
	7				
	8				

### 2.2.2. Reflectometer Based on $4 \times 4$ Butler Matrix Consisting of Tapered-Coupled-Line Directional Couplers

The analysis, similar to the one presented in Subsection 2.2.1, can be performed for a  $4 \times 4$  Butler matrix consisting of tapered-coupled-line directional couplers. The measuring system consisting of such a Butler matrix is presented in Fig. 2.6. The system configuration strictly corresponds to the one discussed in Subsection 2.2.1. Therefore, assuming an ideal  $4 \times 4$  Butler matrix, the relation between the measured power and the measured reflection coefficient  $\Gamma$  can be expressed with the same formula, as in case of a classic  $4 \times 4$  Butler matrix, i.e. (2.1), however here, the  $S$ -parameters are related to the  $4 \times 4$  Butler matrix consisting of four  $0/180^\circ$  tapered-line directional couplers, which is shown in Fig. 2.6 and may be described with the following  $S$ -matrix [83]:

$$S = \frac{1}{2} \begin{bmatrix} 0 & 0 & 0 & 0 & e^{-j\frac{3\pi}{2}} & e^{-j\pi} & e^{-j\frac{\pi}{2}} & e^{-j0} \\ 0 & 0 & 0 & 0 & e^{-j\pi} & e^{-j\frac{3\pi}{2}} & e^{-j0} & e^{-j\frac{\pi}{2}} \\ 0 & 0 & 0 & 0 & e^{-j\pi} & e^{-j0} & e^{-j\pi} & e^{-j0} \\ 0 & 0 & 0 & 0 & e^{-j0} & e^{-j0} & e^{-j0} & e^{-j0} \\ e^{-j\frac{3\pi}{2}} & e^{-j\pi} & e^{-j\pi} & e^{-j0} & 0 & 0 & 0 & 0 \\ e^{-j\pi} & e^{-j\frac{3\pi}{2}} & e^{-j0} & e^{-j0} & 0 & 0 & 0 & 0 \\ e^{-j\frac{\pi}{2}} & e^{-j0} & e^{-j\pi} & e^{-j0} & 0 & 0 & 0 & 0 \\ e^{-j0} & e^{-j\frac{\pi}{2}} & e^{-j0} & e^{-j0} & 0 & 0 & 0 & 0 \end{bmatrix} \quad (2.3)$$

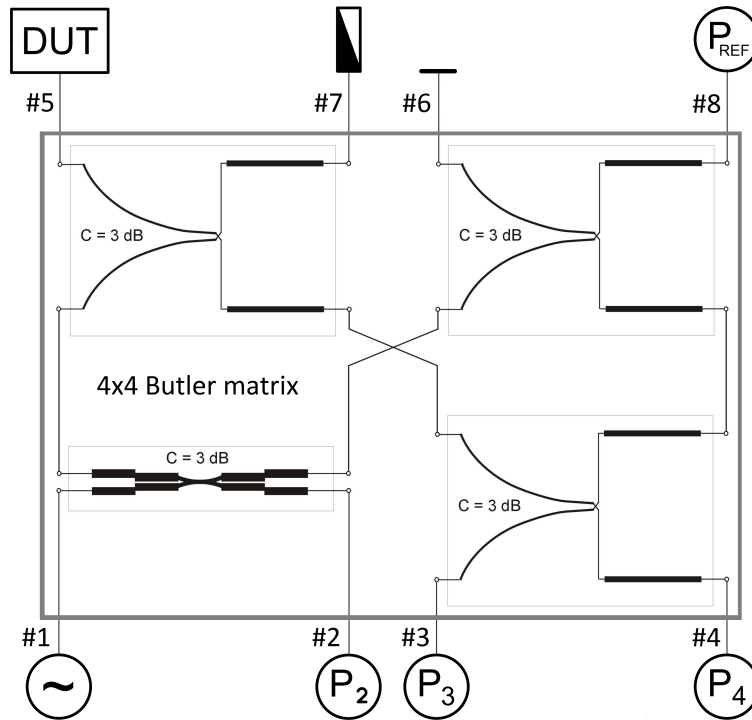


**Figure 2.6:** Schematic diagram of the proposed multiport reflectometer with a single  $4 \times 4$  Butler matrix utilizing tapered-coupled-line directional couplers [37], [83] (Copyright © 2014, SDIWC).

Since the general formula relating the measured power and the measured reflection coefficient is the same, as in case of the classic  $4 \times 4$  Butler matrix consisting of quadrature directional couplers [79], the circle centers' distribution obtainable for the presented measuring system can be expressed with the use of (2.2) [83].

**Table 2.3:** Distribution of circle centers for different choice of measuring port and port with short-circuit, when the  $4 \times 4$  Butler matrix is fed either at port #1 or #2 and  $\Gamma_C = -1$  [83]. (Copyright © 2014, SDIWC)

		Number of short-circuited port $r$			
		5	6	7	8
Number of measuring port $g$	5				
	6				
	7				
	8				

**Table 2.4:** Distribution of circle centers for different choice of measuring port and port with short-circuit, when the  $4 \times 4$  Butler matrix is fed either at port #3 or #4 and  $\Gamma_C = -1$  [83]. (Copyright © 2014, SDIWC)

		Number of short-circuited port $r$			
		5	6	7	8
Number of measuring port $g$	5				
	6				
	7				
	8				

The proposed reflectometer allows also for obtaining a high number of connection combinations. Assuming, that an ideal short-circuit is utilized as a reflective element, the possible circle centers' distributions are shown in Table 2.3 and Table 2.4.

As it is seen the circle centers' distributions obtainable in the proposed measuring system are similar to these obtained with the use of a  $4 \times 4$  Butler matrix consisting of quadrature directional couplers, shown in Subsection 2.2.1. The only difference is their rotation by  $90^\circ$ , which has no impact on the general measurement accuracy, since the mutual locations of particular circle centers are preserved. Moreover, similarly to the system presented in Subsection 2.2.1, some of system configurations listed in Table 2.3 and in Table 2.4 provide only two different circle centers, hence, they do not allow for unambiguous measurement and cannot be utilized.

### 2.2.3. Reflectometer Utilizing Classic $8 \times 8$ Butler Matrix

The multiport reflectometers can be also realized with Butler matrices of higher order. Fig. 2.7 presents an exemplary configuration of the proposed measuring system utilizing a classic  $8 \times 8$  Butler matrix [85]. In order to obtain the proper performance of the reflectometer, the measuring system configuration corresponding to the one presented in Subsection 2.2.1 or 2.2.2 has to be applied. According to the principles of multiport measurement technique, to measure complex reflection coefficient, at least three power meters (excluding the power meter for reference power measurement) have to be applied. As it can be observed in Fig. 2.7, the utilization of an  $8 \times 8$  Butler matrix allows for an application of up to seven such power meters and the resulting redundancy can be used for measurement accuracy enhancement.

Since the  $8 \times 8$  Butler matrix has relatively high number of ports, there are various possible connections of the measuring system, among which one is shown in Fig. 2.7 (all other possible system

configurations are considered in further part of this Subsection). As it is seen it fully corresponds to the measuring systems utilizing  $4 \times 4$  Butler matrices presented in Subsections 2.2.1 and 2.2.2.

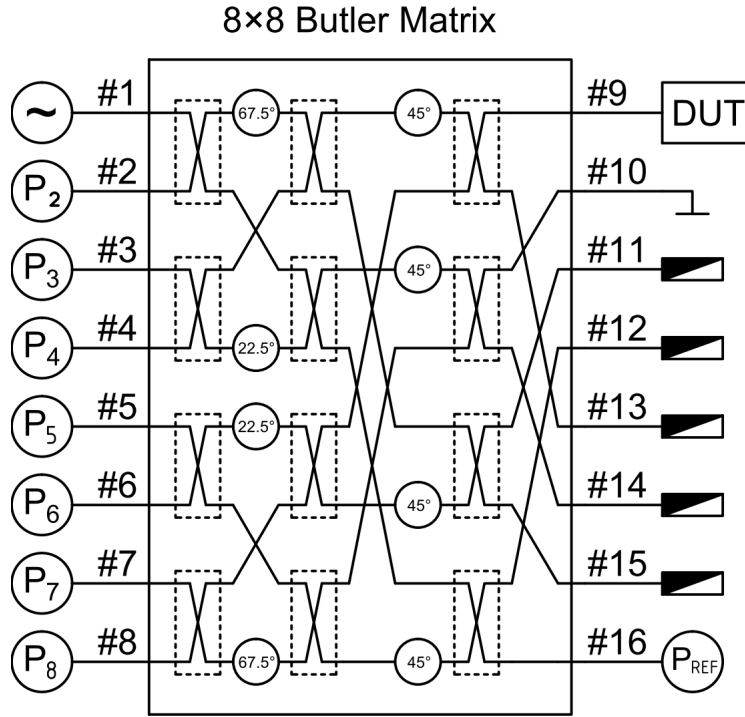


**Figure 2.7:** Schematic diagram of the proposed multipoint measuring system with a single  $8 \times 8$  Butler matrix allowing for reflection coefficient measurement [85]. (Copyright © 2014, IEEE)

To analyze whether the proposed system can provide a proper measurement its power distribution defining the circle centers' distribution has to be investigated. The distribution of circle centers corresponding to the proposed reflectometer can be derived using the  $S$ -matrix of an ideal  $8 \times 8$  Butler matrix, having the following form:

$$S = \frac{1}{\sqrt{8}} \begin{bmatrix} 0 & A \\ A^T & 0 \end{bmatrix} \quad (2.4)$$

where

$$A = \begin{bmatrix} e^{-j\frac{5\pi}{8}} & e^{-j\frac{3\pi}{4}} & e^{-j\frac{7\pi}{8}} & e^{-j\pi} & e^{-j\frac{9\pi}{8}} & e^{-j\frac{5\pi}{4}} & e^{-j\frac{11\pi}{8}} & e^{-j\frac{3\pi}{2}} \\ e^{-j\frac{9\pi}{8}} & e^{-j\frac{\pi}{4}} & e^{-j\frac{11\pi}{8}} & e^{-j\frac{\pi}{2}} & e^{-j\frac{13\pi}{8}} & e^{-j\frac{3\pi}{4}} & e^{-j\frac{15\pi}{8}} & e^{-j\pi} \\ e^{-j\frac{3\pi}{4}} & e^{-j\frac{11\pi}{8}} & e^{-j0} & e^{-j\frac{5\pi}{8}} & e^{-j\frac{5\pi}{4}} & e^{-j\frac{15\pi}{8}} & e^{-j\frac{\pi}{2}} & e^{-j\frac{9\pi}{8}} \\ e^{-j\frac{5\pi}{4}} & e^{-j\frac{7\pi}{8}} & e^{-j\frac{\pi}{2}} & e^{-j\frac{\pi}{8}} & e^{-j\frac{7\pi}{4}} & e^{-j\frac{11\pi}{8}} & e^{-j\pi} & e^{-j\frac{5\pi}{8}} \\ e^{-j\frac{5\pi}{8}} & e^{-j\pi} & e^{-j\frac{11\pi}{8}} & e^{-j\frac{7\pi}{4}} & e^{-j\frac{\pi}{8}} & e^{-j\frac{\pi}{2}} & e^{-j\frac{7\pi}{8}} & e^{-j\frac{5\pi}{4}} \\ e^{-j\frac{9\pi}{8}} & e^{-j\frac{\pi}{2}} & e^{-j\frac{15\pi}{8}} & e^{-j\frac{5\pi}{4}} & e^{-j\frac{5\pi}{8}} & e^{-j0} & e^{-j\frac{11\pi}{8}} & e^{-j\frac{3\pi}{4}} \\ e^{-j\pi} & e^{-j\frac{15\pi}{8}} & e^{-j\frac{3\pi}{4}} & e^{-j\frac{13\pi}{8}} & e^{-j\frac{\pi}{2}} & e^{-j\frac{11\pi}{8}} & e^{-j\frac{\pi}{4}} & e^{-j\frac{9\pi}{8}} \\ e^{-j\frac{3\pi}{2}} & e^{-j\frac{11\pi}{8}} & e^{-j\frac{5\pi}{4}} & e^{-j\frac{9\pi}{8}} & e^{-j\pi} & e^{-j\frac{7\pi}{8}} & e^{-j\frac{3\pi}{4}} & e^{-j\frac{5\pi}{8}} \end{bmatrix} \quad (2.5)$$

The relation between the measured power and the unknown reflection coefficient  $\Gamma$  can be expressed with the same formula as in case of a  $4 \times 4$  Butler matrix and classic six-port reflectometers, i.e. (2.1) [24], however, it has to be augmented by the increased number of ports with applied power meters. Similarly,

the circle centers  $c$  related to the presented measuring system with an ideal  $8 \times 8$  Butler matrix can be derived from (2.2). It is seen, therefore, that in case of a short-circuit utilized as a reflective element (having  $|\Gamma_C| = 1$ ), all circle centers are located on a circumference of the unity circle. Using (2.2) it can be shown that there are 448 possible combinations of the measurement set-up configurations. Similarly to the analysis of  $4 \times 4$  Butler matrices, only a part of possible configurations provides circle centers' distributions ensuring unambiguous determination of the measured  $\Gamma$ . In general, one can distinguish three groups of connections, providing seven, four or only two circle centers [85]. Nevertheless, configurations providing only two different circle centers cannot be utilized in measurements due to ambiguous results. Hence, in order to provide seven circle centers arranged on a unity circle with angular distance of  $45^\circ$  the port number with connected reflective element has to fulfill the following condition:

$$r = g \pm \{1, 3, 5, 7\} \quad (2.6)$$

The choice of the input port, at which the Butler matrix is supplied rotates the entire circle centers' distribution, therefore, it has no impact on the measurement accuracy. Four circle centers arranged uniformly also on a circumference of the unity circle with angular distance of  $90^\circ$  can be provided, if the number of port with connected reflective element is chosen according to the following formula:

$$r = g \pm \{2, 6\} \quad (2.7)$$

The choice of the Butler matrix feeding port does not change the circle centers' distribution. The remaining combinations, fulfilling the following condition:

$$r = g \pm 4 \quad (2.8)$$

provide only two different circle centers, leading to the ambiguous measurement, therefore, they cannot be utilized. From the investigated three groups of circle centers' distribution, the first one can be rotated by  $90^\circ$  (by the choice of excitation port), providing four different distributions. The circle centers in the remaining two groups does not rotate with respect to the chosen input port supplying the Butler matrix, therefore, in case of the proposed reflectometer with an  $8 \times 8$  Butler matrix, six groups of circle centers, shown in Fig. 2.8, can be distinguished.

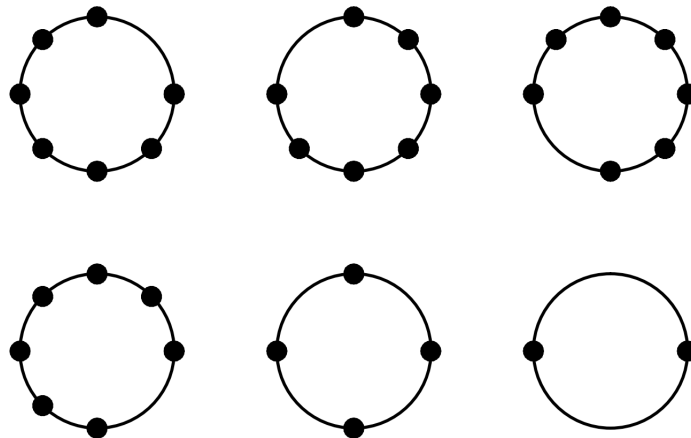


**Figure 2.8:** All possible distributions of circle centers related to the  $8 \times 8$  Butler matrix. The last distribution, containing only two circle centers cannot be utilized in measurements, due to ambiguous results [85]. (Copyright © 2014, IEEE)

The considerations presented above refer to ideal  $N \times N$  Butler matrices. However, the real networks exhibit some imperfections, i.e. coupling imbalance, deviation of the phase difference, imperfect impedance match and imperfect isolations, which affect circle centers' distribution. Nevertheless, even significantly deteriorated circle centers' distribution allows for a precise measurement, as long as the proper power distribution is preserved.

### 2.3. Calibration for Reflection Coefficient Measurements

The key problem related to measurements with the use of multiport reflectometers is the calibration procedure. A great number of different approaches to the calibration has been reported in literature [60], [25], [100], [75], [16], [29], [23]. Nevertheless, a majority of them provides the solutions, which are relatively highly sensitive to the applied power detectors' uncertainty. In [26] a solution based on a least-squares approach is presented, which allows to decrease the influence of the power readings' uncertainty on the measurement results. The main drawback of this approach is, however, the assumption that the calibration constants are precisely known, what is never true in practical measuring systems. Apart from analytical solutions, also the numerical algorithms allowing for calibration of a multiport have been investigated. As it has been recently shown in [79] and in [68], a numerical approach to the reflectometer's calibration in general ensures higher robustness to the power readings' uncertainty, leading to the higher accuracy of measurements.

This Section presents a two-step approach to the calibration of a linear multiport having an arbitrary number of the applied power meters [89]. The first step of the proposed algorithm is a numerical calibration of a multiport, based on the Levenberg-Marquardt algorithm for the solution of a least-squares fitting problem. The second step of the developed calibration procedure is an extension of a well-known approach, in which a considered reflectometer is modeled as a connection of an ideal reflectometer and the error box network [31]. Moreover, a simple algorithm allowing for a proper choice of calibration standards is presented, which allows for the reflectometer's calibration in a wide, multioctave frequency range [88].

#### 2.3.1. Comparison of Direct Analytical Approach and Numerical Procedure for Calibration of Multiport Reflectometers

In order to compare the accuracy of the calibration procedures based on a direct analytical method and with the use of a numerical algorithm and their robustness to the power meters uncertainty a simple simulation of an ideal six-port reflectometer, shown in Subsection 2.1.1, can be performed. The calibration of the six-port structure, involving ideal single-section coupled-line directional couplers, has been simulated with the use of *AWR Microwave Studio* software. Since typical commercially available power meters feature the measurement error at the level of  $\pm 0.1$  dB, the calibration has been simulated with power measurement uncertainty modeled as additive white noise having amplitude corresponding to  $\pm 0.1$  dB error. The obtained values of measured power have been utilized further in two calibration procedures. The first one is a direct analytical approach, proposed in [60]. The second

one is based on Levenberg-Marquardt numerical algorithm utilizing least-squares fitting [59], [66]. Both methods can be compared using an exemplary circle center  $c_4$ , which according to description given in Subsection 2.1.1, features the magnitude of  $\sqrt{2}$  at the center frequency (the application of single-section coupled-line directional couplers slightly relocates the circle centers) [79]. The obtained results are presented in Fig. 2.9. As it is seen the calibration utilizing the direct analytical approach with power readings affected by 0.1 dB error results in the circle center deviation reaching 14%. Such discrepancy of calibration results precludes correct measurements. On the other hand, the numerical approach gives the error not exceeding 3%. The achieved considerable improvement is caused by the fact, that in the analytical procedure a single intersection of circles for all calibration standards is assumed, whereas the introduced power reading uncertainty affects circles' radii and therefore, instead of a single point of intersection, a number of intersection points between pairs of circles in a close vicinity occurs. The analytical procedure is not convergent, whereas the numerical procedure gives a solution being close approximation of an ideal circle center in the sense of the used least-squares fitting, which ensures a higher robustness of calibration procedure [79].

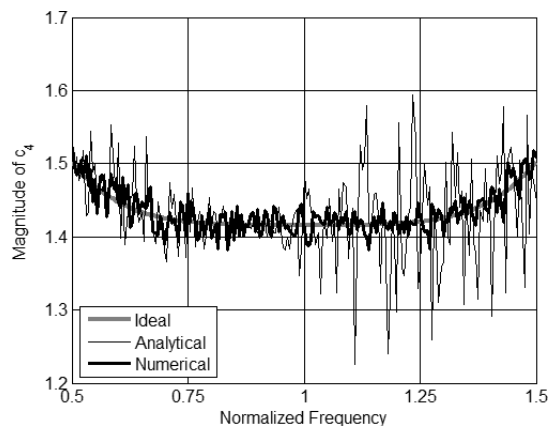


**Figure 2.9:** The distance between the circle center  $c_4$  and the origin of a complex plane as a comparison between the calibration procedures based on direct analytical approach and on numerical algorithm [79]. (Copyright © 2013, IEEE)

The above consideration shows that the calibration procedure based on the numerical algorithm provides more accurate results than the direct analytical procedure. Moreover, it must be emphasized that the presented example is related to the classic six-port structure featuring only three ports, at which the power is measured, which is the minimum number required for a proper measurement of reflection coefficient. However, in order to improve the measurement accuracy, reflectometers having more than three ports at which the power is measured can be proposed. In such a case some redundancy occurs, since there are more than three intersecting circles on a complex plane. Therefore, the numerical approach based on least-squares fitting comprises a very flexible tool allowing for taking into account all redundant measurements in order to ensure a great robustness of the obtained results to the power measurement uncertainty.

### 2.3.2. Multiport Calibration

As it is said in Section 1.1, the general relationship between the power readings  $P_i$  and the measured reflection coefficient  $\Gamma$ , for an arbitrary linear  $N$ -port microwave reflectometer, can be expressed by the following formula [60]:

$$p_i = \frac{P_i}{P_{REF}} = q_i \left| \frac{1 + A_i \Gamma}{1 + A_0 \Gamma} \right|^2 \quad (2.9)$$

Having a set of known calibration reflections  $\Gamma_k$  ( $k = 1, 2, \dots, K$ ), the multiport can be calibrated using the procedures reported in literature. In order to apply the chosen calibration procedure, (2.9) can be expressed by real numbers only:

$$|\Gamma_k|^2 (q_i \alpha_i^2 - p_{ik} \alpha_0^2) + 2\Re[\Gamma_k] (q_i a_i - p_{ik} a_0) + 2\Im[\Gamma_k] (p_{ik} b_0 - q_i b_i) + q_i = p_{ik} \quad (2.10)$$

where

$$\alpha_i = \sqrt{a_i^2 + b_i^2} \quad (2.11)$$

$$\alpha_0 = \sqrt{a_0^2 + b_0^2} \quad (2.12)$$

and

$$a_i = \Re[A_i] \quad (2.13)$$

$$b_i = \Im[A_i] \quad (2.14)$$

$$a_0 = \Re[A_0] \quad (2.15)$$

$$b_0 = \Im[A_0] \quad (2.16)$$

According to the consideration presented in Subsection 2.3.1, the direct analytical calibration procedures feature higher sensitivity to the power readings' uncertainty than the ones based on numerical least-squares fitting algorithm. Therefore, in this Subsection, the numerical calibration procedure utilizing Levenberg-Marquardt algorithm is proposed, in which additionally the influence of an imperfectly matched load on the calibration results is decreased. To obtain the optimal solution of the proposed calibration procedure in a sense of the least-squares fitting, the Levenberg-Marquardt algorithm has been utilized. It is based on the minimizing the following formula [89]:

$$R = \sum_{i=1}^N \sum_{k=1}^K f_{ik}^2 \quad (2.17)$$

where  $N$  is the number of ports, at which the power is measured,  $K$  is the number of calibration reflections and  $f_{ik}$  is the residuum of the corresponding equation (2.10), expressed as follows:

$$f_{ik} = |\Gamma_k|^2 (q_i \alpha_i^2 - p_{ik} \alpha_0^2) + 2\Re[\Gamma_k] (q_i a_i - p_{ik} a_0) + 2\Im[\Gamma_k] (p_{ik} b_0 - q_i b_i) + q_i - p_{ik} \quad (2.18)$$

According to the investigation shown in [60] (2.10) represents a set of quadratic equations, which leads to two solutions. To choose the proper one the additional power readings  $p_{iL}$ , corresponding to the measuring port terminated with a matched load, can be utilized. It is seen from (2.9), that if a perfectly matched load is applied, then  $p_{iL} = q_i$ . Therefore, from the obtained two sets of solutions, the proper one

can be chosen, which results in  $q_i \approx p_{iL}$ . As it has been mentioned in [60], in order to choose the solution, in which coefficients  $q_i$  are close to  $p_{iL}$ , the applied matched load should feature  $\text{VSWR} \leq 1.05$ . In case of the presented numerical calibration procedure, such an explicit choice of cannot be done. Despite of choosing  $q_i = p_{iL}$  as the initial values, the numerical algorithm can be divergent. Therefore, to ensure the convergence to the proper solution, (2.17) can be augmented as follows [89]:

$$R = \sum_{i=1}^N \left[ \sum_{k=1}^K (f_{ik}^2) + ug_i^2 \right] \quad (2.19)$$

where

$$g_i = q_i - p_{iL} \quad (2.20)$$

and  $u$  is the weighting factor. It can be observed that in (2.20) the utilization of an ideally matched load is assumed, whereas the typical commercially available matched loads feature  $\text{VSWR}$  being close to 1.05. However, the proposed approach ensures the convergence of the calibration procedure to the proper solution. Furthermore, among  $N(K + 1)$  of all equations, there are only  $N$  functions  $g_i$ , which introduce the above discussed inaccuracy. Hence, their influence on the calibration results is limited. Moreover, if a high quality matched load is utilized in calibration, the weighting factor  $u$  can be increased, reducing the number of iterations and improving the robustness of the calibration procedure. Nevertheless, to eliminate the impact of imperfectly matched load, the second step of calibration proposed in Subsection 2.3.3, can be applied.

The obtained calibration constants  $q_i$ ,  $A_i$  and  $A_0$  can be further utilized in the measurements of reflection coefficient  $\Gamma$ . For multiport reflectometers having more than three ports, at which the power is measured, (2.9) represents an overdetermined set of equations. Therefore, it can be solved with the use of the least-squares approach. Since all calibration constants are known, the measured reflection coefficient can be determined using the following residua:

$$f_i = |\Gamma|^2 (q_i \alpha_i^2 - p_i \alpha_0^2) + 2\Re[\Gamma] (q_i a_i - p_i a_0) + 2\Im[\Gamma] (p_i b_0 - q_i b_i) + q_i - p_i \quad (2.21)$$

As it can be seen, (2.21) is a simplified form of (2.18), in which the reflection coefficient is unknown. According to the least-squares approach, to find the measured value  $\Gamma$ , the following form has to be minimized:

$$R_\Gamma = \sum_{i=1}^N f_i^2 \quad (2.22)$$

Therefore, the overdetermined set of equations can be transformed into the set of equations having a single unique solution, being the optimal one in a sense of least-squares fitting [59]:

$$\frac{\partial R_\Gamma}{\partial X} = 0 \quad \text{and} \quad \frac{\partial R_\Gamma}{\partial Y} = 0 \quad (2.23)$$

where  $X$  and  $Y$  are the real part and the imaginary part of the measured reflection coefficient  $\Gamma$ , respectively. By solving (2.23), one can obtain the measured reflection coefficient expressed as follows [89]:

$$\Gamma = \frac{\delta\kappa - \epsilon\eta + j(\epsilon\delta - \beta\kappa)}{\beta\eta - \delta^2} \quad (2.24)$$

where

$$\beta = \sum_{i=1}^N \sum_{j=i+1}^N (F_i - F_j)^2 \quad (2.25)$$

$$\delta = \sum_{i=1}^N \sum_{j=i+1}^N (F_i - F_j)(G_i - G_j) \quad (2.26)$$

$$\epsilon = \sum_{i=1}^N \sum_{j=i+1}^N (F_i - F_j)(H_i - H_j) \quad (2.27)$$

$$\eta = \sum_{i=1}^N \sum_{j=i+1}^N (G_i - G_j)^2 \quad (2.28)$$

$$\kappa = \sum_{i=1}^N \sum_{j=i+1}^N (G_i - G_j)(H_i - H_j) \quad (2.29)$$

and the parameters  $F_i$ ,  $G_i$  and  $H_i$  can be obtained from the calibration constants:

$$F_i = 2 \frac{q_i a_i - p_i a_0}{q_i \alpha_i^2 - p_i \alpha_0^2} \quad (2.30)$$

$$G_i = 2 \frac{p_i b_0 - q_i b_i}{q_i \alpha_i^2 - p_i \alpha_0^2} \quad (2.31)$$

$$H_i = 2 \frac{q_i - p_i}{q_i \alpha_i^2 - p_i \alpha_0^2} \quad (2.32)$$

It is worth mentioning that in case of a six-port reflectometers, for which  $N = 3$  (three ports, at which the power is measured), equations (2.24)-(2.32) simplify to the relationships given in [60].

### 2.3.3. Error Box Calibration

An actual reflectometer can be modeled as a cascade connection of an ideal reflectometer and an error box network, as illustrated in Fig. 2.10 [31]. Such an approach can be used in the second step of the presented calibration procedure, for elimination of the influence of imperfectly matched load used in the first step [89].

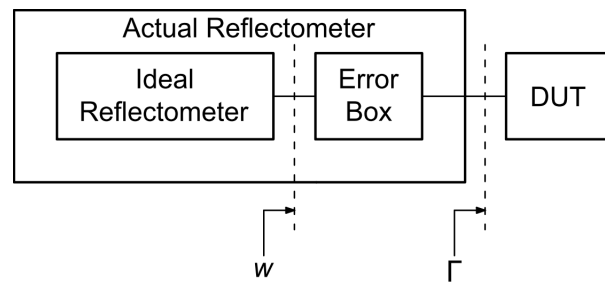


**Figure 2.10:** Actual reflectometer modeled as an ideal reflectometer connected to an error box network [31], [89]. (Copyright © 2013, IEEE)

Utilizing the basic microwave network theory, one can derive the value  $w$ , which is measured by the ideal reflectometer shown in Fig. 2.10. It can be expressed as follows:

$$w = \frac{D\Gamma + E}{C\Gamma + 1} \quad (2.33)$$

where  $\Gamma$  is the desired reflection coefficient,  $C$ ,  $D$  and  $E$  are the system constants, which can be defined using the  $S$ -parameters of the error box network  $S_{xx}^{eb}$ :

$$C = -S_{22}^{eb} \quad (2.34)$$

$$D = S_{21}^{eb}S_{12}^{eb} - S_{11}^{eb}S_{22}^{eb} \quad (2.35)$$

$$E = S_{11}^{eb} \quad (2.36)$$

In order to proceed to the measurements, the parameters  $C$ ,  $D$ ,  $E$  have to be determined. In practice it is usually done with the use of the SOL (*short-open-load*) technique [31]. Nevertheless, such a method is based on assumption that the utilized load is perfectly matched, which introduces some calibration error. In the previous calibration step described in Subsection 2.3.2, a number of calibration standards having known reflection coefficients  $\Gamma_k$  have been used. Therefore, it is convenient to utilize them also in the second step of the calibration procedure. In general, to find three complex constants, three equations (2.33) with three known reflection coefficients  $\Gamma$  are necessary. On the other hand, in the calibration of a multiport reflectometer, at least four different calibration standards (excluding a matched load) are required. By increasing the number of calibration standards one can determine the error-box parameters with the use of a least-squares approach, which provides better calibration accuracy in comparison to a direct solution [89]. The desired parameters of an error box network can be calculated as follows:

$$\begin{bmatrix} \Re[E] \\ \Im[E] \\ \Re[D] \\ \Im[D] \\ \Re[C] \\ \Im[C] \end{bmatrix} = (M^T M)^{-1} M^T V \quad (2.37)$$

where

$$M = \begin{bmatrix} 1 & 0 & \Re[\Gamma_1] & -\Im[\Gamma_1] & -\Re[w_1\Gamma_1] & \Im[w_1\Gamma_1] \\ 0 & 1 & \Im[\Gamma_1] & \Re[\Gamma_1] & -\Im[w_1\Gamma_1] & -\Re[w_1\Gamma_1] \\ \dots & \dots & \dots & \dots & \dots & \dots \\ \dots & \dots & \dots & \dots & \dots & \dots \\ 1 & 0 & \Re[\Gamma_K] & -\Im[\Gamma_K] & -\Re[w_K\Gamma_K] & \Im[w_K\Gamma_K] \\ 0 & 1 & \Im[\Gamma_K] & \Re[\Gamma_K] & -\Im[w_K\Gamma_K] & -\Re[w_K\Gamma_K] \end{bmatrix} \quad (2.38)$$

$$V = \begin{bmatrix} \Re[w_1] \\ \Im[w_1] \\ \dots \\ \dots \\ \Re[w_K] \\ \Im[w_K] \end{bmatrix} \quad (2.39)$$

Moreover,  $K$  is the number of the applied calibration standards and  $w_x$  is the measured value corresponding to the calibration standard  $\Gamma_x$ . Having known the parameters given by (2.37), the desired

reflection coefficient  $\Gamma$  can be calculated using (2.33) rearranged to the form:

$$\Gamma = \frac{E - w}{Cw - D} \quad (2.40)$$

### 2.3.4. Choice of Calibration Standards in Broadband Calibration

In order to calibrate an arbitrary multiport reflectometer, a set of calibration standards (calibration kit) has to be utilized. Usually it contains open, short, offset-open, offset-short and additionally matched load for removing final non-ambiguity. However, the described elements do not ensure the proper distribution of reflection standards on a complex plane for the reflectometer calibration in a wide frequency range. Since the phase shift of the applied offsets is linearly dependent on frequency and the phases of open and short calibration standards remain constant (equal to  $0^\circ$  and  $180^\circ$  respectively), calibration reflections overlap at some frequencies, as it is schematically illustrated in Fig. 2.11 [88].

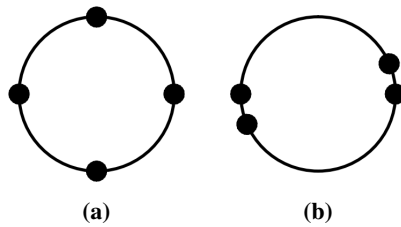


**Figure 2.11:** The influence of operating frequency on calibration reflections' distribution. The optimal reflections' distribution for properly chosen offset value at a given frequency  $f_1$  (a) and the corresponding distribution for frequency  $f_2 \approx 2f_1$  (b) [88].

(Copyright © 2013, IEEE)

Therefore, such a set of calibration standards is not sufficient for a calibration procedure in broad bandwidth. In order to obtain wide, multioctave frequency range, one has to apply additional offsets. Having several different values of phase shifts corresponding to the utilized offsets, for each frequency of measurement the optimum one can be chosen. It is worth mentioning that the numerical calibration of multiport reflectometer, especially for reflectometers with a high number of the applied power meters, is a relatively complex procedure. Moreover, the simultaneous utilization of several offsets significantly increases the computation effort and does not improve the calibration accuracy. On the other hand, the numerical algorithms ensure higher convergence than the analytical solutions [79]. Therefore, an algorithm for the choice of one optimal offset value for each frequency can be proposed [88]. To find the optimal offset value for a specified frequency, for each offset the minimum difference between any pair of the calibration standards' phases has to be found:

$$\Delta_i = \min_{j \neq k} |\arg[\Gamma_{ij}] - \arg[\Gamma_{ik}]| \quad (2.41)$$

where  $j$  and  $k$  are the indices of investigated calibration reflections corresponding to  $i^{\text{th}}$  offset, i.e.  $(j, k) \in \{\text{open}, i^{\text{th}}\text{offset-open}, \text{short}, i^{\text{th}}\text{offset-short}\}$ . Assuming the same phase shift value for both open and short (i.e. constant phase difference being equal to  $180^\circ$  for each frequency), the minimum difference between phases of arbitrary chosen calibration reflections, for a given offset value, cannot be greater than  $90^\circ$ , what corresponds to the optimal distribution of calibration reflections. After calculating values of  $\Delta_i$

for each offset, the index of the optimal offset can be determined, as the one corresponding to the highest value of  $\Delta_i$ . Due to the frequency dependence of the calibration reflections' distribution, the chosen offset has to be changed within the entire measurement frequency range.

### 2.3.5. Description of Utilized Calibration Standards

The algorithm presented in Subsection 2.3.4 has been applied to ensure a proper distribution of the calibration standards for frequencies up to 8 GHz. The utilized elements are: open-circuit standard HP85052-60008, short-circuit standard HP85033-60013 and four female-male SMA adapters (called further offsets A, B, C and D) serving as phase shifters. The electrical lengths of the mentioned elements are listed in Table 2.5.

**Table 2.5:** Characterization of the calibration standards allowing for calibration of the broadband reflectometers presented in this Chapter.

Calibration standard	Electrical length at 1 GHz
open	11.44°
short	11.48°
offset A	21.20°
offset B	32.44°
offset C	38.40°
offset D	46.52°

For the cascade connection of the offset X and open-circuit, having the electrical lengths  $\Theta_X$  and  $\Theta_O$ , respectively, the phase of reflection coefficient is as follows:

$$\varphi_{XO} = -2(\Theta_X + \Theta_O) \frac{f}{f_0} \quad (2.42)$$

whereas for such a connection with the use of short-circuit, the reflection coefficient's phase is equal to:

$$\varphi_{XS} = 180^\circ - 2(\Theta_X + \Theta_S) \frac{f}{f_0} \quad (2.43)$$

where  $\Theta_S$  is the electrical length of short-circuit. In equations (2.42) and (2.43)  $f_0$  is the frequency, at which the given electrical lengths are specified. Furthermore, if open-circuit or short-circuit is used without any offset, then  $\Theta_X = 0^\circ$ . The reflection coefficients' phases for each possible connection of the calibration standards given in Table 2.5 are shown in Table 2.6.

To illustrate the fact that for multioctave calibration more than one offset is needed, the phases of reflections used in calibration obtained with the use of offset A are shown in Fig. 2.12. As it can be observed for frequencies being close to 4 GHz two pairs of reflections overlap precluding the correct calibration.

Therefore, for such frequencies a different offset has to be applied. Following the procedure described in Subsection 2.3.4 for four applied offsets, one can calculate the minimum angle differences  $\Delta_i$ , which are plotted in Fig. 2.13.

**Table 2.6:** Frequency dependance of the calibration standards realized as open-circuit, short-circuit and cascade connections of open- or short-circuits with chosen offsets.

Offset	Open	Short
–	$-22.88^\circ \cdot f[\text{GHz}]$	$180^\circ - 22.96^\circ \cdot f[\text{GHz}]$
A	$-65.28^\circ \cdot f[\text{GHz}]$	$180^\circ - 65.36^\circ \cdot f[\text{GHz}]$
B	$-87.76^\circ \cdot f[\text{GHz}]$	$180^\circ - 87.84^\circ \cdot f[\text{GHz}]$
C	$-99.68^\circ \cdot f[\text{GHz}]$	$180^\circ - 99.76^\circ \cdot f[\text{GHz}]$
D	$-115.92^\circ \cdot f[\text{GHz}]$	$180^\circ - 116.00^\circ \cdot f[\text{GHz}]$

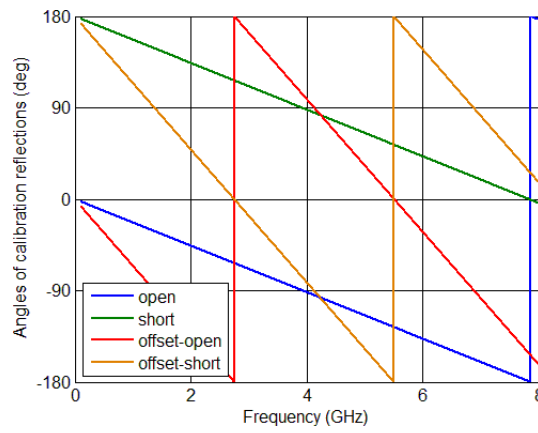


**Figure 2.12:** The angles of calibration standards obtained with the use of offset A.

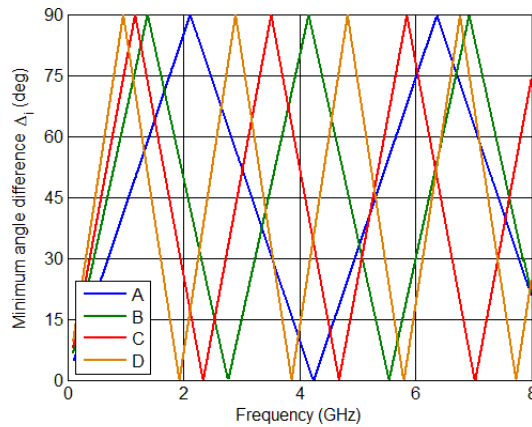


**Figure 2.13:** Minimum angle differences for four offsets utilized in the calibration procedure.

Having the value of minimum angle difference  $\Delta_i$  for each offset, the one corresponding to the maximum angle difference for a given frequency can be chosen [88]. Fig. 2.14 shows the choice of the offset ensuring optimal distribution of the calibration reflection coefficients at a specific frequency within the analyzed frequency range. The division for eleven subintervals is seen. Fig. 2.15 presents the minimum angle difference corresponding to the chosen offsets.

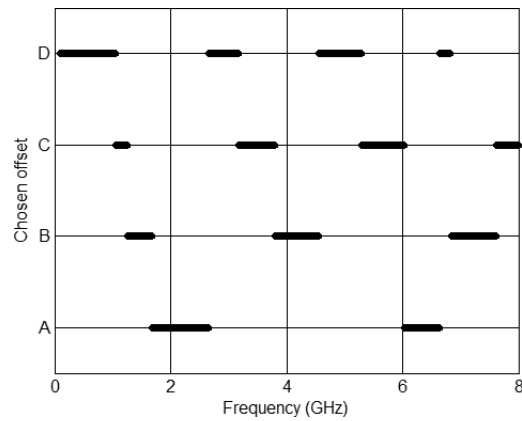


**Figure 2.14:** Chosen offset number vs. measurement frequency.

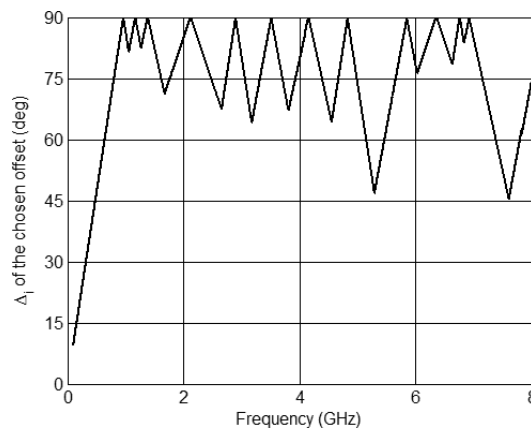


**Figure 2.15:** The minimum angle difference corresponding to the chosen offset vs. measurement frequency.

## 2.4. Measurement Accuracy Analysis of Multiport Reflectometers

The goal of the calibration procedure applied for a chosen multiport reflectometer is to derive multiport's parameters, which are essential for further measurements. Although a large number of multiport calibration techniques has been reported in literature [60], [25], [100], [75], [16], [29], [23], including numerical algorithms based on artificial neural networks [68], the resulting accuracy in each case is limited by the uncertainty of applied power detectors. The quality of a given multiport reflectometer and its usefulness in measurements can be estimated with the use of the geometric description presented in Section 1.1 [10]. The measurement error results from both applied power detectors uncertainty and the properties of the chosen multiport. As it has been shown in [80], the distribution on a complex plane of such an error is non-uniform. Furthermore, the utilization of the classic theory of error propagation does not provide the explicit minimum condition [10]. Therefore, a general measurement accuracy can be investigated only by numerical algorithms.

This Section presents a comprehensive analysis of the impact of circle centers' distribution of several multiport reflectometers on the measurement accuracy [81]. A theoretical investigation for an arbitrary multiport is shown, allowing for determination of the reflection coefficient's magnitude, for which the measured results become indefinite. Moreover, the worst case numerical analysis of measurement error

related to the group of reflectometers has been performed. The obtained results are given in a wide range from 0 to -40 dB of the reflection coefficient magnitude. It is shown that both a uniform angular distance and equal magnitude of circle centers resulting from multiports' properties provide higher accuracy and ensure lower limit of the properly measured reflection coefficient's magnitude.

### 2.4.1. Theoretical Limitations on Multiport Measurements

The measurements of complex reflection coefficients with the use of multiport technique require at least four power measurements, among which one constitutes a reference value. A higher number of power measurements provides a redundancy which, as it is shown further in this Section, allows for an enhancement of the measurement accuracy. As it is stated in Section 1.1, results of measurements with the use of multiport techniques may be interpreted geometrically as an intersection of several circles on a complex plane [24], [27], [10]. The distribution of circle centers depends on the design of a particular multiport reflectometer. Due to the imperfect accuracy of power detectors, the mentioned circles have radii that slightly differ from the theoretical ones. Therefore, instead of a single intersection point, being the measured reflection coefficient, several such points in a close vicinity occur. To analyze the measurement accuracy, the mentioned circles can be transformed into rings, having widths resulting from power measurement uncertainty [80] [81], as illustrated in Fig. 2.16. The measured reflection coefficient is a value located inside the bolded rings' intersection area (RIA) presented in Fig. 2.16c.

The shape of the mentioned area results from both the circle centers' distribution and the power measurement uncertainty  $\Delta_{PD}$ . The maximum measurement error is the distance between the genuine value and the most remote point within the bolded area. Utilizing the above presented geometrical considerations of the measurement accuracy, one can derive the limit of the reflection coefficient measurement. The measurement limit is the maximum magnitude of a measured reflection coefficient, for which the origin of the complex plane belongs to RIA. In such a case the magnitude measurement error expressed in dB goes to infinity and the measured phase becomes indefinite (phase error reaches  $\pm 180^\circ$ ) [81]. To explain this effect, the measurement of a reflection coefficient having magnitude close to zero (in linear scale) has to be investigated. Since the distances between the measured value and circle centers  $c_i$  are large in comparison to the size of RIA, it can be assumed that the shape of RIA, in case of reflection coefficients having magnitude close to zero, does not change significantly vs. the measured value. If a sufficiently low reflection coefficient is measured, one of the vertices can reach the origin of the complex plane. Assuming the worst case of power measurement uncertainty, the resulting value can be equal to 0 ( $-\infty$  dB), whereas, the magnitude of a genuine reflection coefficient is greater than zero. Moreover, the phase of such a measurement is indeterminate, hence, the phase measurement error reaches maximum value of  $\pm 180^\circ$ . To determine the above described theoretical limit of reflection coefficient measurement, one has to analyze the measurement of a reflection coefficient being equal to zero. Assuming that the typical value of power detector uncertainty is equal to  $\Delta_{PD} = \pm 0.1$  dB, the width of each ring is very small in comparison to their radii. Hence, the rings' borders in a close proximity of the complex plane origin may be approximated by straight lines described with the use of a general formula  $\Im[\Gamma] = a\Re[\Gamma] + b$ . As it is presented in Subsection 2.4.2, such a simplification causes

negligible errors. In the presented approach, it is assumed that the approximating lines pass through points either  $p_i$  or  $q_i$ . The points  $p_i$  ( $q_i$ ) belong to the inner (outer) rings having centers  $c_i$  and have minimal distances to the origin.

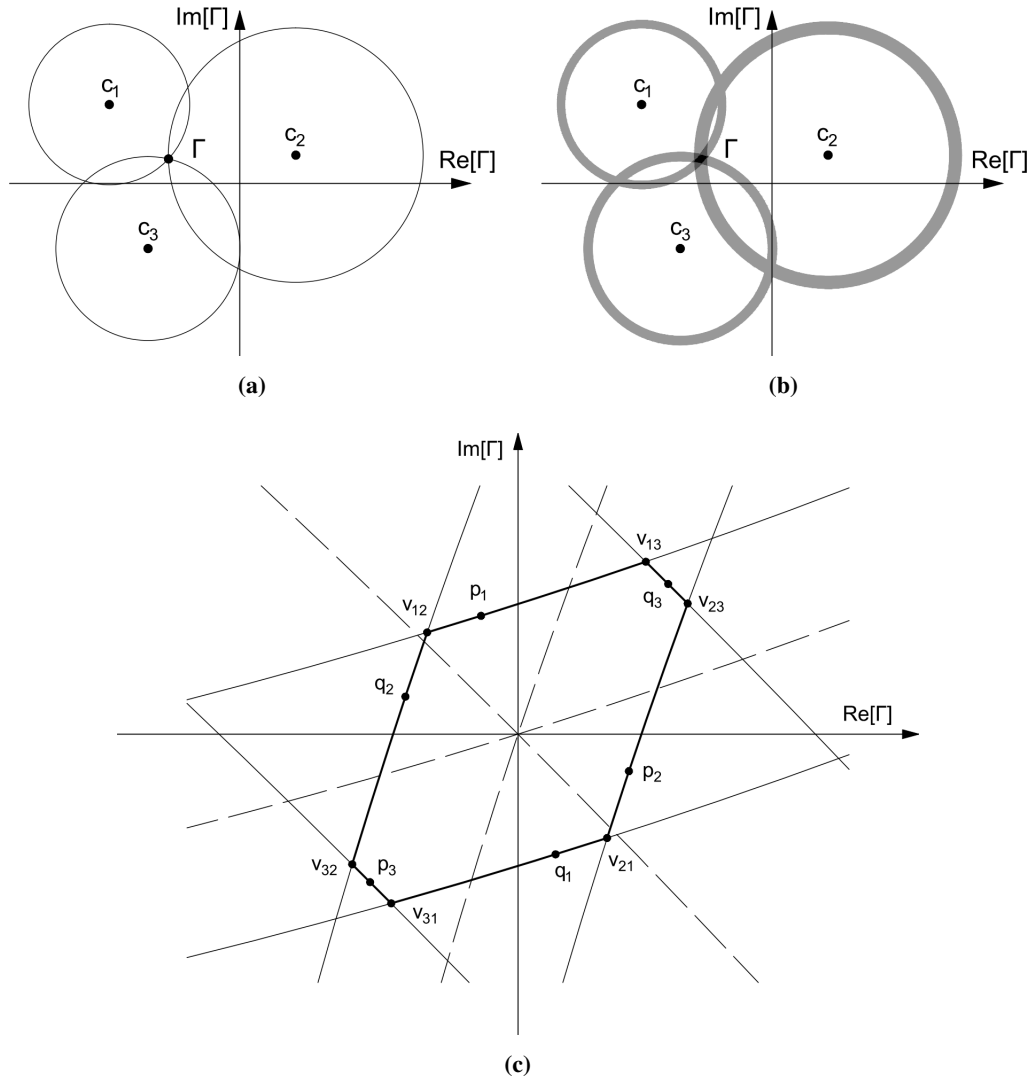


**Figure 2.16:** Influence of power measurement uncertainty on the circles radii. Ideal case with a single intersection point (a). Real case with detectors uncertainty taken into account (b). Detailed view of the rings' intersection area – RIA, where dashed lines present circles from Fig. 2.16a and solid lines present the borders of rings for the case of  $\Gamma = 0$  (c) [81]. (Copyright © 2013, IEEE)

To find the limiting value of reflection coefficient magnitude, one has to determine the vertex of the polygon that approximates RIA, which is the most distant from the origin of the complex plane. The procedure can be summarized as follows [81]:

- calculation of coefficients  $a$ ,  $b$  of lines passing through points  $p_i$  and  $q_i$ ,
- determination of vertices being intersections of the lines,
- selection of the vertex being the most distant from the origin of a complex plane.

Having arbitrarily chosen  $N$  circle centers  $c_i$ , where  $i = 1, 2, \dots, N$ , the slopes of approximating lines  $a_i$  can be found:

$$a_i = -\frac{\Re[c_i]}{\Im[c_i]} \quad (2.44)$$

Further, to determine the remaining coefficients  $b_i$ , the intersections of each circle with the line passing through its center  $c_i$  and the origin can be found. Assuming the power measurement accuracy  $\Delta_{PD}$ , one can obtain:

$$p_i = c_i \frac{\delta_{PD} - 1}{\delta_{PD}} \quad (2.45)$$

$$q_i = c_i (1 - \delta_{PD}) \quad (2.46)$$

where

$$\delta_{PD} = 10^{\frac{|\Delta_{PD}|}{20}} \quad (2.47)$$

As it is seen in Fig. 2.16, there are  $N$  pairs of parallel straight lines, therefore,  $2N$  coefficients  $b$  can be found:

$$b_{p_i} = \Im[p_i] - a_i \Re[p_i] \quad (2.48)$$

$$b_{q_i} = \Im[q_i] - a_i \Re[q_i] \quad (2.49)$$

where  $b_{p_i}$  corresponds to the inner border of a given ring and  $b_{q_i}$  is related to the outer one. For six-port reflectometers in general, the approximating lines can have up to twelve intersection points, as shown in Fig. 2.16c. However, not all of them belong to RIA. It can be observed, that each vertex of RIA is an intersection of lines approximating opposite borders of rings, hence the number of vertices that have to be considered does not exceed six. The desired points can be derived from the following formula:

$$v_{ik} = -\frac{b_{p_i} - b_{q_k}}{a_i - a_k} + j \frac{a_i b_{q_k} - a_k b_{p_i}}{a_i - a_k} \quad (2.50)$$

where  $i \neq k$ . It must be emphasized that in case of multiports having more than six ports (more than three circles in geometrical representation) equation (2.50) does not hold and the selection of vertices belonging to RIA is more complex. Once all the required vertices are found, the theoretical measurement limit  $|\Gamma|_{\min}$  for a given multiport can be determined as follows:

$$|\Gamma|_{\min} = 20 \log_{10} \left( \max_{i \neq k} \{|v_{ik}|\} \right) \quad (2.51)$$

The presented analysis has been applied for the comparison of four six-ports reported in literature, featuring different circle centers' distributions with the multiports utilizing Butler matrices described in Section 2.2. The analyzed multiports are:

- standard six-port presented by Engen in [24] (SPstd),
- six-port having elliptic circle distribution described in [73] (SPell),
- six-port featuring equally distributed circle centers on the unity circle (SPid1),
- six-port featuring equally distributed circle centers on a circle having radius equal to 2 (SPid2),
- six-port utilizing a standard  $4 \times 4$  Butler matrix (BM4x4<sub>3p</sub>),

- multiport utilizing a standard  $8 \times 8$  Butler matrix with four circle centers (BM8x8<sub>4p</sub>),
- multiport utilizing a standard  $8 \times 8$  Butler matrix with seven circle centers (BM8x8<sub>7p</sub>).

It is worth mentioning that the rotation of the circle centers' distribution does not influence the investigated limit. Therefore, the  $4 \times 4$  Butler matrix consisting of tapered-coupled-line directional couplers presented in Subsection 2.2.2 features the same limit value as a standard  $4 \times 4$  Butler matrix described in Subsection 2.2.1. Following this principle, for the  $8 \times 8$  Butler matrix with seven circle centers any of four possibilities shown in Fig. 2.8 can be used. The theoretical limit for each multiport obtained with the use of the presented analysis are listed in Table 2.7.

**Table 2.7:** Circle center distributions and corresponding theoretical limits of measured reflection coefficient magnitude for seven different multiports, assuming  $\Delta_{PD} = \pm 0.1$  dB

Multiport	Circle centers $c_i$	Magnitude of Reflection Coefficient (dB)
SPid2	$2e^{i\frac{2\pi}{3}}$ ( $i = 0, 1, 2$ )	-31.52
SPell	$-2 + j0, 0 + j0.5, 0 - j0.5$	-32.54
SPstd	$0 + j, -1 - j, 1 - j$	-32.77
BM4x4 <sub>3p</sub>	$e^{i\frac{\pi}{2}}$ ( $i = 0, 1, 2$ )	-35.79
BM8x8 <sub>4p</sub>	$e^{i\frac{\pi}{2}}$ ( $i = 0, 1, 2, 3$ )	-35.79
SPid1	$e^{i\frac{2\pi}{3}}$ ( $i = 0, 1, 2$ )	-37.54
BM8x8 <sub>7p</sub>	$e^{i\frac{\pi}{4}}$ ( $i = 0, 1, 2, \dots, 6$ )	-38.17

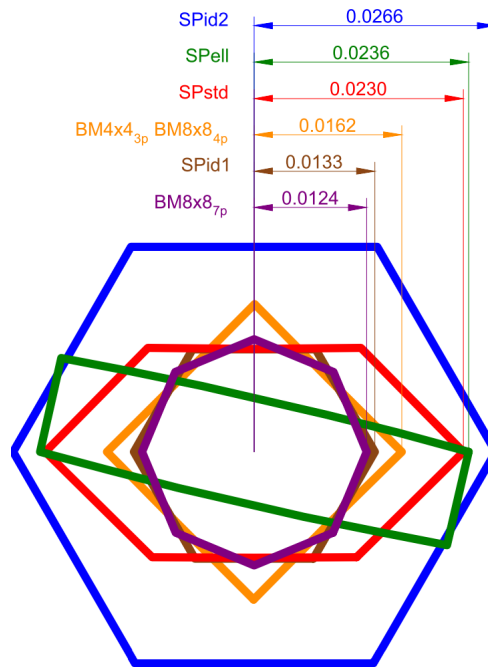


**Figure 2.17:** The comparison of RIA for seven analyzed multiports with assumed power detector uncertainty equal to  $\pm 0.1$  dB.

The shape of RIA for each analyzed multiport is presented in Fig. 2.17. As it is seen despite of the same detector uncertainty the limits differ. This is caused by two factors: the angular circle centers'

distribution and the distances of the circle centers from the origin of a complex plane. The lowest limit of the measured reflection coefficient magnitude among the investigated six-ports is obtained for the six-port having circle centers equally spaced on the unity circle (SPid1), which results from isometric shape of RIA. The mentioned intersection in case of the  $4 \times 4$  Butler matrix has a regular (square) shape, hence the limit of a reflection coefficient magnitude is also lower in comparison to the remaining six-ports. The lowest accuracy is obtained for the six-port having equally distributed circle centers on a circle having radius equal to 2, due to the greater distances between circle centers and the measured value, causing an increased width of rings.

It can be also observed that the multiport utilizing a standard  $8 \times 8$  Butler matrix with four circle centers features the same limit as the multiport utilizing a standard  $4 \times 4$  Butler matrix with three circle centers. It results from the same shape of RIA, which is a consequence of a specific arrangement of circle centers related to both mentioned multiports. The lowest limit has been achieved for the multiport utilizing a standard  $8 \times 8$  Butler matrix with seven circle centers (BM8x8<sub>7p</sub>), due to highly regular, octagonal shape of RIA.

#### 2.4.2. Magnitude and Phase Measurement Error Distribution

The analysis described in Subsection 2.4.1 can be performed not only for the origin of a complex plane, but also for any point representing the reflection coefficient. Having a given reflection coefficient one can find the rings' intersection area (RIA) and the maximum measurement error, determined as the largest possible distance between the genuine value of reflection coefficient and the most remote point belonging to RIA [80]. Following this principle the distribution of the measurement error on a complex plane can be obtained. The presented analysis has been performed for seven multiport reflectometers described in Subsection 2.4.1 for reflection coefficients having the magnitude not exceeding 1 (0 dB). The results obtained for the assumed power measurement uncertainty equal to  $\pm 0.1$  dB, together with the circle centers' distributions of the corresponding reflectometers, are presented in Fig. 2.18.

It can be observed that the measurement error distribution is strictly related to the circle centers' distribution of a given reflectometer. The lowest error occurs for the reflection coefficients, for which the distance to each circle center is approximately the same, which ensures uniform shape of RIA. The measurement error increases in proximity of circle centers, which results from the growing disproportion between the circles' radii, leading to the irregular shape of RIA. For the reflection coefficient value being nearly equal to one of the circle centers the value of measurement error rapidly decreases, due to the very low area of one of the rings [80].

As it is seen Fig. 2.18 presents the measurement error distribution defined as the distance between genuine and measured value of reflection coefficient on a complex plane. However, it is more convenient to present the magnitude measurement error and the phase measurement error separately. Such an analysis requires to find all characteristic points of RIA, which constitute the set of points, among which one is the most distant from the theoretical value in a sense of magnitude or phase. To obtain the maximum errors for a given reflection coefficient magnitude, all reflection coefficients having this magnitude have to be considered (analysis performed along a circle with a given radius). For a given

RIA, one can determine two types of characteristic points [81]:

- The first group contains the intersection points of rings' borders, as shown in Fig. 2.16,
- The second group incorporates points resulting from irregularity of the analyzed shape, which occurs in case of significant disproportion of circle centers radii, as presented in Fig. 2.19.

For both inner and outer borders of each ring, the points  $p_i$  having the lowest absolute value and the points  $q_i$  having the highest absolute value have to be found:

$$p_{IN_i} = c_i \left( 1 - \frac{r_{IN_i}}{|c_i|} \right) \quad (2.52)$$

$$q_{IN_i} = c_i \left( 1 + \frac{r_{IN_i}}{|c_i|} \right) \quad (2.53)$$

$$p_{OUT_i} = c_i \left( 1 - \frac{r_{OUT_i}}{|c_i|} \right) \quad (2.54)$$

$$q_{OUT_i} = c_i \left( 1 + \frac{r_{OUT_i}}{|c_i|} \right) \quad (2.55)$$

where  $r_{IN_i}$  and  $r_{OUT_i}$  represent the inner and outer radii of  $i^{\text{th}}$  ring. Furthermore, for outer borders of each ring, the tangency points  $t_i$ , obtained for tangent line crossing the origin of a complex plane, have to be determined:

$$t_{iA} = \sqrt{|c_i|^2 - r_{OUT_i}^2} \exp \left\{ j \left[ \arg [c_i] + \arcsin \left( \frac{r_{OUT_i}}{|c_i|} \right) \right] \right\} \quad (2.56)$$

$$t_{iB} = \sqrt{|c_i|^2 - r_{OUT_i}^2} \exp \left\{ j \left[ \arg [c_i] - \arcsin \left( \frac{r_{OUT_i}}{|c_i|} \right) \right] \right\} \quad (2.57)$$

Two above mentioned points exist if the following condition is fulfilled:

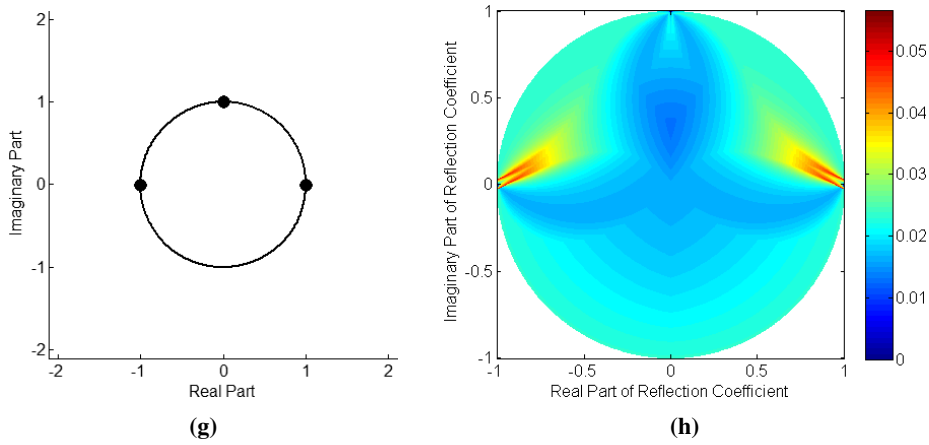
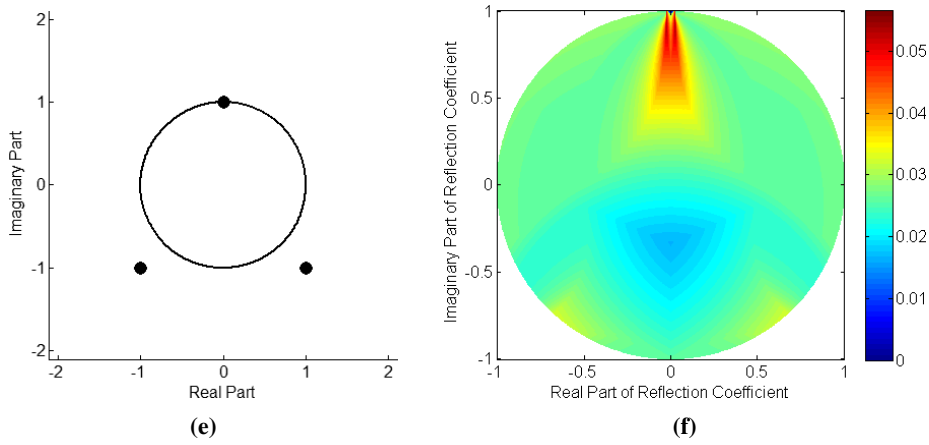
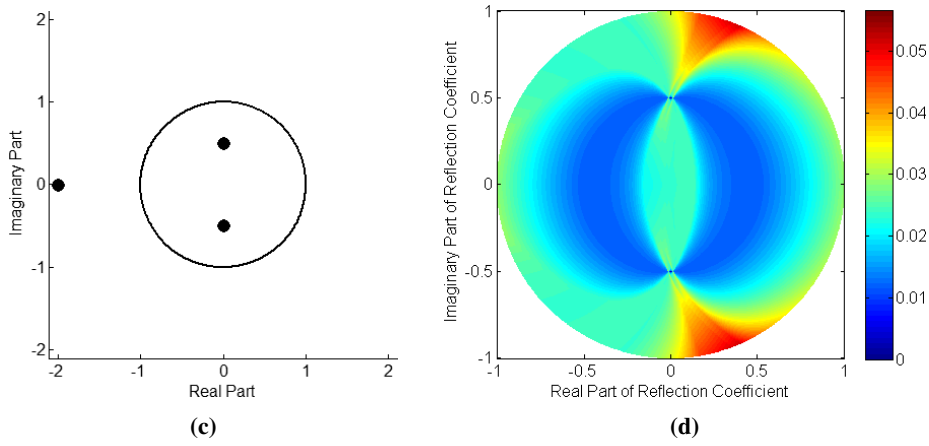
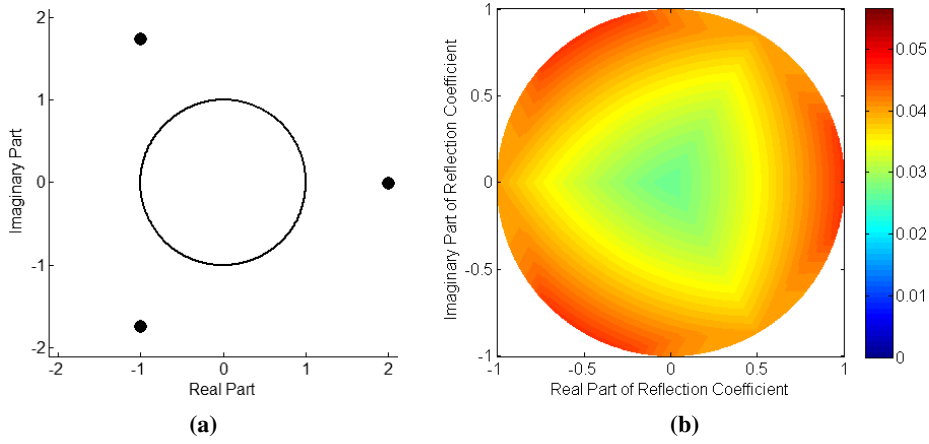
$$r_{OUT_i} < |c_i| \quad (2.58)$$

Once all the described above characteristic points are calculated for each ring, the ones being in the intersection area have to be selected. Further, the maximum magnitude measurement error  $e_{mag}$  and the maximum phase measurement error  $e_{arg}$  can be calculated with the use of the following formulas:

$$e_{mag} = \max_n \{ |20 \log_{10} (|w_n|) - 20 \log_{10} (|\Gamma|)| \} \quad (2.59)$$

$$e_{arg} = \max_n \{ |\arg [w_n] - \arg [\Gamma]| \} \quad (2.60)$$

where  $w_n$  indicates an  $N$ -element set of characteristic points of RIA. Such a procedure allows for determining the maximum errors for a given reflection coefficient. To find the worst cases for a given magnitude of the reflection coefficient, the described algorithm has to be performed for a large number of reflection coefficients having arbitrary phase (range from  $-180^\circ$  to  $180^\circ$ ). The mentioned procedure performed for a wide range of reflection coefficient magnitudes provides the desired maximum measurement errors' distribution in terms of magnitude and phase. The analysis described above has been performed within a range of reflection coefficient magnitude from 0 dB to -40 dB, for seven



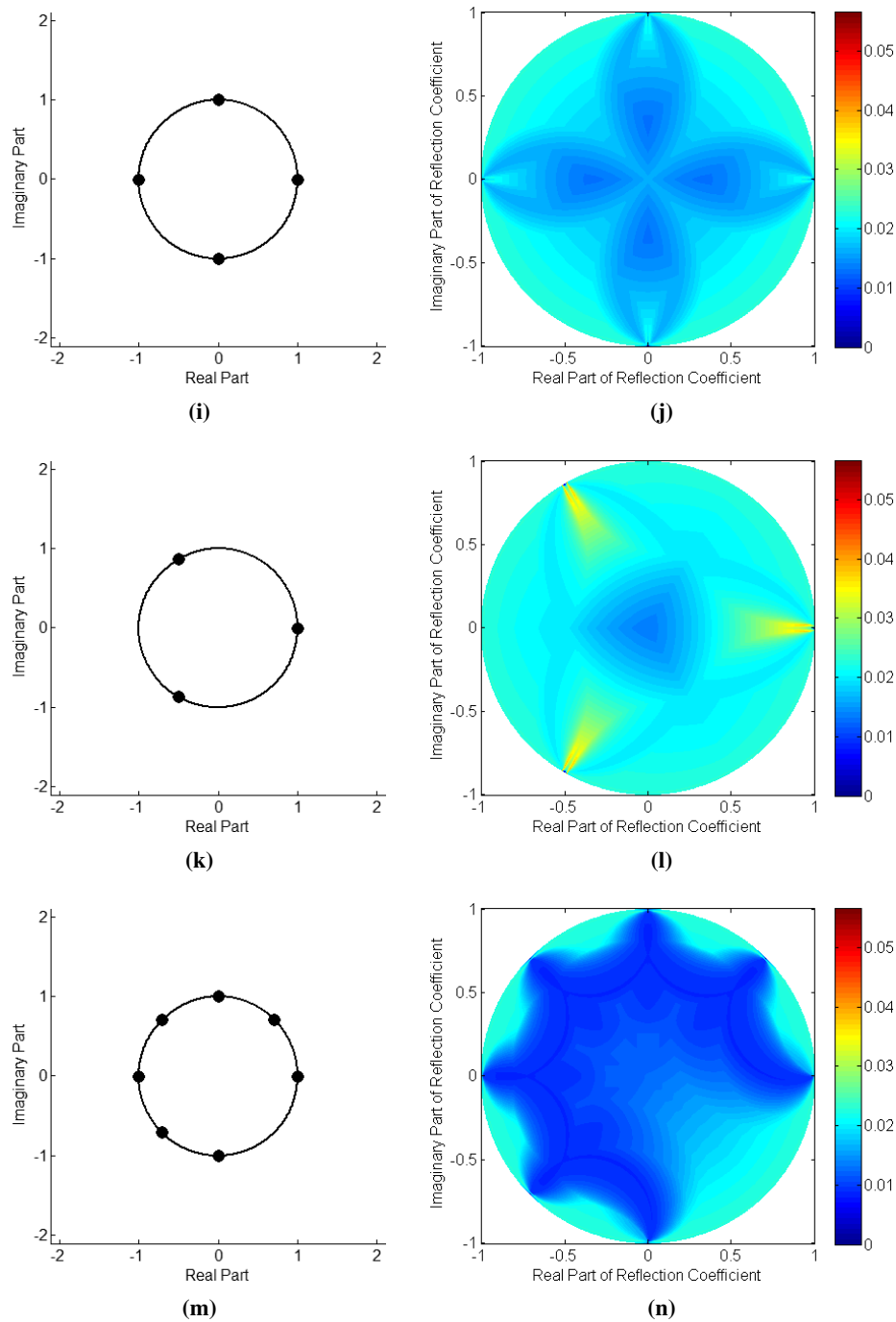


**Figure 2.18:** Circle centers' distribution and the corresponding distribution of the maximum measurement error for seven analyzed multiport reflectometers: SPid2 (a) and (b), SPell (c) and (d), SPstd (e) and (f), BM4x4<sub>3p</sub> (g) and (h), BM8x8<sub>4p</sub> (i) and (j), SPid1 (k) and (l), BM8x8<sub>7p</sub> (m) and (n). The assumed power detectors uncertainty  $\Delta_{PD} = \pm 0.1$  dB.

multiport reflectometers considered in Subsection 2.4.1. The obtained maximum magnitude error and the maximum phase error, respectively, are shown in Fig. 2.20. The rapid increase of both errors for low reflection coefficient magnitude can be observed. The reflection coefficient magnitudes, at which the magnitude error goes to infinity and phase becomes indefinite is in excellent agreement with the theoretical predictions of such limits presented in Table 2.7, where linear approximation has been applied. The discrepancy between the results does not exceed 0.1 dB.

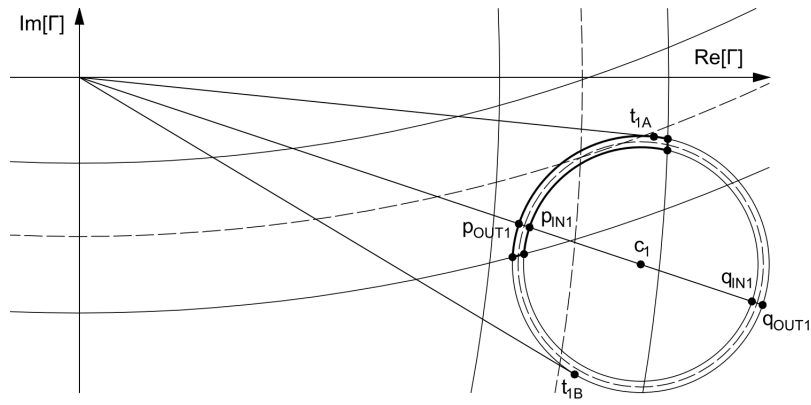


**Figure 2.19:** The analysis of rings intersection area in a close proximity of one of the circle centers. The distinct irregularity of intersection area is seen [81]. (Copyright © 2013, IEEE)

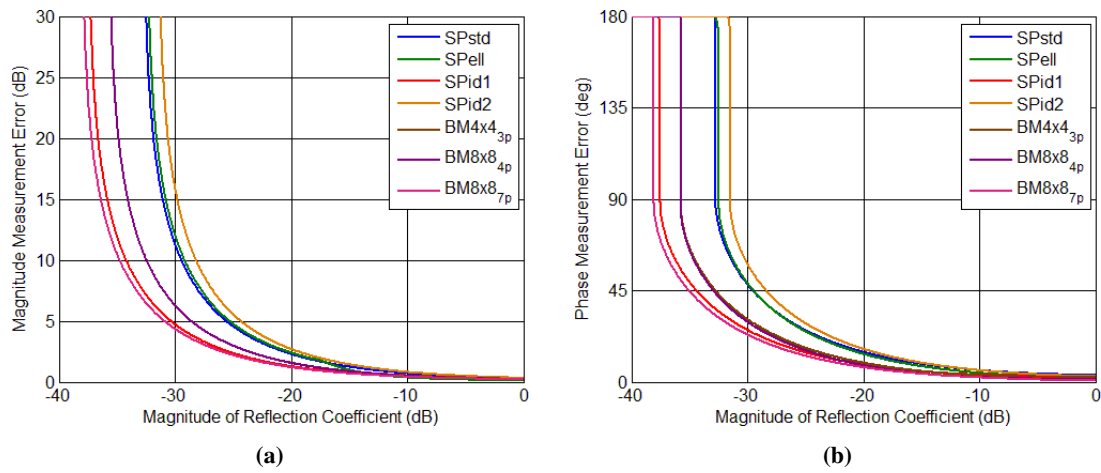


**Figure 2.20:** The maximum magnitude (a) and phase (b) measurement error vs. magnitude of reflection coefficient for seven different multiport reflectometers. The assumed power detectors uncertainty  $\Delta_{PD} = \pm 0.1$  dB.

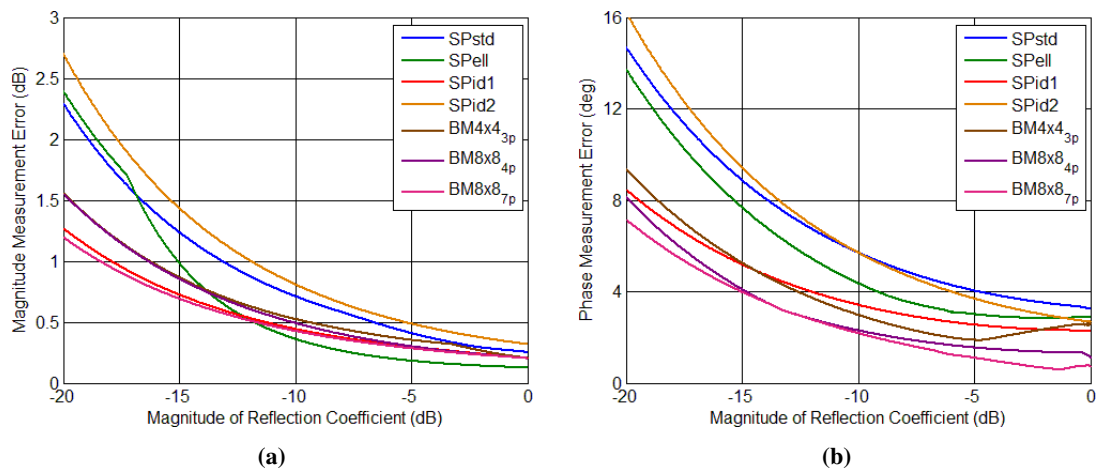


**Figure 2.21:** The maximum magnitude (a) and phase (b) measurement error vs. magnitude of reflection coefficient for seven different multiport reflectometers, for reflection coefficient magnitude range from -20 dB to 0 dB. The assumed power detectors uncertainty  $\Delta_{PD} = \pm 0.1$  dB.

The maximum magnitude measurement error and the maximum phase measurement error in a narrower range from 0 dB to -20 dB are shown in Fig. 2.21. As it is seen the standard six-port (SPstd) and the six-port having uniformly distributed circle centers on a radius equal to 2 (SPid2) are the most inaccurate. For the standard six-port, the inaccuracy is increased by the non-uniform distribution of circle centers. In case of the second mentioned reflectometer, it is caused by a large distance between circle centers and the measured value. The elliptic six-port introduces the smallest error of magnitude measurement for higher values of reflection coefficient magnitude. However, for lower reflection coefficient magnitudes the error increases very rapidly. From the presented results one can see that the six-port reflectometer featuring circle centers distributed on a unity circle (SPid1) and the  $4 \times 4$  Butler matrix, provide the smallest errors of both magnitude and phase among the investigated six-ports. Such circuits ensure simultaneously low limit of reflection coefficient magnitude measurement exceeding -35 dB. Further enhancement of measurement precision can be obtained by the reflectometers providing higher number of circle centers distributed on the circle having radius equal to 1 (BM8x8<sub>4p</sub> and BM8x8<sub>7p</sub>).

The presented analysis is related to the multiport reflectometers operating at a specific frequency, at which the investigated circle centers' distribution is ensured. However, depending on its design, the multiport reflectometer can be utilized in a wide frequency range (covering several octaves). The described analysis is accurate as long as the investigated circle centers' distribution is preserved. It must be emphasized that in case of some multiports the circle centers' distribution rotates in terms of frequency, however, the mutual arrangement of the circle centers is constant (constant magnitude of each circle center and angular distance between any pair of circle centers) [80]. Since in the presented analysis for a given magnitude of reflection coefficient all reflection coefficients having the chosen magnitude are examined (calculation performed along a circle with a given radius), therefore, the rotation of entire circle centers' distribution has no impact on the estimated measurement accuracy in a sense of maximum magnitude and phase error [81].

## 2.5. Experimental Verification

This Section presents the performance of five measuring systems, in which the reflectometers described in this Chapter have been applied. Each system has been excited by the swept signal generator 8350B with RF plug-in HP 83595A by Hewlett Packard, which provides signal having 10 dBm of power in the frequency range from 10 MHz to 26.5 GHz. For power measurements the USB Power Sensors PWR-8GHS produced by Mini-Circuits have been utilized. They feature power measurement uncertainty equal to  $\pm 0.1$  dB. Each reflectometer has been calibrated following the calibration procedure described in Section 2.3. The measurement capability of the considered reflectometers has been experimentally verified by the reflection coefficient measurement of a set of broadband SMA attenuators terminated with a short-circuit. The following attenuation values have been chosen: 1 dB, 2 dB, 3 dB, 6 dB, 10 dB and 13 dB, which correspond to the magnitudes of the measured reflection coefficients being equal to -2 dB, -4 dB, -6 dB, -12 dB, -20 dB and -26 dB, respectively. The measurement accuracy for each reflectometer has been estimated utilizing the circle centers' distribution obtained during the

calibration and the procedure shown in Section 2.4. To examine the obtained measurement results the reference measurements with the use of commercial vector network analyzer N5224A by Agilent have been performed. VNA has been calibrated with the use of a standard SOL (*short-open-load*) technique, with 85052D Calibration Kit by Agilent. The uncertainty of the used VNA has been derived using *Vector Network Analyzer Uncertainty Calculator* software [2].

Five following Subsections are related to the particular reflectometers presented in this Chapter. In each Subsection the description of the developed measuring system is given. Further the calibration results, i.e. circle centers' distribution related to the considered reflectometer and the impedance match of the measuring port are shown. At the end the measurement results and reference values with the estimated measurement accuracy are illustrated.

### 2.5.1. Broadband Six-Port Reflectometer

The six-port presented in Subsection 2.1.1 has been designed in a stripline structure using ARLON 25N laminate featuring  $\epsilon_r = 3.38$  and  $\tan \delta = 0.002$  utilizing the directional couplers realized in a broadside coupled-line technique, which have been previously shown in [95]. They feature the operational frequency range from 2.5 GHz to 3.5 GHz. The cross-sectional view of the homogeneous dielectric structure used for the design is shown in Fig. 2.22. It consists of two 1.52 mm thick laminates, between which a thin laminate layer having thickness 0.15 mm has been placed, for realization of coupled-line directional couplers [95].

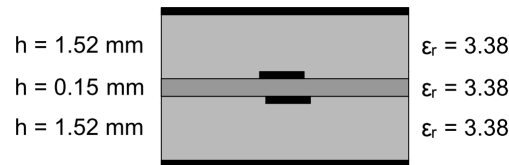


**Figure 2.22:** Cross-sectional view of the stripline layers used for the design of the broadband six-port reflectometer [80].

(Copyright © 2013, Wiley Periodicals, Inc.)

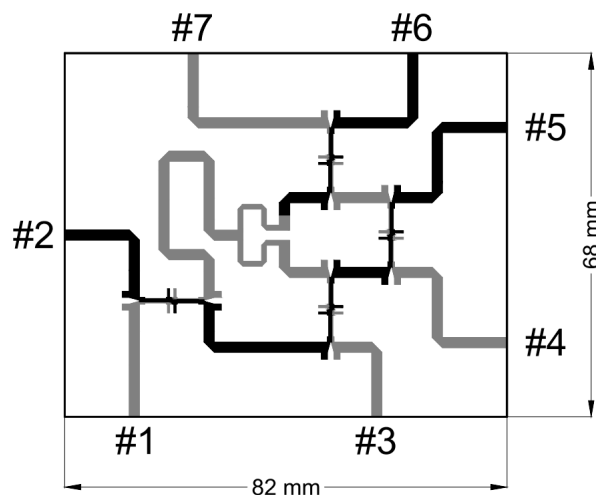


**Figure 2.23:** Layout of the presented broadband six-port reflectometer [80]. Top metallization layer is marked black, whereas bottom metallization layer is marked gray. (Copyright © 2013, Wiley Periodicals, Inc.)

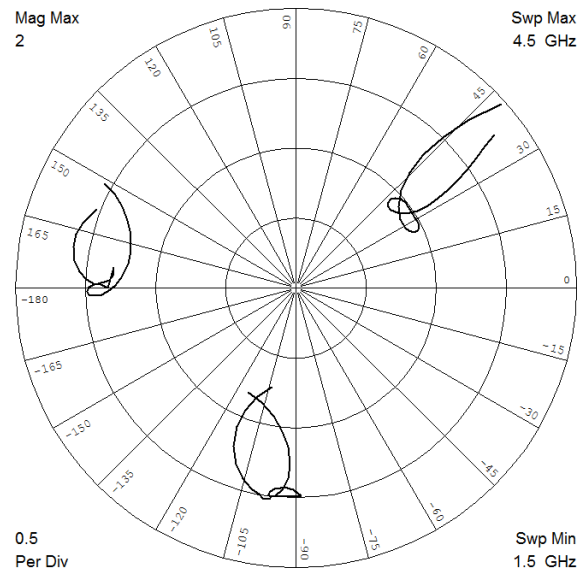


**Figure 2.24:** Circle centers' distribution of the six-port presented in Fig. 2.23. Results of electromagnetic calculations [80].

(Copyright © 2013, Wiley Periodicals, Inc.)

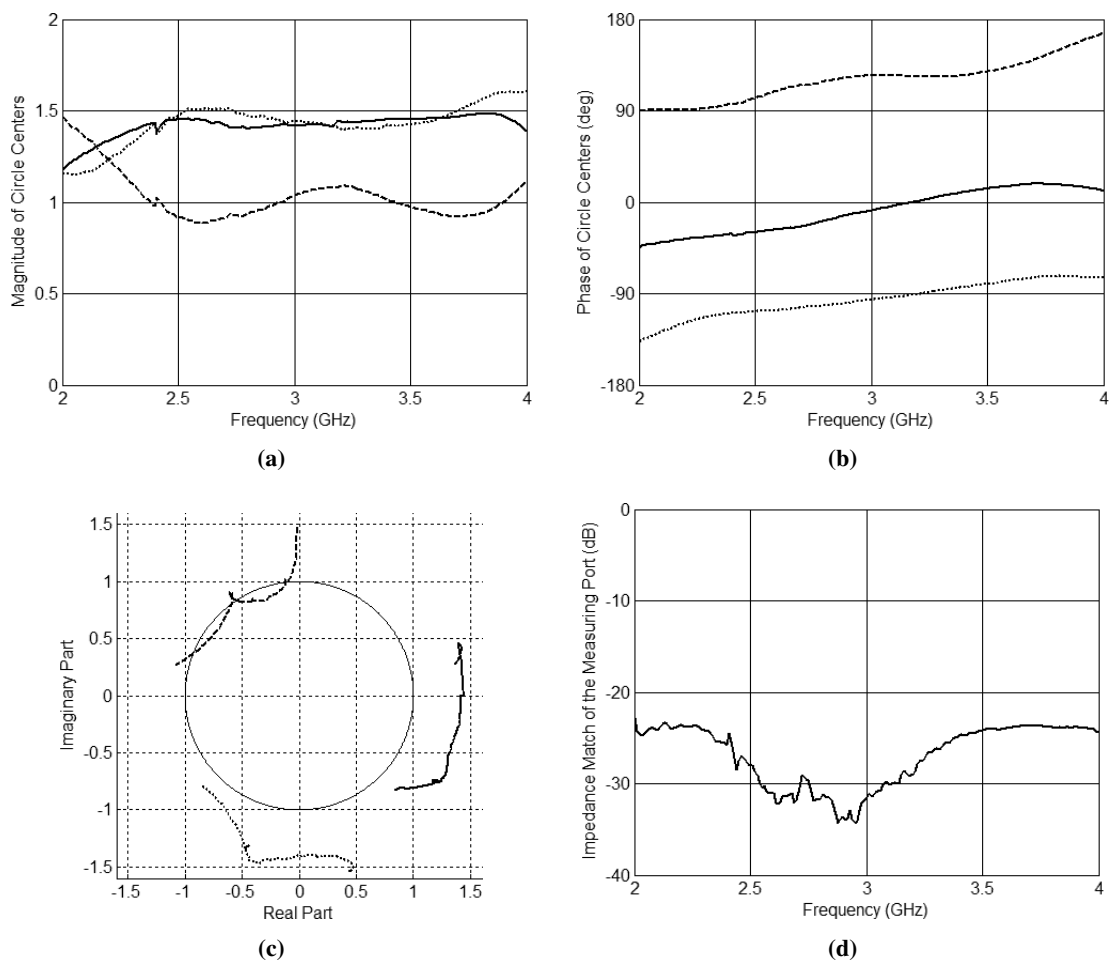


**Figure 2.25:** Results of the calibration procedure for the broadband six-port reflectometer described in Subsection 2.1.1: magnitude (a) and phase (b) of circle centers, circle centers' distribution on a complex plane (c) and the magnitude of reflection coefficient seen at the measuring port (d).

Fig. 2.23 shows the final layout of the designed broadband six-port reflectometer. The coupled-line directional couplers, the Wilkinson power divider and the transmission line section TL are seen. The circle centers' distribution resulting from electromagnetic calculations are illustrated in Fig. 2.24.

The reflectometer has been calibrated in the frequency range 2 – 4 GHz. The obtained circle centers' distribution, as well as the impedance match of the measuring port are presented in Fig. 2.25, whereas the measured reflection coefficients are illustrated in Fig. 2.26.

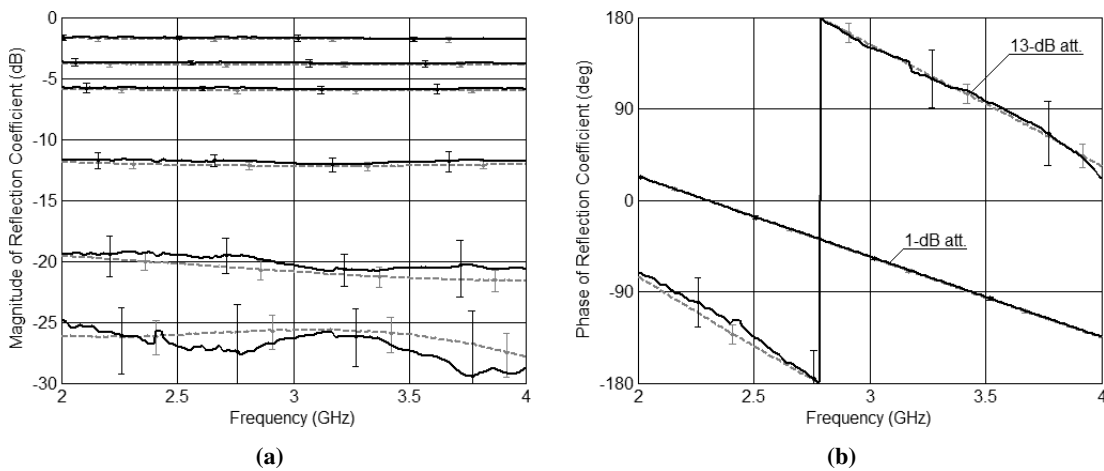


**Figure 2.26:** Reflection coefficients of a set of shorted attenuators measured using the broadband six-port reflectometer described in Subsection 2.1.1: magnitude (a) and phase (b). Solid lines represents the measurements obtained with the use of the proposed reflectometer, dashed lines correspond to the reference values.

### 2.5.2. Ultra-Broadband Six-Port Reflectometer

The ultra-broadband six-port reflectometer presented in Subsection 2.1.2 has been designed also in stripline technique. In order to ensure wide operational frequency range the three-section symmetrical coupled-line directional couplers, shown previously in [35], have been used. These couplers feature bandwidth from 1.15 to 5.1 GHz and their coupling imbalance does not exceed  $\pm 0.25$  dB. They have been designed using a symmetric stripline dielectric structure presented in Fig. 2.27, in which the entire proposed six-port reflectometer has been designed as well.

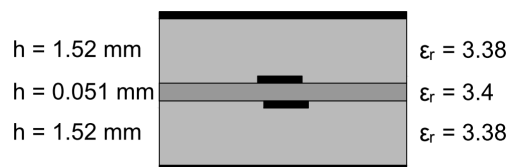


**Figure 2.27:** Cross-sectional view of the dielectric structure used for the design of the ultra-broadband six-port reflectometer [86]. (Copyright © 2014, IEEE)

The simplified Magic-T circuit described in Subsection 2.5.2 has been designed using the same three-section directional coupler and a single-section Schiffman 'C' section. The coupled-line section of the phase shifter has been designed for the maximum coupling coefficient available in the dielectric structure shown in Fig. 2.27 with the use of a single metallization layer and assumed gap width being

equal to  $s = 0.1$  mm. The obtained coupling coefficient is equal to  $k = 0.416$  (modal characteristic impedances:  $Z_{oe} = 78.1 \Omega$  and  $Z_{oo} = 32.3 \Omega$ ). The parameters of the designed phase shifter obtained in electromagnetic calculations are presented in Fig. 2.28. The described directional couplers and Magic-T circuit have been used to assembly the six-port reflectometer network, the layout of which is presented in Fig. 2.29 [86]. As it can be observed the isolated port of the coupler B and the unused port of Magic-T circuit are connected, as it has been discussed above. Furthermore, the connection of directional couplers A and D requires an application of long transmission line having the electrical length  $\Theta_{AD} = 275^\circ$  at the center frequency  $f_0 = 3$  GHz, which significantly affects the circle centers' distribution. Therefore, to stabilize the location of each circle center in terms of frequency, the electrical length of the transmission line TL connecting coupler A and port #1 of Magic-T circuit is chosen to  $\Theta_{TL} = 260^\circ$  at the center frequency. The difference of  $15^\circ$  results from the other connections between the remaining components of the six-port.

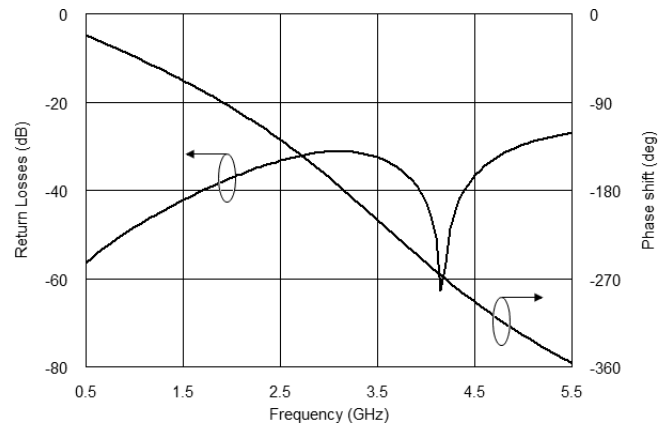


**Figure 2.28:** Return loss and phase shift of the designed single-section Schiffman phase shifter. Results of electromagnetic calculations [86]. (Copyright © 2014, IEEE)

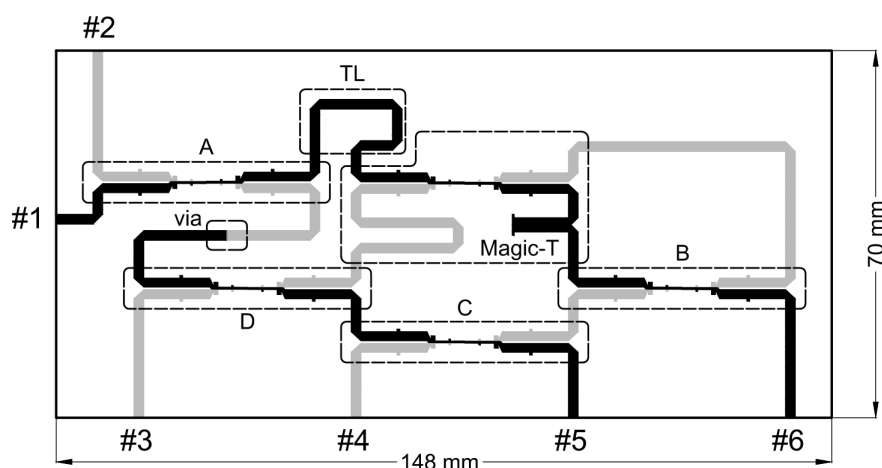


**Figure 2.29:** Layout of the proposed ultra-broadband six-port reflectometer [86]. Top metallization layer is marked black, whereas bottom metallization layer is marked gray. (Copyright © 2014, IEEE)

The circle centers' distribution resulting from electromagnetic calculations is presented in Fig. 2.30. As it is seen the simulated circle centers' location allows for a proper reflection coefficient measurements

in a frequency band being wider than the one resulting from the frequency response of the utilized directional couplers (from 0.5 GHz to 5.5 GHz).

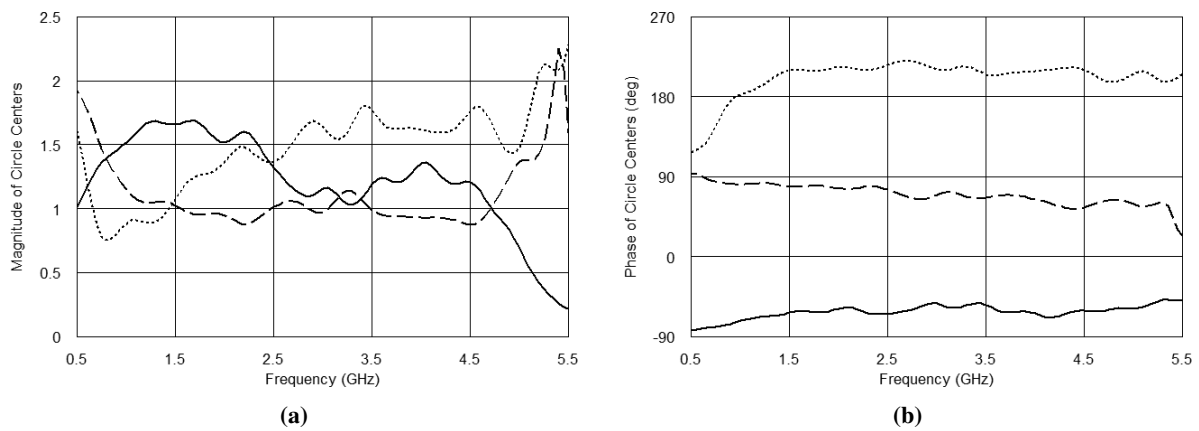


**Figure 2.30:** Circle centers' distribution of the proposed ultra-broadband six-port reflectometer obtained with the use of electromagnetic calculations: magnitude (a) and phase (b) of circle centers [86]. (Copyright © 2014, IEEE)

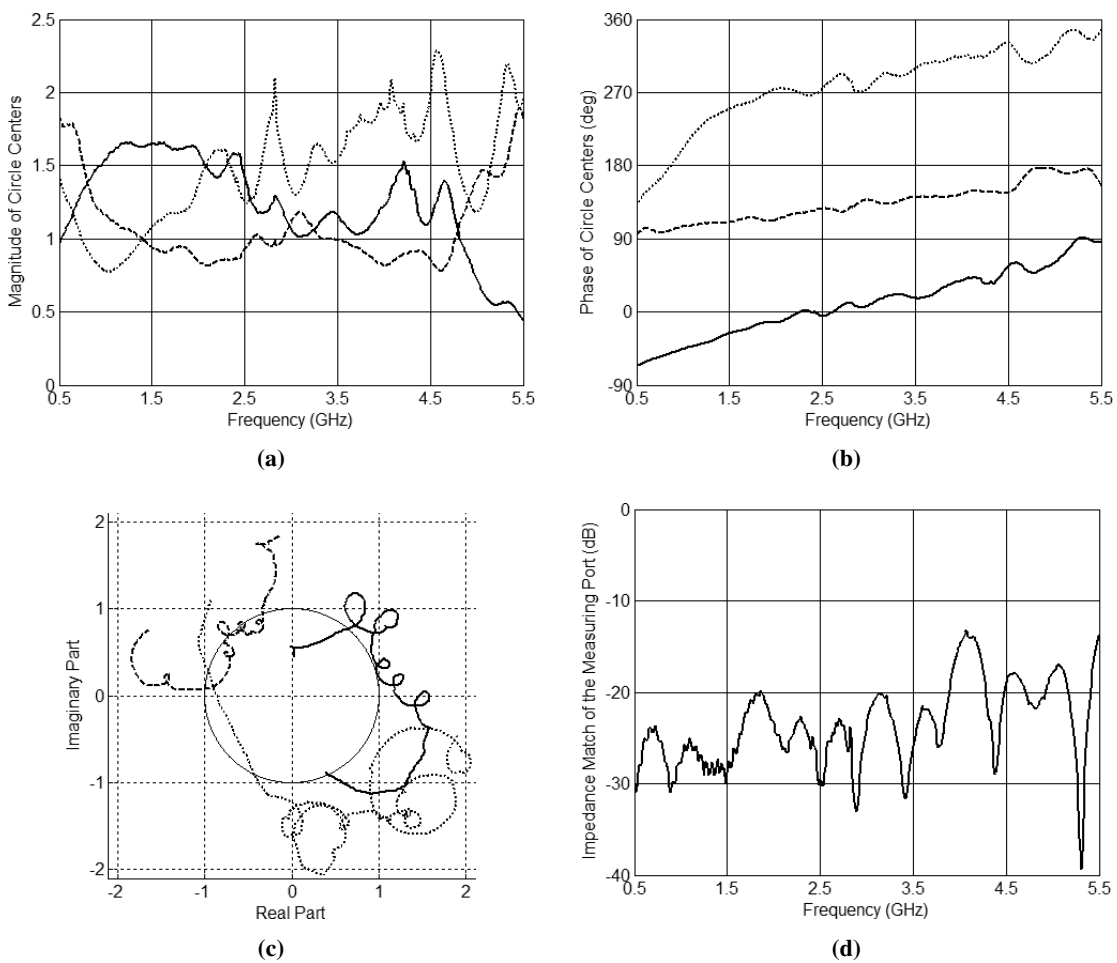


**Figure 2.31:** Results of the calibration procedure for the ultra-broadband six-port reflectometer described in Subsection 2.1.2: magnitude (a) and phase (b) of circle centers, circle centers' distribution on a complex plane (c) and the magnitude of reflection coefficient seen at the measuring port (d) [86]. (Copyright © 2014, IEEE)

The developed reflectometer has been calibrated in the frequency range from 0.5 GHz to 5.5 GHz. The results of calibration are given in Fig. 2.31. As it is seen the proposed six-port reflectometer provides circle centers' distribution allowing for an accurate measurement of the reflection coefficient within the assumed frequency range. The slope of the circle centers' phase is caused by the non-zero electrical length of the added SMA connector at port #2 (please see schematic diagram shown in Fig. 2.4). The measured values of reflection coefficients are presented in Fig. 2.32.

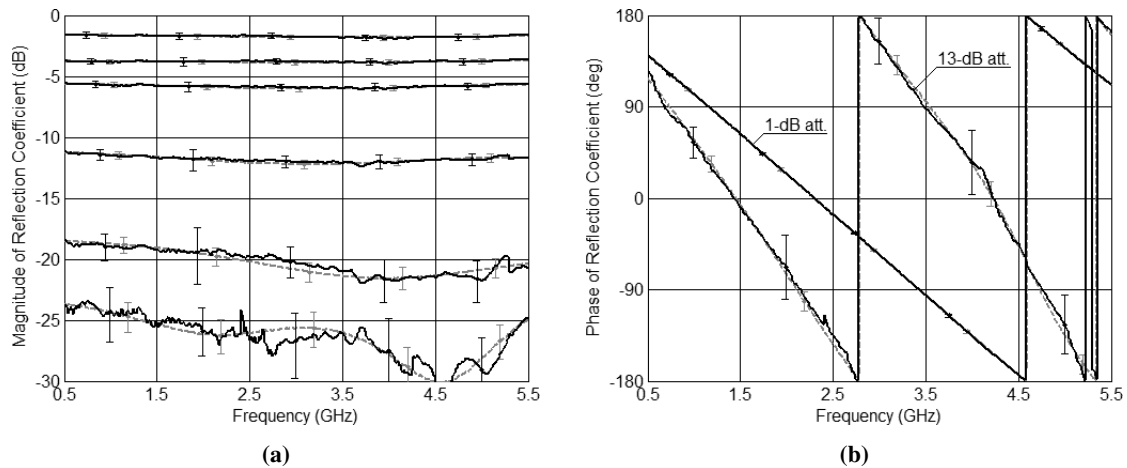


**Figure 2.32:** Reflection coefficients of a set of shorted attenuators measured using the ultra-broadband six-port reflectometer described in Subsection 2.1.2: magnitude (a) and phase (b). Solid lines represents the measurements obtained with the use of the proposed reflectometer, dashed lines correspond to the reference values.

### 2.5.3. Broadband Reflectometer Utilizing Classic $4 \times 4$ Butler Matrix

The multiport reflectometer utilizing a standard  $4 \times 4$  Butler matrix described in Subsection 2.2.1 has been built with the use of the broadband  $4 \times 4$  Butler matrix shown in [36], which operates in the frequency range from 1 GHz to 5 GHz. The utilized matrix features the impedance match and isolation being not worse than 20 dB. The measured amplitude imbalance is equal to  $\pm 1$  dB, whereas the deviation of the phase characteristics does not exceed  $\pm 8^\circ$ . Such properties allow for using the mentioned Butler matrix in the measuring system. The calibration for the system configured as shown in Fig. 2.5 has been performed in the bandwidth 1 – 5 GHz. The obtained results are presented in Fig. 2.33. As it can be observed the achieved circle centers' distribution clearly corresponds to the theoretical assumptions. The measured reflection coefficients are illustrated in Fig. 2.34.

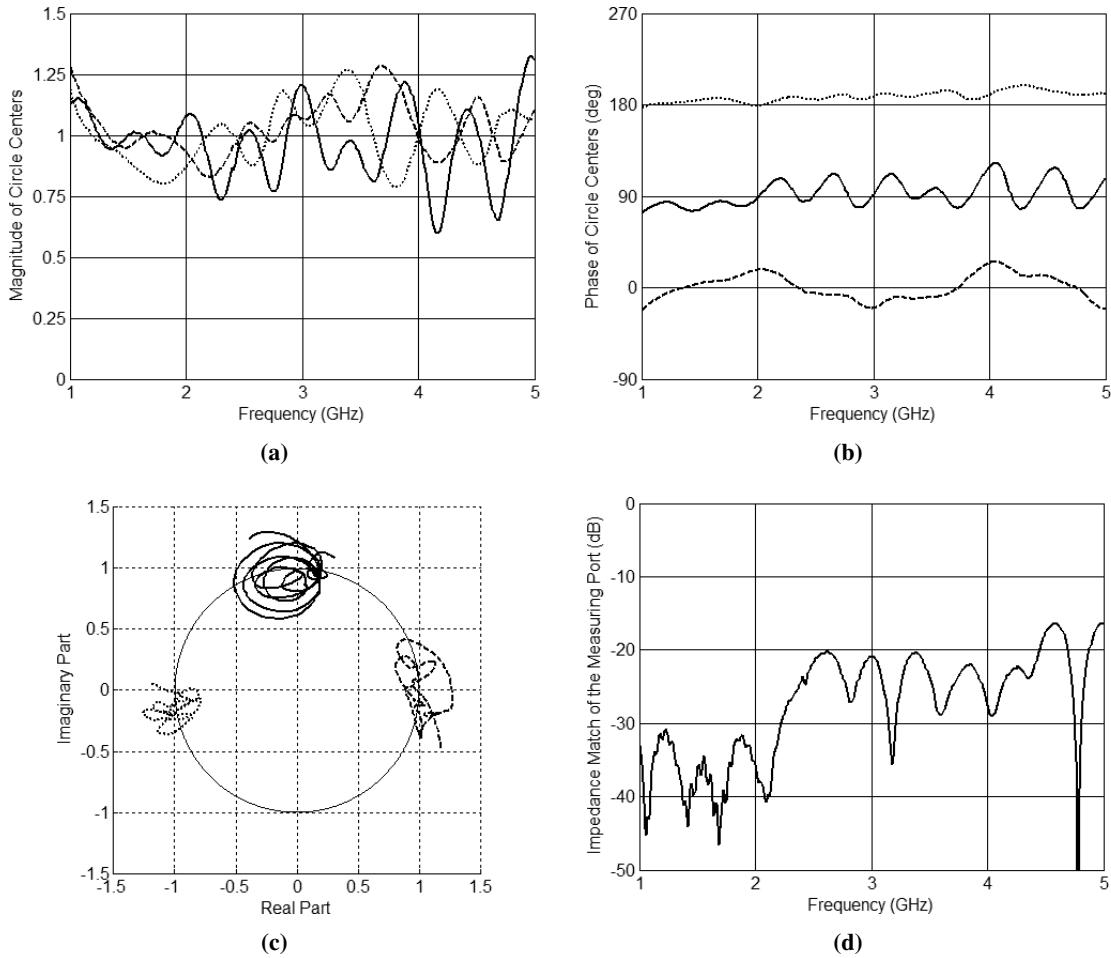


**Figure 2.33:** Results of the calibration procedure for the reflectometer utilizing  $4 \times 4$  Butler matrix described in Subsection 2.2.1: magnitude (a) and phase (b) of circle centers, circle centers' distribution on a complex plane (c) and the magnitude of reflection coefficient seen at the measuring port (d).

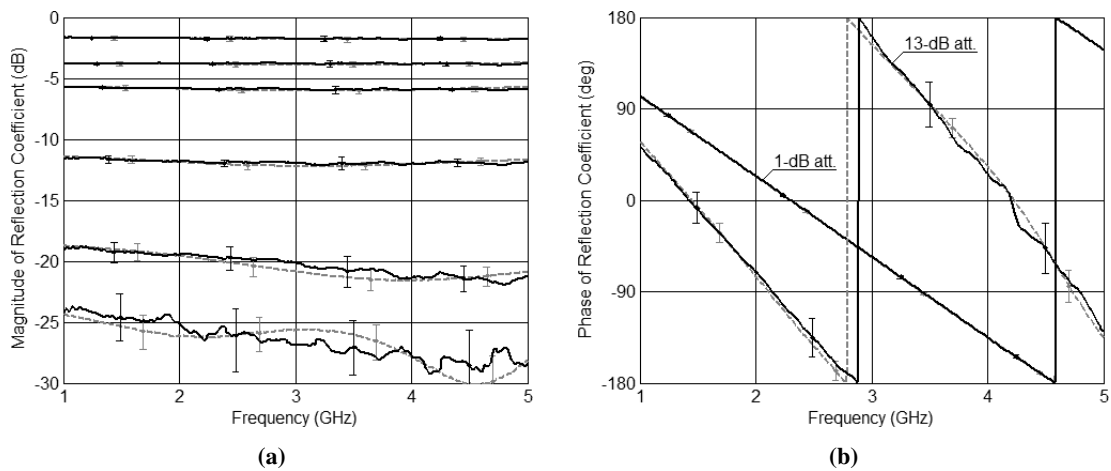


**Figure 2.34:** Reflection coefficients of a set of shorted attenuators measured using the reflectometer utilizing  $4 \times 4$  Butler matrix described in Subsection 2.2.1: magnitude (a) and phase (b). Solid lines represents the measurements obtained with the use of the proposed reflectometer, dashed lines correspond to the reference values.

### 2.5.4. Ultra-Broadband Reflectometer Based on $4 \times 4$ Butler Matrix Consisting of Tapered-Coupled-Line Directional Couplers

The multiport reflectometer presented in Subsection 2.2.2 has been developed for an experimental verification with the use of the ultra-broadband  $4 \times 4$  Butler matrix consisting of  $0/180^\circ$  tapered-line directional couplers described in [37]. Although the operational bandwidth is claimed to be 2 – 8 GHz, the measuring system has been calibrated in the frequency range from 1 GHz to 8 GHz. Within this frequency interval the applied Butler matrix exhibits the following parameters: impedance match and isolation being not worse than 10 dB, the amplitude imbalance exceeding  $\pm 2$  dB and the deviation of frequency characteristics about  $\pm 20^\circ$  [83].

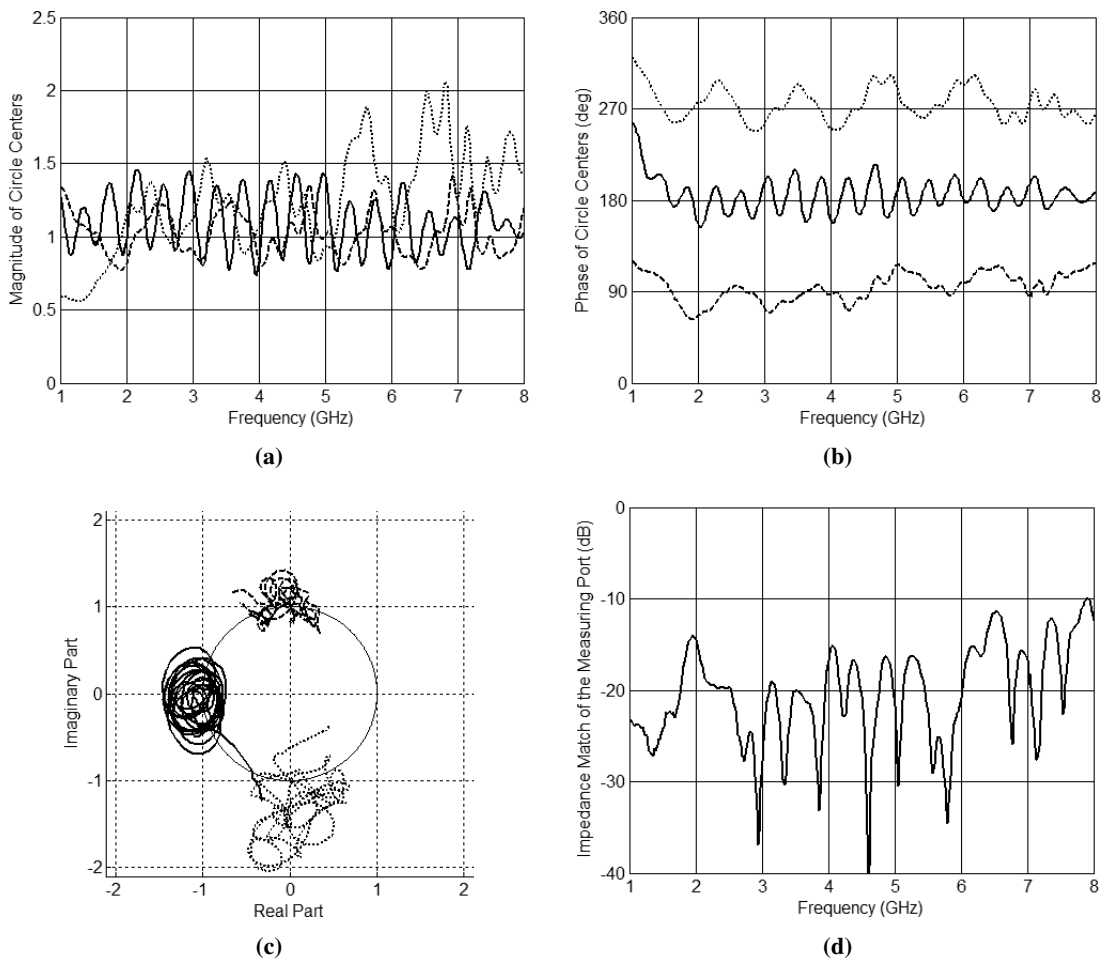


**Figure 2.35:** Results of the calibration procedure for the reflectometer utilizing  $4 \times 4$  Butler matrix consisting of tapered-coupled-line directional couplers described in Subsection 2.2.2: magnitude (a) and phase (b) of circle centers, circle centers' distribution on a complex plane (c) and the magnitude of reflection coefficient seen at the measuring port (d) [83].

(Copyright © 2014, SDIWC)

As it can be observed the power distribution of the considered Butler matrix significantly differs from the ideal one. Therefore, one should expect a distinct deterioration of the circle centers' distribution, reflecting in a decreased measurement accuracy. The measuring system in the configuration shown in Fig. 2.6 has been calibrated and the obtained results are presented in Fig. 2.35. A significant degradation

of the circle centers' distribution can be observed, however, for each considered frequency the mutual arrangement of circle centers allows for correct measurements. The results of reflection coefficient measurements are shown in Fig. 2.36. As seen despite of significant degradation of circle centers' distribution the obtained results are in a good agreement with the reference values.

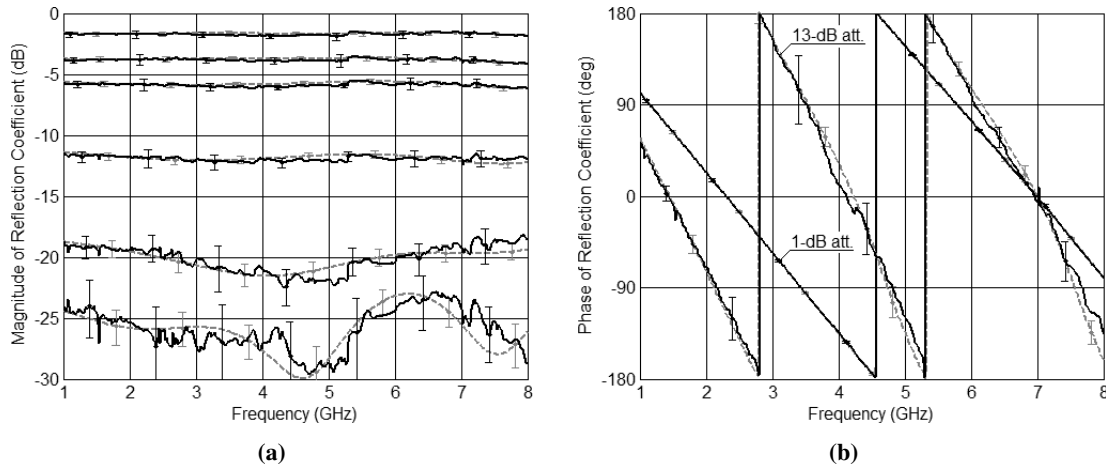


**Figure 2.36:** Reflection coefficients of a set of shorted attenuators measured using the reflectometer utilizing  $4 \times 4$  Butler matrix consisting of tapered-coupled-line directional couplers described in Subsection 2.2.2: magnitude (a) and phase (b). Solid lines represents the measurements obtained with the use of the proposed reflectometer, dashed lines correspond to the reference values.

### 2.5.5. Broadband Reflectometer Incorporating Classic $8 \times 8$ Butler Matrix

The multiport reflectometer with a standard  $8 \times 8$  Butler matrix described in Subsection 2.2.3 has been built utilizing the broadband  $8 \times 8$  Butler matrix, which has been previously shown in [95]. It features the frequency range from 2.5 GHz to 3.5 GHz, however, the operational bandwidth has been extended to the interval of one octave, i.e. 2 – 4 GHz. Within this frequency range the impedance match of the applied matrix is not worse than 18 dB, the isolation is better than 22 dB, whereas the amplitude imbalance reaches  $\pm 4$  dB and the deviation of differential phase characteristics is about  $\pm 20^\circ$ . The system has been configured as shown in Fig. 2.7, however, only four power meters have been applied (excluding reference power measurement) at the input ports, which correspond to four circle centers located on a unitary circle with angular distance of  $90^\circ$ . The results of calibration are shown in Fig. 2.37. As seen the obtained circle centers' distribution fully corresponds to the theoretical predictions, despite of the extended frequency range. Four uniformly arranged circle centers allow for correct measurements, the results of which are shown in Fig. 2.38.

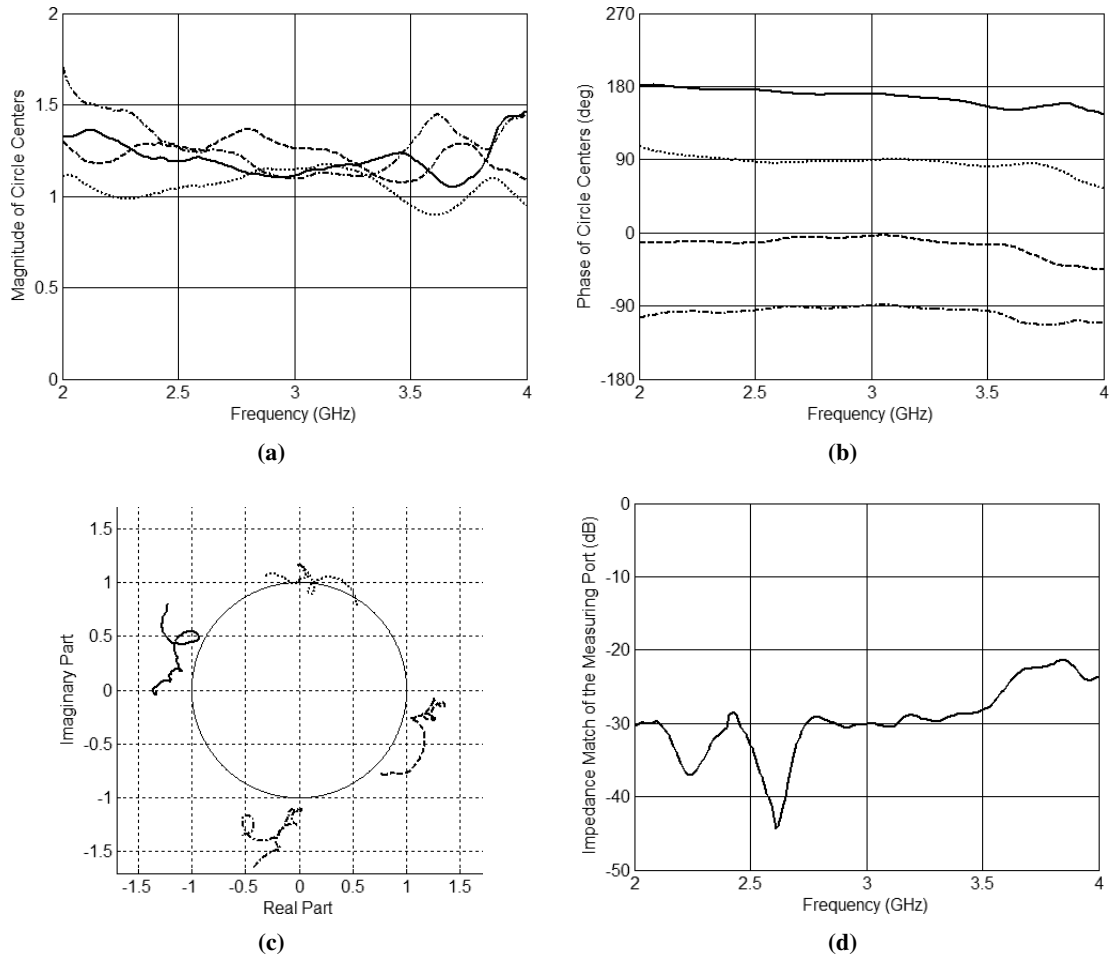


**Figure 2.37:** Results of the calibration procedure for the reflectometer utilizing  $8 \times 8$  Butler matrix described in Subsection 2.2.3: magnitude (a) and phase (b) of circle centers, circle centers' distribution on a complex plane (c) and the magnitude of reflection coefficient seen at the measuring port (d).

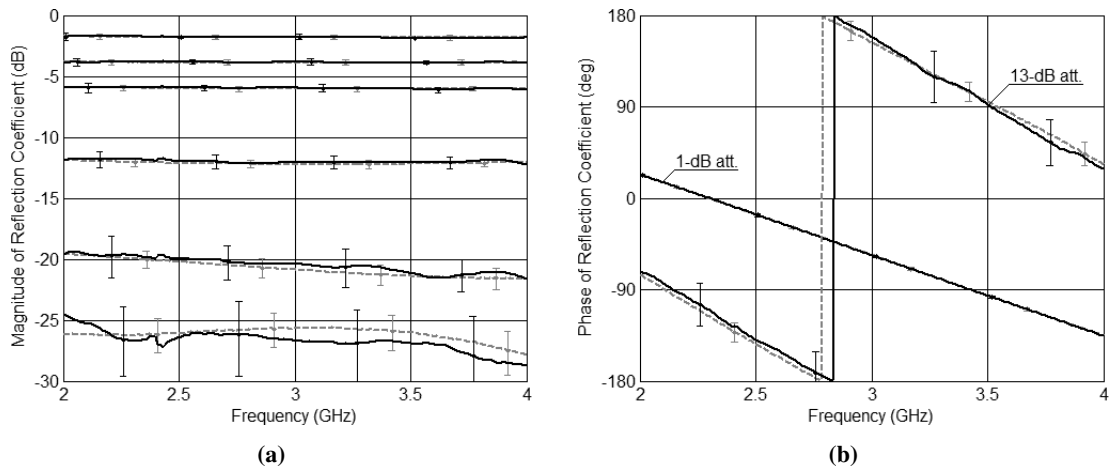


**Figure 2.38:** Reflection coefficients of a set of shorted attenuators measured using the reflectometer utilizing  $8 \times 8$  Butler matrix described in Subsection 2.2.3: magnitude (a) and phase (b). Solid lines represents the measurements obtained with the use of the proposed reflectometer, dashed lines correspond to the reference values.

### 2.5.6. Analysis of Measurement Results

The measurement results obtained for five broadband reflectometers described in this Section confirm the correct design of the presented six-port reflectometers and the usability of Butler matrices in the measurements of reflection coefficient. For each considered reflectometer it can be observed, that the measured values are close to the reference ones within the entire frequency range of particular reflectometer in terms of both magnitude and phase. It is seen that the measurement error increases with the decreasing magnitude of the measured value, which confirms the theoretical investigation given in Subsection 2.4.2. For each considered reflectometer the magnitude and phase measurement error vs. the magnitude of the measured reflection coefficient has been calculated. The measurement error values have been determined as the maximum difference between the measurement results and the corresponding reference values (VNA measurements) within the entire operational frequency range of the particular reflectometer. The obtained results are shown in Fig. 2.39.

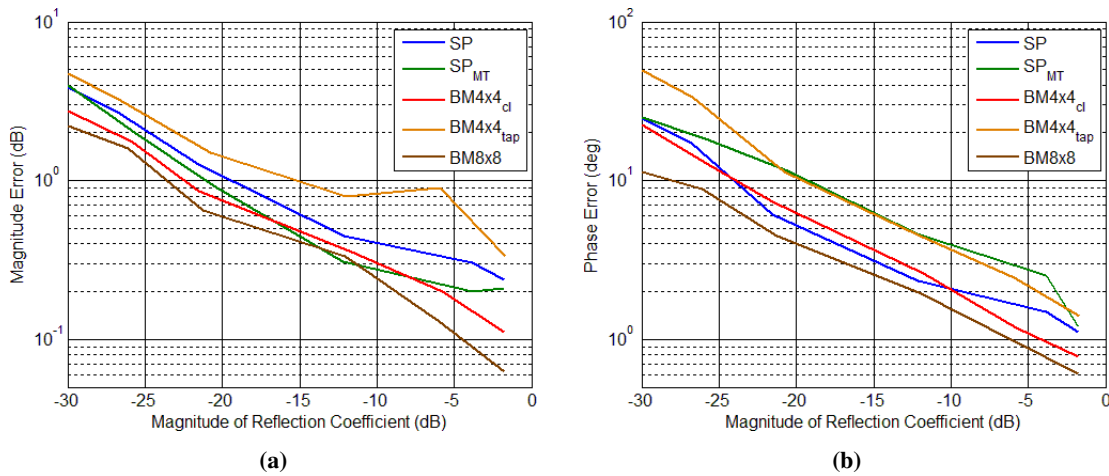


**Figure 2.39:** Maximum magnitude (a) and phase (b) measurement error vs. the magnitude of the measured reflection coefficient for five broadband reflectometers described in Section 2.5.

It must be emphasized that for the theoretical investigation described in Subsection 2.4.2 all the reflection coefficients have been taken into account, whereas in this case the error distribution has been calculated utilizing only the measured values, which do not always constitute the worst case. Furthermore, it is worth mentioning that the circle centers' distribution related to each considered reflectometer deviates with frequency, which affects the measurement accuracy at a given frequency. Moreover, as the reference values the results of measurements with the use of VNA have been utilized, which are somehow deteriorated due to imperfect accuracy. Therefore, the obtained measurement error distributions shown in Fig. 2.39 slightly differ from the theoretical predictions illustrated in Fig. 2.20 and in Fig. 2.21.

Analyzing the obtained results of the measurements it can be observed, that the requirements related to the parameters of Butler matrices utilized in measurements are not excessive. The phase differences can vary by about  $20^\circ$  from the ideal value of  $90^\circ$ , the coupling imbalance exceeding 1 dB can be satisfactory and the isolation and return losses not worse than 15 dB are acceptable, since a suitable

calibration procedure is able to take into account all of these imperfections. Therefore, the performance requirements of the Butler matrices used in measurement systems, are lower than in case of the Butler matrices intended to use in antenna applications. As a result a given Butler matrix can be used in the measurements within a bandwidth being wider than the one, in which the Butler matrix can serve in antenna feeding networks [79], [83], [85].

Further analysis of the measurement error distributions shown in Fig. 2.39 reveals, that the reflectometer utilizing a classic  $8 \times 8$  Butler matrix features the best measurement accuracy. It is due to the uniform arrangement of circle centers on a complex plane and their high stability in the operational frequency range. It can be observed that the reflectometer utilizing the classic  $4 \times 4$  Butler matrix provides higher measurement accuracy than the reflectometer involving the  $4 \times 4$  Butler matrix utilizing tapered-coupled-line directional couplers, despite of the same theoretical circle centers' distributions. The decreased accuracy of the latter reflectometer is caused by a significant deterioration of its circle centers' distribution resulting from poor isolation and impedance match. Finally, it must be stated that the reflectometer utilizing the classic  $4 \times 4$  Butler matrix provides higher measurement accuracy in comparison to classic six-port reflectometers reported in literature [24].

## 2.6. Conclusions

In this Chapter the complete investigation of reflection coefficient measurements with the use of multiport measurement technique has been presented. In particular five reflectometers have been investigated. Two of them are classic six-port reflectometers with applied modifications, which allow for broadband operation. Further three reflectometers constitute novel measuring systems, in which Butler matrices serve as power distribution networks. It has been shown that a classic  $4 \times 4$  Butler matrix, as well as a  $4 \times 4$  Butler matrix consisting of tapered-coupled-line 3-dB  $0/180^\circ$  directional couplers and a classic  $8 \times 8$  Butler matrix feature an advantageous circle centers' distribution allowing for precise measurements in a wide frequency range. The additional advantage of such measuring systems results from relatively high number of Butler matrix's ports in comparison to the classic six-port reflectometers. This fact allows for the utilization of different configurations. Each of them introduces a different inner power division, what has the same effect as a different multiport application. Therefore, to increase the measurement accuracy, several measurement results, obtained with different connection combinations, may be collected and averaged. Such a procedure may not be applied in standard six-port reflectometers, having only one possible connection combination.

Further in the Chapter, the two-step calibration of linear multiports, having an arbitrary number of ports, has been presented. The first step constitutes a numerical procedure of a multiport calibration utilizing the Levenberg-Marquardt algorithm for least-squares fitting. Such an approach ensures higher accuracy due to enhanced robustness to the power detectors' uncertainty in comparison to the standard analytical procedures. Moreover, the analytical solution allowing to calculate the measured reflection coefficient, for a multiport having an arbitrary number of ports, is given. As the second step the extension of a well-known approach has been applied, in which an actual reflectometer is modeled as a connection of an ideal reflectometer and an error box network. This procedure has allowed for eliminating the

influence of the imperfectly matched load on the calibration results. Moreover, in order to calibrate a given reflectometer within a wide frequency range, the simple algorithm, allowing for the choice of the optimal set of calibration standards, has been proposed.

Furthermore, the influence of circle centers' distribution on measurement accuracy has been comprehensively analyzed. A theoretical investigation, allowing for determining the limitation of reflection coefficient measurement for arbitrary circle centers' distribution, has been presented. It has been shown that multiport reflectometers featuring uniformly distributed circle centers on a unitary circle provide higher accuracy of measurements, allowing simultaneously for measurements of reflection coefficients having lower magnitudes. Taking into account the above statement it can be concluded that Butler matrices can serve as high quality reflectometers, ensuring higher measurement accuracy than the classic six-ports reported in literature.

Finally, five broadband reflectometers presented in this Chapter have been built for an experimental verification and the reflection coefficients of the set of broadband reflective elements have been measured. Each reflectometer has been calibrated using the described calibration procedure and its measurement accuracy has been estimated following the presented algorithm. The obtained results are very close to reference values obtained with the use of a commercial vector network analyzer. Moreover, all measured values are located in the estimated accuracy interval, proving the correctness of measurement accuracy analysis. The comparison of the measurement results confirms, that the multiport reflectometers based on Butler matrices feature higher measurement accuracy in comparison to the classic six-port reflectometers.

### 3. Transmission Coefficient Measurements

Multiport measurement technique, as it has been mentioned in Section 1.1, can be also applied for transmission coefficient measurements. Such a procedure can be performed following two different approaches. The first one is based on the measuring system incorporating two reflectometers excited through power divider and isolators [17], [47], [61], [15], [41], [40]. In the second approach the number of reflectometers is reduced to only one [45], [18].

The Chapter discusses both techniques of transmission coefficient measurements with the use of two novel multiport systems proposed by the Author, which are capable of  $S$ -parameter measurements (both reflection and transmission coefficients). In either case classic Butler matrices as power division networks have been utilized. The presented analysis shows that by the application of Butler matrices in such systems the number of required components can be reduced and the obtained system simplification does not impair the measurements quality. For both measuring systems a complete theoretical analysis of the transmission coefficient measurements is shown. Moreover, for each measurement technique the Author proposes the calibration procedure providing enhanced measurement accuracy. The measurement results presented at the end of this Chapter confirm the correctness of the described theoretical investigations.

The following Chapter constitutes a compilation of the papers concerning the multiport measurements of transmission coefficient recently published by the Author in [79] and [85].

#### 3.1. Measurements With the Use of Two Classic $4 \times 4$ Butler Matrices

In order to measure the transmission coefficient the reflectometer based on a single classic  $4 \times 4$  Butler matrix described in Subsection 2.2.1 can be extended by the addition of the second  $4 \times 4$  Butler matrix as shown in Fig. 3.1 [79]. The presented system allows for the measurement of both reflection and transmission coefficients. It is composed of two classic  $4 \times 4$  Butler matrices with neither additional power dividers nor isolators, allowing for a significant simplification of measuring setup without any impairment of the measurement accuracy. Elimination of isolators, being in general narrow-band elements, allows for broadband operation limited only by bandwidth of the utilized Butler matrices.

Since the reflection coefficient measurements can be done following the procedure described in Chapter 2, in this Section only the measurements of transmission coefficient are investigated. In this Section a complete theoretical analysis based on ideal  $4 \times 4$  Butler matrices is presented. Further, fully analytical calibration procedure for transmission coefficient measurements based on the least-squares

approach that can be applied to a multiport system having an arbitrary number of power meters, is presented. Finally, a comprehensive analysis of the simplified model for the transmission coefficient measurements is discussed.

### 3.1.1. Theoretical Analysis

To illustrate the transmission coefficient measurement with the use of the system presented in Fig. 3.1 a similar analysis to the one shown in case of reflectometers utilizing Butler matrix described in Subsections 2.2.1, 2.2.2 and 2.2.3 can be conducted. In case of transmission coefficient measurements, the measured power is the sum of two signals, one depending on the measured transmission coefficient value and the second being a reference signal. To satisfy this condition, two input ports of the Butler matrix B, mutually isolated, have to be chosen. The sum of the two signals can be measured at each of the output ports of the Butler matrix B. Fig. 3.1, similarly as in the case of reflection coefficient measurement, presents an exemplary connections of the measurement system.

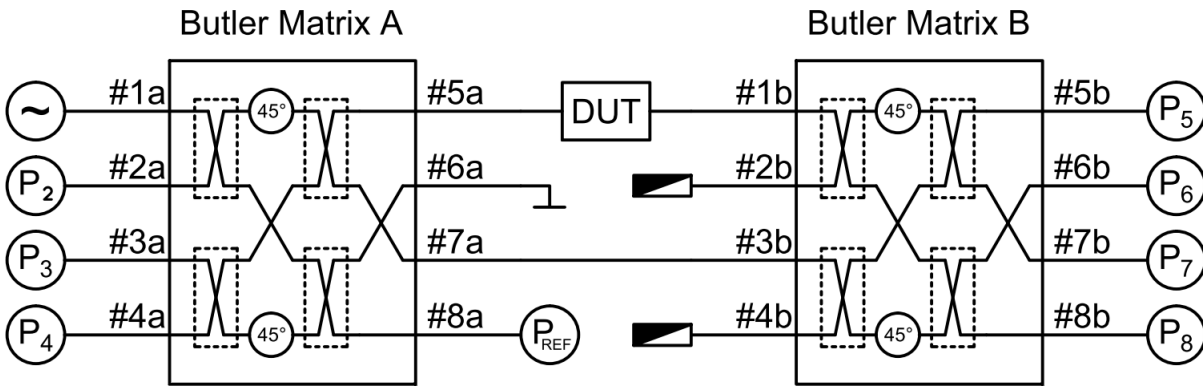


**Figure 3.1:** Schematic diagram of a multiport measuring system with two  $4 \times 4$  Butler matrices allowing for transmission coefficient measurements [79].

In case of ideal Butler matrices, the power incident to power meters  $P_5 - P_8$  can be expressed as follows [79]:

$$p_{ikm} = \frac{P_{ikm}}{P_{REF}} = |S_{51}TS_{i1} + S_{k1}S_{im}|^2 \quad (3.1)$$

where  $p$  – normalized power,  $P$  – measured power,  $i$  – port number at which the power is measured (#5b – #8b),  $P_{REF}$  – reference power measured at port #8a,  $k$  and  $m$  – numbers of directly connected ports of Butler matrices A and B, respectively, and  $T$  – the measured transmission coefficient of DUT. The circle centers in the case of transmission coefficient measurements are equal to:

$$c_{ikm} = -\frac{S_{k1}S_{im}}{S_{51}S_{i1}} \quad (3.2)$$

It must be emphasized that equations (3.1) and (3.2) describe the situation when DUT is connected between port #5a of the matrix A and port #1b of the matrix B, however, other combinations are possible, i.e. the port at which the Butler matrix A is excited, as well as ports between which DUT is connected can be chosen differently. Therefore, the resulting circle centers' distribution is a function of five parameters. It can be shown that the number of possible configuration is equal to 576, however,

they correspond to only five different circle centers' distributions shown in Fig. 3.2. As it can be observed there are only two distributions having four different circle centers. The remaining ones lead to ambiguity described in Section 1.1, hence they cannot be utilized in measurements. Furthermore, according to the investigation of measurement accuracy described in Section 2.4, both distributions containing four circle centers provide exactly the same distribution of magnitude and phase measurement error.

To obtain distribution with four circle centers the input ports of the Butler matrix B, to which DUT and the reference signal are connected, must be chosen correctly. This can be done by the analysis of the schematic diagram of the  $4 \times 4$  Butler matrix seen in Fig. 3.1. To ensure four different circle centers, the signal related to the measured value and the reference signal have to excite different internal directional couplers of the Butler matrix B, which ensures the maximum variety of the phase shifts for these two signals seen at the output ports of the  $4 \times 4$  Butler matrix. Therefore, if the second port of DUT is connected to port #1b or #2b, the reference signal has to be provided to port #3b or #4b. On the other hand the choice of the output ports of the Butler matrix A (#5a – #8a) rotates the entire circle centers' distribution by  $45^\circ$ , what does not affect the measurement conditions. The choice of the input port of the Butler matrix A, at which the system is excited does not influence the circle centers' distribution.

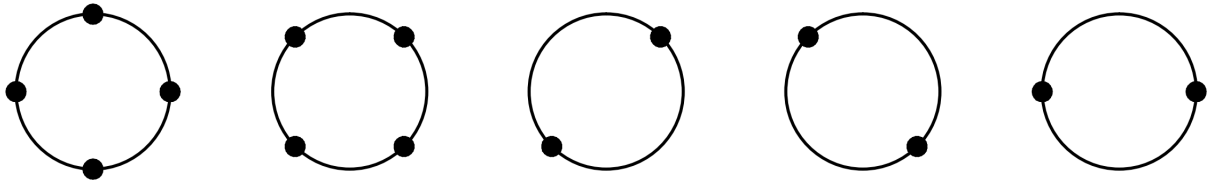


**Figure 3.2:** All possible distributions of circle centers related to the multiport measuring system incorporating two  $4 \times 4$  Butler matrices.

### 3.1.2. Calibration for Transmission Coefficient Measurements Using System Composed of Two Butler Matrices

As it has been mentioned at the beginning of this Section, the measuring system presented in Fig. 3.1 allows for the measurements of reflection and transmission coefficients. All details related to the measurements of reflection coefficient are presented in Chapter 2. This Section is related to the transmission coefficient measurements, which require a separate calibration procedure.

The equation (3.1) shows the relation between the measured power and transmission coefficient  $T$  for ideal Butler matrices, i.e. ideal impedance match and perfect isolations of both matrices are assumed. However, this condition cannot be fulfilled in practice. Hence, to achieve a satisfying measurement accuracy the developed model has to take into account the imperfect parameters. Fig. 3.3a presents the signal flow, in which all non-ideal parameters of the proposed measuring system are seen. As it can be observed the Butler matrix A is represented by the three-port network, the  $S$ -parameters of which are indicated as  $S_{Axx}$ . The Butler matrix B has been simplified to the three-port network with  $S$ -parameters indicated as  $S_{Bxx}$ , whereas the connection between both matrices is represented by a two-port network, the  $S$ -parameters of which are indicated as  $S_{Cxx}$ . It has to be emphasized, that such a simplification does not provide any inaccuracy and this model can be used separately for each output port of the Butler matrix B, at which the power is measured (#5b – #8b).

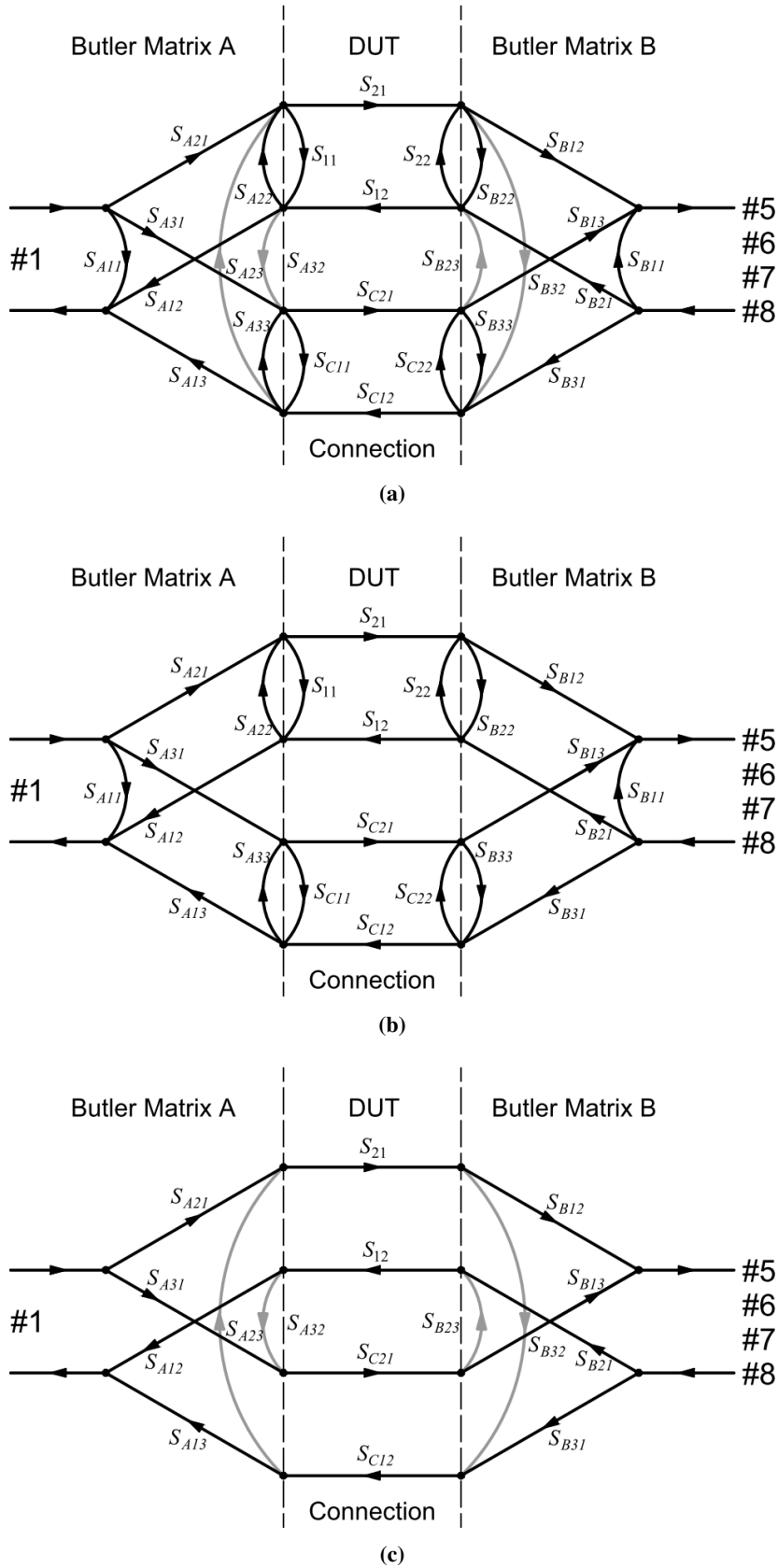


**Figure 3.3:** Signal flow in the multiport measuring system composed of two  $4 \times 4$  Butler matrices for transmission coefficient measurements: graph of the entire measuring system with all imperfect parameters (a), graph of the measuring system with neglected imperfect isolations (b), graph of the measuring system with imperfect isolations and with assumed perfect impedance match of all components (c).

In Fig. 3.3a it can be observed, that the accurate model of a real measuring system is complex and would require a highly sophisticated calibration procedure involving large number of parameters. Therefore, the imperfect isolations of both three-ports ( $S_{A23}$ ,  $S_{A32}$ ,  $S_{B23}$  and  $S_{B32}$  marked gray in Fig. 3.3a) have been neglected, which significantly simplifies the signal flow to the form shown in Fig. 3.3b. It has to be underlined that such a simplification introduces some inaccuracy, however, as it is shown in Subsection 3.1.3, the error caused by the described simplification is significantly lower in comparison to the error caused by the inaccuracy of commercially available power meters. Using the simplified signal flow shown in Fig. 3.3b one can derive the relation between the measured transmission coefficient and the power measured at the output ports of the utilized Butler matrix B:

$$p_i = q_i |1 + A_i T|^2 \quad (3.3)$$

where  $q_i$  and  $A_i$  ( $i = 5, 6, 7, 8$ ) are the calibration constants to be found during the calibration procedure and coefficient  $T$  is given as follows:

$$T = \frac{S_{21}}{(1 - \Gamma_1 S_{11})(1 - \Gamma_2 S_{22}) - S_{12} S_{21} \Gamma_1 \Gamma_2} \quad (3.4)$$

where  $\Gamma_1$  and  $\Gamma_2$  are the reflection coefficients seen at the measuring ports between which DUT is inserted. Moreover, assuming that the impedance match of both measuring ports is about 20 dB equation (3.4) may be simplified:

$$T^* = \frac{S_{21}}{(1 - \Gamma_1 S_{11})(1 - \Gamma_2 S_{22})} \quad (3.5)$$

It is seen, therefore, that to obtain the entire  $S$ -matrix of a given two-port one has to perform four measurements. First, the reflection coefficient  $S_{11}$  has to be found (utilizing power readings  $P_2 - P_4$  in the procedure described in Chapter 2). Subsequently, the transmission coefficient  $T^*$  given by (3.5) can be measured. Further, DUT has to be reversed and the same procedure has to be repeated, resulting in determination of reflection coefficient  $S_{22}$  and reverse transmission coefficient  $T_{rev}^*$ . After these four measurements the exact transmission coefficients  $S_{21}$  and  $S_{12}$  can be calculated. It must be emphasized, that for reversed DUT equation (3.5) takes the modified form:

$$T_{rev}^* = \frac{S_{12}}{(1 - \Gamma_1 S_{22})(1 - \Gamma_2 S_{11})} \quad (3.6)$$

If the measured device is reciprocal, i.e.  $S_{21} = S_{12}$ , only one measurement of transmission coefficient is necessary, therefore, the number of measurements can be reduced to three.

The multiport system involving two Butler matrices for transmission coefficient measurement can be calibrated using several different sections of matched transmission lines introducing phase shift  $\varphi_k$  (the electrical length of the first transmission line can be assumed zero) and two matched loads. It is worth mentioning that the requirements related to the impedance match of the needed calibration standards are not excessive. Since the total isolation between two measuring ports to which DUT is connected is a sum (if expressed in dB) of isolations of both utilized Butler matrices, the wave reflected from the imperfect calibration standards is almost undetectable by the applied power meters (more comprehensive analysis is presented in Subsection 3.1.3).

It can be observed that having both measuring ports terminated with a matched load ( $T = 0$ ), the measured power  $p_{iL}$  is equal to the corresponding coefficients  $q_i$ :

$$q_i = p_{iL} \quad (3.7)$$

where  $i$  indicates the number of port at which the power is measured ( $i = 5, 6, 7, 8$ ). In order to find the remaining coefficients  $A_i$ , (3.3) can be rewritten as:

$$p_{ik} = q_i |1 + A_i W_k|^2 \quad (3.8)$$

where  $W_k$  indicates the known transmission coefficient of  $k^{\text{th}}$  calibration standard ( $k = 1, 2, \dots, K$ ) and  $p_{ik}$  is the power measured at  $i^{\text{th}}$  port, when  $k^{\text{th}}$  calibration standard is applied. The coefficient  $W_k$ , given by:

$$W_k = \frac{e^{-j\varphi_k}}{1 - \Gamma_1 \Gamma_2 e^{-2j\varphi_k}} \quad (3.9)$$

corresponds to the  $k^{\text{th}}$  section of matched transmission line introducing phase shift  $\varphi_k$ . Having measured  $K$  values of power  $p_{ik}$  for each output port of the Butler matrix B, one can obtain the coefficients  $A_i$  as follows:

$$A_i = \frac{\beta \delta_i - \gamma \epsilon_i + j(\gamma \delta_i - \alpha \epsilon_i)}{\alpha \beta - \gamma^2} \quad (3.10)$$

where

$$\alpha = \sum_{k=1}^K \sum_{n=k+1}^K \left( \frac{\Re[W_k]}{|W_k|^2} - \frac{\Re[W_n]}{|W_n|^2} \right)^2 \quad (3.11)$$

$$\beta = \sum_{k=1}^K \sum_{n=k+1}^K \left( \frac{\Im[W_k]}{|W_k|^2} - \frac{\Im[W_n]}{|W_n|^2} \right)^2 \quad (3.12)$$

$$\gamma = \sum_{k=1}^K \sum_{n=k+1}^K \left( \frac{\Re[W_k]}{|W_k|^2} - \frac{\Re[W_n]}{|W_n|^2} \right) \left( \frac{\Im[W_k]}{|W_k|^2} - \frac{\Im[W_n]}{|W_n|^2} \right) \quad (3.13)$$

$$\delta_i = \frac{1}{2} \sum_{k=1}^K \sum_{n=k+1}^K \left( \frac{\Re[W_k]}{|W_k|^2} - \frac{\Re[W_n]}{|W_n|^2} \right) \left( \frac{p_{ik}}{q_i |W_k|^2} - \frac{p_{in}}{q_i |W_n|^2} - \frac{1}{|W_k|^2} + \frac{1}{|W_n|^2} \right) \quad (3.14)$$

$$\epsilon_i = \frac{1}{2} \sum_{k=1}^K \sum_{n=k+1}^K \left( \frac{\Im[W_k]}{|W_k|^2} - \frac{\Im[W_n]}{|W_n|^2} \right) \left( \frac{p_{ik}}{q_i |W_k|^2} - \frac{p_{in}}{q_i |W_n|^2} - \frac{1}{|W_k|^2} + \frac{1}{|W_n|^2} \right) \quad (3.15)$$

and  $k$  and  $n$  are the indices of the calibration standards ( $k = 1, 2, \dots, K; n = 2, 3, \dots, K$ ). The genuine circle centers for transmission coefficient measurements can be derived using the calculated coefficients as follows:

$$c_i = -\frac{1}{A_i} \quad (3.16)$$

It can be observed that the presented calibration procedure can be applied to a measuring system having an arbitrary number of ports at which the power is measured ( $N$ ). Moreover, the number of sections of transmission lines utilized in calibration ( $K$ ) can be also arbitrarily chosen, however, at least two are required. It is worth mentioning that a higher number of calibration standards decreases the influence of the measurement inaccuracy of the applied power meters on the calibration results. Having the measuring

system calibrated one can proceed to the measurements of transmission coefficient. The measured transmission coefficient  $T$  given by (3.4), (3.5) or (3.6) can be calculated as follows:

$$T = \frac{\mu\rho - \kappa\nu + j(\eta\rho - \mu\nu)}{\eta\kappa - \mu^2} \quad (3.17)$$

where

$$\eta = 2 \sum_{i=1}^N \sum_{j=i+1}^N \left( \frac{\Re[A_i]}{|A_i|^2} - \frac{\Re[A_j]}{|A_j|^2} \right)^2 \quad (3.18)$$

$$\kappa = 2 \sum_{i=1}^N \sum_{j=i+1}^N \left( \frac{\Im[A_i]}{|A_i|^2} - \frac{\Im[A_j]}{|A_j|^2} \right)^2 \quad (3.19)$$

$$\mu = 2 \sum_{i=1}^N \sum_{j=i+1}^N \left[ \left( \frac{\Re[A_i]}{|A_i|^2} - \frac{\Re[A_j]}{|A_j|^2} \right) \left( \frac{\Im[A_i]}{|A_i|^2} - \frac{\Im[A_j]}{|A_j|^2} \right) \right] \quad (3.20)$$

$$\nu = \sum_{i=1}^N \sum_{j=i+1}^N \left[ \left( \frac{\Re[A_i]}{|A_i|^2} - \frac{\Re[A_j]}{|A_j|^2} \right) \left( \frac{1}{|A_i|^2} - \frac{1}{|A_j|^2} - \frac{p_i}{q_i |A_i|^2} + \frac{p_j}{q_j |A_j|^2} \right) \right] \quad (3.21)$$

$$\rho = \sum_{i=1}^N \sum_{j=i+1}^N \left[ \left( \frac{\Im[A_i]}{|A_i|^2} - \frac{\Im[A_j]}{|A_j|^2} \right) \left( \frac{1}{|A_i|^2} - \frac{1}{|A_j|^2} - \frac{p_i}{q_i |A_i|^2} + \frac{p_j}{q_j |A_j|^2} \right) \right] \quad (3.22)$$

and  $i$  and  $j$  are the indices of the second Butler matrix's output ports with power meters connected ( $i = 1, 2, \dots, N; j = 2, 3, \dots, N$ ).

### 3.1.3. Influence of Model Simplification on Transmission Coefficient Measurements

As said in Subsection 3.1.2, the applied simplification of the measuring system model for transmission coefficient measurements introduces some inaccuracy, which has to be investigated in order to confirm the usefulness of such an approach. The utilized model takes into account the imperfect impedance match of all used components and only imperfect isolations have been neglected. Therefore, to ensure a clarity of the following analysis, the impact of the introduced simplification of the proposed model has been verified with the assumed ideal impedance match of all components, as shown in Fig. 3.3c. It has to be emphasized that influence of the imperfect isolations on the measurement results is dependent on almost each  $S$ -parameter distinguished in Fig. 3.3a including the reflection coefficients seen at the measuring ports and measured scattering parameters of DUT. However, the consideration of such a complex dependence requires too many parameters and the presentation of obtained results would not be legible. Therefore, the presented analysis of the imperfect isolation's impact on transmission coefficient measurements is rather an estimate than the exact value of maximum error, nevertheless, assuming the reasonable impedance match of the utilized components (say 20 dB) it can be sufficiently accurate.

Utilizing the signal flow shown in Fig. 3.3c one can derive the expression for the normalized measured power as:

$$p_i = \left| \frac{S_{A31}S_{C21}S_{B13}}{1 - S_{C21}S_{B23}S_{12}S_{A32}} + \frac{S_{A21}S_{21}S_{B12}}{1 - S_{21}S_{B32}S_{C12}S_{A23}} \right|^2 \quad (3.23)$$

Assuming the reciprocity of utilized components and measured device one can introduce:

$$T = S_{21} = S_{12} \quad (3.24)$$

$$I = S_{B32}S_{C12}S_{A23} = S_{A32}S_{C21}S_{B23} \quad (3.25)$$

where  $I$  is the isolation between measuring ports derived utilizing signal flow shown in Fig 3.3c. Further (3.23) can be expressed as follows:

$$p_i = \left| \frac{S_{A31}S_{C21}S_{B13}}{1 - TI} + \frac{S_{A21}S_{B12}}{S_{A31}S_{C21}S_{B13}} T \right|^2 \quad (3.26)$$

which can be simplified to the form:

$$p_i = \frac{q_i^*}{|1 - TI|^2} |1 + A_i^* T|^2 \quad (3.27)$$

It can be observed that (3.27) has the form being close to (3.3). Analyzing (3.27) one can see, that the imperfect isolation can be considered as a factor modifying coefficients  $q_i$  shown in (3.3) without affecting the remaining coefficients  $A_i$ . Since the coefficients  $q_i$  are linearly related to the measured power  $p_i$ , one can introduce the relative power reading error caused by the imperfect isolations:

$$e_P = \left| \frac{1}{|1 - TI|^2} - 1 \right| \quad (3.28)$$

It is seen that  $e_P$  depends on both isolation  $I$  and the measured transmission coefficient  $T$ . Further investigation reveals that the maximum relative error for a given magnitude of the measured reflection coefficient can be obtain if:

$$\arg [TI] = 0 \quad (3.29)$$

Therefore, the maximum relative power reading error can be expressed as a function of magnitudes:

$$e_{P \max} = |T| |I| \frac{2 - |T| |I|}{(1 - |T| |I|)^2} \quad (3.30)$$

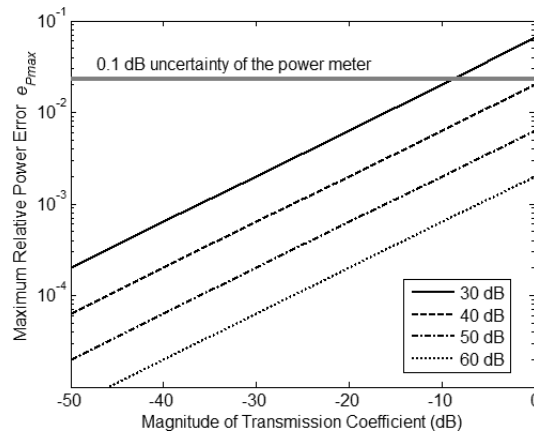


**Figure 3.4:** Estimated maximum relative power reading error vs. magnitude of the measured transmission coefficient (black lines) for four different values of isolations  $I$  compared to the  $\pm 0.1$  dB uncertainty of the power meters (gray line).

To verify the impact of the model simplification on the measurement accuracy the obtained values of  $e_{P_{\max}}$  given by (3.30) have to be compared with the measurement inaccuracy of the power meters, as shown in Fig. 3.4. A typical measurement accuracy of the high-class microwave power meters is about  $\pm 0.1$  dB, which corresponds to the relative power reading error being equal to 0.0233 indicated by the gray line. It is seen that if the isolation between measuring ports is not worse than 40 dB the power reading error caused by simplification of the measuring system model is lower than the error resulting from the power meters uncertainty and decreases with smaller magnitudes of the measured transmission coefficient.

It is worth mentioning that the obtained maximum relative power reading error is an estimate derived on the basis of the simplified signal flow shown in Fig 3.3c. In practice, however, the imperfect impedance match of measuring port and measured device can increase this error. On the other hand, in the presented analysis of the simplified signal flow shown in Fig. 3.3c the worst case given by (3.29) has been assumed which almost never occurs in practice, what justifies the presented analysis.

Another analysis has to be performed for the simplification of the formula for transmission coefficient (3.4) into the form given by (3.5). Since the ratio of (3.4) and (3.5) is equal to:

$$\frac{T^*}{T} = 1 - \frac{S_{12}S_{21}\Gamma_1\Gamma_2}{(1 - \Gamma_1S_{11})(1 - \Gamma_2S_{22})} \quad (3.31)$$

the maximum magnitude and phase error resulting from such a simplification can be easily estimated. It can be observed that (3.5) takes into account the imperfect impedance match of the measured device, therefore, for better clarity of this investigation it has been assumed that  $S_{11} = S_{22} = 0$ . Moreover, it can be concluded from (3.31) that the maximum error occurs for high magnitude of transmission coefficients of DUT. Hence, zero-insertion loss has been assumed ( $S_{21} = S_{12} = 1$ ). The reflection coefficients seen at the measuring ports  $\Gamma_1$  and  $\Gamma_2$  are assumed to be equal (called further  $\Gamma_{MS}$ ). The mentioned assumptions allow for rewriting (3.31) as follows:

$$\frac{T^*}{T} = 1 - \Gamma_{MS}^2 \quad (3.32)$$

Since (3.32) represents the ratio of the exact and approximated values of transmission coefficient, it allows for estimating the maximum measurement error caused by the introduced simplification of (3.4) into (3.5) in terms of both magnitude and phase. The maximum magnitude error expressed in dB is equal to:

$$\Delta_{mag} = \pm \log_{10} \left( 1 - |\Gamma_{MS}|^2 \right) \quad (3.33)$$

whereas the maximum phase error can be estimated as follows:

$$\Delta_{phase} \cong \pm \arctan \left( |\Gamma_{MS}|^2 \right) \quad (3.34)$$

The estimated errors vs. magnitude of the impedance match of the measured ports have been plotted in Fig. 3.5. It is seen that for the impedance match not worse than 20 dB the simplification given by (3.5) introduces the magnitude error not exceeding  $\pm 0.1$  dB and the phase error being lower than  $\pm 1^\circ$ . Moreover, it has to be emphasized that for any greater insertion loss of DUT these errors are smaller.

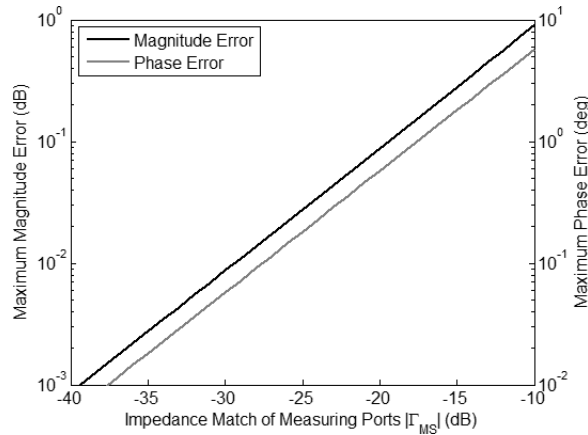


**Figure 3.5:** Estimated maximum error of transmission coefficient measurements introduced by the utilization of simplified formula (3.5) for an ideally matched two-port having zero-insertion loss ( $S_{21} = S_{12} = 1$ ).

## 3.2. Measurements With the Use of Single $8 \times 8$ Butler Matrix

In this Section an extension of the reflectometer utilizing a classic  $8 \times 8$  Butler matrix described in Subsection 2.2.3 is presented [85]. The addition of single isolator and switch allows for the measurement of all  $S$ -matrix coefficients of any two-port device. Simultaneously, the measuring system requires a decreased number of power meters with respect to the system shown in Section 3.1, since for the measurements of reflection and transmission coefficients the same power meters are utilized.

The application of the classic  $8 \times 8$  Butler matrix in multiport measurements of reflection coefficient has been comprehensively described in Subsection 2.2.3, therefore, in this Section only the extension of the reflectometer allowing for transmission coefficient measurements is investigated. In particular, a model of single-reflectometer system is developed and fully analytical calibration procedure is given.

### 3.2.1. Theoretical Analysis

In Subsection 2.2.3 the utilization of a classic  $8 \times 8$  Butler matrix in reflection coefficient measurements is discussed. However, if a single isolator and switch are added, as shown in Fig. 3.6, the resulting system is also capable of the transmission coefficient measurements. To perform such measurements the measured device has to be fed at its second port. In such a case, the measured reflection coefficient is a result of all  $S$ -parameters of the measured device. After suitable number of measurements, each  $S$ -parameter can be derived, providing complete information about the examined device. As a secondary port that supplies the measured device, one of the output ports of the Butler matrix can be utilized.

It is worth mentioning that Fig. 3.6 shows an exemplary configuration of the measuring system. Since only four output ports of the Butler matrix are utilized, there is a number of possible configurations. The choice of measuring port and port with reflective element (ports #9 and #10 in Fig. 3.6, respectively) is restricted by the required circle centers' distribution, as described in Subsection 2.2.3, whereas the output port to which switch SW is connected can be chosen arbitrarily [85].

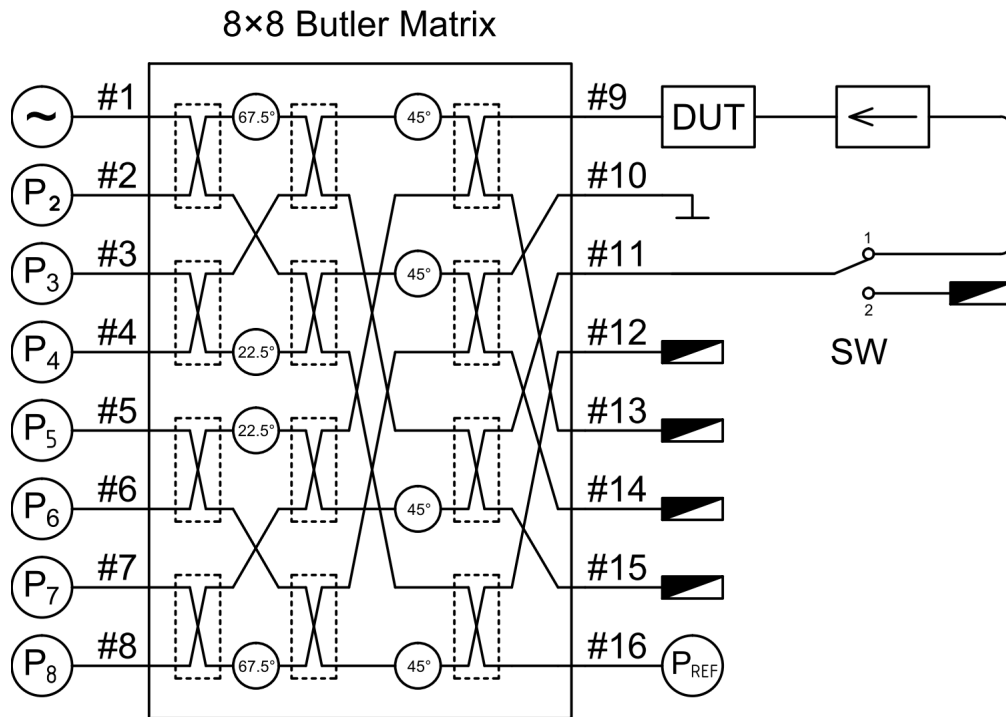


**Figure 3.6:** Schematic diagram of the proposed multiport measuring system with a single  $8 \times 8$  Butler matrix allowing for reflection and transmission coefficients measurements [85]. (Copyright © 2014, IEEE)

### 3.2.2. Model of Single-Multiport Reflectometer for $S$ -Parameter Measurements

Sun Jia has shown in [45] that the entire  $S$ -matrix of a measured device (reflection and transmission coefficients) can be obtained with the use of a single-multiport reflectometer. Such an approach can be also utilized in the proposed measuring system involving an  $8 \times 8$  Butler matrix. The particular  $S$ -parameters are inferred on the basis of the reflection coefficient measured at the measuring port in two modes: with an isolator connected to the secondary port of DUT (called active mode) and without exciting the secondary port of DUT (passive mode). It has been presented in [43] that by four measurements of DUT, i.e. in passive and active modes performed for two directions of inserted DUT, the complete  $S$ -matrix of the examined two-port can be obtained.

In the analysis shown in both [45] and [43], the ideal isolation between both ports connected to DUT is assumed. The applied isolators have to ensure that the ratio of both waves that are incident to DUT remains unaffected by the reflection coefficient seen from the measuring port of a reflectometer. It must be emphasized that such a condition cannot be fulfilled in the proposed measuring system, in which the isolation between Butler matrix's output ports is imperfect. Nevertheless, the analysis shown in this Subsection reveals that such a measurement can be done with imperfect isolation between the mentioned ports [85]. This allows for connecting an isolator to one of the output ports of a Butler matrix (having finite isolation with respect to the measuring port) and decreases the number of necessary isolators to only one.

Fig. 3.7a presents the signal flow of a measuring system consisting of a single multiport, an isolator and an examined two-port (DUT). As it is seen the isolation between the measuring port #2 and the port supplying the isolator #3 is imperfect. In order to simplify the presented analysis, the multiport together

with the isolator can be considered as a new multiport having the signal flow, as shown in Fig. 3.7b. The new multiport can be described with the following  $S$ -matrix:

$$S_{mi} = \begin{bmatrix} S_{m11} + \frac{S_{m31}S_{is11}S_{m13}}{1-S_{m33}S_{is11}} & S_{m12} + \frac{S_{m23}S_{is11}S_{m13}}{1-S_{m33}S_{is11}} & 0 \\ S_{m21} + \frac{S_{m31}S_{is11}S_{m23}}{1-S_{m33}S_{is11}} & S_{m22} + \frac{S_{m32}S_{is11}S_{m23}}{1-S_{m33}S_{is11}} & 0 \\ \frac{S_{m31}S_{is21}}{1-S_{m33}S_{is11}} & \frac{S_{m32}S_{is21}}{1-S_{m33}S_{is11}} & S_{is22} \end{bmatrix} \quad (3.35)$$

where  $S_m$  indicate  $S$ -parameters of the utilized multiport, and  $S_{is}$  represent the  $S$ -parameters of the applied isolator. Fig. 3.7c presents the signal flow of the measuring system, in which the multiport and the isolator are considered as one multiport, with the imperfect isolation from port #2 to port #3 ( $S_{mi32} \neq 0$ ). From the microwave network theory, one can obtain that the reflection coefficient seen at the measuring port #2 with DUT inserted between ports #2 and #3 can be expressed as follows [85]:

$$\Gamma = \frac{S_{x11} + S_{mi33}(S_{x21}S_{x12} - S_{x11}S_{x22}) + S_{x12}\frac{S_{mi31}}{S_{mi21}}}{1 - S_{x22}S_{mi33} + S_{x12}\left(\frac{S_{mi31}S_{mi22}}{S_{mi21}} - S_{mi32}\right)} \quad (3.36)$$

where  $S_x$  indicate the  $S$ -parameters of DUT. The expression (3.36) can be rewritten in the following form:

$$\Gamma = \frac{S_{x11} + B(S_{x21}S_{x12} - S_{x11}S_{x22}) + S_{x12}C}{1 - S_{x22}B + S_{x12}A} \quad (3.37)$$

where

$$A = \frac{S_{mi31}S_{mi22}}{S_{mi21}} - S_{mi32} \quad (3.38)$$

$$B = S_{mi33} \quad (3.39)$$

$$C = \frac{S_{mi31}}{S_{mi21}} \quad (3.40)$$

are the system constants that have to be found in a calibration procedure. It can be observed that (3.37) has the same form as it has been shown in [43], therefore, to find these system constants one can utilize the calibration procedure presented in [43]. Nevertheless, in the presented model constant  $A$  has a slightly different physical meaning, since it takes into account the imperfect isolation  $S_{mi32}$ , which in [43] has been assumed to be ideal. The above analysis proves that in the measuring systems involving a single reflectometer only one isolator is necessary [85]. Furthermore, it is shown that the well-known approach to the measurement of  $S$ -parameters with the use of a single multiport reflectometer can be applied in case of an  $N \times N$  Butler matrix.

It can be concluded that the classic  $8 \times 8$  Butler matrix constitutes a great candidate for the application in the measurement technique described in this Section. Due to the sufficiently high number of available ports, the isolator can be connected to one of the Butler matrix's output ports, hence, an additional power divider is not necessary. Simultaneously, the requirements of the isolation level of the utilized Butler matrix are relaxed.

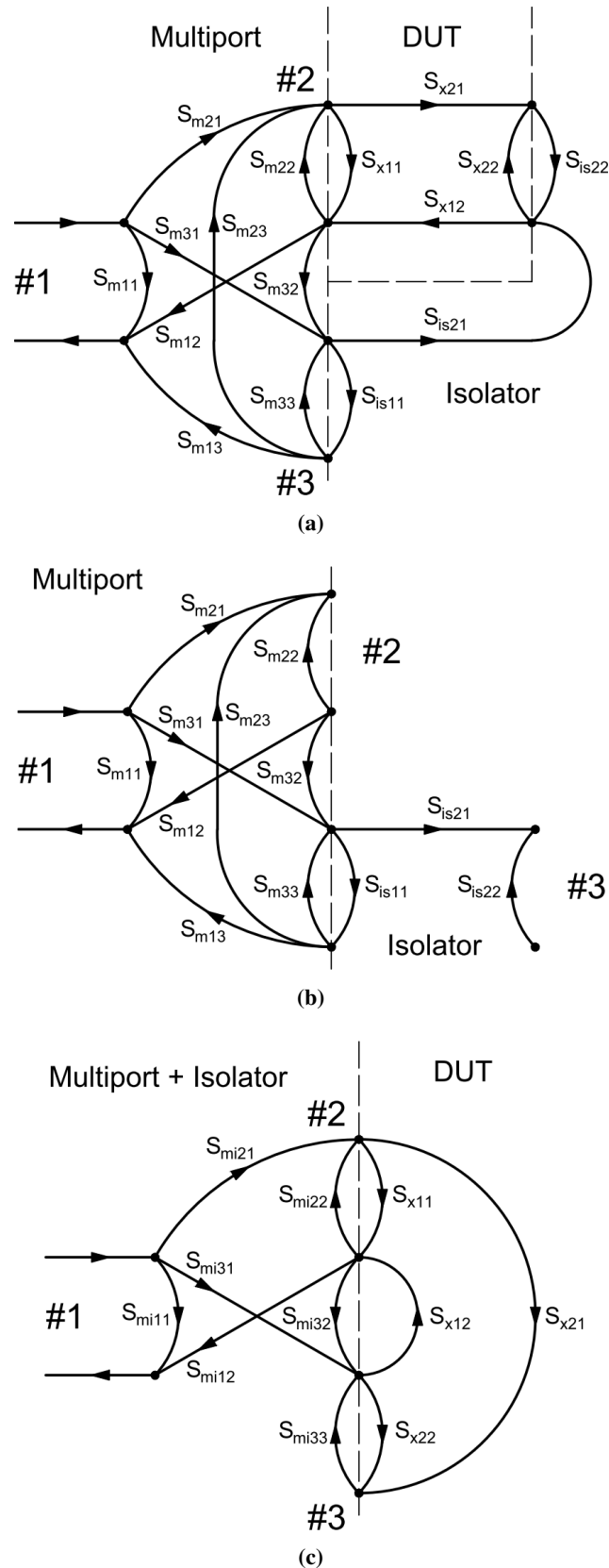


**Figure 3.7:** The flow graph of a single multiport reflectometer having imperfect isolation between its ports, allowing for the measurements of  $S$ -parameters: graph of the entire measuring system (a), graph of the extracted multiport having imperfectly isolated ports with an isolator connected (b), graph of the measuring system with the multiport created from the actual multiport and isolator (c) [85]. (Copyright © 2014, IEEE)

### 3.2.3. Calibration of Single Reflectometer for $S$ -Parameter Measurements

The calibration of the considered measuring system can be divided into two steps. The first one is the calibration for the reflection coefficient measurements, which can be performed following the procedure given in Section 2.3. Having the reflectometer calibrated, one can proceed to the second step of the calibration in order to obtain the constants required for transmission coefficient measurements with the use of the secondary port and the isolator. As it is seen from (3.37), three calibration constants have to be found. The constant  $B$  represents the reflection coefficient of the isolator, which can be found by a single measurement of the reflection coefficient, when the isolator is connected to the measuring port and the switch SW is in position 2 (passive mode). For the remaining constants  $A$  and  $C$ , Hunter and Somlo in [43] have proposed a direct analytical solution, requiring two measurements in an active mode (switch SW in position 1), with two sections of matched transmission lines introducing phase shift  $\varphi_k$  (the electrical length of the first transmission line can be assumed zero).

The measurements of a transmission coefficient with the use of a single multiport reflectometer are more prone to the inaccuracy of power measurement than the measuring systems utilizing two reflectometers [101]. The accuracy of calibration procedure has a direct impact on subsequent measurements, hence, the enhanced accuracy of calibration procedure is crucial. Therefore, the number of calibration measurements can be increased and the obtained redundancy can be utilized in the least-squares approach to calibration. In each calibration measurement, a transmission-line section introducing known phase shift  $\varphi_k$  ( $k = 1, 2, \dots, K$ ) replaces DUT, and the reflection coefficient  $\Gamma_k$  is measured. Having at least two such measurements, the calibration constants  $A$  and  $C$  can be obtained [85]:

$$\begin{bmatrix} \Re[A] \\ \Im[A] \\ \Re[C] \\ \Im[C] \end{bmatrix} = (M^T M)^{-1} M^T v \quad (3.41)$$

where  $M$  and  $v$  can be written as follows:

$$M = \begin{bmatrix} \Re[\Gamma_1] \cos(\varphi_1) + \Im[\Gamma_1] \sin(\varphi_1) & \Re[\Gamma_1] \sin(\varphi_1) - \Im[\Gamma_1] \cos(\varphi_1) & -\cos(\varphi_1) & -\sin(\varphi_1) \\ -\Re[\Gamma_1] \sin(\varphi_1) + \Im[\Gamma_1] \cos(\varphi_1) & \Re[\Gamma_1] \cos(\varphi_1) + \Im[\Gamma_1] \sin(\varphi_1) & \sin(\varphi_1) & -\cos(\varphi_1) \\ \dots & \dots & \dots & \dots \\ \dots & \dots & \dots & \dots \\ \Re[\Gamma_K] \cos(\varphi_K) + \Im[\Gamma_K] \sin(\varphi_K) & \Re[\Gamma_K] \sin(\varphi_K) - \Im[\Gamma_K] \cos(\varphi_K) & -\cos(\varphi_K) & -\sin(\varphi_K) \\ -\Re[\Gamma_K] \sin(\varphi_K) + \Im[\Gamma_K] \cos(\varphi_K) & \Re[\Gamma_K] \cos(\varphi_K) + \Im[\Gamma_K] \sin(\varphi_K) & \sin(\varphi_K) & -\cos(\varphi_K) \end{bmatrix} \quad (3.42)$$

and

$$v = \begin{bmatrix} \Re[B] \cos(2\varphi_1) + \Im[B] \sin(2\varphi_1) - \Re[\Gamma_1] \\ -\Re[B] \sin(2\varphi_1) + \Im[B] \cos(2\varphi_1) - \Im[\Gamma_1] \\ \dots \\ \dots \\ \Re[B] \cos(2\varphi_K) + \Im[B] \sin(2\varphi_K) - \Re[\Gamma_K] \\ -\Re[B] \sin(2\varphi_K) + \Im[B] \cos(2\varphi_K) - \Im[\Gamma_K] \end{bmatrix} \quad (3.43)$$

Once the calibration constants are obtained, the measurements can be performed. If during the measurements any series adapter has to be utilized, the shift of the measurement plane has to be taken into account. Assuming the transmission coefficient of the utilized adapter:

$$t = \exp(-j\varphi_{con}) \quad (3.44)$$

and its perfect impedance match the calibration constants  $A$ ,  $B$ ,  $C$  can be transformed:

$$A \leftarrow \frac{A}{t} \quad (3.45)$$

$$B \leftarrow \frac{B}{t^2} \quad (3.46)$$

$$C \leftarrow \frac{C}{t} \quad (3.47)$$

If the series adapter is not applied then  $t = 1$ . In order to find four  $S$ -parameters of the examined two-port (DUT), four measurements have to be performed: in passive and active modes ( $\Gamma_{P1}$  and  $\Gamma_{A1}$  respectively) and the corresponding measurements after reversing DUT ( $\Gamma_{P2}$  and  $\Gamma_{A2}$ ). The  $S$ -parameters of DUT can be obtained from the formulas shown in [43], modified by the factor  $t$ :

$$S_{11} = \frac{\Gamma_{P1} - B\alpha_1\alpha_2}{\alpha_3 t^2} \quad (3.48)$$

$$S_{22} = \frac{\Gamma_{P2} - B\alpha_1\alpha_2}{\alpha_3 t^2} \quad (3.49)$$

$$S_{21} = \frac{\alpha_2 (1 - B\Gamma_{P1})}{\alpha_3 t^2} \quad (3.50)$$

$$S_{12} = \frac{\alpha_1 (1 - B\Gamma_{P2})}{\alpha_3 t^2} \quad (3.51)$$

where

$$\alpha_1 = \frac{\Gamma_{A1} - \Gamma_{P1}}{C - A\Gamma_{A1}} \quad (3.52)$$

$$\alpha_2 = \frac{\Gamma_{A2} - \Gamma_{P2}}{C - A\Gamma_{A2}} \quad (3.53)$$

$$\alpha_3 = 1 - B^2\alpha_1\alpha_2 \quad (3.54)$$

As it can be observed, to find each  $S$ -parameter of DUT all the coefficients  $\alpha_1$ ,  $\alpha_2$  and  $\alpha_3$ , which are determined by  $\Gamma_{A1}$ ,  $\Gamma_{P1}$ ,  $\Gamma_{A2}$ , and  $\Gamma_{P2}$ , have to be known. Therefore, one cannot consider a single measurement as being related to a single  $S$ -parameter of DUT, and to determine any  $S$ -parameter all four measurements have to be performed. Exceptionally, if the used isolator features good impedance match ( $B \approx 0$ ) the reflection coefficients  $S_{11}$  and  $S_{22}$  can be calculated from a single measurement for  $\Gamma_{P1}$  and  $\Gamma_{P2}$ , respectively [85].

### 3.3. Analysis of Calibration Standards for Broadband Calibration

Both calibration procedures described in Subsections 3.1.2 and 3.2.3 require transmission-line sections having known electrical lengths  $\Theta_k$  ( $k = 1, 2, \dots, K$ ). For this purpose SMA adapters described in Subsection 2.3.5 can be used. Their electrical lengths are listed in Table 2.5. As it has been mentioned in Subsection 2.3.4, the phase of such calibration standards depends on frequency, therefore, for wideband calibration their electrical lengths have to be appropriately chosen.

The calibration procedure can be considered as a process opposite to measurement. In calibration the parameters of the measured components (calibrations standards) are known, whereas, the system constants relating the measured transmission coefficient to the power reading have to be calculated. To obtain a high calibration precision one has to provide the maximum variety of the applied calibration standards. The phase of transmission coefficient for a perfectly match section of transmission line (realized as SMA adapters) can be expressed as follows:

$$\varphi_k = -\Theta_k \frac{f}{f_0} \quad (3.55)$$

where  $\Theta_k$  is the electrical length of the  $k^{\text{th}}$  calibration standard at specified frequency  $f_0$  (similarly as described in Subsection 2.3.5). All calibration standards have transmission coefficients located on a circumference of a unitary circle on a complex plane with their angle depending on the frequency. The phase of each transmission coefficient of a particular calibration standards increases with frequency and the greater the electrical length  $\Theta_k$  the greater change of the transmission coefficient phase. Only the direct connection (transmission line having the electrical length equal to  $0^\circ$ ) introduces calibration standard, which does not depend on frequency, having phase equal to  $0^\circ$ . The exemplary distribution of five calibration standards is illustrated in Fig. 3.8. The point with phase equal to  $0^\circ$  corresponds to direct connection, whereas remaining four points represent four sections of transmission line having different electrical lengths.

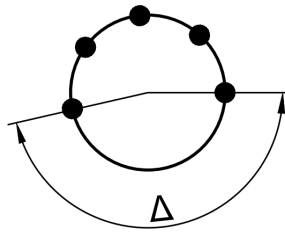


**Figure 3.8:** Exemplary distribution of calibration standards for a given frequency. The maximum angle difference  $\Delta$  is shown.

Similarly as in case of calibration for reflection coefficient measurements, the most uniform distribution of the calibration standards provides the highest precision of calibration procedure. For a verification of the calibration standards' distribution one can introduce the angle  $\Delta$  which indicates the largest angle between two adjacent calibration standards, as shown in Fig. 3.8. Optimal value of this angle is equal to

$$\Delta_{opt} = \frac{360^\circ}{K + 1} \quad (3.56)$$

where  $K$  is the number of the applied calibration standards (excluding direct connection). The maximum angle difference  $\Delta$  takes value from  $\Delta_{opt}$ , which in considered case is equal to  $72^\circ$ , to  $360^\circ$  indicating that all calibration standards overlap, precluding correct calibration.

In order to choose the optimal set of calibration standards one has to calculate the maximum angle difference  $\Delta$  for each possible configuration of available calibration standards for each frequency point. Assuming  $N$  available calibration standards and  $K$  chosen standards (each calibration standard can be chosen more than once) to utilize in calibration procedure, one obtains the number of possible combinations being equal to:

$$M = \binom{K + N - 1}{N - 1} = \frac{(K + N - 1)!}{K!(N - 1)!} \quad (3.57)$$

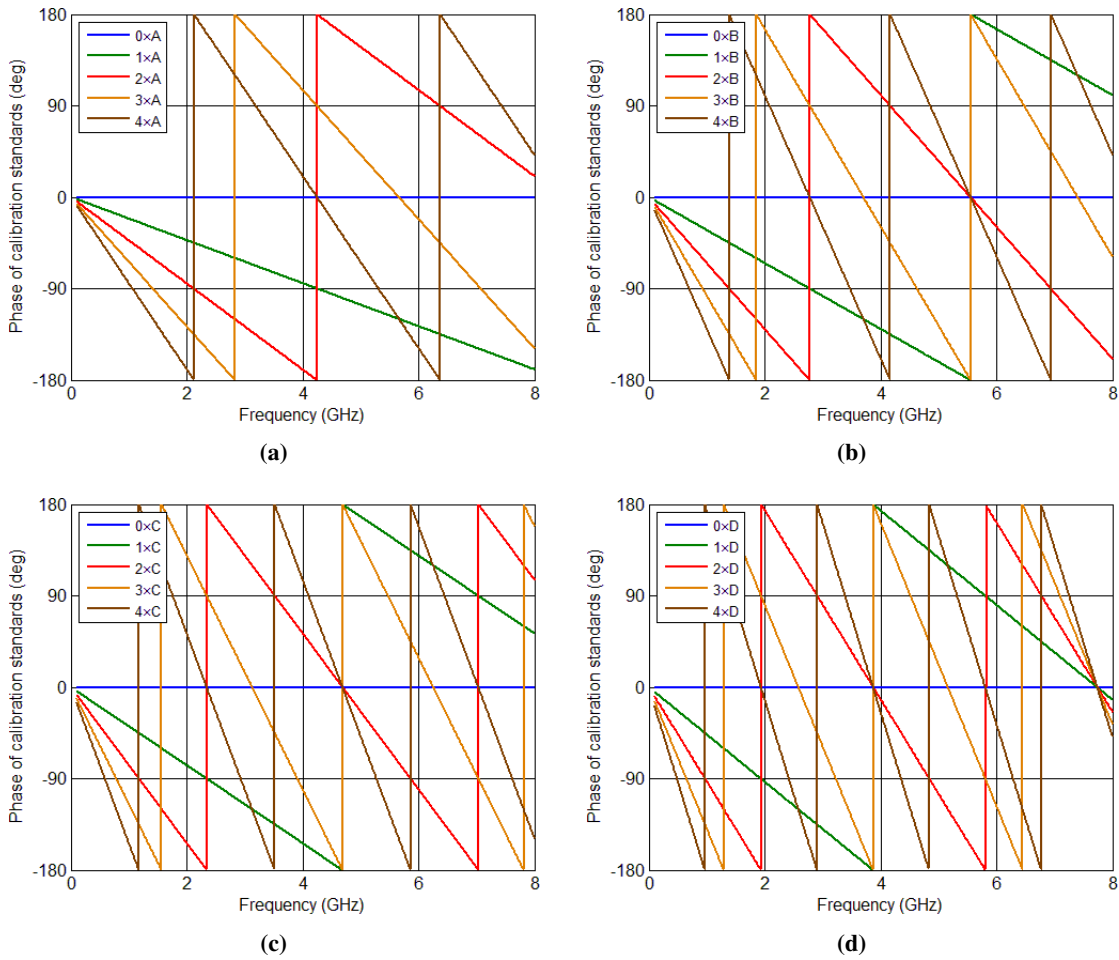


**Figure 3.9:** Phase of the analyzed calibration standards listed in Table 2.5 vs. frequency.

In both calibration procedures for transmission coefficient measurement described in this Chapter an arbitrary number of calibration standards can be applied. Assuming that three calibration standards are chosen ( $K = 3$ ) from four available offsets listed in Table 2.5 ( $N = 4$ ) one obtains 20 possible combinations and this number rapidly increases with higher number of utilized calibration standards. Due to such a high number of possible combinations the presented analysis is limited only to the

utilization of a single type of calibration standards ( $N = 1$ ), whereas their number is equal to four. Such an approach simplifies the calibration procedure, since the calibration measurements are performed for direct connection, single offset, and further for cascade connection of increasing number of offsets of the same type. The achieved distribution of calibration standards in the entire considered frequency range may be not optimal, however, the increased number of the applied offsets (theoretically, as pointed in Subsections 3.1.2 and 3.2.3 only two are required) greatly enhances the robustness of the calibration procedure. The phase of the analyzed calibration standards listed in Table 2.5 vs. frequency, assuming that four offsets of each type are applied, is shown in Fig. 3.9. The corresponding maximum angle differences  $\Delta$  are illustrated in Fig. 3.10. As it can be observed the optimum distribution is obtained only for particular frequencies (depending on the offset's choice), nevertheless, the increased number of the applied calibration standards allows for broadband calibration with only one exception, which can be seen at the frequency 7.74 GHz for offset D. In this case all calibration standards overlap ( $\Delta = 360^\circ$ ), precluding correct calibration. For calibration in this frequency range offset B or C should be chosen since these two offsets provide the lowest value of maximum angle difference.

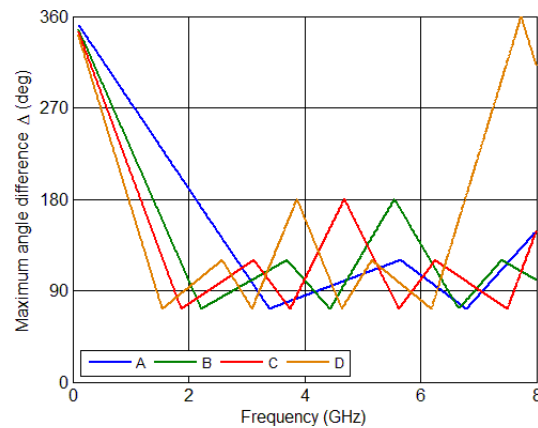


**Figure 3.10:** Maximum angle difference calculated for the analyzed calibration standards listed in Table 2.5 vs. frequency.

### 3.4. Experimental Verification

In this Section two measuring systems described in this Chapter have been experimentally verified. In both systems the same signal generator and power meters have been utilized as in case of reflection coefficient measurements (for details please see Section 2.5). Each measuring system has been calibrated following the appropriate calibration procedure.

The measurement performance of the considered systems has been experimentally verified by the transmission coefficient measurements of a set of broadband SMA attenuators, having attenuation 1 dB, 2 dB, 3 dB, 6 dB, 10 dB, 13 dB, 16 dB, 20 dB and 26 dB. For further examination two microwave bandpass filters have been measured.

In order to estimate the measurement accuracy, similarly to the reflection coefficient measurements, the circle centers' distribution related to a given system has to be analyzed. It can be observed that both systems feature the same mutual arrangement of circle centers as the reflectometer utilizing a classic  $8 \times 8$  Butler matrix shown in Subsection 2.2.3, i.e. four circle centers arranged uniformly

on the circumference of the unitary circle. However, in general the measurement of transmission coefficient is more complex than reflection coefficient measurement, since for transmission coefficient more measurements are required (both reflection coefficients of DUT  $S_{11}$  and  $S_{22}$ , as well as reflection coefficients seen at the measuring ports have to be known). This situation simplifies if a well-matched two-ports are to be measured, in which the transmission coefficient is the only relevant  $S$ -parameter. In such a case the measured value  $T$  (described in Subsection 3.1.2) or  $\Gamma_{A1}$  (described in Subsection 3.2.3) is very close to the desired transmission coefficient  $S_{21}$ . Hence, the estimation of measurement accuracy based on circle centers' distribution can be accurate. In case of measured two-ports, featuring higher reflection coefficients, the transmission coefficient has to be calculated using higher number of measurements, which introduces additional inaccuracy. Therefore, in the following Subsections the measurement accuracy is estimated only for measurement of SMA attenuators.

The reference measurements for the examination of the measurement results have been obtained with the use of commercial vector network analyzer N5224A by Agilent. VNA has been calibrated with the use of a standard SOLT (*short-open-load-thru*) technique, with 85052D Calibration Kit by Agilent. The uncertainty of the used VNA has been derived using *Vector Network Analyzer Uncertainty Calculator* software [2].

Two following Subsections are related to the particular measuring systems described in this Chapter. Each Subsection contains a description of the developed measuring system together with the calibration results. At the end the measurement results and reference values with the estimated measurement accuracy are illustrated.

### 3.4.1. Broadband Measurements of Transmission Coefficient With the Use of Two Classic $4 \times 4$ Butler Matrices

The multiport measuring system utilizing two classic  $4 \times 4$  Butler matrices described in Subsection 3.1.1 has been built for an experimental verification. As matrix A in Fig. 3.1 Butler matrix shown in [36] has been used, whereas as matrix B the Butler matrix presented in [98] has been applied. The most relevant parameters of both matrices are listed in Table 3.1.

**Table 3.1:** Parameters of two  $4 \times 4$  Butler matrices utilized in the measuring system.

Parameter	Butler matrix A [36]	Butler matrix B [98]
Bandwidth	1 – 5 GHz	1.1 – 4.5 GHz
Impedance match	20 dB	16 dB
Isolation	20 dB	21 dB
Amplitude imbalance	$\pm 1$ dB	$\pm 0.9$ dB
Phase deviation	$\pm 8^\circ$	$\pm 10^\circ$

The system has been calibrated in the frequency range 1 – 5 GHz, which is greater than the operational bandwidth of the Butler matrix B. It is worth mentioning that for frequency interval from

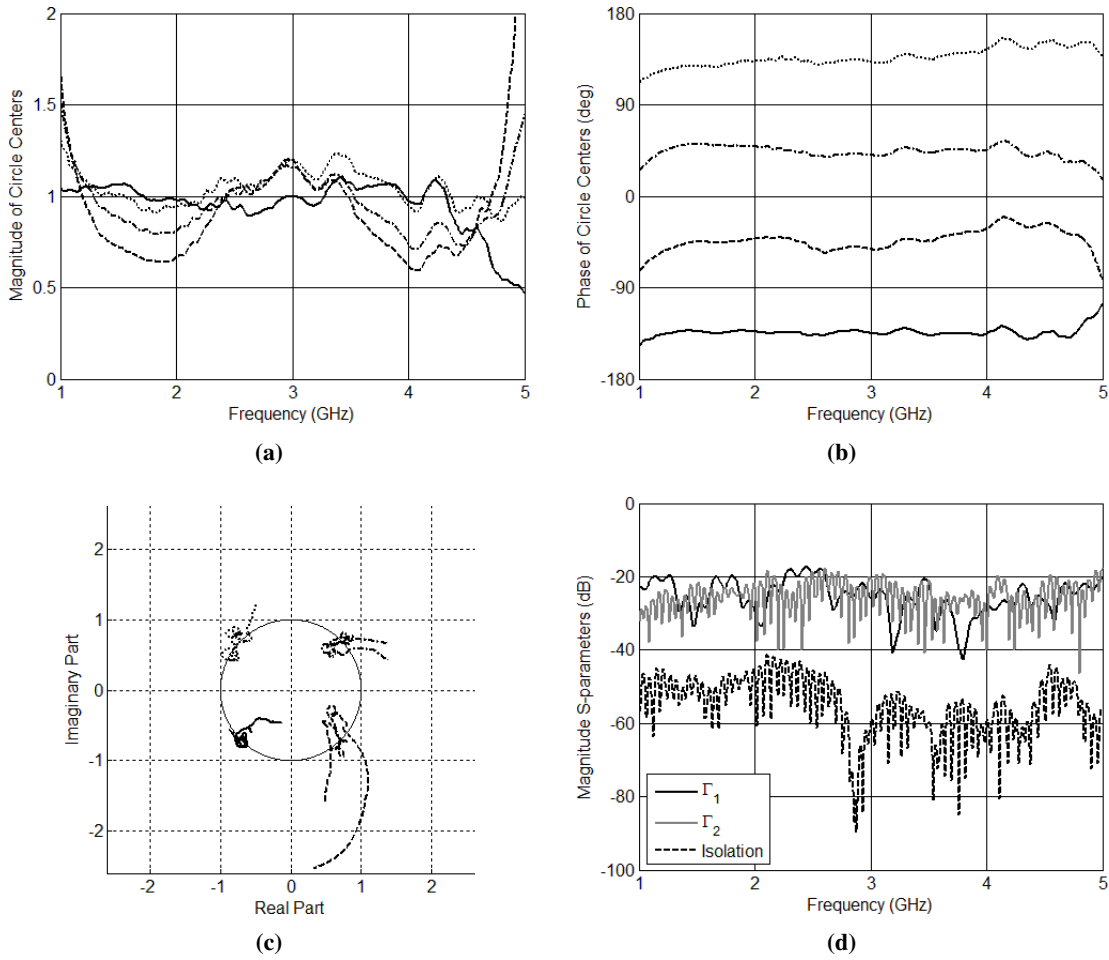


**Figure 3.11:** Results of the calibration procedure for the measuring system utilizing two  $4 \times 4$  Butler matrices described in Subsection 3.1.1: magnitude (a) and phase (b) of circle centers, circle centers' distribution on a complex plane (c), impedance match of the measuring ports and isolation between measuring ports (d).

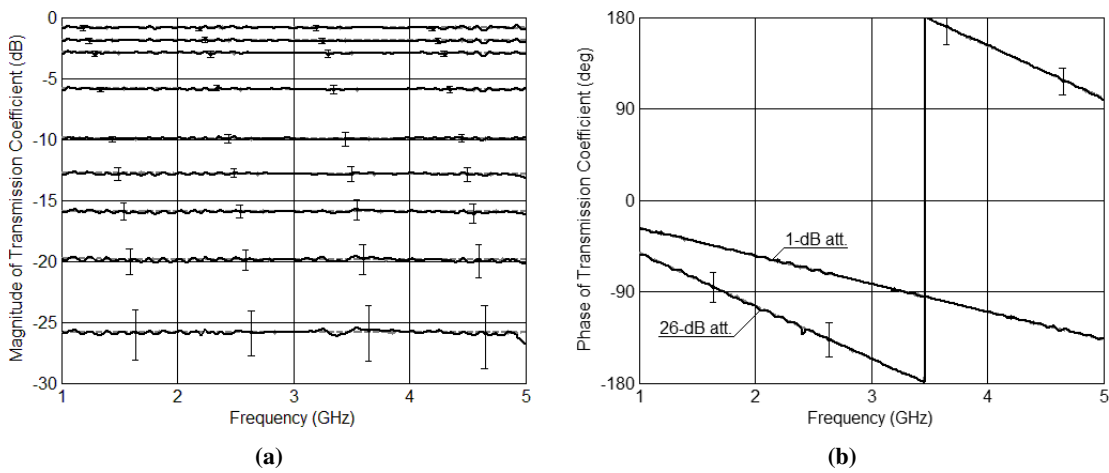


**Figure 3.12:** Transmission coefficients of a set of attenuators measured using the measuring system utilizing  $4 \times 4$  Butler matrices described in Subsection 3.1.1: magnitude (a) and phase (b). Solid lines represents the measurements obtained with the use of the presented system, dashed lines correspond to the reference values.

4.5 GHz to 5 GHz the phase deviation of the second matrix increases to  $\pm 20^\circ$ , therefore, a distinct deterioration of circle centers can be expected. The calibration results are illustrated in Fig. 3.11. It is seen that the obtained circle centers' distribution is close to theoretical predictions, however, some deterioration, due to imperfect parameters of both applied matrices is seen. Furthermore, in Fig. 3.11d it can be seen, that the impedance match of the measuring ports, as well as the isolation between these ports allow for the simplifications of the measuring system's model, which have been discussed in Subsection 3.1.3. The measured transmission coefficients of SMA attenuators are presented in Fig. 3.12.

For further examination the bandpass filter has been measured. The obtained results are shown in Fig. 3.13. The deterioration of measured transmission coefficient results from the summation of measurement inaccuracy from particular measurements, as well as from the assumed simplifications of the measuring system.

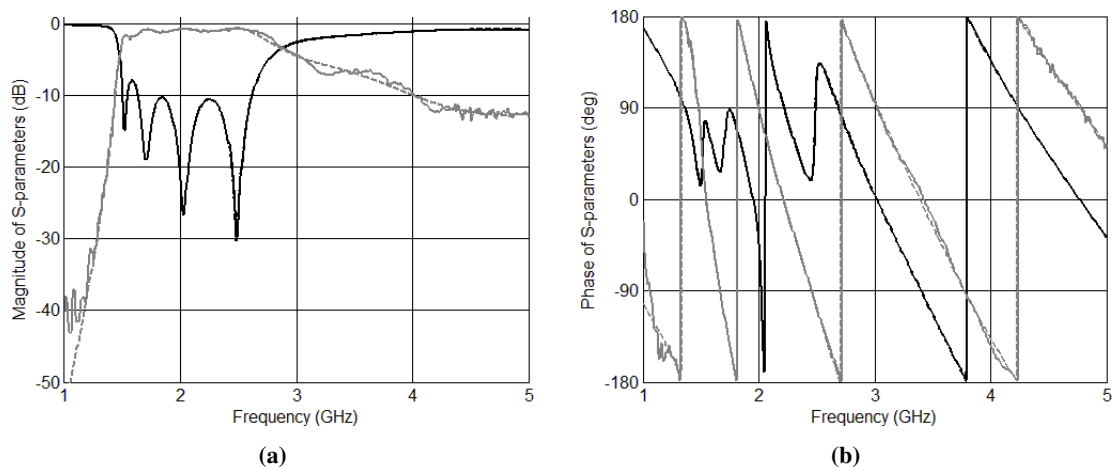


**Figure 3.13:**  $S$ -parameters of the bandpass filter measured using the measuring system utilizing  $4 \times 4$  Butler matrices described in Subsection 3.1.1: magnitude (a) and phase (b). Solid lines represents the measurements obtained with the use of the presented system, dashed lines correspond to the reference values. Reflection coefficient is marked black, whereas transmission coefficient is marked gray.

### 3.4.2. Broadband Measurements of Transmission Coefficient Utilizing Single $8 \times 8$ Butler Matrix

The multiport measuring system described in Subsection 3.2.1 has been developed for an experimental verification with the use of the broadband  $8 \times 8$  Butler matrix described in [95]. The system described in Subsection 2.5.5 has been extended by switch and isolator, having parameters as shown in Fig. 3.14. It can be seen that the isolation provided by the applied isolator is comparable to the noise floor of the used VNA, therefore, it can be considered as ideal. Furthermore, in Fig. 3.14 the isolation between measuring port (#9) and port to which the isolator is connected (#11), is presented. The model of the measuring system provided in Subsection 3.2.2 takes into account this imperfection, therefore, it has no impact on the measurement results [85].

Three constants  $A$ ,  $B$  and  $C$ , being the results of calibration for transmission coefficient measurements with the use of a single reflectometer are presented in Fig. 3.15.

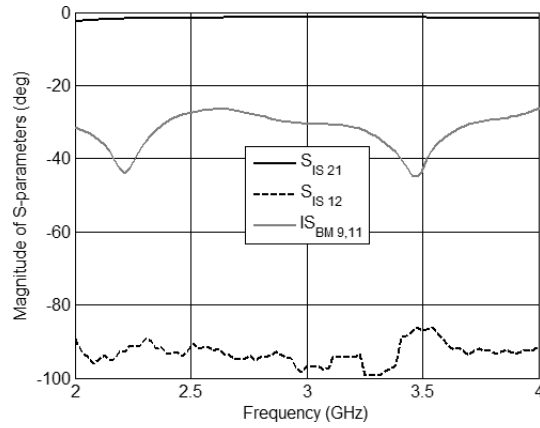


**Figure 3.14:** Measured transmission coefficients of the utilized isolator  $S_{IS21}$  and  $S_{IS12}$  and isolation of the utilized  $8 \times 8$  Butler matrix between the measuring port and the port to which the isolator is connected  $S_{BM9,11}$ .

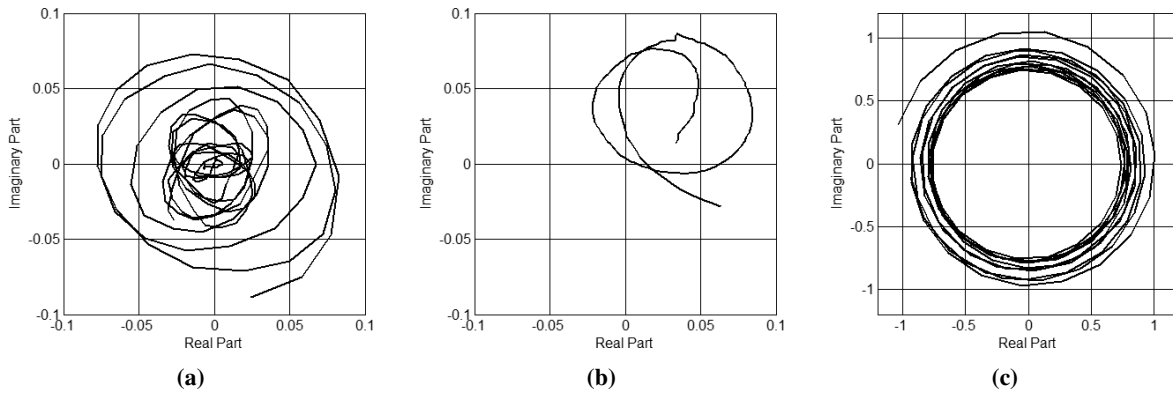


**Figure 3.15:** Results of the calibration procedure for the measuring system involving the single  $8 \times 8$  Butler matrix. Calibration constants  $A$  (a),  $B$  (b) and  $C$  (c) vs. frequency.

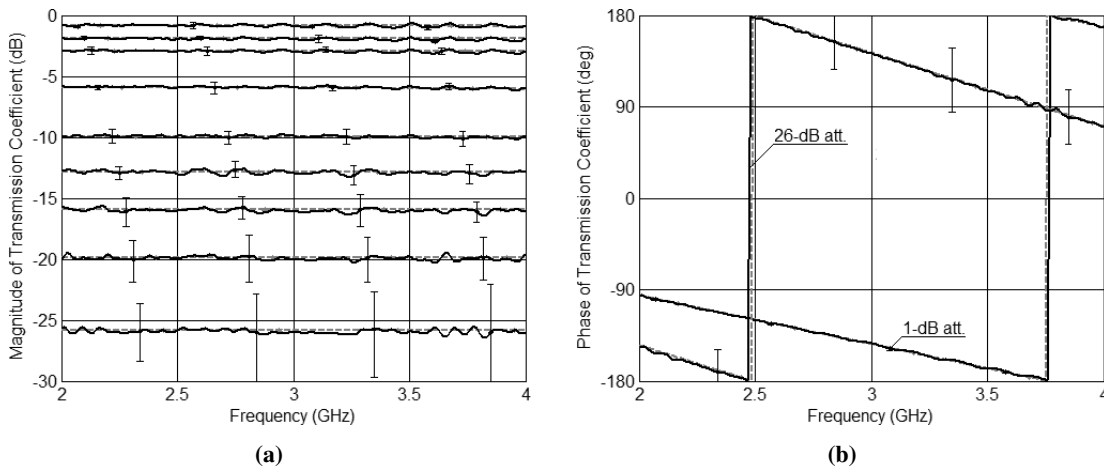


**Figure 3.16:** Transmission coefficients of a set of attenuators measured using the measuring system utilizing the single  $8 \times 8$  Butler matrix described in Subsection 3.2.1: magnitude (a) and phase (b). Solid lines represents the measurements obtained with the use of the presented system, dashed lines correspond to the reference values.

The measured transmission coefficients of SMA attenuators are presented in Fig. 3.16. Similarly as in the previous measuring system, for further verification of system's performance the  $S$ -parameters of a narrow-band bandpass filter have been measured. As it can be seen in Fig. 3.16 and Fig. 3.17, a very good agreement between the measured results and the reference values has been obtained, which proves that in multiport measurements of transmission coefficient with the use of a single reflectometer the number of isolators can be reduced to only one [85].

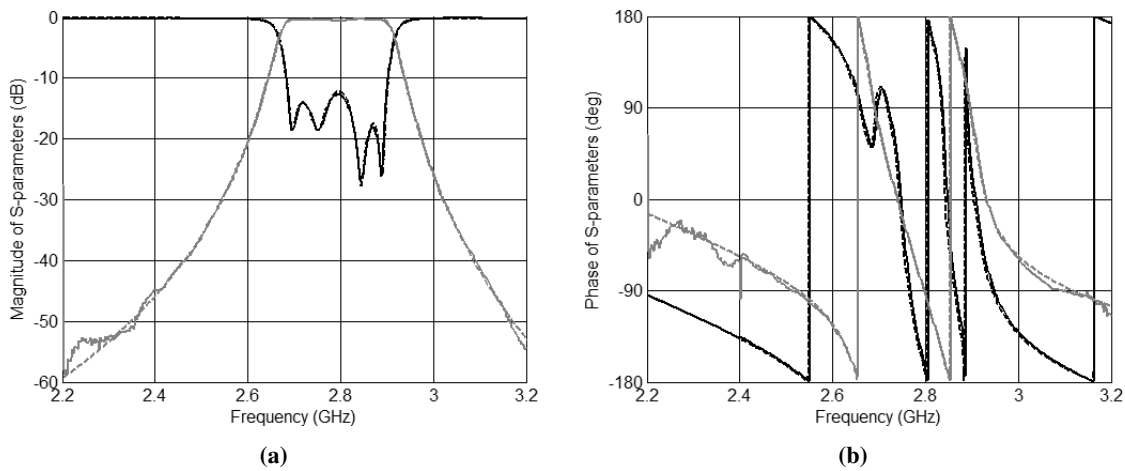


**Figure 3.17:**  $S$ -parameters of the bandpass filter measured using the measuring system utilizing the single  $8 \times 8$  Butler matrix described in Subsection 3.2.1: magnitude (a) and phase (b). Solid lines represent the measurements obtained with the use of the presented system, dashed lines correspond to the reference values. Reflection coefficient is marked black, whereas transmission coefficient is marked gray.

### 3.4.3. Analysis of Measurement Results

The performed experimental verification of both measuring systems considered in this Chapter confirms the usefulness of Butler matrices in the transmission coefficient measurements, since the obtained results are very close to the reference values. Similarly as in case of reflection coefficient measurements, the increase of measurement error with decreasing magnitude of the measured transmission coefficient is observed, which strictly corresponds to the theoretical predictions. For both measuring systems the magnitude and phase measurement error vs. magnitude of the measured transmission coefficient within the entire operational bandwidth has been calculated as the maximum difference between the measured results and the corresponding reference values (VNA measurements). The achieved results are shown in Fig. 3.18.

It can be observed that the obtained magnitude error distributions for both measuring systems are comparable. In case of phase measurement the system composed of two  $4 \times 4$  Butler matrices provides higher accuracy. It is worth mentioning that both obtained error distributions do not exceed the theoretically calculated error distribution shown in Fig. 2.20 and Fig. 2.21. The error distributions presented in Fig. 3.18 are calculated as a worst case using only the results obtained from the measurement of SMA attenuators. It can be observed that the measurement error for measured filters is in general higher, which is clearly seen in case of measuring system composed of two  $4 \times 4$  Butler matrices

(Fig. 3.13). The increased inaccuracy results from the error propagation from prior measurements required to calculate  $S_{21}$  coefficient, i.e. both reflection coefficients of the measured filter, as well as reflection coefficients of the measuring ports between which DUT is inserted. Furthermore, the utilized SMA adapter, which was necessary to connect DUT to the system, has been considered as ideal, which slightly increases the obtained measurement error. The same sources of measurement errors can be found in the measuring system involving a single  $8 \times 8$  Butler matrix, however, in this case the isolation level is very close to ideal (Fig. 3.14). Moreover, the impedance match of the measuring port seen in Fig. 2.37d and the applied isolator's impedance match (Fig. 3.15b) are better than the impedance match of measuring ports in the system composed of two  $4 \times 4$  Butler matrices (Fig. 3.11d). All these advantages allowed for achieving very high dynamics of the measured magnitude which, as can be seen in Fig. 3.17, is about 50 dB. Nevertheless, the operational bandwidth is limited by the applied isolator. This drawback does not appear in the measuring system involving two  $4 \times 4$  Butler matrices, the achieved bandwidth of which is equal to 5:1.

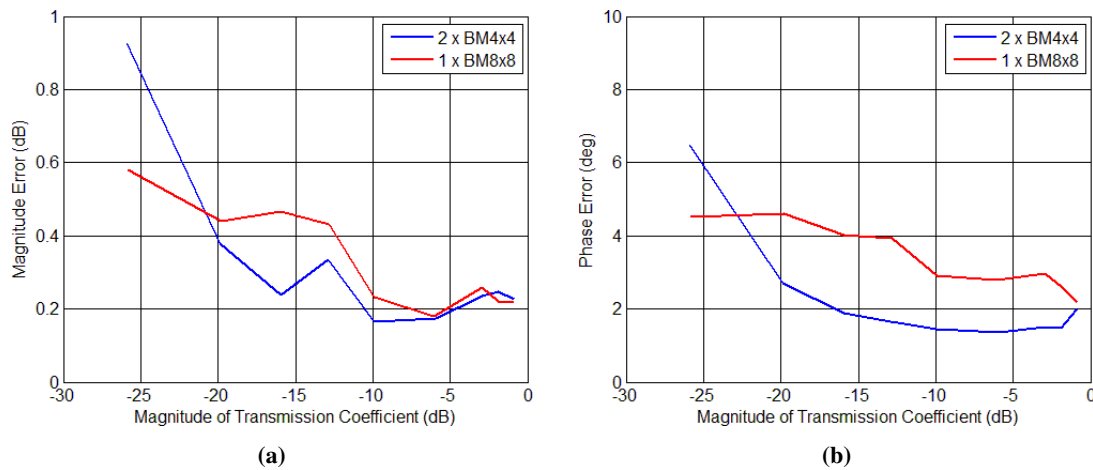


**Figure 3.18:** Maximum magnitude (a) and phase (b) measurement error vs. the magnitude of the measured transmission coefficient for two broadband measuring systems described in Section 3.4.

### 3.5. Conclusions

In this Chapter the transmission coefficient measurements with the use of two different multipoint techniques have been presented. The first one utilizes the system composed only of two  $4 \times 4$  Butler matrices, with neither additional power dividers nor isolators, which has allowed for a significant simplification of the measuring system and its broadband operation. The second system incorporates a single  $8 \times 8$  Butler matrix and an isolator. Such a solution allows for decreasing the number of required power meters to only five (including reference power measurement), whereas in the former system eight power meters are required. The main advantage of both presented measuring systems is that the role of dedicated six-ports applied commonly in such multipoint-based systems is performed by standard Butler matrices. Additionally the increased number of ports of Butler matrices with respect to the classic six-ports allows for the utilization of different system configurations introducing a different inner power

division, what has the same effect as the application of a different multiport network. Therefore, different system's configurations can be utilized in order to increase the measurement accuracy.

Both the presented measuring systems have been theoretically analyzed and the conditions for their proper performance are given. Further, for each solution the theoretical model taking into account the imperfections resulting from the practical realizations, has been developed and the conditions for a correct system's performance have been presented. Moreover, it has been proved that for measuring systems involving a single multiport reflectometer the number of applied isolators can be reduced to only one. On the basis of the presented models two different analytical calibration procedures utilizing the least-squares approach for systems having an arbitrary number of ports have been proposed. Additionally, the utilization of the SMA adapters in calibration procedure has been discussed.

Further, both measuring systems have been experimentally verified by the measurements of a set of broadband SMA attenuators and two bandpass filters. The obtained results are in a good agreement with the values measured using a commercial vector network analyzer and fully correspond to the estimated accuracy intervals. The achieved measurement results clearly prove the usability of Butler matrices in transmission coefficient measurements with the use of multiport technique.



## 4. *S*-parameter Measurements With the Use of Tunable Multiport Systems

The analysis of the measurement accuracy presented in Section 2.4 reveals that the measurement error depends on the circle centers' distribution of a given measuring system. In the mentioned analysis the geometrical interpretation of the measurement with the use of multiport measurement technique has been utilized, in which the measured value (reflection or transmission coefficient) is an intersection point of several circles. For the measurement accuracy estimation, these circles have been transformed into rings, having the widths corresponding to the power measurement uncertainty of the applied power meters, as it has shown in Fig. 2.16.

In Section 2.4 it has been shown, that the measurement error arises from non-uniform distribution of circle centers (causing irregular shape of rings' intersection area RIA) and from the rings' width. The latter is directly related to the distance between circle centers and the measured value. Therefore, a uniform scaling of the mentioned distance for each circle center, with simultaneous preservation of their angular distances, may result in improvement of measurement accuracy for the *S*-parameters having small magnitudes.

In this Chapter the concept of the scalable circle centers' distribution in multiport measuring systems is presented. In particular, the Author proposes two novel measuring systems, which feature scalable circle centers' distributions and allow for the measurements of both reflection and transmission coefficients. The theoretical analysis of the systems' performance together with the estimation of the measurement accuracy are given. Further, the calibration of multiport systems with scalable distribution of circle centers is discussed. Finally, the experimental verification of both measuring systems is presented, which confirms the enhanced measurement accuracy of the proposed systems.

The following Chapter consists of the Author's research results focused on the multiport systems featuring scalable circle centers' distribution published recently in [81], [82] and in [87].

### 4.1. Tunable System With Isolator

In this Section a multiport system capable of reflection and transmission coefficients measurements is presented [87]. It is composed of a standard  $4 \times 4$  Butler matrix, additional directional coupler, switch and isolator. The proposed system features a uniform circle centers' distribution which can be additionally scaled in order to increase the measurement accuracy. Moreover, the influence of the coupler's parameters on the measurement conditions has been analyzed and the results are given.

### 4.1.1. Theoretical Analysis

The schematic diagram of the proposed measuring system allowing for reflection and transmission coefficients measurements is illustrated in Fig. 4.1. It can be observed that, similarly to the system presented in Section 3.2, the system shown in Fig. 4.1 is composed of a single reflectometer with added isolator and switch allowing for measuring the entire *S*-matrix (reflection coefficients as well as transmission coefficients) of the Device Under Test (DUT) according to the procedure given in Subsection 3.2.3. The distinctive differences are: (i) the reflectometer is realized as a connection of classic  $4 \times 4$  Butler matrix and an external directional coupler and (ii) the reflective element connected to port #6 is realized as an adjustable attenuator terminated with short-circuit. Both proposed modifications are explained in further part of this Section.

As it has been revealed in Subsection 2.2.1, the reflectometer involving a single  $4 \times 4$  Butler matrix provides three circles having centers located on the circumference of a unity circle with the angular distance of  $90^\circ$ . Since there are only three circle centers, their distribution with respect to all possible reflection coefficients, being located inside the unitary circle, is not uniform. This disadvantage can be overcome by the application of an  $8 \times 8$  Butler matrix shown in Subsection 2.2.3, which can provide a uniform distribution of four circles having centers on the circumference of a unity circle with angular distance of  $90^\circ$ . Nevertheless, such uniform measurement conditions are obtained at the expense of complexity of the utilized 16-port network. Moreover, in that case only one half of the  $8 \times 8$  Butler matrix is effectively utilized.

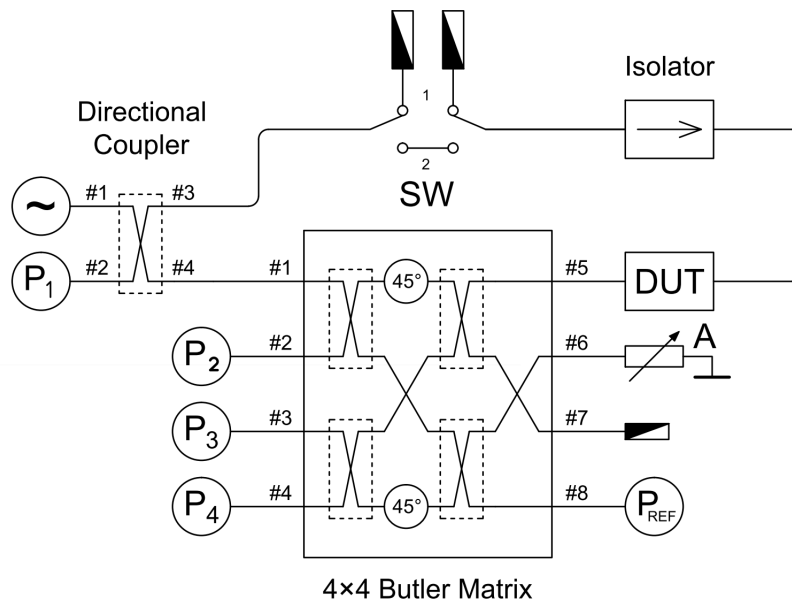


**Figure 4.1:** Schematic diagram of the proposed tunable measuring system with an isolator [87]. (Copyright © 2015, IEEE)

The advantages of multiport reflectometers utilizing both  $4 \times 4$  Butler matrix and  $8 \times 8$  Butler matrix can be combined in the measuring system presented in Fig. 4.1 [82]. It utilizes a single  $4 \times 4$  Butler matrix with an additional directional coupler. Such a modification introduces a fourth circle providing a highly uniform circle centers' distribution, as in case of  $8 \times 8$  Butler matrix application. Simultaneously, the system complexity is significantly decreased. It can be observed that the system arrangement is

similar to the system involving a single  $4 \times 4$  Butler matrix or a single  $8 \times 8$  Butler matrix presented in Subsections 2.2.1 and 2.2.3, respectively.

Since the  $4 \times 4$  Butler matrix is fed at port #1, the relations between power measured at ports #2 – #4 and the measured reflection coefficient  $\Gamma$  remain the same as described in Subsection 2.2.1. Therefore, ports #2 – #4 of the utilized  $4 \times 4$  Butler matrix are related to the circle centers located on the circumference of a unitary circle with angular distance being equal to  $90^\circ$ . Such circle centers' distribution is restricted by a proper choice of the measuring port and port with the reflective element connected, which has been a subject of a comprehensive analysis in Subsection 2.2.1 [79]. Having known the phase relations in a  $4 \times 4$  Butler matrix one can predict, that port #1, which in the reflectometer shown in Subsection 2.2.1 has been used for exciting the measurement system, is related to the fourth circle. The external coupler allows for exciting the  $4 \times 4$  Butler matrix and simultaneously provides an additional port, at which the power reflected from DUT can be measured introducing the fourth circle. It can be shown that if the proper measuring port and port with a reflective element are chosen (according to the procedure shown in Subsection 2.2.1), one can obtain four circle centers distributed uniformly on a unitary circle.

#### 4.1.2. Application of External Directional Coupler

The theoretical investigation conducted in Subsection 4.1.1 reveals, that all four circle centers are located uniformly on a unitary circle. The imperfect impedance match as well as non-ideal isolations of the  $4 \times 4$  Butler matrix affect the circle centers' location, however, as it has been shown in Subsection 2.5.3, their influence on the measurement accuracy is not significant. Therefore, the requirements related to the Butler matrix's parameters are not excessive. Nevertheless, the impact of the additional directional coupler on the location of the circle center related to port #2 of the directional coupler has to be investigated [82].

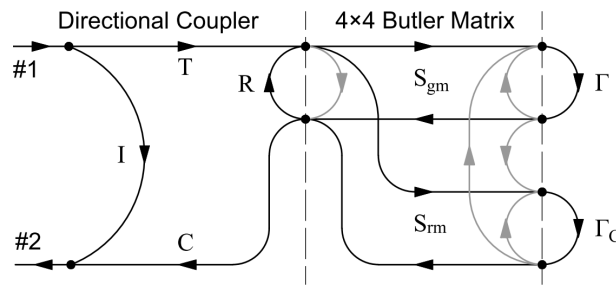


**Figure 4.2:** Signal flow for the transmission between port #1 and port #2 of the directional coupler connected to a  $4 \times 4$  Butler matrix. Signal paths corresponding to imperfections of the Butler matrix are marked gray [82]. (Copyright © 2014, Wiley Periodicals, Inc.)

The signal flow between port #1 and port #2 of the added directional coupler is shown in Fig. 4.2. It is seen that the imperfect isolation  $I$  and return losses  $R$  of the directional coupler are assumed. To increase the clarity of this investigation the imperfect isolations and non-ideal impedance match of the  $4 \times 4$  Butler matrix (marked gray in Fig. 4.2) have been neglected. Therefore, the relation between the power measured at port #2 of the coupler and the measured reflection coefficient  $\Gamma$ , assuming reciprocity ( $S_{ij} = S_{ji}$ ), is as follows:

$$p_1 = \frac{P_1}{P_{IN}} = \left| I + TC \frac{S_{gm}^2 \Gamma + S_{rm}^2 \Gamma_C}{1 - R(S_{gm}^2 \Gamma + S_{rm}^2 \Gamma_C)} \right|^2 \quad (4.1)$$

where  $T$  and  $C$  are transmission and coupling coefficients of the coupler, respectively,  $S_{gm}$  and  $S_{rm}$  are the particular  $S$ -parameters of an ideal  $4 \times 4$  Butler matrix and  $\Gamma_C$  is the reflection coefficient of the reflective element connected to port #6. Assuming that  $|R| \ll 1$  (4.1) can be approximated as follows:

$$p_1 = \frac{P_1}{P_{IN}} \cong |I + \alpha TC (S_{gm}^2 \Gamma + S_{rm}^2 \Gamma_C)|^2 \quad (4.2)$$

where

$$\alpha = 1 + R(S_{gm}^2 \Gamma + S_{rm}^2 \Gamma_C) \quad (4.3)$$

It is seen that the introduced coefficient  $\alpha$  depends on both return losses  $R$  and on the measured reflection coefficient  $\Gamma$ . Assuming the return losses of the utilized directional coupler  $R = 10$  dB and an ideal  $4 \times 4$  Butler matrix, for which  $|S_{gm}^2| = |S_{rm}^2| = 0.25$ , the magnitude of coefficient  $\alpha$  does not exceed the range of  $0.921 - 1.079$ , and for  $R = 20$  dB this range narrows to  $0.975 - 1.025$ . It is seen that even in case of relatively poor impedance match of the applied directional coupler, the coefficient  $\alpha$  is very close to the ideal value  $\alpha_{ideal} = 1$ , which corresponds to the perfect impedance match of the utilized directional coupler. Therefore, it can be said that the imperfect impedance match of the external directional coupler has a negligible impact on the circle centers' distribution of the proposed reflectometer [82].

Apart from the impedance match of the utilized external coupler, its imperfect isolation has to be investigated. Analyzing (4.1) one can observe that the coupler's imperfect isolation has a direct impact on the power reading. Since the analysis shown in the previous paragraph has revealed insignificance of the coupler's imperfect impedance match, in further consideration the external coupler is assumed to be ideally matched. Therefore, (4.1) can be rewritten:

$$p_1 \approx |TC S_{gm}^2|^2 |\Gamma - c_1|^2 \quad (4.4)$$

where  $c_1$  is the circle center related to port #1 of the Butler matrix, expressed as follows:

$$c_1 = - \left( \frac{I}{TC S_{gm}^2} + \frac{S_{rm}^2 \Gamma_C}{S_{gm}^2} \right) \quad (4.5)$$

As it is seen, if the perfect coupler's isolation is assumed, the added directional coupler does not influence  $c_1$  and its location results only from the utilized  $4 \times 4$  Butler matrix. However, in case of imperfect isolation, the circle center  $c_1$  can be deteriorated proportionally to the coupler's isolation. Moreover, this deterioration depends on the coupling coefficient of the used coupler, therefore, the optimum coupling value has to be determined. In general, the chosen coupling coefficient is a compromise between two requirements. On one hand it is desired to provide the maximum power to the Butler matrix, which can be ensured by the minimum coupling, but on the other hand the maximum power delivered to the power meter  $P_1$  is also crucial (maximum coupling required). Both these requirements result from high dynamics of the measured power with respect to the average dynamics of applied power

detectors. Taking into account both aspects it can be stated, that a 3-dB directional coupler is the optimum solution. Assuming an ideal Butler matrix and an ideal 3-dB directional coupler, it can be shown that:

$$|TCS_{gm}^2| = \frac{1}{8} \quad (4.6)$$

Therefore (4.5) becomes:

$$c_1 = 8Ie^{j\varphi_1} + \Gamma_C e^{j\varphi_2} \quad (4.7)$$

where  $\varphi_1$  and  $\varphi_2$  are the angles resulting from phase relations in the  $4 \times 4$  Butler matrix. It can be observed that the application of a 3-dB directional coupler maximizes (4.6), which ensures the minimum influence of the coupler's isolation on the location of circle center  $c_1$ . In (4.7) one can notice, that the distance between the circle center  $c_1$  and the origin of a complex plane also depends directly on  $|\Gamma_C|$ , exactly in the same way as three remaining circle centers (please see Subsection 2.2.1). It has to be underlined, however, that the location of  $c_1$  is sensitive to the isolation of the applied directional coupler, which can result in a greater displacement of circle center  $c_1$  in a practical realization in comparison to the remaining circle centers [82].

### 4.1.3. Application of Adjustable Attenuator

As it has been mentioned at the beginning of this Chapter, a uniform scaling of the mentioned distance for each circle center, with simultaneous preservation of their angular distances, may improve the measurement accuracy for the  $S$ -parameters having small magnitudes. According to the investigation presented in Subsections 2.2.1 and 4.1.2, the distance between each circle center and the origin of a complex plane (called further the magnitude of circle centers' distribution) is the same and is proportional to the magnitude of reflection coefficient  $\Gamma_C$  [81]:

$$|c_i| \approx |\Gamma_C| \quad (4.8)$$

The reflective element can be realized as a shorted adjustable attenuator, connected to port #6 of a Butler matrix, as shown in Fig. 4.1, and may be used for scaling the magnitude of circle centers' distribution. Circle centers being close to the origin of a complex plane result in lower ring widths without any impact on the shape of their intersection area. Hence, the measurement accuracy for reflection coefficients having small magnitudes is significantly improved.

Assuming an ideal Butler matrix and perfect short-circuit, the mentioned distance  $|c_i|$  can be derived as follows:

$$|c_i| = 10^{-\frac{\alpha}{10}} \quad (4.9)$$

where  $\alpha$  is the attenuation of an applied attenuator expressed in dB. For  $\alpha = 0$  dB one obtains  $|c_i| = 1$ , which corresponds to the circle centers' distributions of the reflectometers investigated in Subsections 2.2.1, 2.2.2 and 2.2.3. It has to be underlined that (4.9) refers to the ideal Butler matrix. In case of a real Butler matrix, its imperfect parameters, i.e. magnitude imbalance, imperfect isolation and imperfect impedance match, deteriorate circle centers from the theoretical positions, therefore, the maximum attenuation  $\alpha_{\max}$  is limited to the value, for which the circle centers are located in the origin of a complex plane [81].

## 4.2. Tunable System Without Isolator

This Section shows a multiport measuring system allowing for measurements of scattering parameters. It is composed of two directional couplers and a standard  $4 \times 4$  Butler matrix, and does not require any isolators. The presented system features a uniform power distribution providing the high precision of measurements, which can be tuned for enhancement of the measurement accuracy.

### 4.2.1. Theoretical Analysis

The schematic diagram of the multiport system allowing for the measurements of reflection and transmission coefficients is illustrated in Fig. 4.3. The presented system is excited by a signal source applied to the directional coupler  $Q_1$ , which allows for the measurement of the reference power  $P_{REF}$ . The second directional coupler  $Q_2$  is used to split the signal from  $Q_1$  into the reference signal provided through the adjustable attenuator  $A$  to the 4<sup>th</sup> port of the  $4 \times 4$  Butler matrix and the second signal, which is provided to the measured device DUT. The applied switch  $SW$  allows for measuring reflection coefficient (switch in position 1) or transmission coefficient (switch in position 2). In case of reflection coefficient measurement the signal reflected from DUT is transmitted through the directional coupler  $Q_2$  and is provided to port #1 of the Butler matrix. For the transmission coefficient measurement, the signal transmitted through the measured device (DUT) is provided to port #1. Both signals applied to port #1 and port #4 of the  $4 \times 4$  Butler matrix are summed with different phase relations and measured by four power meters connected to the output ports of the Butler matrix. It can be observed that in the proposed measuring system for each measurement all the applied power meters are utilized. It allows for an enhancement of the measurement precision with decreased number of power meters in comparison to the measuring systems involving two multiports, in which at least seven power meters are required [17], [47], [61], [15], [41], [40].

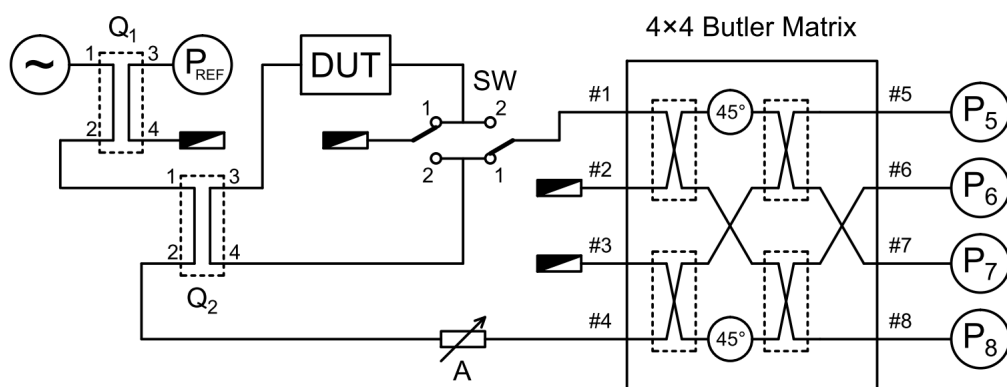


**Figure 4.3:** Schematic diagram of the proposed measuring system composed of a  $4 \times 4$  Butler matrix and two directional couplers.

Further analysis of the proposed measuring system is performed with the assumption, that all the utilized components feature ideal isolations, as well as perfect impedance match. The relations between power readings  $P_i$  ( $i = 5, \dots, 8$ ) and the measured reflection and transmission coefficients  $\Gamma$  and  $T$ ,

respectively, are as follows:

$$p_{\Gamma ink} = \frac{P_{\Gamma ink}}{P_{REF}} = |T_1 T_2|^2 |A S_{ik} + C_2 S_{in} \Gamma|^2 \quad (4.10)$$

$$p_{T ink} = \frac{P_{T ink}}{P_{REF}} = |T_1|^2 |A T_2 S_{ik} + C_2 S_{in} T|^2 \quad (4.11)$$

where  $i$  – number of Butler matrix port, at which the power is measured,  $n$  – number of Butler matrix port, to which switch SW is connected,  $k$  – number of Butler matrix port, to which the adjustable attenuator is connected,  $T_x, C_x$  – transmission and coupling coefficients of the directional coupler  $Q_x$ ,  $A$  – attenuation of the adjustable attenuator,  $S_{xx}$  –  $S$ -parameters of the utilized  $4 \times 4$  Butler matrix. The distributions of circle centers for reflection coefficient measurements  $c_{\Gamma}$  and for transmission coefficient measurements  $c_T$  are as follows:

$$c_{\Gamma ink} = -\frac{A S_{ik}}{C_2 S_{in}} \quad (4.12)$$

$$c_{T ink} = -A \frac{T_2 S_{ik}}{C_2 S_{in}} \quad (4.13)$$

It can be observed that the applied adjustable attenuator allows for uniform scaling of the distance between the origin of a complex plane and all circle centers (magnitude of circle centers' distribution), which can be utilized in order to enhance the measurement accuracy. Moreover, it is seen that the directional coupler  $Q_1$  does not influence the circle centers' distributions. It is applied only to provide the reference power measurement, therefore, the requirements related to its parameters are relaxed and its nominal coupling may be very weak (e.g. 10 – 20 dB). Assuming that the directional coupler  $Q_2$  is an ideal 3-dB quadrature directional coupler, (4.12) and (4.13) can be expressed as:

$$c_{\Gamma ink} = -A \sqrt{2} \frac{S_{ik}}{S_{in}} \quad (4.14)$$

$$c_{T ink} = -j A \frac{S_{ik}}{S_{in}} \quad (4.15)$$

and the magnitude of the circle centers' distribution can be adjusted by setting the desired attenuation:

$$|c_{\Gamma}| = \sqrt{2} \cdot 10^{-\frac{A}{20}} \quad (4.16)$$

$$|c_T| = 10^{-\frac{A}{20}} \quad (4.17)$$

where attenuation  $A$  is expressed in dB.

The above discussion is related to the applied directional couplers and adjustable attenuator. As it has been shown the magnitude of circle centers' distribution can be scaled by the applied attenuator. However, the mutual angular distance between circle centers  $\arg [c]$  results only from the  $4 \times 4$  Butler matrix's parameters and can be chosen by a proper selection of the Butler matrix's input ports. Table 4.1 and Table 4.2 present all possible configurations of the proposed system for the directional coupler  $Q_2$  having 3-dB coupling level and attenuation of the adjustable attenuator being equal to 0 dB. It can be seen that some of the possible configurations cannot be utilized in measurements, since the circle centers overlap, leading to ambiguous measurements. This fact can be explained with the use of schematic diagram of the  $4 \times 4$  Butler matrix seen in Fig. 4.3. To ensure four different circle centers, the signal

related to the measured value and the reference signal have to excite different internal directional couplers of the Butler matrix, which ensures the maximum variety of the phase shifts for these two signals seen at the output ports of the  $4 \times 4$  Butler matrix.

**Table 4.1:** Distribution of circle centers for reflection coefficient measurements, assuming  $A = 0$  dB,  $C_2 = 3$  dB,  $n$  – port of Butler matrix, to which switch SW is connected and  $k$  – port of Butler matrix, to which adjustable attenuator is connected.

		$k$			
		5	6	7	8
$n$	5				
	6				
	7				
	8				

**Table 4.2:** Distribution of circle centers for transmission coefficient measurements, assuming  $A = 0$  dB,  $C_2 = 3$  dB,  $n$  – port of Butler matrix, to which switch SW is connected and  $k$  – port of Butler matrix, to which adjustable attenuator is connected.

		$k$			
		5	6	7	8
$n$	5				
	6				
	7				
	8				

### 4.3. Measurement Accuracy for Measuring Systems Featuring Scalable Circle Centers' Distribution

Both measuring systems presented in Sections 4.1 and 4.2 feature the circle centers' distribution composed of four circles uniformly arranged on a circumference of the circle having radius  $|c_i|$  resulting from the chosen attenuation of the applied attenuator. The measurement accuracy for circle centers' magnitude  $|c_i|$  taking values from 0.1 to 1 have been calculated numerically with the use of algorithm described in Subsection 2.4.2. The achieved results are presented in Fig. 4.4. As it is seen shifting the circle centers towards the origin of a complex plane significantly decreases the magnitude measurement error. On the other hand by adjusting the attenuator the phase error characteristic can be shifted in such a way, that its minimum corresponds to the magnitude of the measured  $S$ -parameters [81]. The proposed technique is advantageous, since the phase error increases very rapidly for lower and higher magnitudes of measured scattering parameters.

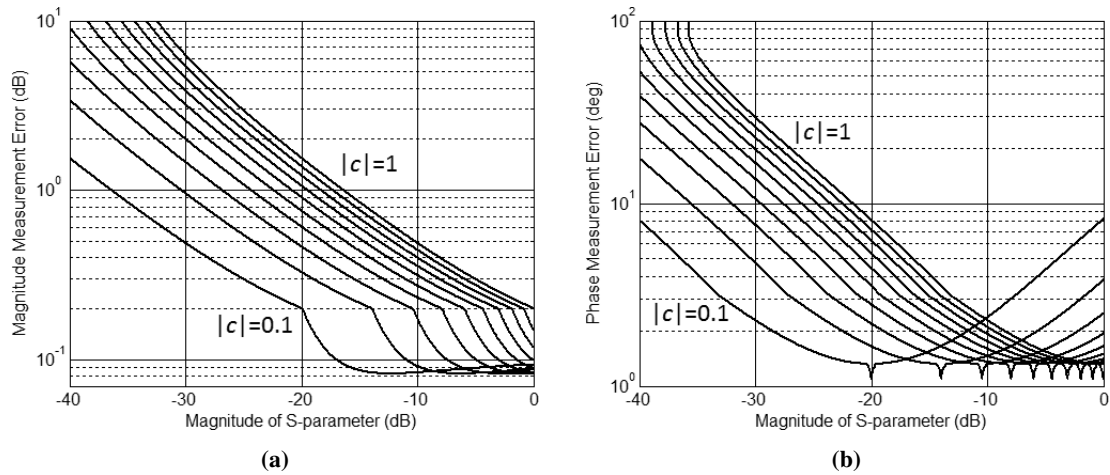


**Figure 4.4:** The maximum magnitude (a) and phase (b) measurement error for the measuring systems featuring scalable circle centers' distributions presented in Sections 4.1 and 4.2. The assumed power detectors uncertainty  $\Delta_{PD} = \pm 0.1$  dB.

### 4.4. Calibration Accuracy for Measuring Systems Featuring Scalable Circle Centers' Distribution

The investigation presented in Section 2.4 is related to the measurements of reflection coefficient (and transmission coefficient) under the assumption that the circle centers' distribution of a given multiport system is known precisely. In practice, each measuring system has to be calibrated in order to determine its circle centers' distribution [60], [25], [100], [75], [16], [29], [23]. Such a procedure is analogous to the subsequent measurement, however, in case of calibration, the reflection or transmission coefficients are known and the circle centers' distribution has to be found. Therefore, in order to estimate the calibration accuracy an approach similar to the one described in Subsection 2.4.2 may be applied. It has to be underlined that both imperfect calibration and measurements with a given uncertainty have impact on

the final measurement results. However, combining these two procedures does not allow for defining the worst case (maximum error). Therefore, the calibration procedure is analyzed separately [81].

For the analysis of calibration, the optimal set of four calibration standards has been assumed, as shown in Fig. 4.5, for which the calibration inaccuracy is minimized (minimum RIA). In case of the calibration accuracy analysis, a separate calculation of the magnitude and phase error is not a good measure. Instead, a convenient measure of calibration accuracy is the error in a sense of maximum distance between the genuine circle center's position and the one calculated in calibration (similarly as the estimation of the measurement accuracy presented at the beginning of Subsection 2.4.2). Since the most remote point from real value within the RIA is one of its vertices (Fig. 2.16 and Fig. 2.19), only the intersections of ring borders have to be considered.

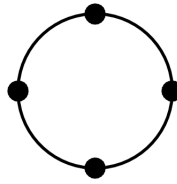


**Figure 4.5:** The optimal distribution of four calibration standards for calibration accuracy analysis [81]. (Copyright © 2013, IEEE)

Moreover, due to the two lines of symmetry of the considered calibration standards' distribution, the resulting calibration error distribution has also two lines of symmetry. Therefore, only a quarter of a complex plane has to be investigated. Hence, to define the maximum error, for a given radius, on which the circle centers are placed, the angles in a range from  $0^\circ$  to  $90^\circ$  have to be considered. Fig. 4.6 presents the results of analysis of calibration accuracy, for the circle centers being located at a distance  $0.1 - 2.5$  from the origin and the assumed power measurement uncertainty  $\Delta_{PD} = \pm 0.1$  dB. As it is seen better accuracy is obtained for smaller distances between circle centers and the origin of a complex plane. The increase of calibration error for larger distances is caused by increasing width of each ring, leading to the increase of intersection area [81].

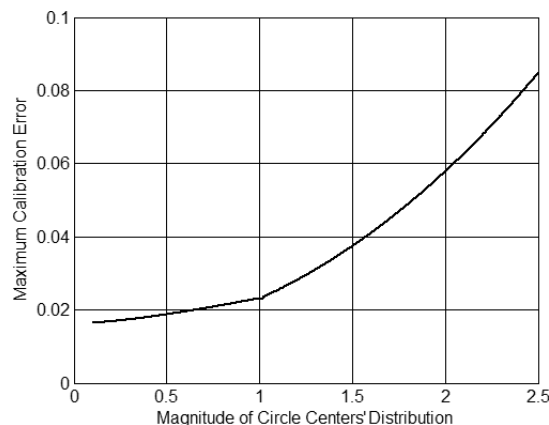


**Figure 4.6:** The maximum calibration error in a sense of distance between the genuine circle center and the one calculated in calibration vs. the magnitude of circle centers' distribution. The assumed power detectors uncertainty  $\Delta_{PD} = \pm 0.1$  dB [81].

(Copyright © 2013, IEEE)

## 4.5. Experimental Verification

This Section presents the experimental verification of two measuring systems described in Sections 4.1 and 4.2. For both systems the applied signal source, as well as the utilized power meters are the same as the ones utilized in previous measurements (for details please see Section 2.5). Each measuring system has been calibrated with the appropriate calibration procedure described in former Chapters. It is worth mentioning that in case of measuring systems featuring scalable circle centers' distribution the calibration has to be done for each chosen magnitude of the circle centers' distribution. Nevertheless, both presented systems cannot be considered as multi-state systems, since a particular measurement of  $S$ -parameters can be done utilizing a single calibration. However, having the system calibrated for several different magnitudes of circle centers' distribution, one can enhance the measurement accuracy by the choice of a proper magnitude ensuring optimal measurement error distribution. Hence, if  $S$ -parameters having large magnitude (highly reflective elements or two-ports having low insertion loss) are to be measured, the chosen magnitude of circle centers' distribution should be close to 1. On the other hand, for the measurements of scattering parameters having small magnitude (e.g. well-matched attenuators) the decreased magnitude of circle centers' distribution is advantageous, according to the measurement accuracy estimation given in Fig. 4.4.

The performance of both measuring systems presented in this Chapter has been verified experimentally, similarly to the systems presented in Sections 2.5 and 3.4, i.e. with the use of a set of broadband SMA attenuators, which for reflection coefficient measurements have been terminated with a short-circuit. Further, the scattering parameters of two filters have been measured. As it is shown in Section 4.3, in case of both measuring systems the measurement accuracy depends on the chosen magnitude of circle centers' distribution. Therefore, the errorbars indicating the estimated accuracy in figures presenting the measurement results correspond to the circle centers' distribution utilized for a particular measurement.

In two following Subsections a description of the developed measuring system with the results of calibration performed for a set of chosen magnitudes of circle centers' distributions is shown. Further, the measurement results and reference values with the estimated measurement accuracy are presented.

### 4.5.1. Broadband Measuring System With Isolator

The tunable measuring system with an isolator described in Subsection 4.2.1 has been built for an experimental verification with the use of the same broadband  $4 \times 4$  Butler matrix as utilized in the reflectometer described in Subsection 2.5.3 [36] and the directional coupler shown in [35] operating within the frequency range 1 – 5 GHz. The utilized directional coupler features impedance match of 26 dB and the isolation better than 29 dB, whereas its amplitude imbalance is equal to  $\pm 0.25$  dB and the deviation of phase characteristics does not exceed  $\pm 2^\circ$ . As it can be noticed both utilized components operate in a broad frequency range 1 – 5 GHz, however the bandwidth of the entire developed system has been decreased to the range 2 – 4 GHz, due to the applied isolator having the parameters as shown in Fig. 3.14 (the same as used in the system involving a single  $8 \times 8$  Butler matrix).

The system has been calibrated following the procedures given in Section 2.3 and Subsection 3.2.3 for three different settings of the adjustable attenuator, which allows for scaling the magnitude of circle centers' distribution. The chosen attenuations with corresponding theoretical magnitude of circle centers' distributions are listed in Table 4.3. The calibration results are illustrated in Fig. 4.7, 4.8 and 4.9.

**Table 4.3:** Applied attenuation of the adjustable attenuator and the corresponding theoretical magnitude of circle centers' distribution [87].

Attenuation (dB)	Theoretical magnitude of circle centers' distribution (linear scale)
0	1.00
1	0.79
2	0.63

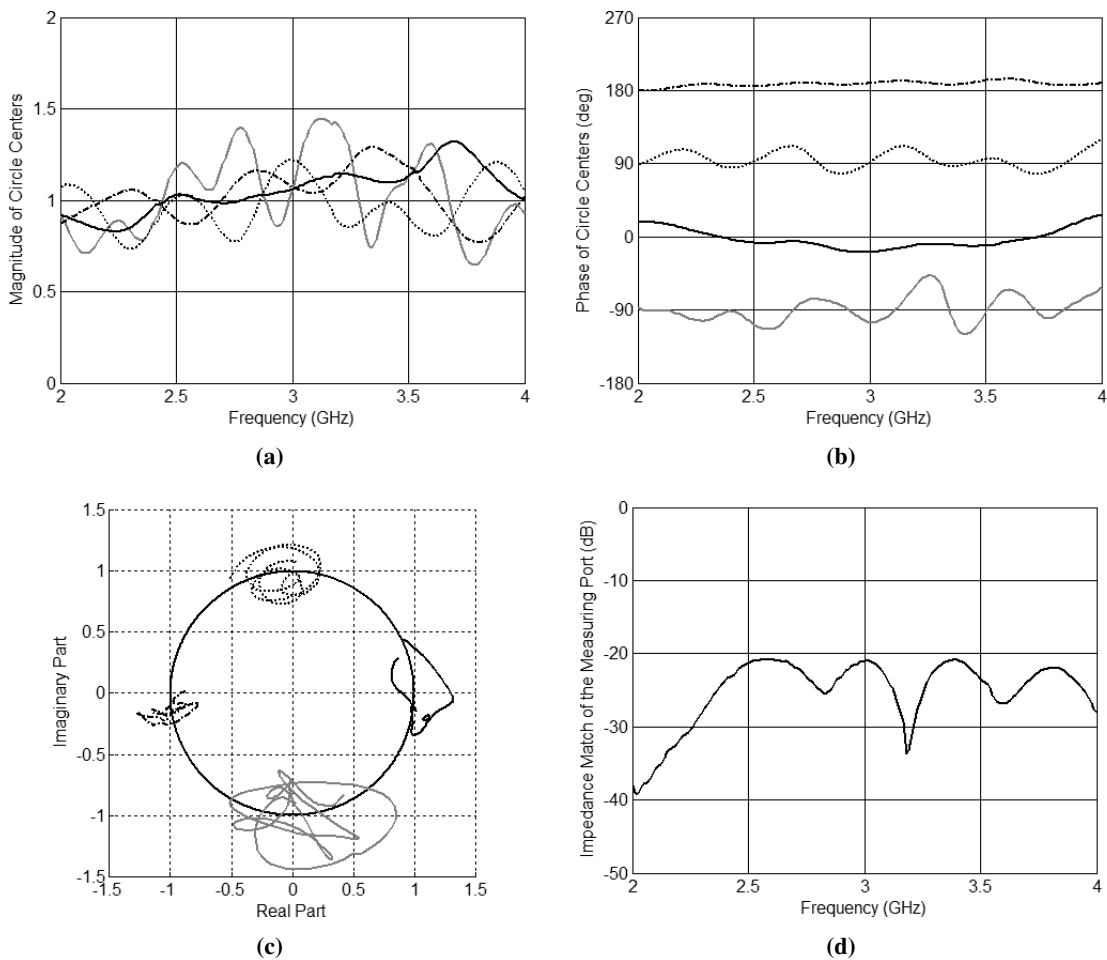


**Figure 4.7:** Results of the calibration procedure for the tunable measuring system with isolator described in Subsection 4.1.1 for theoretical magnitude of circle centers' distribution equal to 1: magnitude (a) and phase (b) of circle centers, circle centers' distribution on a complex plane (c) and the magnitude of reflection coefficient seen at the measuring port (d). The additional circle center resulting from the use of the additional coupler is marked gray.

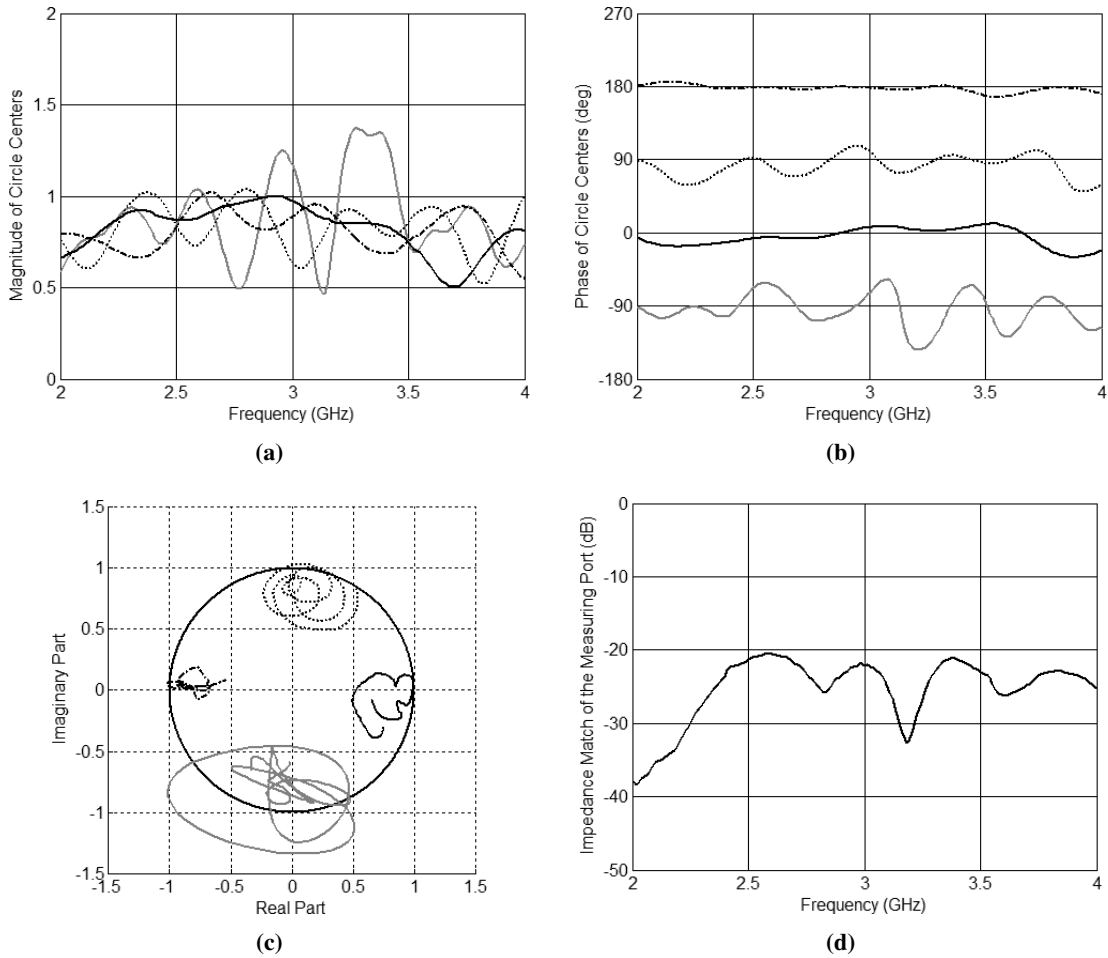


**Figure 4.8:** Results of the calibration procedure for the tunable measuring system with isolator described in Subsection 4.1.1 for theoretical magnitude of circle centers' distribution equal to 0.79: magnitude (a) and phase (b) of circle centers, circle centers' distribution on a complex plane (c) and the magnitude of reflection coefficient seen at the measuring port (d). The additional circle center resulting from the use of the additional coupler is marked gray.

For each chosen magnitude of circle centers' distribution three constants  $A$ ,  $B$  and  $C$ , described in Subsection 3.2.2 have been calculated. The choice of magnitude of circle centers' distribution does not affect their values, therefore, in Fig. 4.10 only the parameters corresponding to the magnitude of circle centers' distribution being equal to 1 are presented.

It can be observed that the obtained circle centers' distributions correspond to the theoretical predictions given in Subsection 4.1.1, however, some deteriorations, due to imperfect parameters of the applied Butler matrix and directional coupler are seen. The most deteriorated circle center is related to the power meter  $P_1$  applied to the external directional coupler, which is in agreement with the theoretical predictions described in Subsection 4.1.2. Moreover, a distinct scalability of the circle centers' distribution is observable, which confirms the utilization of the adjustable attenuator for scaling the circle centers' distribution (please see schematic diagram in Fig. 4.1).

The measurements of  $S$ -parameters have been done for all three distributions of circle centers. Further, from each triple of the obtained results corresponding to a particular measurement, the results featuring the highest accuracy have been chosen. They are shown in Fig. 4.11 and 4.12.

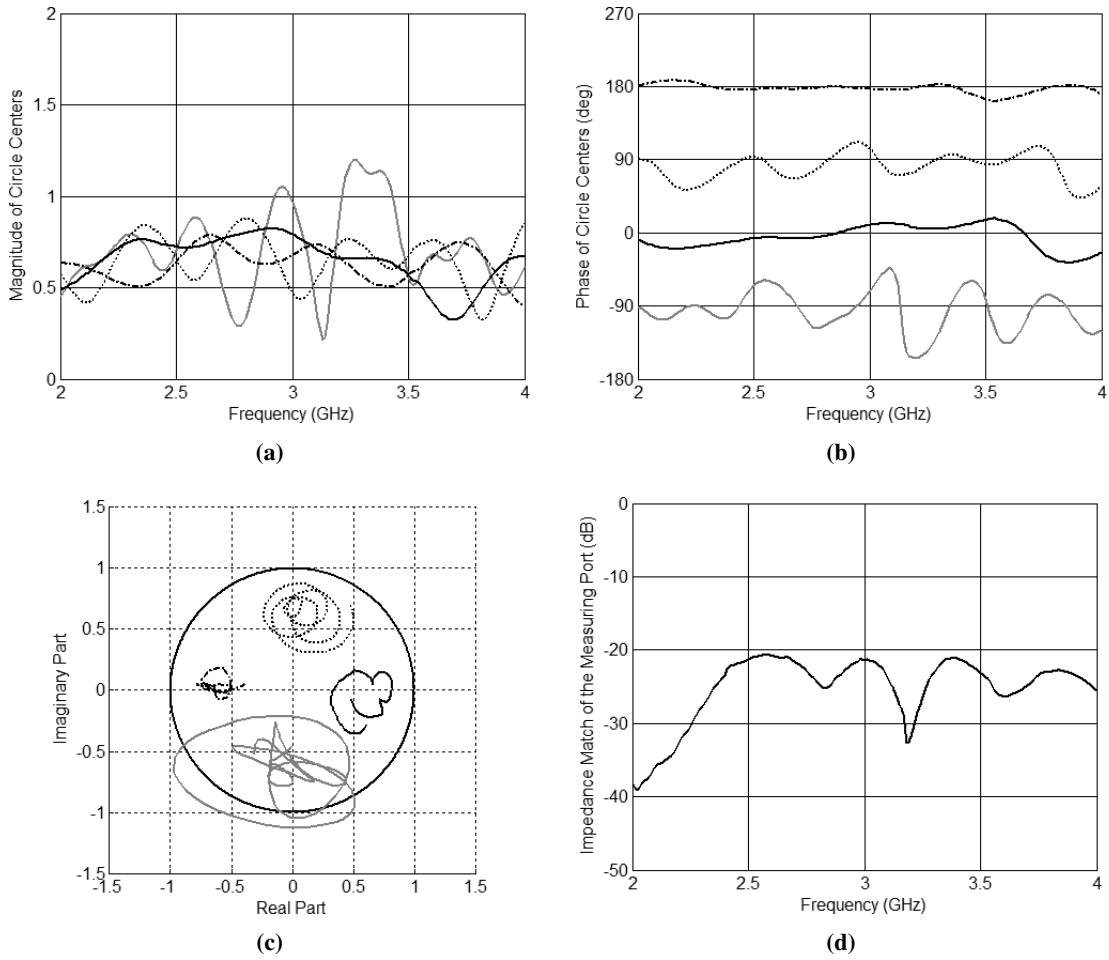


**Figure 4.9:** Results of the calibration procedure for the tunable measuring system with isolator described in Subsection 4.1.1 for theoretical magnitude of circle centers' distribution equal to 0.63: magnitude (a) and phase (b) of circle centers, circle centers' distribution on a complex plane (c) and the magnitude of reflection coefficient seen at the measuring port (d). The additional circle center resulting from the use of the additional coupler is marked gray.

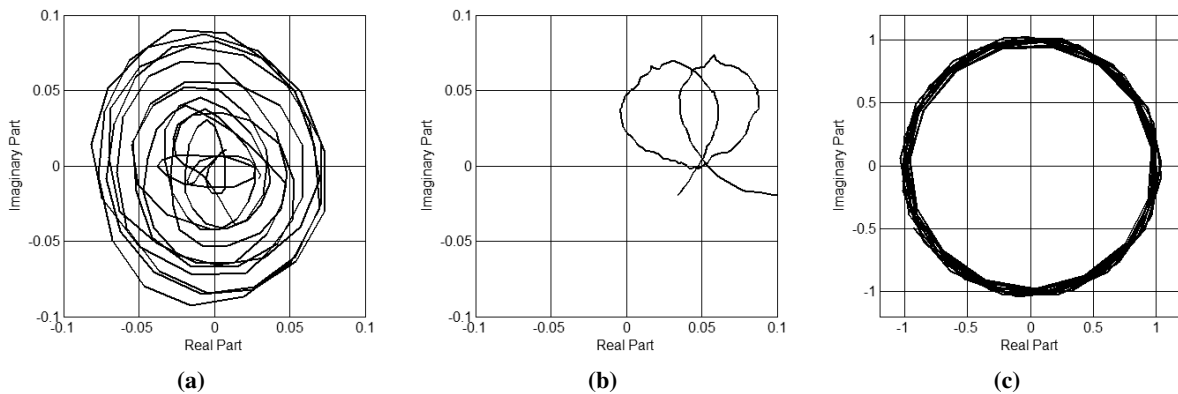


**Figure 4.10:** Results of the calibration procedure of the tunable measuring system with isolator described in Subsection 4.1.1 for transmission coefficient measurements. Calibration constants  $A$  (a),  $B$  (b) and  $C$  (c) vs. frequency.

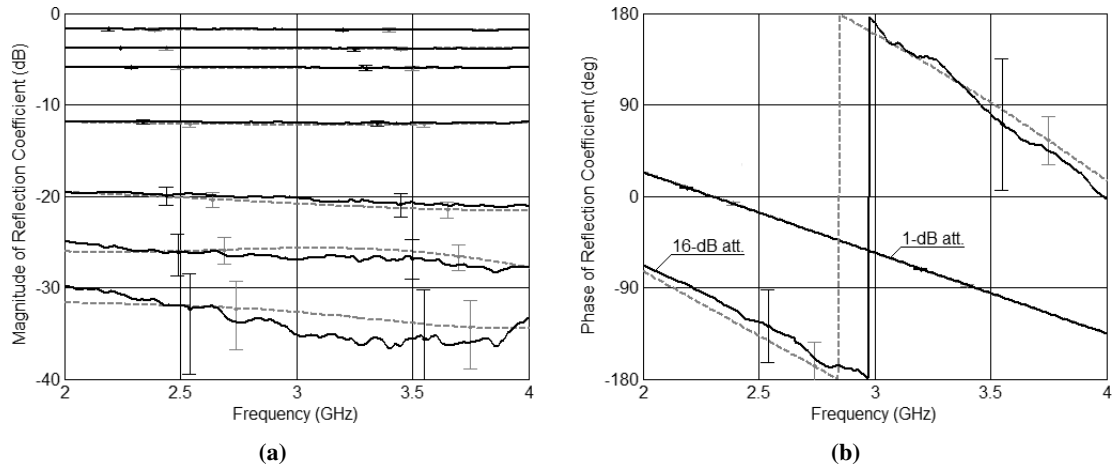


**Figure 4.11:** Reflection coefficients of a set of attenuators terminated with a short-circuit measured using the tunable measuring system with isolator described in Subsection 4.1.1: magnitude (a) and phase (b). Solid lines represents the measurements obtained with the use of the presented system, dashed lines correspond to the reference values.

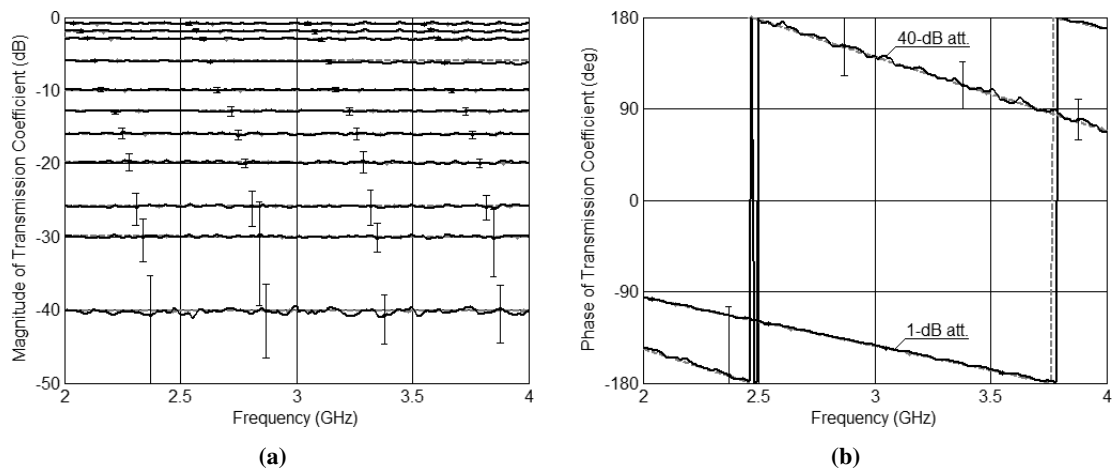


**Figure 4.12:** Transmission coefficients of a set of attenuators measured using the tunable measuring system with isolator described in Subsection 4.1.1: magnitude (a) and phase (b). Solid lines represents the measurements obtained with the use of the presented system, dashed lines correspond to the reference values.

The obtained results are very close to the reference values in a wide range of the measured  $S$ -parameters' magnitude. As it can be observed in Fig. 4.7, 4.8 and 4.9, the circle centers' distribution is distinctly deteriorated, therefore, the enhancement of the measurement accuracy for values shown in Fig. 4.11 and 4.12 is not significant. The advantage of the scalable circle centers' distribution can be shown more clearly for the measurement of  $S$ -parameters having smaller magnitudes. Therefore, the bandpass filter has been measured and the results are illustrated in Fig. 4.13. It is seen that if the magnitudes of the measured values are higher than -30 dB the obtained measurement results are in a very good agreement with the reference values in terms of both magnitude and phase. For smaller magnitudes some discrepancy occurs. Analyzing Fig. 4.13c one can see that smaller magnitude of circle centers' distribution ensures higher accuracy of the obtained results. For the theoretical magnitude of 1.00 (0 dB attenuation) the measurements of values having magnitude lower than -30 dB become inaccurate.

However, if attenuation of the attenuator A is set to 2 dB, which corresponds to theoretical magnitude of circle centers' distribution of 0.63, this limit is decreased to -55 dB. As long as the measured magnitude is not smaller than -55 dB also the phase is measured correctly. It is seen, therefore, that the scalable circle centers' distribution has extended the measurement dynamic by 25 dB [87].

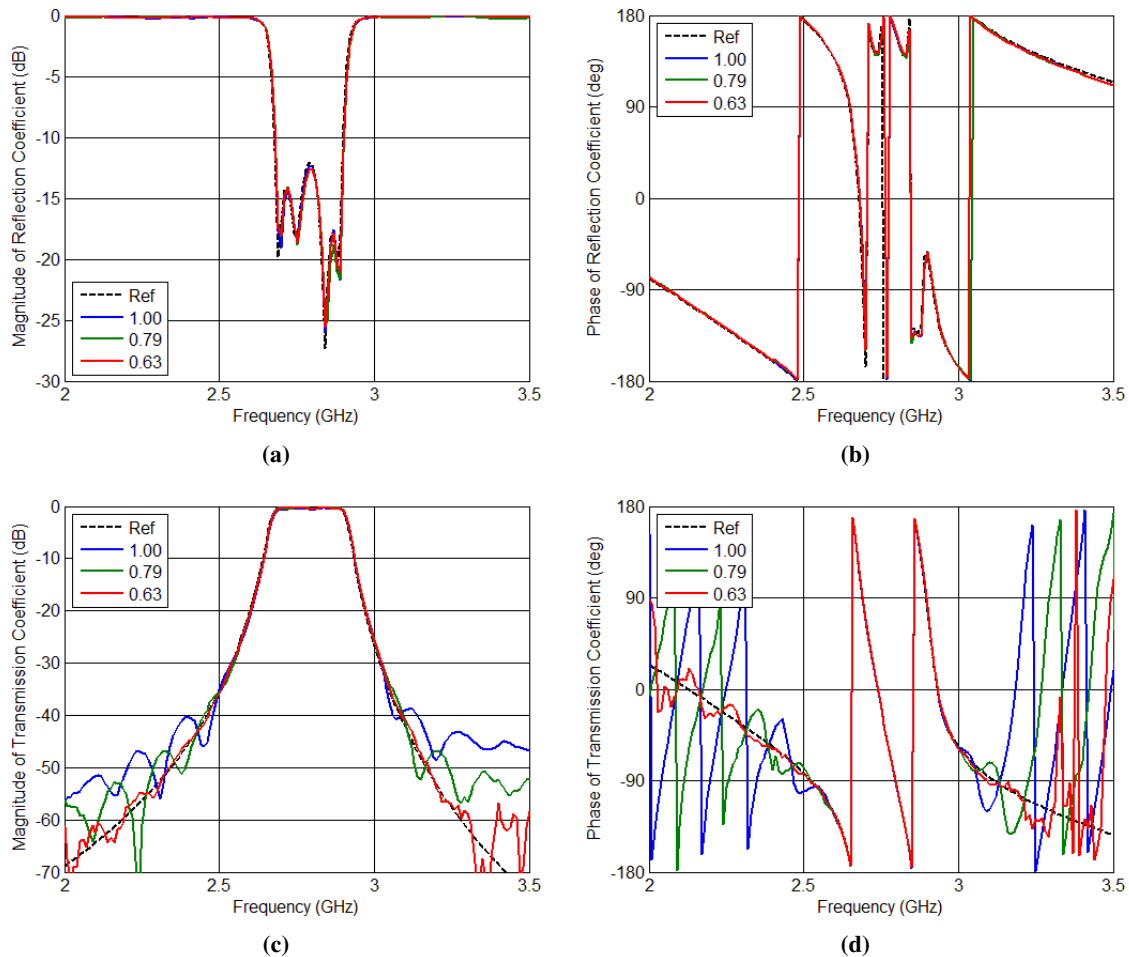


**Figure 4.13:** *S*-parameters of the bandpass filter measured using the tunable measuring system with isolator described in Subsection 4.1.1: magnitude (a) and phase (b) of reflection coefficient and magnitude (c) and phase (d) of transmission coefficient. The measurement results have been obtained for three different magnitudes of circle centers' distribution: 1.00, 0.79 and 0.63. Solid lines represents the measurements obtained with the use of the presented system, dashed lines correspond to the reference values [87]. (Copyright © 2015, IEEE)

#### 4.5.2. Broadband Measuring System Without Isolator

The tunable measuring system without an isolator described in Subsection 4.2.1 has been developed for an experimental verification. As the directional coupler  $Q_1$ , the coupled-line multisection directional coupler shown in [34] has been utilized. It features the nominal coupling being equal to 8.34 dB and operates in the frequency range 1 – 5 GHz. Since that coupler is used for the reference power measurement, a low coupling level is advantageous. The 3-dB directional coupler described in Subsection 4.5.1 [35], operating in the same frequency range has been used as the coupler  $Q_2$ . For the signals' summation the broadband  $4 \times 4$  Butler matrix described in Subsection 2.5.3 [36] has been applied.

The system has been calibrated utilizing two separate calibration procedures for five different sets of the adjustable attenuator, which provide the scalability of the circle centers' distribution. The applied attenuations with corresponding theoretical magnitudes of circle centers' distributions for reflection and transmission coefficients measurements are listed in Table 4.4. Calibration for reflection coefficient measurements has been done following the procedure described in Sections 2.3, whereas for transmission coefficient measurements the system has been calibrated according to the procedure given in Subsection 3.1.2. The obtained results are illustrated in Fig. 4.14 – 4.23.

**Table 4.4:** Attenuations of the adjustable attenuator and corresponding theoretical magnitude of circle centers' distributions for reflection and transmission coefficient measurements.

Attenuation for reflection coefficient measurement (dB)	Attenuation for transmission coefficient measurement (dB)	Theoretical magnitude of circle centers' distribution (linear scale)
3	0	1.00
4	1	0.89
5	2	0.79
6	3	0.71
9	6	0.50

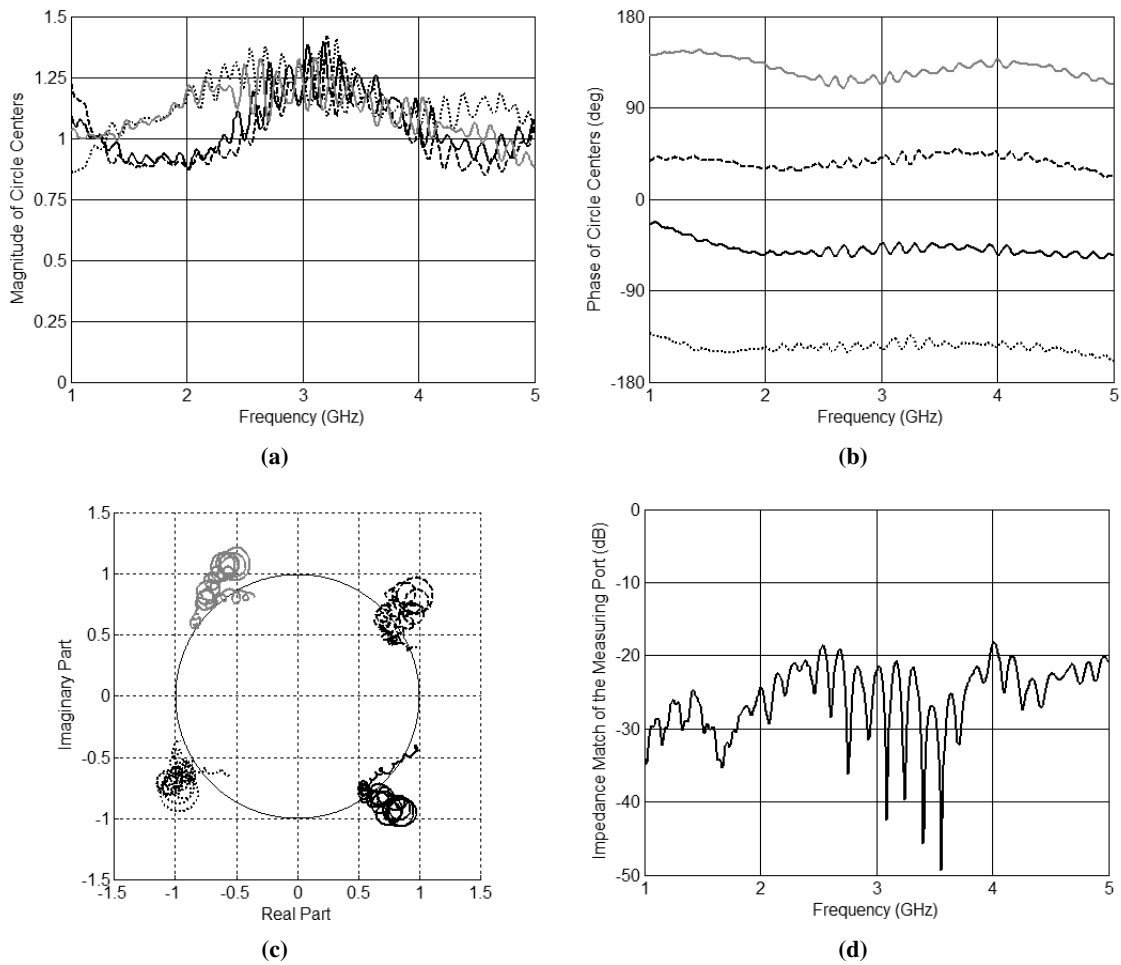


**Figure 4.14:** Results of the calibration procedure for reflection coefficient measurements utilizing the tunable measuring system without isolator described in Subsection 4.2.1 for theoretical magnitude of circle centers' distribution equal to 1: magnitude (a) and phase (b) of circle centers, circle centers' distribution on a complex plane (c) and the magnitude of reflection coefficient seen at the measuring port (d).

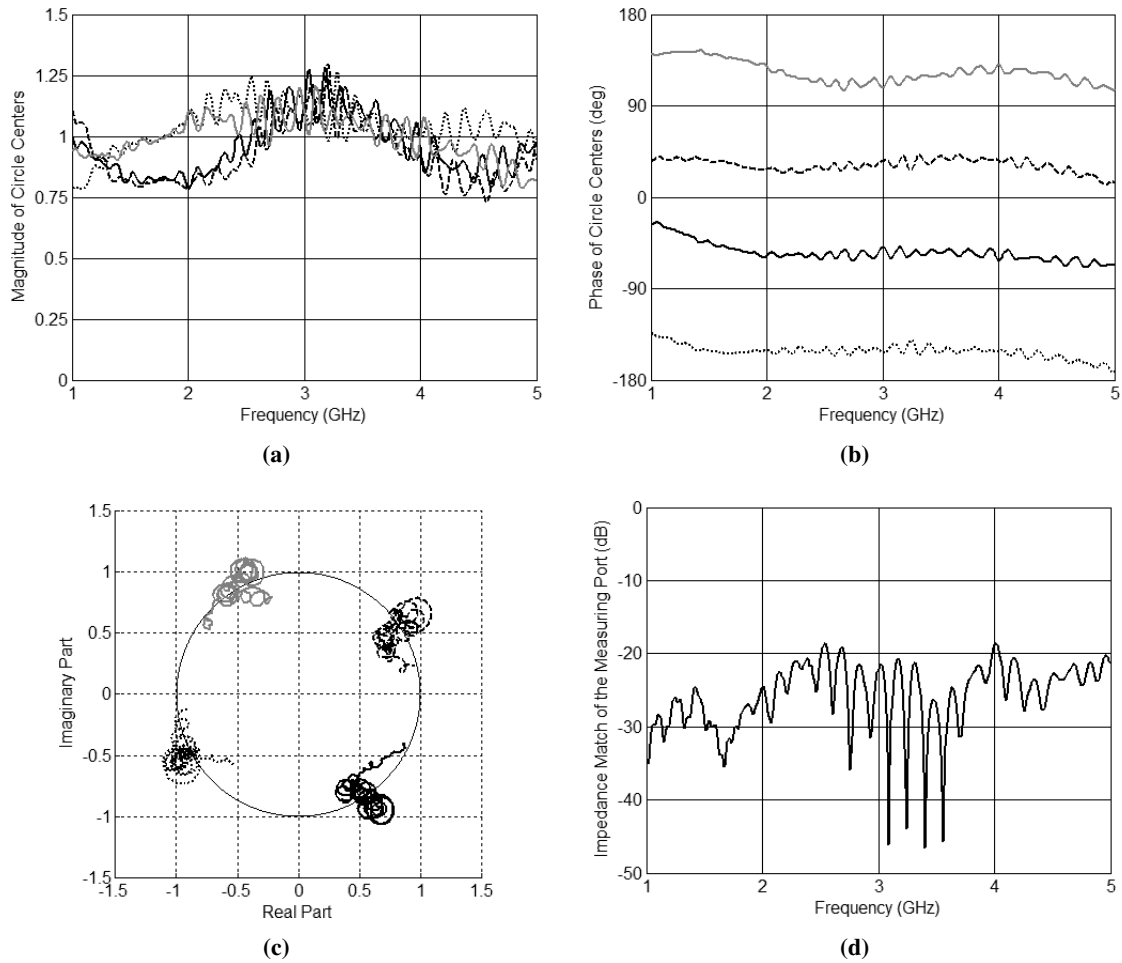


**Figure 4.15:** Results of the calibration procedure for reflection coefficient measurements utilizing the tunable measuring system without isolator described in Subsection 4.2.1 for theoretical magnitude of circle centers' distribution equal to 0.89: magnitude (a) and phase (b) of circle centers, circle centers' distribution on a complex plane (c) and the magnitude of reflection coefficient seen at the measuring port (d).

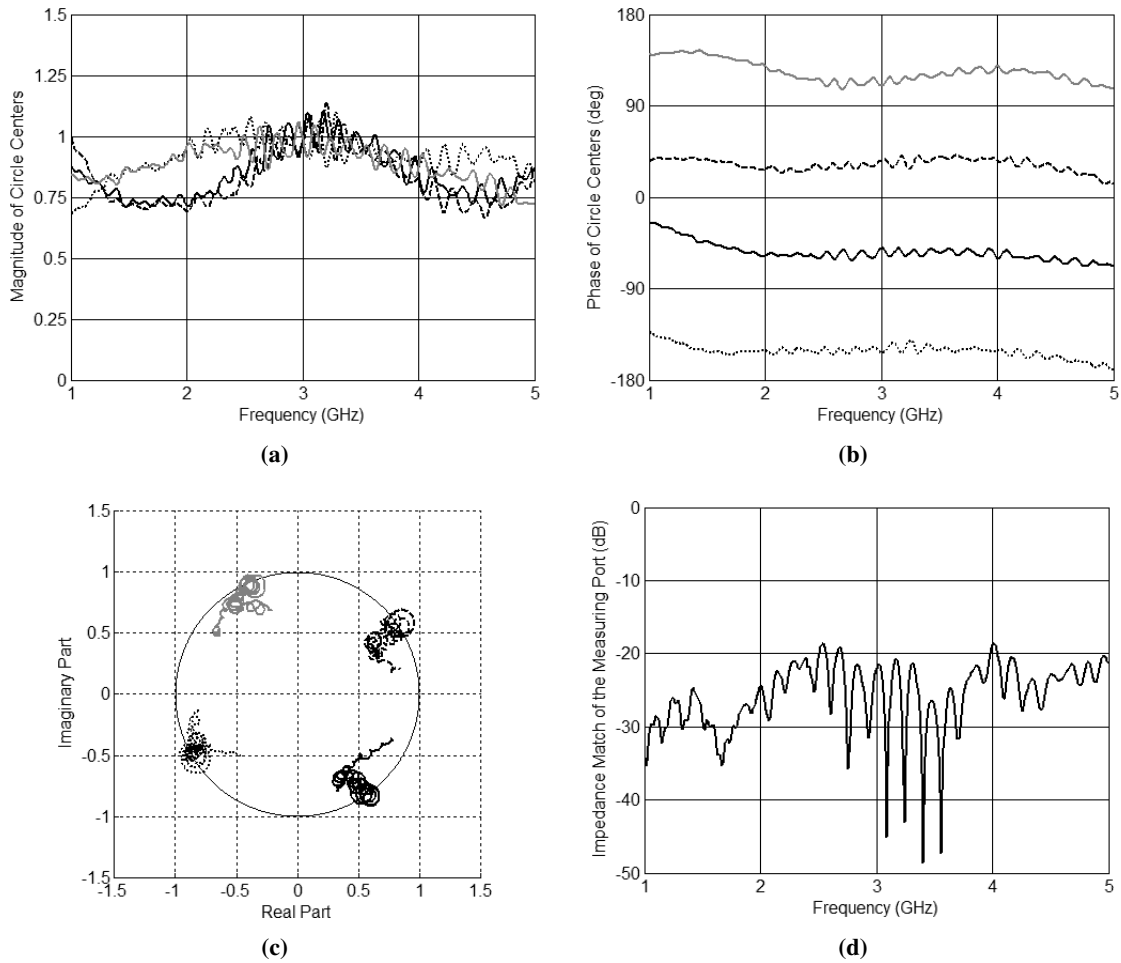


**Figure 4.16:** Results of the calibration procedure for reflection coefficient measurements utilizing the tunable measuring system without isolator described in Subsection 4.2.1 for theoretical magnitude of circle centers' distribution equal to 0.79: magnitude (a) and phase (b) of circle centers, circle centers' distribution on a complex plane (c) and the magnitude of reflection coefficient seen at the measuring port (d).

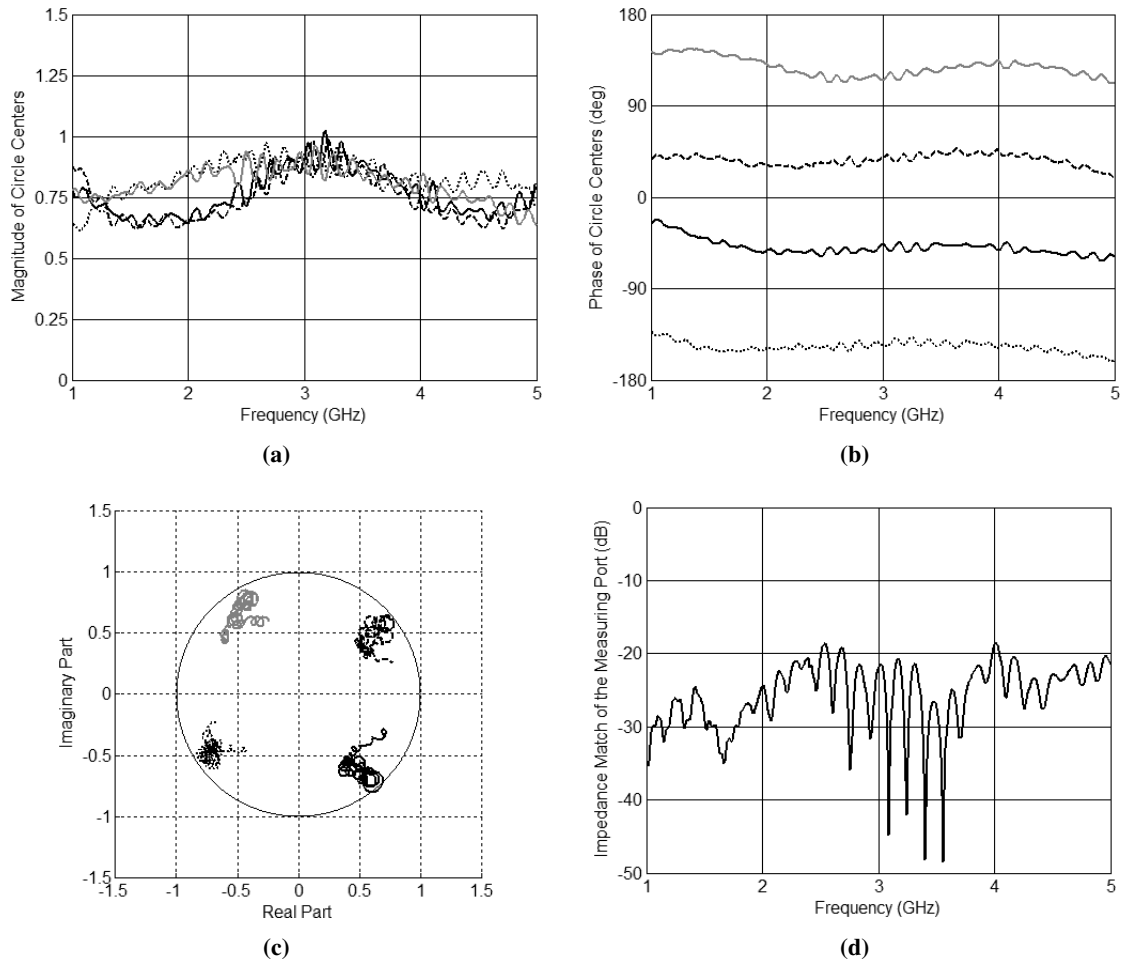


**Figure 4.17:** Results of the calibration procedure for reflection coefficient measurements utilizing the tunable measuring system without isolator described in Subsection 4.2.1 for theoretical magnitude of circle centers' distribution equal to 0.71: magnitude (a) and phase (b) of circle centers, circle centers' distribution on a complex plane (c) and the magnitude of reflection coefficient seen at the measuring port (d).

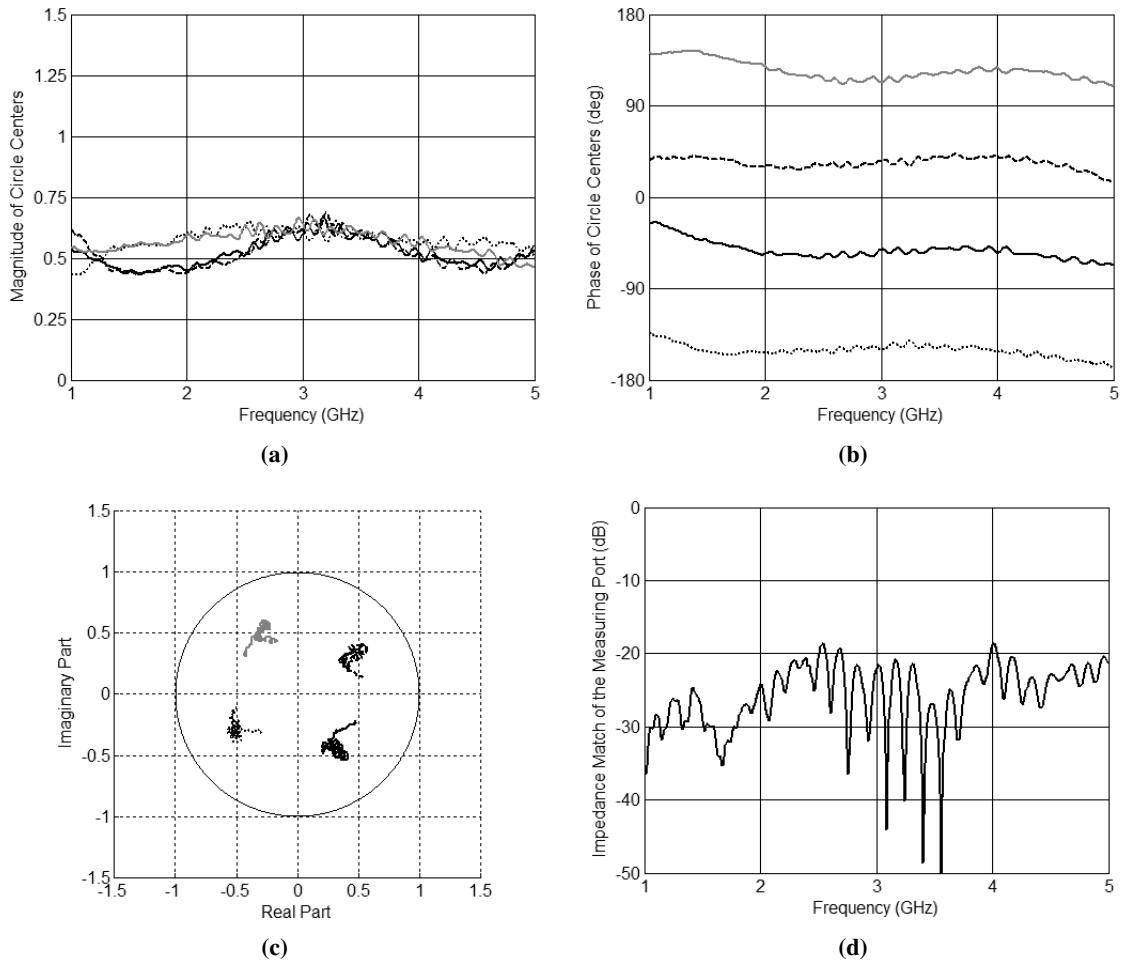


**Figure 4.18:** Results of the calibration procedure for reflection coefficient measurements utilizing the tunable measuring system without isolator described in Subsection 4.2.1 for theoretical magnitude of circle centers' distribution equal to 0.50: magnitude (a) and phase (b) of circle centers, circle centers' distribution on a complex plane (c) and the magnitude of reflection coefficient seen at the measuring port (d).

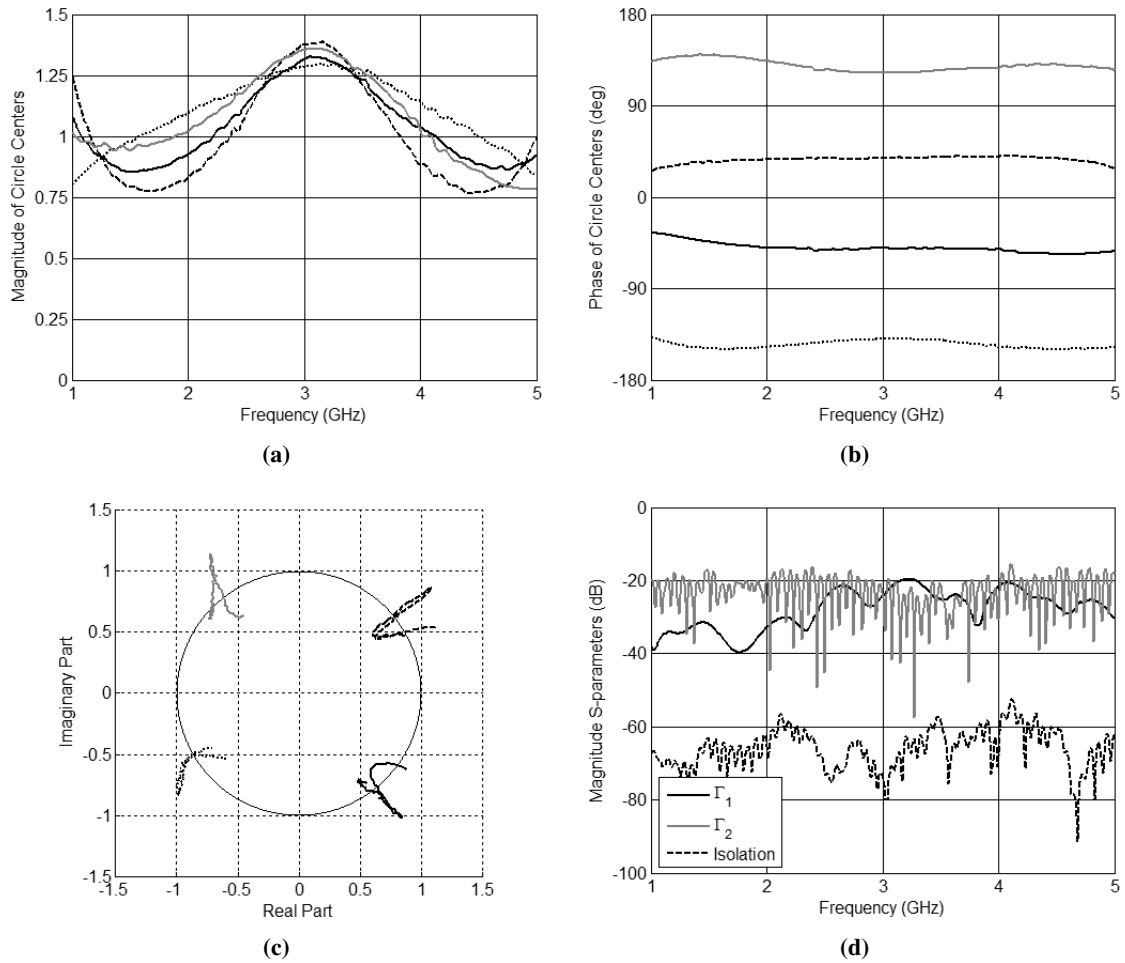


**Figure 4.19:** Results of the calibration procedure for transmission coefficient measurements utilizing the tunable measuring system without isolator described in Subsection 4.2.1 for theoretical magnitude of circle centers' distribution equal to 1: magnitude (a) and phase (b) of circle centers, circle centers' distribution on a complex plane (c), impedance match of the measuring ports and isolation between measuring ports (d).

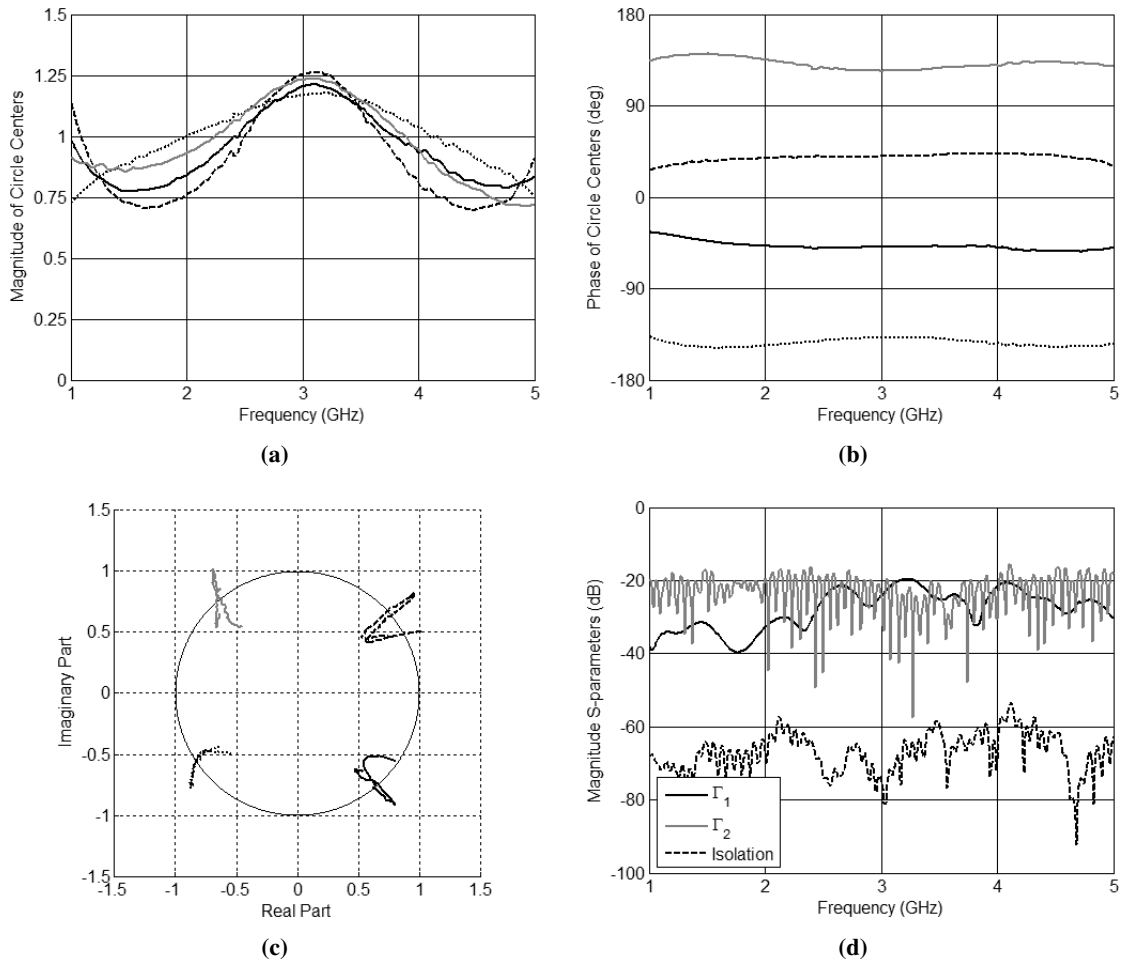


**Figure 4.20:** Results of the calibration procedure for transmission coefficient measurements utilizing the tunable measuring system without isolator described in Subsection 4.2.1 for theoretical magnitude of circle centers' distribution equal to 0.89: magnitude (a) and phase (b) of circle centers, circle centers' distribution on a complex plane (c), impedance match of the measuring ports and isolation between measuring ports (d).

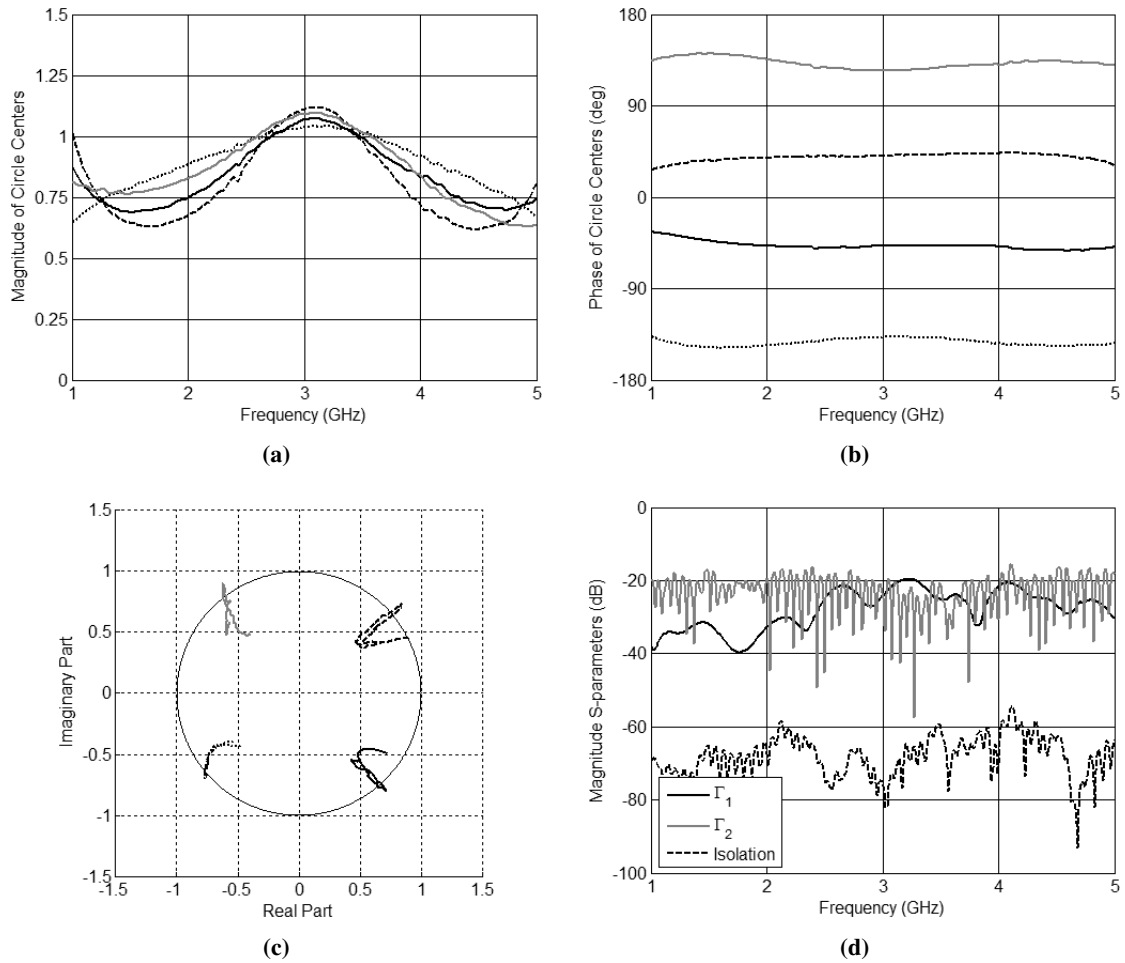


**Figure 4.21:** Results of the calibration procedure for transmission coefficient measurements utilizing the tunable measuring system without isolator described in Subsection 4.2.1 for theoretical magnitude of circle centers' distribution equal to 0.79: magnitude (a) and phase (b) of circle centers, circle centers' distribution on a complex plane (c), impedance match of the measuring ports and isolation between measuring ports (d).

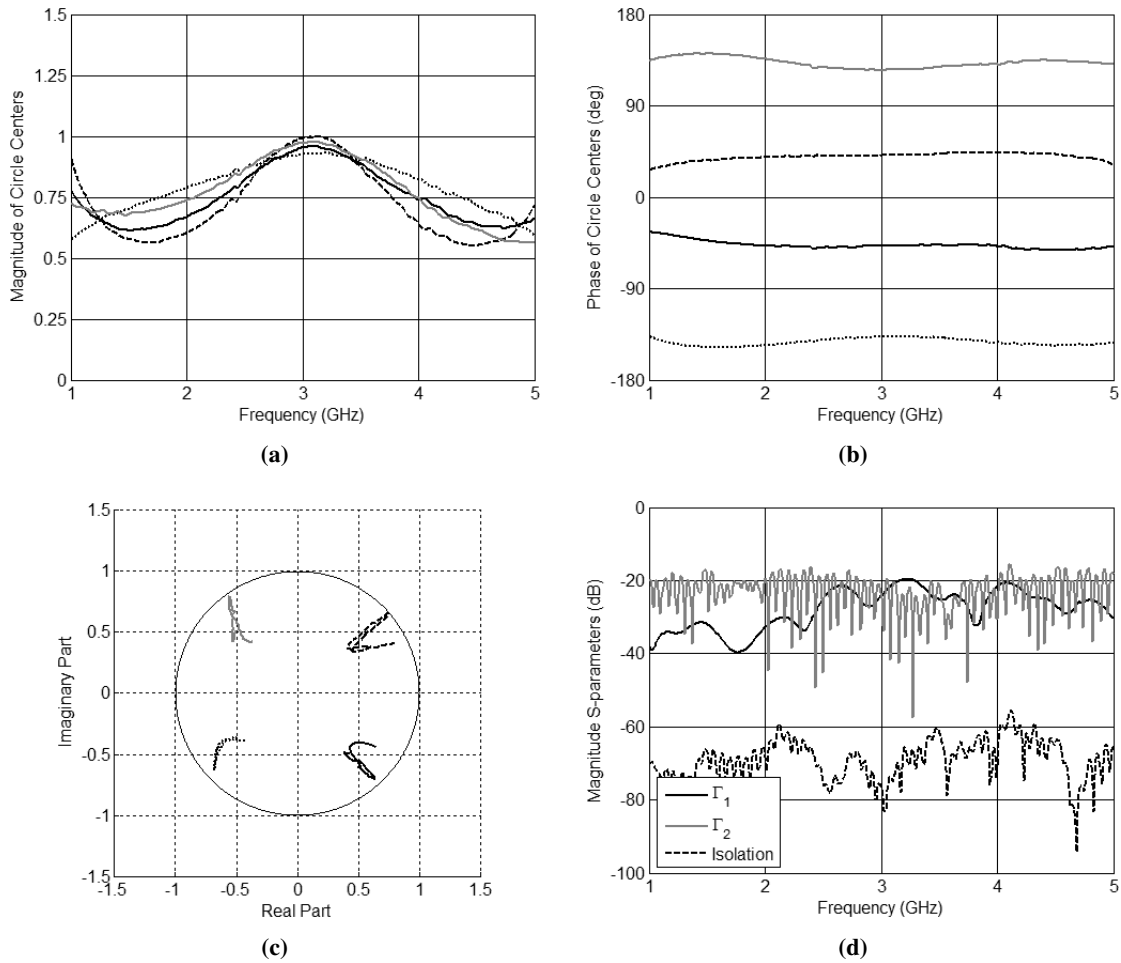


**Figure 4.22:** Results of the calibration procedure for transmission coefficient measurements utilizing the tunable measuring system without isolator described in Subsection 4.2.1 for theoretical magnitude of circle centers' distribution equal to 0.71: magnitude (a) and phase (b) of circle centers, circle centers' distribution on a complex plane (c), impedance match of the measuring ports and isolation between measuring ports (d).

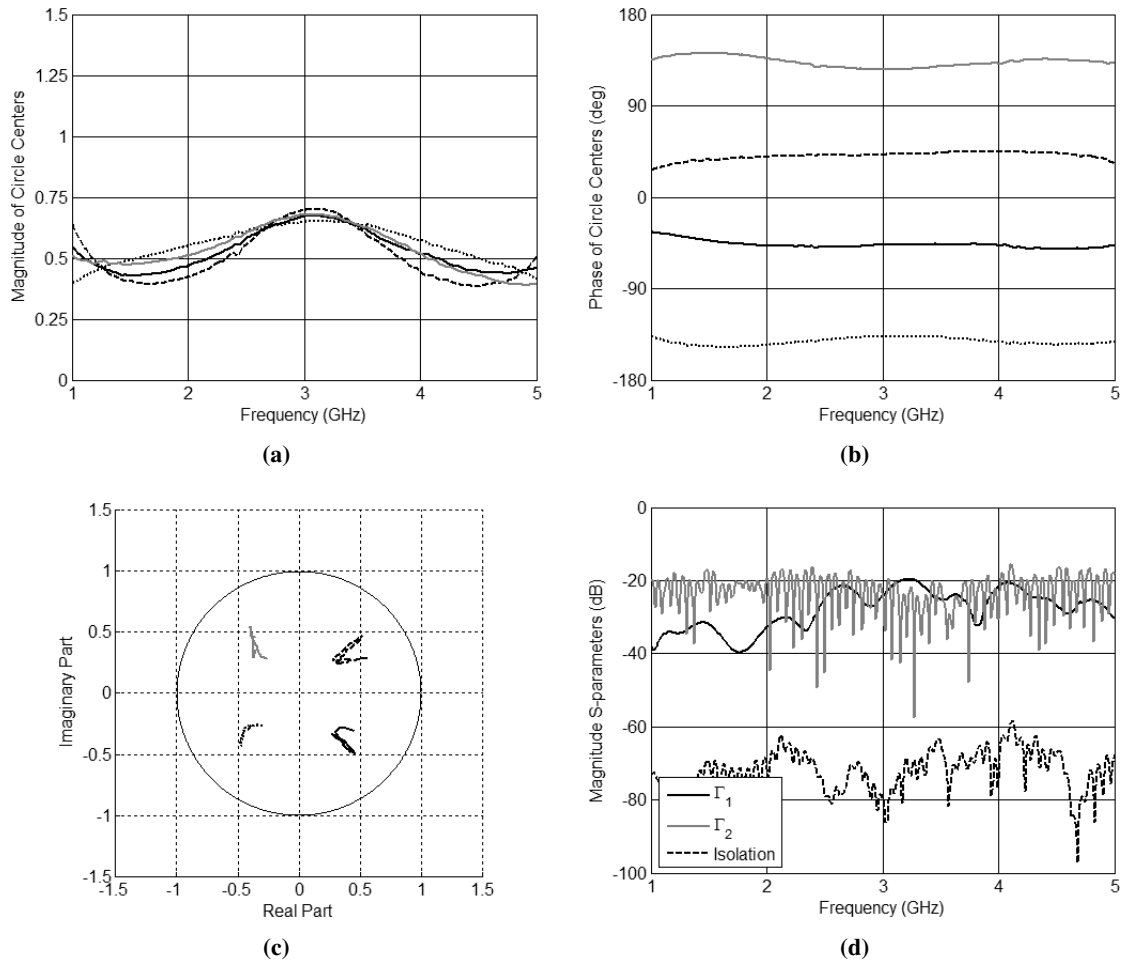


**Figure 4.23:** Results of the calibration procedure for transmission coefficient measurements utilizing the tunable measuring system without isolator described in Subsection 4.2.1 for theoretical magnitude of circle centers' distribution equal to 0.50: magnitude (a) and phase (b) of circle centers, circle centers' distribution on a complex plane (c), impedance match of the measuring ports and isolation between measuring ports (d).

As it can be observed for both calibrations, regardless of the chosen attenuation of the adjustable attenuator, a highly uniform arrangement of the circle centers has been achieved. The obtained circle centers' distributions allow for proper measurements of scattering parameters. Moreover, the isolation between measuring ports is not worse than 55 dB in the entire considered frequency range. As it is shown in Fig. 3.4, such a level of isolation introduces power measurement error being at least ten times lower than the one resulting from the power meters inaccuracy. Therefore, the proposed simplification can be applied in the developed measuring system. Moreover, as presented in Fig. 3.5, the obtained impedance match of both measuring ports allows for using the simplified formula (3.5) for the measured transmission coefficients.

The measurements of  $S$ -parameters have been done for all five circle centers' distributions. Further, similarly as in Subsection 4.5.1, from each five results corresponding to a particular measurement, the measurement results featuring the highest accuracy have been chosen. They are presented in Fig. 4.24 and 4.25.

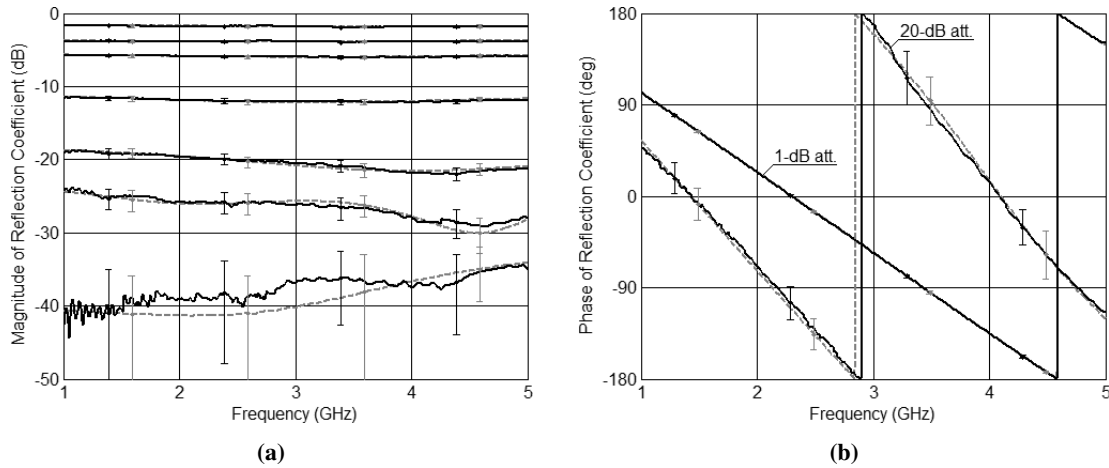


**Figure 4.24:** Reflection coefficients of a set of attenuators terminated with a short-circuit measured using the tunable measuring system without isolator described in Subsection 4.2.1: magnitude (a) and phase (b). Solid lines represents the measurements obtained with the use of the presented system, dashed lines correspond to the reference values.

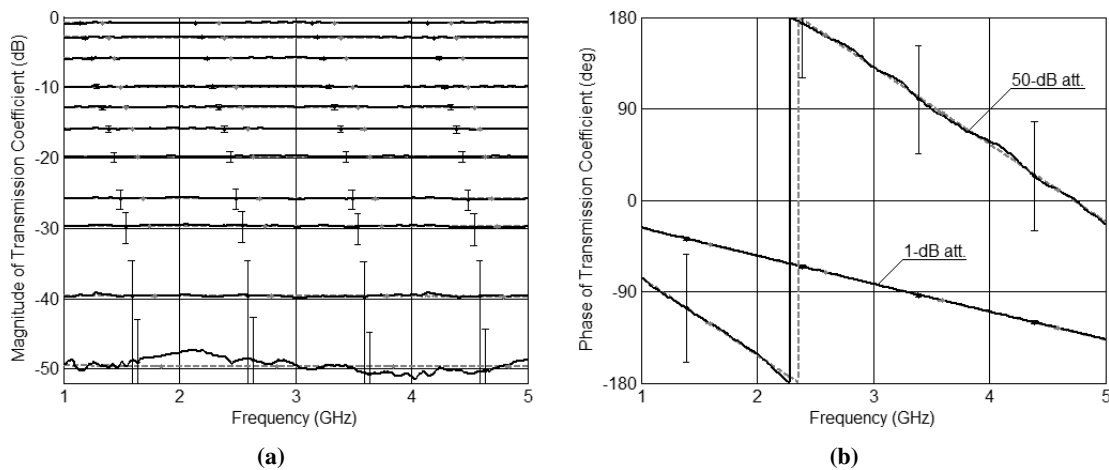


**Figure 4.25:** Transmission coefficients of a set of attenuators measured using the tunable measuring system without isolator described in Subsection 4.2.1: magnitude (a) and phase (b). Solid lines represents the measurements obtained with the use of the presented system, dashed lines correspond to the reference values.

It is seen that the obtained results are in a very good agreement with the reference values in the 50 dB range of measured values' magnitude. It must be underlined that the discrepancy between the measurement results and the reference values occurring for reflection coefficients having small magnitude results from different techniques of calibration. In the calibration procedure utilized for calibration of VNA it is assumed, that the applied matched load is ideal, whereas the calibration described in Section 2.3 takes into account the imperfection of the utilized matched load. This effect does not occur in transmission coefficient, for which the utilized vector network analyzer features very small inaccuracy (the errorbars for reference values are barely seen in Fig. 4.25). Therefore, to observe reduction of the measurement error resulting from the scalable circle centers' distribution the transmission coefficient measurements are more appropriate. In Fig. 4.26 the transmission coefficient of the attenuator having

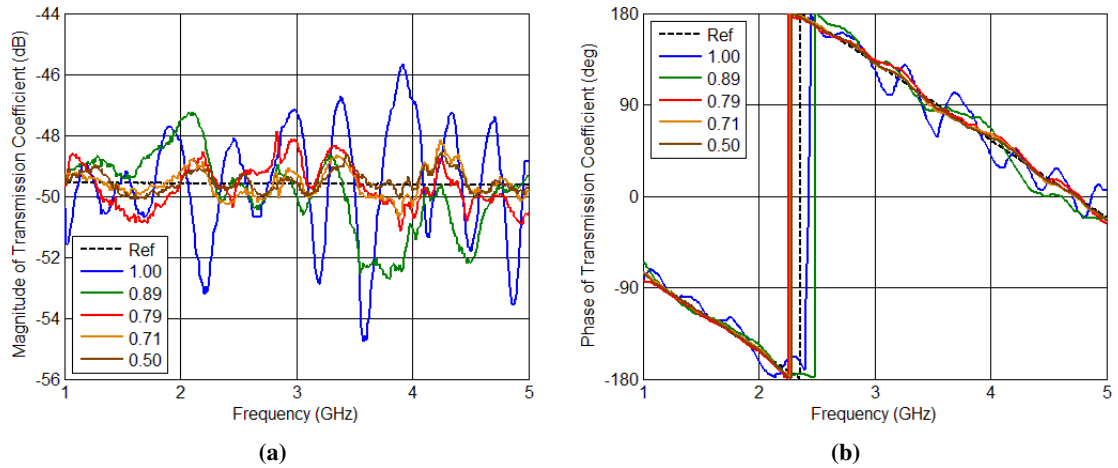


**Figure 4.26:** Transmission coefficients of the attenuator having attenuation of 50 dB measured with different magnitudes of circle centers' distribution. Solid lines represents the measurements obtained with the use of the presented system, dashed line corresponds to the reference values.

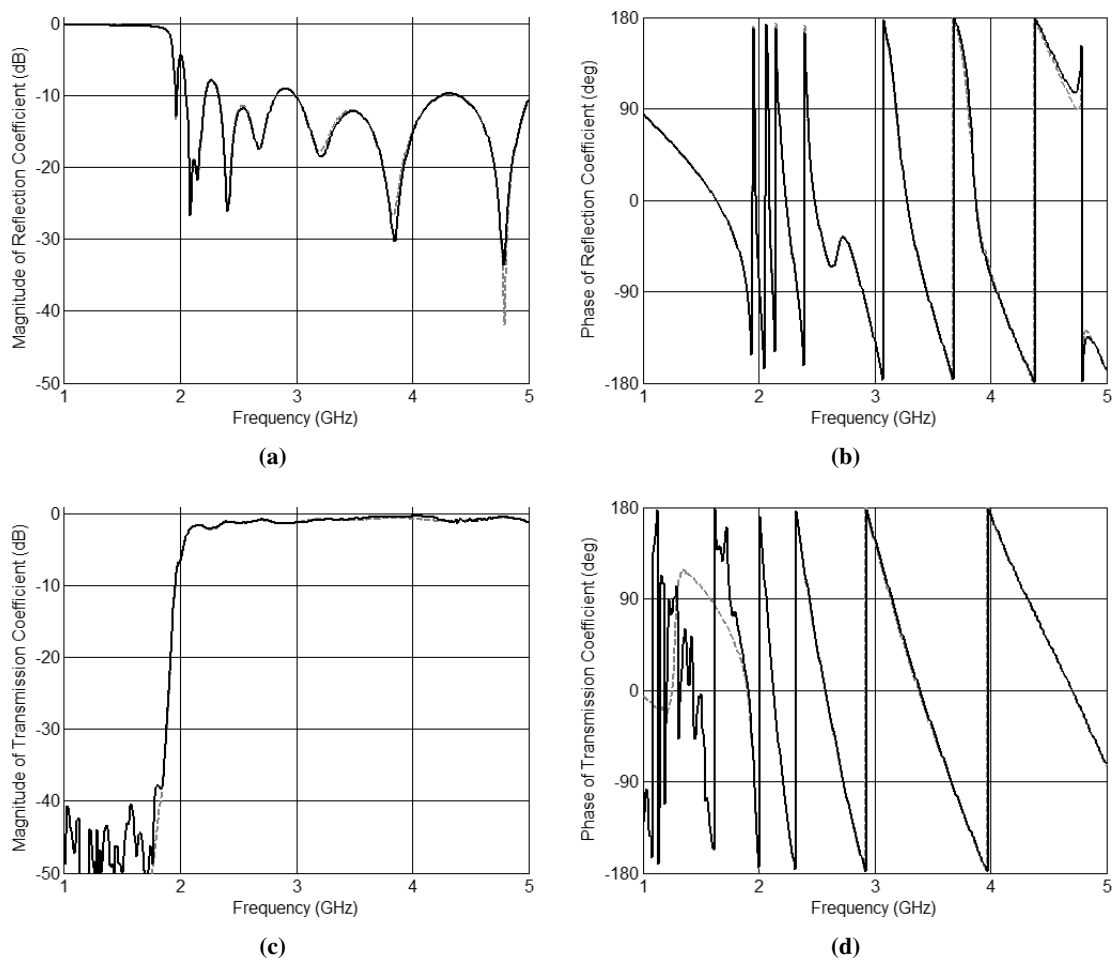


**Figure 4.27:**  $S$ -parameters of the highpass filter measured using the tunable measuring system without isolator described in Subsection 4.2.1: magnitude (a) and phase (b) of reflection coefficient and magnitude (c) and phase (d) of transmission coefficient. Solid lines represents the measurements obtained with the use of the presented system, dashed lines correspond to the reference values.

attenuation of 50 dB measured with different magnitudes of circle centers' distribution is shown. The magnitude and phase measurement errors for the circle centers' distribution having magnitude equal to 1 are 5.1 dB and  $32.8^\circ$ , respectively. For the magnitude of circle centers' distribution decreased to the value of 0.50 these errors become 1.1 dB and  $6.0^\circ$ . As a result one can state that the application of the scalable circle centers' distribution has allowed for increasing the measurement accuracy five times. Further the investigated measuring system has been examined by *S*-parameter measurements of a highpass filter. The achieved results are presented in Fig. 4.27.

The measurement results are very close to the reference values obtained with the use of vector network analyzer. The negligible discrepancy between measured *S*-parameters and the reference values, as well as the distortion of the transmission coefficient for magnitudes smaller than 35 dB are caused by two major factors: (i) utilization of the non-ideal SMA adapter, which was necessary to connect the measured filter to the measuring system, and (ii) imperfect matched load featuring  $VSWR \approx 1.1$  which has been used for filter termination in reflection coefficient measurement. Nevertheless, the proposed measuring system allows for precise measurements of *S*-parameters having magnitude not smaller than -35 dB, which is more than sufficient in many practical applications.

### 4.5.3. Analysis of Measurement Results

The experimental verification presented in Subsections 4.5.1 and 4.5.2 confirms that the application of scalable circle centers' distribution in multiport measurements of *S*-parameters enhances the measurement accuracy. Two measuring systems have been examined, however, the first one presented in Subsection 4.1.1 features a significant deterioration of the circle centers' distribution obtained in calibration procedure with respect to the theoretical assumptions. Therefore, the analysis of measurement accuracy described in further part of this Subsection is limited only to the second system, i.e. tunable measuring system without isolator presented in Subsection 4.2.1.

To elaborate the system performance the maximum magnitude and phase measurement errors vs. the magnitude of the measured *S*-parameters have been calculated using the reference results obtained with VNA. It is seen in Fig. 4.28 4.29, that the scalable circle centers' distribution significantly improves the measurement accuracy for both reflection and transmission coefficient measurements. In general the presented maximum magnitude and phase measurement errors for both reflection and transmission coefficient measurements clearly correspond to the theoretical predictions shown in Fig. 4.4, nevertheless, some discrepancy is seen. It must be emphasized that the theoretical predictions shown in Fig. 4.4 have been estimated assuming precisely known circle centers' distribution. However, in practical measuring systems the circle centers' distribution is calculated in the calibration procedure, which always introduces inaccuracy due to the power measurement error. Furthermore, as seen in Fig. 4.24 the vector network analyzer used for measuring the reference values features the inaccuracy being comparable to the proposed system. Hence, the measurement error shown in Fig. 4.28 is not the difference between measured and genuine values of the reflection coefficients, but in fact is the difference between measured values and the reference values which are somehow deteriorated. The good agreement between theoretically calculated measurement error and the experimentally obtained measurement error

is clearly seen in case of transmission coefficient measurements. In Fig. 4.25 it is seen, that the utilized VNA features significantly lower measurement inaccuracy comparing to the proposed measuring system. Since the reference values are very close to the genuine ones, the calculated measurement error shown in Fig. 4.29 is in agreement with the theoretical assumption presented in Fig. 4.4. Finally, as described in Section 2.4, the measurement accuracy strictly depends on the circle centers' distribution. The measurements have been performed within the frequency range covering more than 2 octaves, hence, some deterioration of circle centers' location occurs. Since each circle center fluctuates independently, the mutual arrangement of these four points somehow changes in terms of frequency, which affects the measurement accuracy. Therefore, the maximum measurement errors insignificantly differ from the estimated ones.

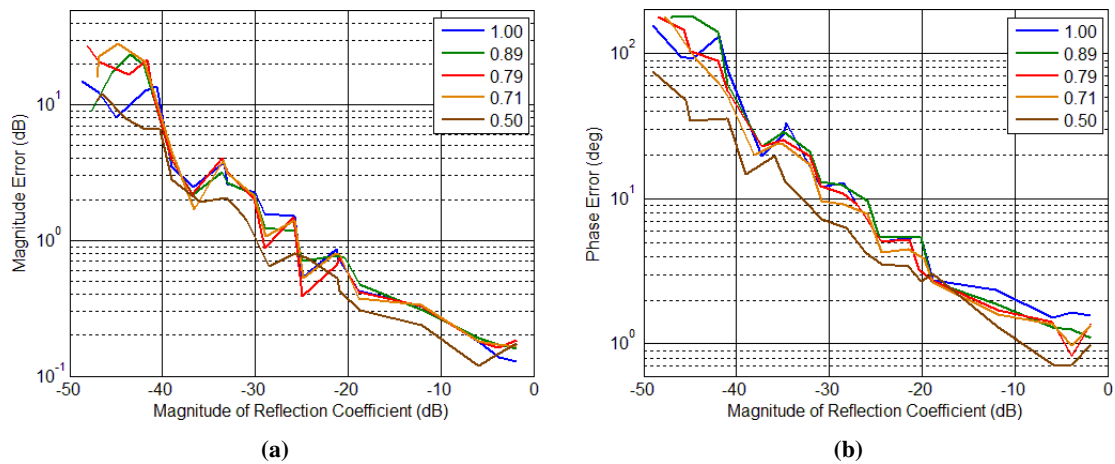


**Figure 4.28:** Maximum magnitude (a) and phase (b) measurement error vs. the magnitude of the measured reflection coefficient for the broadband tunable measuring system without isolator described in Subsection 4.5.2.

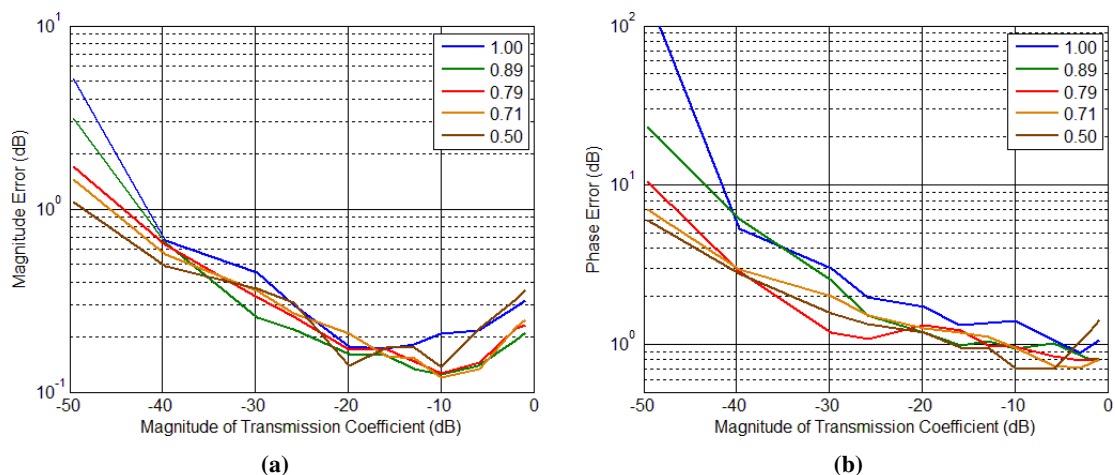


**Figure 4.29:** Maximum magnitude (a) and phase (b) measurement error vs. the magnitude of the measured transmission coefficient for the broadband tunable measuring system without isolator described in Subsection 4.5.2.

## 4.6. Conclusions

In this Chapter, the analysis of scalable circle centers' distribution in multiport measurements of *S*-parameters has been presented. Two systems allowing for broadband measurements of both reflection and transmission coefficients have been shown, in which the application of an adjustable attenuator provides the scalability of circle centers' distribution. For both systems the magnitude and phase measurement error distribution in terms of the magnitude of circle centers' distribution has been estimated. As shown in this Chapter, shifting circle centers towards the origin of a complex plane allows for a significant decrease of the magnitude measurement error. Moreover, by an appropriate choice of the circle centers' distribution the phase measurement error characteristic can be shifted in such a way, that its minimum is related to the measured values, providing the maximum measurement accuracy. Such an approach is advantageous, since the phase error increases very rapidly for lower and higher magnitudes of measured scattering parameters. Apart from the measurement accuracy analysis, the verification of calibration accuracy has been performed. It has been presented that the multiport systems having circle centers located close to the origin of a complex plane can be calibrated more accurately. Hence, the scalability of circle centers' distribution enhances both measurement and calibration accuracy.

The concept of the scalable circle centers' distribution has been experimentally verified by scattering parameter measurements with the use of two broadband multiport systems analyzed theoretically in this Chapter. Both proposed systems feature an advantageous power distribution, which can be appropriately tuned in order to enhance the measurement accuracy for the measurement of *S*-parameters having small magnitudes. The measurement results show a very good agreement with the ones obtained using a commercial VNA. Moreover, by the application of the scalable circle centers' distributions a significant enhancement of the measurement accuracy has been achieved for reflection and transmission coefficient measurements over the entire considered frequency range, which proves the usability of the proposed concept of the multiport measuring systems featuring scalable circle centers' distribution.

## 5. Summary

In this Thesis the application of Butler matrices in scattering parameter measurements with the use of multiport techniques has been presented. Several novel multiport systems have been proposed, in which instead of dedicated multiport power distribution networks the Butler matrices have been utilized. It has been shown that the measuring systems involving Butler matrices not only allow for the *S*-parameter measurements, but also provide higher measurement accuracy comparing to the accuracy of the classic solutions utilizing six-port reflectometers. The enhancement of measurement accuracy has been theoretically investigated and has been confirmed in practical measurements. It is worth mentioning that, besides the increased measurement accuracy, the application of Butler matrices in multiport measurement technique has several advantages. First, the Butler matrices comprise well-known and easily available microwave components. Such commonness results in many techniques of fabrications, including miniaturized structures. Additionally, the Butler matrix-based measuring systems feature in general higher number of possible system configurations, which can be utilized for enhancement of the measurement accuracy. Such feature does not occur in case of classic reflectometers, in case of which only one possible system arrangement is possible. Finally, Butler matrices can be realized with the use of multisection coupled-line directional couplers providing very broad bandwidth.

The performed analysis of the developed systems has revealed that the measuring systems, in which the Butler matrices are applied, can be calibrated using the same methods as classic multiport systems. However, to increase the measurement accuracy three novel calibration procedures have been proposed by the Author. They allow for broadband calibration for both reflection and transmission coefficient measurements. Each procedure is based on a least-squares approach and can be applied for an arbitrary number of calibration standards and for multiport systems having an arbitrary number of ports, at which the power is measured. Moreover, it has been shown that the calibration in the frequency range exceeding one decade can be done utilizing standard SMA adapters. The appropriate algorithms have been introduced.

A significant effort has been put into the analysis of the measurement accuracy. The performed studies of the geometrical interpretation of the scattering parameter measurements with the use of multiport techniques have revealed that the systems, in which Butler matrices are applied feature the circle centers' distribution being close to optimal. Further research performed by the Author has led to the development of a novel class of measuring systems featuring scalable circle centers' distribution. The presented analysis has shown that by appropriate tuning of power distribution, what can be simply done by the application of an adjustable attenuator, the measurement accuracy can be significantly

increased. The theoretically developed concept has been experimentally confirmed in measurements of both reflection and transmission coefficients, proving the enhancement of the measurement accuracy provided by the developed measuring systems.

The original achievements of the Author presented in this Thesis can be summarized as follows:

- Development of the broadband six-port reflectometer utilizing single-section coupled-line directional couplers, published in [80].
- Development of the ultra-broadband six-port reflectometer incorporating multisection coupled-line directional couplers and the Magic-T circuit having the operational frequency range exceeding one decade, published in [86].
- Development of the broadband multipoint system utilizing two classic  $4 \times 4$  Butler matrices allowing for the broadband measurement of reflection and transmission coefficients, published in [79].
- Development of the ultra-broadband multipoint reflectometer utilizing the  $4 \times 4$  Butler matrix consisting of tapered-coupled-line directional couplers, published in [83].
- Development of the broadband measuring system involving the single  $8 \times 8$  Butler matrix, being capable of reflection and transmission coefficients measurements, published in [85].
- Theoretical proof, confirmed experimentally, that in measuring systems involving a single multipoint network only one isolator is required and their number can be reduced without any impairment of the measurement accuracy. Investigations published in [85].
- Development of the calibration procedure for reflection coefficient measurements applicable for arbitrary multipoint reflectometer, published in [89].
- Development of the algorithm for the optimal choice of calibration standards allowing for calibration of multipoint systems in multi-octave frequency range, published in [88].
- Development of calibration procedure for transmission coefficient measurements with the use of measuring systems incorporating two multipoints.
- Development of calibration procedure for transmission coefficient measurements using the measuring systems involving a single multipoint network, published in [85].
- Development of the algorithm for the determination of the minimum magnitude of the measured scattering parameters that can be measured with an arbitrary multipoint system, published in [81].
- Development of the procedure allowing for calculation of the magnitude and phase measurement error distribution for an arbitrary multipoint system, published in [81].
- Development of the multipoint measuring systems featuring tunable power distribution ensuring enhanced measurement accuracy, published in [82], [87].

In the view of the above listed achievements it can be concluded, that the theses stated in Introduction (Section 1.3) have been proved. It has been shown that Butler matrices can serve in multiport systems as power distribution networks, allowing for measurements of both reflection and transmission coefficients (thesis I). Moreover, the modification of measuring systems involving Butler matrices allowing for obtaining a scalable circle centers' distribution significantly increases the measurement accuracy (thesis II). Finally, utilizing the proposed procedures, an arbitrary multiport measuring system can be precisely calibrated in a multi-octave frequency band with the use of a set of phase shifters (thesis III).

The Author believes that the research results presented in the Thesis can be useful in further development of multiport measurement techniques, particularly in the context of growing field of applications for such measurement methods.

Further research on multiport measurement technique will be focused on methods allowing for widening of the operational frequency range. An interesting alternative for multiports composed of coupled-line couplers constitute the multiprobe reflectometers [14]. They feature very simple design, however, their bandwidth is very narrow. Recently it has been shown in [49], [64] and in [65] that by the application of increased number of non-uniformly distributed probes the operational frequency range can be significantly increased, which opens a new direction of multiport technique's development.

Another promising direction of further research can be found in the design of multiport systems featuring the circle centers' distribution composed of three circles arranged uniformly on the circumference of a circle (with the angular distances of  $120^\circ$ ). To date several such designs have been reported [105], [104], however, according to the analysis presented in the Thesis their measurement accuracy can be further increased. Moreover, their broadband realization is still an open issue.



## Author's Achievements

### JOURNAL PAPERS FOCUSED DIRECTLY ON THE DISSERTATION'S SUBJECT:

- K. Staszek, S. Gruszczynski and K. Wincza, "Broadband measurements of S-parameters utilizing 4 x 4 Butler matrices," *IEEE Transactions on Microwave Theory and Techniques*, vol. 61, no. 4, pp. 1692–1699, April 2013.
- K. Staszek, S. Gruszczynski and K. Wincza, "Theoretical limits and accuracy improvement of reflection coefficient measurements in six-port reflectometers," *IEEE Transactions on Microwave Theory and Techniques*, vol. 61, no. 8, pp. 2966–2974, August 2013.
- K. Staszek, S. Gruszczynski and K. Wincza, "Broadband measurements of S-parameters with the use of a single 8 x 8 Butler matrix," *IEEE Transactions on Microwave Theory and Techniques*, vol. 62, no. 2, pp. 352–360, February 2014.
- K. Staszek, S. Gruszczynski and K. Wincza, "Design and accuracy analysis of a broadband six-port reflectometer utilizing coupled-line directional couplers," *Microwave and Optical Technology Letters*, vol. 55, no. 7, pp. 1485–1490, July 2013.
- K. Staszek, S. Gruszczynski and K. Wincza, "Accurate broadband multiport reflectometer," *Microwave and Optical Technology Letters*, vol. 56, no. 12, pp. 2884–2887, December 2014.
- K. Staszek, S. Gruszczynski and K. Wincza, "Broadband Butler matrices with the use of high-pass LC sections as left-handed transmission lines," *Radioengineering*, vol. 23, no. 1, pp. 236–243, April 2014.

### JOURNAL PAPERS NOT RELATED TO THE DISSERTATION'S SUBJECT:

- K. Staszek, K. Wincza and S. Gruszczynski, "Multisection couplers with coupled-line sections having unequal lengths," *IEEE Transactions on Microwave Theory and Techniques*, vol. 62, no. 7, pp. 1461–1469, July 2014.
- K. Staszek, K. Wincza and S. Gruszczynski, "Phase property of matched lossless four-ports having central-symmetry and its application in coupled-line directional couplers," *IEEE Microwave and Wireless Components Letters*, vol. 24, no. 6, pp. 370–372, June 2014.

- K. Staszek, P. Kaminski, K. Wincza and S. Gruszczynski, "Reduced-length two-section directional couplers designed as coupled-line sections connected with the use of uncoupled lines," *IEEE Microwave and Wireless Components Letters*, vol. 24, no. 6, pp. 376–378, June 2014.
- J. Sorocki, K. Staszek, I. Piekarz, K. Wincza and S. Gruszczynski, "Directional couplers with reduced coupling requirements as a connection of coupled-line sections and left-handed transmission lines," *IET Microwaves, Antennas & Propagation*, vol. 8, no. 8, pp. 580–588, June 2014.
- K. Staszek, J. Sorocki, P. Kaminski, K. Wincza and S. Gruszczynski, "A broadband 3-dB tandem coupler utilizing right/left handed transmission line sections," *IEEE Microwave and Wireless Components Letters*, vol. 24, no. 4, pp. 236–238, April 2014.
- K. Staszek, S. Gruszczynski and K. Wincza, "Complex permittivity and permeability estimation by reflection measurements of open and short coaxial transmission line," *Microwave and Optical Technology Letters*, vol. 56, no. 3, pp. 727–732, March 2014.
- K. Staszek, K. Wincza and S. Gruszczynski, "Broadband three-section symmetrical directional couplers with reduced coupling coefficient requirements," *Microwave and Optical Technology Letters*, vol. 55, issue 3, pp. 639–645, March 2013.
- S. Gruszczynski, K. Wincza and K. Staszek, "Broadband waveguide-to-microstrip transition with coupled tuning elements," *Microwave and Optical Technology Letters*, vol. 54, no. 12, pp. 2787–2789, December 2012.

#### CONFERENCE COMMUNICATES FOCUSED DIRECTLY ON THE DISSERTATION'S SUBJECT:

- K. Staszek, S. Gruszczynski K. Wincza and A. Rydosz, "Broadband measurements of reflection coefficient with the use of Butler matrix," in *Proc. of International Microwave and Optoelectronics Conference IMOC 2013*, Rio de Janeiro, Brazil, August 2013, pp. 1–4.
- K. Staszek, P. Kaminski, A. Rydosz, S. Gruszczynski and K. Wincza, "A least-squares approach to the calibration of multiport reflectometers," in *Proc. of International Microwave & RF Conference IMaRC 2013*, New Delhi, India, December 2013, pp. 1–4.
- K. Staszek, S. Gruszczynski and K. Wincza, "Application of the 4 x 4 Butler matrix consisting of tapered-coupled-line directional couplers in an ultra-broadband multiport reflectometer," in *Proc. of The Second International Conference on Technological Advances in Electrical, Electronics and Computer Engineering TAECE 2014*, Kuala Lumpur, Malaysia, March 2014, pp. 1–6.
- K. Staszek, S. Gruszczynski and K. Wincza, "Ultra-broadband six-port reflectometer," in *Proc. of the 14th Mediterranean Microwave Symposium MMS 2014*, Marrakech, Morocco, December 2014, pp. 1–4.

- K. Staszek, S. Gruszczynski and K. Wincza, "Compact multiport system for broadband measurement of S-parameters," in *Proc. of German Microwave Conference GeMiC 2015*, Nuernberg, Germany, March 2015, pp. 1–4.

**CONFERENCE COMMUNICATES NOT RELATED TO THE DISSERTATION'S SUBJECT:**

- P. Kaminski, K. Staszek, K. Wincza and S. Gruszczynski, "K-band FMCW radar module with interferometric capability for industrial applications," in *Proc. of the 15th International Radar Symposium IRS 2014*, Gdansk, Poland 2014, pp. 1–4.
- K. Staszek, P. Kaminski, A. Rydosz, K. Wincza and S. Gruszczynski, "Broadband miniaturized Butler matrix utilizing left-handed transmission lines," in *Proc. of the 20th International Conference on Microwave, Radar and Wireless Communications MIKON 2014*, Gdansk, Poland 2014, pp. 1–4.
- K. Staszek, S. Gruszczynski and K. Wincza, "Design of multisection asymmetric coupled-line couplers with rotated tightly-coupled section and reduced coupling coefficient requirements," in *Proc. of International Conference on Technological Advances in Electrical, Electronics and Computer Engineering TAECE2014*, Kuala Lumpur, Malaysia 2014, pp. 7–11.
- K. Staszek, P. Kaminski, A. Rydosz, K. Wincza and S. Gruszczynski, "Miniaturized broadband three-section symmetrical directional coupler with reduced coupling coefficient requirements," in *Proc. of International Microwave & RF Conference IMArc 2013*, New Delhi, India 2013, pp. 1–4.
- I. Slomian, A. Rydosz, K. Staszek, K. Wincza and S. Gruszczynski, "Reduced sidelobe switched beam antenna array for driver's fatigue level Doppler sensor," in *Proc. of International Conference on Informatics, Electronics & Vision ICIEV 2013*, Dhaka, Bangladesh 2013, pp. 1–5.
- K. Staszek, L. Krawentek, K. Wincza and S. Gruszczynski, "Multibeam microwave Doppler sensor for application in driver's fatigue monitoring system," in *Proc. of the 12th Mediterranean Microwave Symposium MMS 2012*, Istanbul, Turkey 2012, pp. 1–4.
- K. Staszek, K. Wincza and S. Gruszczynski, "Driver's drowsiness monitoring system utilizing microwave Doppler sensor," in *Proc. of the 19th International Conference on Microwave, Radar and Wireless Communications MIKON 2014*, Warsaw, Poland 2012, pp. 623–626.
- K. Staszek and M. Bogusz, "Simple fringe pattern normalization algorithm," in *Proc. of the 11th IFAC/IEEE International Conference on Programmable Devices and Embedded Systems*, Brno, Czech Republic 2012, pp. 353–356.
- M. Bogusz and K. Staszek, "Phase unwrapping algorithm based on priorities setting," in *Proc. of the 11th IFAC/IEEE International Conference on Programmable Devices and Embedded Systems*, Brno, Czech Republic 2012, pp. 23–28.

- K. Staszek, S. Koryciak and M. Miskowicz, "Performance of send-on-delta sampling schemes with prediction," in *Proc. of IEEE International Symposium on Industrial Electronics ISIE 2011*, Gdansk, Poland 2011, pp. 2037–2042.

#### **PATENT APPLICATIONS:**

- S. Gruszczynski, K. Wincza and K. Staszek, "System for oneports' and multiports' scattering parameters measurements" no. P.400712, 2012.
- S. Gruszczynski, K. Wincza and K. Staszek, "Broadband directional coupler" no. P-400459, 2012.

#### **RESEARCH PROJECTS LED:**

- Research project awarded by the National Science Centre under Preludium 5 Program, entitled "Investigations on microwave passive networks for application in precise  $S$ -parameter multiport measurement techniques". ID project number 2013/09/N/ST7/01219. Project granted for 2014–2017.

#### **PARTICIPATION IN RESEARCH PROJECTS:**

- Research Project awarded by the National Centre for Research and Development in LIDER Program (first edition), entitled "System for driver's fatigue level assessment" – investigator. ID project number LIDER/16/66/L-1/NCBiR/2010. Project granted for 2009–2013.
- Research Project awarded by the Ministry of Science and Higher Education in Iuventus Plus Program (second edition), entitled, "Enhanced-precision measurement technique of scattering parameters utilizing broadband Butler matrices" – investigator. ID project number 0163/IP2/2011/71. Project granted for 2012–2013.
- Research Project awarded by the National Science Centre under Sonata Bis Program, entitled "Research on the transmission lines having negative phase velocity and their application to novel microwave circuits" – investigator. ID project number UMO-2011/01/D/ST7/00789. Project granted for 2011–2015.
- Research Project awarded by the Ministry of Science and Higher Education in Iuventus Plus Program (second edition), entitled, "Broadband microwave directional couplers realized in structures having decreased available coupling coefficient – synthesis methods, design and application to novel microwave electronics" – investigator. ID project number 0604/IP2/2011/71. Project granted for 2011–2015.

**PRIZES AND AWARDS:**

- Scholarship awarded by the Minister of Science and Higher Education for research achievements in 2014.
- Distinguished by the Rector of AGH University of Science and Technology for the research activities in 2013.
- DOCTUS scholarship for the best PhD students in Lesser Poland Region for awarded for 2012–2015.
- Scholarships for the best PhD students awarded for the 1<sup>st</sup>, 2<sup>nd</sup> and 3<sup>rd</sup> year of PhD studies.
- Faculty scholarships awarded for the 1<sup>st</sup>, 2<sup>nd</sup> and 3<sup>rd</sup> year of PhD studies.
- Pro-quality scholarships awarded for the 1<sup>st</sup>, 2<sup>nd</sup> and 3<sup>rd</sup> year of PhD studies.
- Dean's Grants awarded in 2012, 2013 and 2014.



## Bibliography

- [1] V. Adler and K. Hoffmann, "Six-port spatial electromagnetic wave measurement," *IEEE Transactions on Microwave Theory and Techniques*, vol. 62, no. 12, pp. 3161–3171, December 2014.
- [2] Agilent, "Vector Network Analyzer Uncertainty Calculator," <http://www.keysight.com/main/facet.jspx?t=80055.k.3&cc=PL&lc=eng&sm=g&sortKey=title>.
- [3] M. Begin, F. M. Ghannouchi, F. Beaugard, L. Selmi and B. Ricco, "Characterization of the transient behavior of a GaAs MESFET using dynamic I-V and S-parameter measurements," *IEEE Transactions on Instrumentation and Measurement*, vol. 45, no. 1, pp. 231–237, February 1996.
- [4] S. Bensmida, E. Bergeault, G. I. Abib and B. Huyart, "Power amplifier characterization: an active load-pull system based on six-port reflectometer using complex modulated carrier," *IEEE Transactions on Microwave Theory and Techniques*, vol. 54, no. 6, pp. 2707–2712, June 2006.
- [5] E. Bergeault, O. Gibrat, S. Bensmida and B. Huyart, "Multiharmonic source-pull/load-pull active setup based on six-port reflectometers: influence of the second harmonic source impedance on RF performances of power transistors," *IEEE Transactions on Microwave Theory and Techniques*, vol. 52, no. 4, pp. 1118–1124, April 2004.
- [6] M. E. Bialkowski, W. C. Khor and S. Crozier, "A planar microwave imaging system with step-frequency synthesized pulse using different calibration methods," *Microwave and Optical Technology Letters*, vol. 48, no. 3, pp. 511–516, March 2006.
- [7] V. Bilik, "Six-port measurement technique: principles, impact, applications," in *Proc. of International Conference Radioelektronika*, Bratislava, Slovak Republic, May 2002, pp. 1–32, invited paper.
- [8] M. Bona, L. Manholm, J. P. Starski and B. Svensson, "Low-loss compact Butler matrix for a microstrip antenna," *IEEE Transactions on Microwave Theory and Techniques*, vol. 50, no. 9, pp. 2069–2075, September 2002.
- [9] K. Brantervik and E. L. Kollberg, "A new four-port automatic network analyzer: part I – description and performance," *IEEE Transactions on Microwave Theory and Techniques*, vol. 33, no. 7, pp. 563–568, July 1985.

- [10] L. Brunetti, C. Fornero and G. Rietto, "Six-port reflectometer: influence of  $Q$ -points position in  $\Gamma$ -plane on sidearm power detector error propagation," *IEEE Transactions on Instrumentation and Measurement*, vol. 38, no. 2, pp. 484–487, April 1989.
- [11] J. Butler and R. Lowe, "Beam-forming matrix simplifies design of electronically scanned antennas," *Electronic Design*, vol. 9, pp. 170–173, April 1961.
- [12] F. P. Casares-Miranda, E. Márquez-Segura, P. Otero and C. Camacho-Penalosa, "Broadband six-port circuit for direction-finding applications," *Microwave and Optical Technology Letters*, vol. 43, no. 6, pp. 457–458, December 2004.
- [13] B. Centinoneri, Y. A. Atesal and G. M. Rebeiz, "An 8 x 8 Butler matrix in 0.13  $\mu\text{m}$  CMOS for 5–6-GHz multibeam applications," *IEEE Transactions on Microwave Theory and Techniques*, vol. 59, no. 2, pp. 295–301, February 2011.
- [14] K. Chang, M. Li and T. H. Sauter, "Low-cost microwave/millimeter-wave impedance measuring scheme using a three-probe microstrip circuit," *IEEE Transactions on Microwave Theory and Techniques*, vol. 38, no. 10, pp. 1455–1460, October 1990.
- [15] N. S. Chung, J. H. Kim and J. Shin, "A dual six-port automatic network analyzer and its performance," *IEEE Transactions on Microwave Theory and Techniques*, vol. 32, no. 12, pp. 1683–1686, December 1984.
- [16] H. M. Cronson and L. Susman, "A six-port network analyzer," *IEEE Transactions on Microwave Theory and Techniques*, vol. 25, no. 12, pp. 1086–1091, December 1977.
- [17] H. M. Cronson and L. Susman, "A dual six-port automatic network analyzer," *IEEE Transactions on Microwave Theory and Techniques*, vol. 29, no. 4, pp. 372–378, April 1981.
- [18] A. J. B. de Oliveira and S. P. X. Neto, "A single six-port reflectometer measures the scattering parameters of two-port microwave devices," in *Proc. of 25th European Microwave Conference EuMC 1995*, Bologna, Italy, September 1995, pp. 357–359.
- [19] T. Denidni and T. E. Libar, "Wide band four-port Butler matrix for switched multibeam antenna arrays," *14th IEEE Proceedings on Personal, Indoor and Mobile Radio Communications*, vol. 3, pp. 2461–2464, September 2003.
- [20] F. Deshours, E. Bergeault, L. Jallet and B. Huyart, "An active load-pull measurement system using two six-port reflectometers," *Microwave and Optical Technology Letters*, vol. 7, no. 14, pp. 679–684, October 1994.
- [21] F. Deshours, E. Bergeault, L. Jallet and B. Huyart, "Large signal load-pull measurements using six-port reflectometers," in *Conference on Precision Electromagnetic Measurements Digest*, Boulder, USA, June 1994, pp. 294–295.

- [22] A. Doghri, T. Djerafi, A. Ghiotto and K. Wu, "Broadband substrate-integrated-waveguide six-port applied to the development of polarimetric imaging radiometer," in *Proc. of 41st European Microwave Conference EuMC 2011*, Manchester, Great Britain, October 2011, pp. 393–396.
- [23] N. A. El-Deeb, "The calibration and performance of a microstrip six-port reflectometer," *IEEE Transactions on Microwave Theory and Techniques*, vol. 31, no. 7, pp. 509–514, July 1983.
- [24] G. F. Engen, "The six-port reflectometer: an alternative network analyzer," *IEEE Transactions on Microwave Theory and Techniques*, vol. 25, no. 12, pp. 1075–1080, December 1977.
- [25] G. F. Engen, "Calibrating the six-port reflectometer by means of sliding terminations," *IEEE Transactions on Microwave Theory and Techniques*, vol. 26, no. 12, pp. 951–957, December 1978.
- [26] G. F. Engen, "A least squares solution for use in the six-port measurement technique," *IEEE Transactions on Microwave Theory and Techniques*, vol. 28, no. 12, pp. 1473–1477, December 1980.
- [27] G. F. Engen, "A (historical) review of the six-port measurement technique," *IEEE Transactions on Microwave Theory and Techniques*, vol. 45, no. 12, pp. 2414–2417, December 1997.
- [28] G. F. Engen and C. A. Hoer, "Application of an arbitrary six-port junction to power-measurement problems," *IEEE Transactions on Instrumentation and Measurement*, vol. 21, no. 4, pp. 470–474, November 1972.
- [29] G. F. Engen and C. A. Hoer, "'Thru-Reflect-Line': an improved technique for calibrating the dual six-port automatic network analyzer," *IEEE Transactions on Microwave Theory and Techniques*, vol. 27, no. 12, pp. 987–993, December 1979.
- [30] S. C. Gao, L. W. Li, M. S. Leong and T. S. Yeo, "Integrated multibeam dual-polarized planar array," *IEE Proceedings Microwaves, Antennas and Propagation*, vol. 148, no. 3, pp. 174–178, June 2001.
- [31] F. Ghannouchi and A. Mohammadi, *The six-port technique*. Norwood, USA: Artech House, 2009.
- [32] F. M. Ghannouchi, F. Beaugard and A. B. Kouki, "Large-signal stability and spectrum characterization of a medium power HBT using active load-pull techniques," *IEEE Microwave and Guided Wave Letters*, vol. 4, no. 6, pp. 191–193, June 1994.
- [33] F. M. Ghannouchi and R. G. Bosisio, "Measurement of microwave permittivity using a six-port reflectometer with an open-ended coaxial line," *IEEE Transactions on Instrumentation and Measurement*, vol. 38, no. 2, pp. 505–508, April 1989.
- [34] S. Gruszczynski and K. Wincza, "Broadband multisection asymmetric 8.34-dB directional coupler with improved directivity," in *Proc. of Asia Pacific Microwave Conference APMC 2007*, Bangkok, Thailand, December 2007, pp. 1–4.

- [35] S. Gruszczynski and K. Wincza, "Design of high-performance broadband multisection symmetrical 3-dB directional coupler," *Microwave and Optical Technology Letters*, vol. 50, no. 3, pp. 636–638, March 2008.
- [36] S. Gruszczynski and K. Wincza, "Broadband 4 x 4 Butler matrices as a connection of symmetrical multisection coupled-line 3-dB directional couplers and phase correction networks," *IEEE Transactions on Microwave Theory and Techniques*, vol. 57, no. 1, pp. 1–9, January 2009.
- [37] S. Gruszczynski, K. Wincza and K. Sachse, "Broadband 4 x 4 Butler matrices utilizing tapered-coupled-line directional couplers," in *Proc. of Microwaves, Radar and Remote Sensing Symposium MRRS 2011*, Kiev, Ukraine, August 2011, pp. 77–81.
- [38] K. Haddadi and T. Lasri, "Six-port technology for millimeter-wave radar and imaging applications," in *Proc. of IEEE Topical Conference on Wireless Sensors and Sensor Networks WiSNet 2014*, Newport Beach, USA, January 2014, pp. 1–3.
- [39] H. Hayashi, D. A. Hitko and C. G. Sodini, "Four-element planar Butler matrix using half-wavelength open stubs," *IEEE Microwave and Wireless Components Letters*, vol. 12, no. 3, pp. 73–75, March 2002.
- [40] C. A. Hoer, "A network analyzer incorporating two six-port reflectometers," *IEEE Transactions on Microwave Theory and Techniques*, vol. 25, no. 12, pp. 1070–1074, December 1977.
- [41] C. A. Hoer, "Performance of a dual six-port automatic network analyzer," *IEEE Transactions on Microwave Theory and Techniques*, vol. 27, no. 12, pp. 993–998, December 1979.
- [42] C. A. Hoer, "A high-power dual six-port automatic network analyzer used in determining biological effects of RF and microwave radiation," *IEEE Transactions on Microwave Theory and Techniques*, vol. 29, no. 12, pp. 1356–1364, December 1981.
- [43] J. D. Hunter and P. I. Somlo, "S-parameter measurements with a single six-port," *Electronic Letters*, vol. 21, no. 4, pp. 157–158, February 1985.
- [44] B. Huyart, J. Laurin, R. G. Bosisio and D. Roscoe, "A direction-finding antenna system using an integrated six-port circuit," *IEEE Transactions on Antennas and Propagation*, vol. 43, no. 12, pp. 1508–1512, December 1995.
- [45] S. Jia, "New application of a single six-port reflectometer," *Electronic Letters*, vol. 20, no. 22, pp. 920–922, October 1984.
- [46] C. Jiang, S. Jia and Q. Zhang, "A six-port technique application of measuring complex permittivity and permeability," *Microwave and Optical Technology Letters*, vol. 4, no. 9, pp. 376–378, August 1991.
- [47] S. R. Judah and A. S. Wright, "A dual six-port automatic network analyzer incorporating a biphasic - bimodulation element," *IEEE Transactions on Microwave Theory and Techniques*, vol. 38, no. 3, pp. 238–244, March 1990.

- [48] J. R. Juroshek and C. A. Hoer, "A high-power automatic network analyzer for measuring the RF power absorbed by biological samples in a TEM cell," *IEEE Transactions on Microwave Theory and Techniques*, vol. 32, no. 8, pp. 818–824, August 1984.
- [49] B. M. Kats, A. A. Lvov, V. P. Meschanov, E. M. Shatalov and L. V. Shikova, "Synthesis of a wideband multiprobe reflectometer," *IEEE Transactions on Microwave Theory and Techniques*, vol. 56, no. 2, pp. 507–514, February 2008.
- [50] W. C. Khor, M. E. Bialkowski, A. M. Abbosh, N. Seman and S. Crozier, "An ultra wideband microwave imaging system for breast cancer detection," *IEICE Transactions On Communications*, vol. E90-B, no. 9, pp. 2376–2381, September 2007.
- [51] K. Kim, N. Kim, S.-H. Hwang, Y.-K. Kim and Y. Kwon, "A miniaturized broadband multi-state reflectometer integrated on a silicon MEMS probe for complex permittivity measurement of biological material," *IEEE Transactions on Microwave Theory and Techniques*, vol. 61, no. 5, pp. 2205–2214, May 2013.
- [52] A. Koelpin, G. Vinci, B. Laemmle, D. Kissinger and R. Weigel, "The six-port in modern society," *IEEE Microwave Magazine*, vol. 11, no. 7, pp. 35–43, December 2010.
- [53] A. Koelpin, G. Vinci, B. Laemmle, S. Lindner, F. Barbon and R. Weigel, "The six-port technology for traffic safety," *IEEE Microwave Magazine*, vol. 13, no. 3, pp. 118–127, IMS Special Issue, May 2012.
- [54] A. Koelpin and R. Weigel, "Six-port based direction finding and ranging," in *Proc. of 20th International Conference on Microwaves, Radar & Wireless Communications MIKON 2014*, Gdansk, Poland, June 2014, pp. 1–5, invited paper.
- [55] D. I. Kraker, "Asymmetric coupled-transmission-line Magic-T," *IEEE Transactions on Microwave Theory and Techniques*, vol. 12, no. 6, pp. 595–599, November 1964.
- [56] B. Laemmle, K. Schmalz, J. Borngraeber, J. C. Scheytt, R. Weigel, A. Koelpin and D. Kissinger, "A fully integrated 120-GHz six-port receiver front-end in a 130-nm SiGe BiCMOS technology," in *Proc. of IEEE 13th Topical Meeting on Silicon Monolithic Integrated Circuits in RF Systems SiRF 2013*, Austin, USA, January 2013, pp. 129–131.
- [57] B. Laemmle, G. Vinci, L. Maurer, R. Weigel and A. Koelpin, "A 77-GHz SiGe integrated six-port receiver front-end for angle-of-arrival detection," *IEEE Journal of Solid-State Circuits*, vol. 47, no. 9, pp. 1966–1973, September 2012.
- [58] F. Lan, C. Akyel, F. M. Ghannouchi, J. Gauthier and S. Khouaja, "A six-port based on-line measurement system using special probe with conical open end to determine relative complex permittivity at radio and microwave frequencies," in *Proc. of the 16th IEEE Instrumentation and Measurement Technology Conference IMTC99*, Venice, Italy, May 1999, pp. 42–47.

- [59] K. Levenberg, "A method for the solution of certain problems in least-squares," *Quarterly Applied Math*, vol. 2, pp. 164–168, 1944.
- [60] S. Li and R. G. Bosisio, "Calibration of multiport reflectometers by means of four open/short circuits," *IEEE Transactions on Microwave Theory and Techniques*, vol. 30, no. 7, pp. 1085–1090, July 1982.
- [61] W. Lin and C. Ruan, "Measurement and calibration of a universal six-port network analyzer," *IEEE Transactions on Microwave Theory and Techniques*, vol. 37, no. 4, pp. 734–742, April 1989.
- [62] S. E. Lipsky, *Microwave passive direction finding*. New York, USA: John Wiley & Sons Inc., 1987.
- [63] H.-C. Lu and T.-H. Chu, "Microwave diversity imaging using six-port reflectometer," *IEEE Transactions on Microwave Theory and Techniques*, vol. 47, no. 1, pp. 84–87, January 1999.
- [64] G. Madonna, A. Ferrero and M. Pirola, "Design of a broadband multiprobe reflectometer," *IEEE Transactions on Instrumentation and Measurement*, vol. 48, no. 2, pp. 622–625, April 1999.
- [65] G. Madonna, A. Ferrero and M. Rostagno, "A new approach to the design of wide-band multiprobe reflectometers," in *IEEE Conference on Precision Electromagnetic Measurements Digest*, Washington, USA, July 1998, pp. 424–425.
- [66] D. Marquardt, "An algorithm for least-squares estimation of nonlinear parameters," *Journal of the Society for Industrial and Applied Mathematics*, vol. 11, no. 2, pp. 431–441, June 1963.
- [67] E. Moldovan, S. O. Tatu, T. Gaman, K. Wu and R. G. Bosisio, "A new 94-GHz six-port collision-avoidance radar sensor," *IEEE Transactions on Microwave Theory and Techniques*, vol. 52, no. 3, pp. 751–759, March 2004.
- [68] J. Monzo-Cabrera, J. L. Pedreno-Molina, A. Lozano-Guerrero and A. Toledo-Moreo, "A novel design of a robust ten-port microwave reflectometer with autonomous calibration by using neural networks," *IEEE Transactions on Microwave Theory and Techniques*, vol. 56, no. 12, pp. 2972–2978, December 2008.
- [69] A. O. Olopade, A. Hasan and M. Helaoui, "Concurrent dual-band six-port receiver for multi-standard and software defined radio applications," *IEEE Transactions on Microwave Theory and Techniques*, vol. 61, no. 12, pp. 4252–4261, December 2013.
- [70] J. A. Paul, "Wideband millimeter-wave impedance measurements," *Microwave Journal*, vol. 26, pp. 95–102, April 1983.
- [71] J. A. Paul and P. C. H. Yen, "Millimeter-wave passive components and six-port network analyzer in dielectric waveguide," *IEEE Transactions on Microwave Theory and Techniques*, vol. 29, no. 9, pp. 948–953, September 1981.

- [72] P. Perez-Lara, J. A. Medina-Rodriguez, I. Molina-Fernandez, J. G. Wanguemert-Perez and A. Gonzalez-Salguero, "Wideband homodyne six-port receiver with high LO-RF isolation," *IET Microwaves, Antennas & Propagation*, vol. 3, no. 5, pp. 882–888, August 2009.
- [73] P. J. Probert and J. Carroll, "Design features of multi-port reflectometers," *Microwaves, Optics and Antennas*, vol. 129, no. 5, pp. 245–252, October 1982.
- [74] J. L. R. Quirarte and J. P. Starski, "Synthesis of Schiffman phase shifters," *IEEE Transactions on Microwave Theory and Techniques*, vol. 39, no. 11, pp. 1885–1889, November 1991.
- [75] G. P. Riblet and E. R. B. Hansson, "Aspects of the calibration of a single six-port using a load and offset reflection standards," *IEEE Transactions on Microwave Theory and Techniques*, vol. 30, no. 12, pp. 2120–2125, December 1982.
- [76] G. Riddels and V. F. Fusco, "A quasilumped six-port reflectometer for cellular radio use," *Microwave and Optical Technology Letters*, vol. 4, no. 5, pp. 191–194, April 1991.
- [77] B. M. Schiffman, "A new class of broadband microwave 90-degree phase shifters," *IRE Transactions on Microwave Theory and Techniques*, vol. 6, no. 2, pp. 232–237, April 1958.
- [78] J. Shelton and K. Kelleher, "Multiple beams from linear arrays," *IRE Transactions on Antennas and Propagation*, vol. 9, no. 2, pp. 154–161, March 1961.
- [79] K. Staszek, S. Gruszczynski and K. Wincza, "Broadband measurements of S-parameters utilizing 4 x 4 Butler matrices," *IEEE Transactions on Microwave Theory and Techniques*, vol. 61, no. 4, pp. 1692–1699, April 2013.
- [80] K. Staszek, S. Gruszczynski and K. Wincza, "Design and accuracy analysis of a broadband six-port reflectometer utilizing coupled-line directional couplers," *Microwave and Optical Technology Letters*, vol. 55, no. 7, pp. 1485–1490, July 2013.
- [81] K. Staszek, S. Gruszczynski and K. Wincza, "Theoretical limits and accuracy improvement of reflection coefficient measurements in six-port reflectometers," *IEEE Transactions on Microwave Theory and Techniques*, vol. 61, no. 8, pp. 2966–2974, August 2013.
- [82] K. Staszek, S. Gruszczynski and K. Wincza, "Accurate broadband multiport reflectometer," *Microwave and Optical Technology Letters*, vol. 56, no. 12, pp. 2884–2887, December 2014.
- [83] K. Staszek, S. Gruszczynski and K. Wincza, "Application of the 4 x 4 Butler matrix consisting of tapered-coupled-line directional couplers in an ultra-broadband multiport reflectometer," in *Proc. of The Second International Conference on Technological Advances in Electrical, Electronics and Computer Engineering TAECE 2014*, Kuala Lumpur, Malaysia, March 2014, pp. 1–6.
- [84] K. Staszek, S. Gruszczynski and K. Wincza, "Broadband Butler matrices with the use of high-pass LC sections as left-handed transmission lines," *Radioengineering*, vol. 23, no. 1, pp. 236–243, April 2014.

- [85] K. Staszek, S. Gruszczynski and K. Wincza, "Broadband measurements of S-parameters with the use of a single 8 x 8 Butler matrix," *IEEE Transactions on Microwave Theory and Techniques*, vol. 62, no. 2, pp. 352–360, February 2014.
- [86] K. Staszek, S. Gruszczynski and K. Wincza, "Ultra-broadband six-port reflectometer," in *Proc. of the 14th Mediterranean Microwave Symposium MMS 2014*, Marrakech, Morocco, December 2014, pp. 1–4.
- [87] K. Staszek, S. Gruszczynski and K. Wincza, "Compact multiport system for broadband measurement of S-parameters," in *Proc. of German Microwave Conference GeMiC 2015*, Nuernberg, Germany, March 2015, pp. 1–4.
- [88] K. Staszek, S. Gruszczynski, K. Wincza and A. Rydosz, "Broadband measurements of reflection coefficient with the use of Butler matrix," in *Proc. of International Microwave and Optoelectronics Conference IMOC 2013*, Rio de Janeiro, Brazil, August 2013, pp. 1–4.
- [89] K. Staszek, P. Kaminski, A. Rydosz, S. Gruszczynski and K. Wincza, "A least-squares approach to the calibration of multiport reflectometers," in *Proc. of International Microwave & RF Conference IMaRC 2013*, New Delhi, India, December 2013, pp. 1–4.
- [90] U. Stumper, "Six-port and four-port reflectometers for complex permittivity measurements at submillimeter wavelengths," *IEEE Transactions on Microwave Theory and Techniques*, vol. 37, no. 1, pp. 222–230, January 1989.
- [91] S. O. Tatu and T. A. Denidni, "A new beam direction finding circuit based on six-port technology," in *IEEE MTT-S International Microwave Symposium Digest*, Long Beach, USA, June 2005, pp. 581–584.
- [92] S. O. Tatu, E. Moldovan, K. Wu and R. G. Bosisio, "A new direct millimeter-wave six-port receiver," *IEEE Transactions on Microwave Theory and Techniques*, vol. 49, no. 12, pp. 2517–2522, December 2001.
- [93] G. Tudosie, R. Vahldieck and A. Lu, "A novel modularized folded highly compact LTCC Butler matrix," in *IEEE MTT-S International Microwave Symposium Digest*, Atlanta, USA, June 2008, pp. 691–694.
- [94] K. Wincza and S. Gruszczynski, "A broadband 4 x 4 Butler matrix for modern-day antennas," in *Proc. of 35th European Microwave Conference EuMC 2005*, Paris, France, October 2005, pp. 1331–1334.
- [95] K. Wincza, S. Gruszczynski and K. Sachse, "Broadband planar fully integrated 8 x 8 Butler matrix using coupled-line directional couplers," *IEEE Transactions on Microwave Theory and Techniques*, vol. 59, no. 10, pp. 2441–2446, October 2011.

- [96] K. Wincza, S. Gruszczynski and K. Sachse, "Ultrabroadband 4 x 4 Butler matrix with the use of multisection coupled-line directional couplers and phase shifters," in *Proc. of Microwaves, Radar and Remote Sensing Symposium MRRS 2011*, Kiev, Ukraine, August 2011, pp. 118–122.
- [97] K. Wincza, S. Gruszczynski, K. Sachse and S. Kuta, "Ultrabroadband 8 x 8 Butler matrix designed with the use of multisection directional couplers and phase correction networks," *Microwave and Optical Technology Letters*, vol. 54, no. 6, pp. 1375–1380, June 2012.
- [98] K. Wincza and K. Sachse, "Broadband 4 x 4 Butler matrix in microstrip multilayer technology designed with the use of three-section directional couplers and phase correction networks," in *Proc. of 18th International Conference on Microwave Radar and Wireless Communication MIKON 2010*, Vilnius, Lithuania, June 2010, pp. 1–4.
- [99] S. M. Winter, A. Koelpin and R. Weigel, "Six-port receiver analog front-end: multilayer design and system simulation," *IEEE Transactions on Circuits and Systems II: Express Briefs*, vol. 55, no. 3, pp. 254–258, March 2008.
- [100] D. Woods, "Analysis and calibration theory of the general 6-port reflectometer employing four amplitude detectors," *IEEE Proceedings*, vol. 126, no. 2, pp. 221–228, February 1979.
- [101] L. Xiao-Ming, "Measurement of two-port networks by a single six-port reflectometer," in *Proc. of International Conference on Millimeter Wave and Far-Infrared Technology ICMWFT 1989*, Beijing, China, June 1989, pp. 370–373.
- [102] X. Xu, R. G. Bosisio and K. Wu, "Analysis and implementation of six-port software-defined radio receiver platform," *IEEE Transactions on Microwave Theory and Techniques*, vol. 54, no. 7, pp. 2937–2943, July 2006.
- [103] T. Yakabe, X. Fengchao, K. Iwamoto, F. M. Ghannouchi, K. Fujii and H. Yabe, "Six-port based wave-correlator with application to beam direction finding," *IEEE Transactions on Instrumentation and Measurement*, vol. 50, no. 2, pp. 377–380, April 2001.
- [104] J. J. Yao, Y. Chen and S. P. Yeo, "Modifying hybrid coupler design to enhance six-port reflectometer performance," in *Proc. of 35th European Microwave Conference EuMC 2005*, Paris, France, October 2005, pp. 256–259.
- [105] J. J. Yao and S. P. Yeo, "Six-port reflectometer based on modified hybrid couplers," *IEEE Transactions on Microwave Theory and Techniques*, vol. 56, no. 2, pp. 493–498, February 2008.
- [106] T. Zak and K. Sachse, "An integrated Butler matrix in multi-layer technology for multi-port amplifier applications," in *Proc. of 14th International Conference on Microwaves, Radar & Wireless Communications MIKON 2002*, Gdansk, Poland, May 2002, pp. 59–62.